Springer Series in Light Scattering

Alexander Kokhanovsky *Editor*

Springer Series in Light Scattering

Volume 8: Light Polarization and Multiple Scattering in Turbid Media

Springer

Springer Series in Light Scattering

The main purpose of is to present recent advances and progress in light scattering media optics. The topic is very broad and incorporates such diverse areas as atmospheric optics, ocean optics, optics of close-packed media, radiative transfer, light scattering, absorption, and scattering by single scatterers and also by systems of particles, biomedical optics, optical properties of cosmic dust, remote sensing of atmosphere and ocean, etc. The topic is of importance for material science, environmental science, climate change, and also for optical engineering. Although main developments in the solutions of radiative transfer and light scattering problems have been achieved in the 20th century by efforts of many scientists including V. Ambartsumian, S. Chandrasekhar, P. Debye, H. C. van de Hulst, G. Mie, and V. Sobolev, the light scattering media optics still have many puzzles to be solved such as radiative transfer in closely packed media, 3D radiative transfer as applied to the solution of inverse problems, optics of terrestrial and planetary surfaces, etc. Also it has a broad range of applications in many branches of modern science and technology such as biomedical optics, atmospheric and oceanic optics, and astrophysics, to name a few. It is planned that the Series will raise novel scientific questions, integrate data analysis, and offer new insights in optics of light scattering media. ***SPRINGER Series in Light Scattering***.

Alexander Kokhanovsky
Editor

Springer Series in Light Scattering

Volume 8: Light Polarization and Multiple Scattering in Turbid Media

Springer

Editor
Alexander Kokhanovsky
Max Planck Institute for Chemistry
Mainz, Germany

ISSN 2509-2790 ISSN 2509-2804 (electronic)
Springer Series in Light Scattering
ISBN 978-3-031-10297-4 ISBN 978-3-031-10298-1 (eBook)
https://doi.org/10.1007/978-3-031-10298-1

© The Editor(s) (if applicable) and The Author(s), under exclusive license to Springer Nature Switzerland AG 2022
This work is subject to copyright. All rights are solely and exclusively licensed by the Publisher, whether the whole or part of the material is concerned, specifically the rights of translation, reprinting, reuse of illustrations, recitation, broadcasting, reproduction on microfilms or in any other physical way, and transmission or information storage and retrieval, electronic adaptation, computer software, or by similar or dissimilar methodology now known or hereafter developed.
The use of general descriptive names, registered names, trademarks, service marks, etc. in this publication does not imply, even in the absence of a specific statement, that such names are exempt from the relevant protective laws and regulations and therefore free for general use.
The publisher, the authors, and the editors are safe to assume that the advice and information in this book are believed to be true and accurate at the date of publication. Neither the publisher nor the authors or the editors give a warranty, expressed or implied, with respect to the material contained herein or for any errors or omissions that may have been made. The publisher remains neutral with regard to jurisdictional claims in published maps and institutional affiliations.

This Springer imprint is published by the registered company Springer Nature Switzerland AG
The registered company address is: Gewerbestrasse 11, 6330 Cham, Switzerland

Contents

Multiple-Path Model of Reflection and Transmission for a Turbid Slab

Geoffrey Rogers

Abstract The multiple-path model of reflection from and transmission through a turbid slab is based on a photon random walk within the slab. In turbid media, light undergoes multiple scattering and each displacement of a photon between scatters is a step in a random walk. The walk ends when the photon reaches a boundary—it is a reflected photon if the photon crosses the surface upon which the light is incident, it is transmitted if it crosses the opposite surface. If the slab has internal reflection, there is a nonzero probability that the photon will step back into the slab when it reaches a boundary and continue its walk. The absorption depends on path length, and the path length is proportional to the number of steps the photon takes before exiting the slab. If the medium is absorptive, the Bouguer law is applied to each path, and the reflectance or transmittance is the probability flux through the surface summed over all paths, each path weighted by the probability of a path of that length. The probability flux is obtained from the path length probability density by Fick's law. The path length probability density for a photon's location is developed. The path length probability density is the probability a the photon is located at a point $\mathbf{r}$ after having walked a distance ξ. The random walk occurs in three dimensions, but the number of steps taken depends only on the walker's motion along the z-axis, since the walk ends when the walker's location is at $z = 0$, the surface of incidence, or $z = t$, the opposite surface where $t =$ thickness of the slab. Therefore the problem is reduced to a random walk with variable step size in one dimension. Two experimentally verified applications of the multiple-path model are discussed: the spectral reflectance of fabric dyed with a mixture of dyes and the diffusion of light within paper. In both applications the multiple-path model is able to accurately predict the experimental measurements.

G. Rogers (✉)
Fashion Institute of Technology, State University of New York,
227 W 27 St, New York City, NY, USA
e-mail: geoffrey_rogers@fitnyc.edu

A. Kokhanovsky (ed.), *Springer Series in Light Scattering*, Springer Series
in Light Scattering, https://doi.org/10.1007/978-3-031-10298-1_1

1 Introduction

There has been interest for some time in calculating the reflectance from and transmission through a colorant layer—a slab consisting of a colorant that selectively absorbs to produce color. Such colorant layers include paint, dyed fabric, gels, and other transparent or non-transparent media of finite thickness and infinite perpendicular extent. There has been interest in the coatings industry, in the textile industry, in printing, and in any systematic application of colorant to give an object color. When the colorant is applied to an object, it often forms a layer—the colorant layer. The colorant layer may be transparent, as is the case with gels or ink on paper, or it may be turbid as is the case with paint or dyed fabric.

If the slab is transparent—no scatter—the reflectance and transmittance of direct light can be predicted by Bouguer law, in which, due to absorption, the radiant intensity decreases by an exponential factor as a function of path length through the medium. If the colorant layer is turbid the Bouguer law cannot be directly used: light is scattered as well as absorbed. Total absorption still depends on path length, but due to scatter and diffusion within the medium, the path length is different for different paths.

A number of techniques have been developed to calculation the reflectance and transmission in such cases of non-transparent media, in particular radiative transfer theory (RT). RT does not admit an analytic solution, except under certain simplifying assumptions (Ishimaru 1978; Groenhuis et al. 1983), but a stable numerical solution has been developed—the discrete ordinate method (Stamnes et al. 1988)—which is widely used. A variety of Monte-Carlo methods have been developed (Wang et al. 1995). An asymptotic analysis of the radiative transfer equation has been made to model the optics of snow (Kokhanovsky 2006).

Light reflection from and transmitted through a turbid slab has been investigated previously (Contini et al. 1997; Keijzer et al. 1988; Farrell et al. 1992). In these models the radiant intensity is found as a solution to the diffusion equation, specifically the diffusion, or P1, approximation to RT (Groenhuis et al. 1983; Kienle et al. 1996; Ishimaru 1978; Chandrasekhar 1960). The multiple-path model of photon migration through turbid media discussed here is similar to models obtained by solution of the diffusion equation, however a major difference is the treatment of photon interaction with slab boundaries.

The assumptions in the multiple-path model are the same as those in RT theory: the distance between scatters is much greater than a wavelength of visible light, and the light is incoherent so interference effects can be ignored and there is no polarization. The light consists of "billiard balls"—photons—that ellastically interact with scatterers.

The multiple-path model of reflection and transmission treats the propagation of light within turbid media as a photon random walk (Rogers 2016; Gandjbakhche and Weiss 1995b, a). The migration of a photon through a disordered medium involves multiple scatterings: the distance traveled between scatters is a step in the random walk. The walk begins when the photon enters the slab and ends when the photon exits the slab: it is reflected if it exits the slab from the surface into which it entered the slab, and it is transmitted if it exits the opposite side. For each path the number of steps taken before exiting the slab is proportional to the path length: Bouguer law is applied to each path, and all paths are summed over weighted by the probability of a path of that length.

A photon takes a random walk in three dimensions. Each step of the walk is the displacement the photon undergoes between scatterings—after each scatter the photon takes a random step: i.e. it travels a random distance in a random direction determined by probability densities, then it scatters again, taking another random step. The model assumes isotropic scattering and the probability density for the step size is exponential. Photons are normally incident on a plane parallel layer of turbid media with physical thickness t.

The medium is characterized by the scattering mean free path $l^* =$ the average distance the photon travels between scatters, and an absorption coefficient $\sigma_a =$ probability per unit length that the photon is absorbed as it travels through the turbid medium. The slab has a thickness t which is larger than the scattering mean free path: $t > l^*$.

The random walk begins at a distance of one mean free path from the surface of the slab upon which the light is incident, and the walk ends when the photon steps through one of the surfaces. If it steps through the surface of incidence it is a reflected photon, or through the opposite surface it is a transmitted photon. On stepping through the surface, there is a probability that the photon steps back into the slab to resume its random walk: it is internally reflected (Singer et al. 2008). To obtain the reflectance or transmittance, one sums over all possible paths a photon may take before exiting the slab. If the medium is absorptive, one applies Bouguer law to each path in the process of summing (Gandjbakhche and Weiss 1995b).

Because the walk begins one mean free path into the layer and scattering is isotropic, the reflectance and transmittance are the diffuse reflectance and diffuse transmittance under normal light illumination. And because scattering is isotropic, the angle of incidence of the incident light does not play a role, except to alter the distance from the slab surface at which the walk begins. The reflectance calculated here is the reflectance of body rays—light which has entered the body of the turbid slab. If there is a difference in index of refraction between air and the slab medium, the total reflectance includes body and surface rays. The surface rays are the light reflected upon change in index from air to slab and may be specular or diffuse, depending on the slab surface texture.

The multiple-path model has been experimentally validated by determining the spectral reflectance of dye mixtures in cotton fabric (Rogers et al. 2017) and by measuring the diffusion of light within paper (Rogers et al. 2019). In both paper and fabric, the turbid slab is fibers in air—photons travel though air and scatter off the fibers within the slab. There is no internal refection when the light passes from the slab into the surrounding medium, which is air. This is not the case for translucent media such as the structures created by 3-D printing. To use the multiple-path model to determine the color of such a translucent slab, one must include the effects of internal reflection at the slab boundaries.

A major difference between this model and models based on solutions to the diffusion equation, is how boundaries are handled. Photon reflection from and transmission through a turbid slab has been investigated previously (Contini et al. 1997; Keijzer et al. 1988; Farrell et al. 1992). In these models the radiant intensity is found as a solution to the diffusion equation, specifically the diffusion, or P1, approximation to radiative transfer equation (Groenhuis et al. 1983; Kienle et al. 1996; Rogers 2015). The multiple-path model of photon migration through turbid media is similar to models obtained by solution of the diffusion equation, however a major difference is the treatment of photon interaction with boundaries. In undergoing a random walk, when a photon reaches a slab boundary it may step through the boundary in which case the walk ends, or if there is internal reflection there is a probability the photon may step back into the slab and continue the walk.

The article is organized as follows: In Sect. 2 it is shown that the reflectance and transmittance can be calculated as a probability flux through the slab surface. A key quantity that characterizes the photon random walk is the probability density for photon's position, and Fick's law gives the flux through the surface. The form of the probability density is determined by the boundary conditions. In Sect. 3 the expressions for reflectance and transmittance for the case of no internal reflection are derived. In Sects. 4 and 5 experimental verification of the multiple-path model for the case of no internal reflection are outlined. Discussed are experiments whose outcomes were predicted using the multiple-path model. Section 4 outlines an experiment in which fabric dyed with a mixture of dyes was measured. Section 5 discusses an experiment in which the diffusion of light in paper was measured. The multiple-path model is extended in Sect. 6 to include internal reflection at the slab boundaries. It is shown that internal reflection significantly affects reflection but has negligible affect on transmission. In Sect. 6.7 plots are shown of the results for reflection and transmission with and without internal reflection. Plots are shown comparing the predictions of the multiple-path model to Monte-Carlo simulations of photon interaction with a turbid slab. In the Conclusion, Sect. 7, the results are summarized.

2 Probability Flux, Reflection, and Transmission

A key quantity in the multiple-path model is the path-length probability density, $P(\xi; \mathbf{r})$, which is the probability that a photon is located at a certain point $\mathbf{r}$ after having "walked" a distance ξ. The slab's reflectance or transmittance is the probability flux from within the slab to outside the slab at the boundary, and the probability flux is obtained from the path length probability density, $P(\xi; \mathbf{r})$, using Fick's law. The reflectance is the probability flux through the surface of incidence and the transmittance is the probability flux through the opposite surface. It is assumed that optical properties of the turbid medium do not depend on $\mathbf{r}$.

As shown below, the three dimensional random walk is reduced to a random walk in one dimension, because one is interested only in motion along the z-axis as the walk ends when the z-coordinate is 0 or t. Due to the symmetry of the model, the probability is constant in the x, y plane. Therefore the quantity of interest is $P_z(\xi; z) = \int P(\xi; \mathbf{r})\,\mathrm{d}\boldsymbol{\rho}$ with $\mathrm{d}\boldsymbol{\rho} = \rho\,\mathrm{d}\phi\,\mathrm{d}\rho$ where ρ is the radial coordinate and ϕ the azimuthal angle of a cylindrical coordinate system. The quantity $P_z(\xi; z)$ is the probability the walker has longitudinal coordinate z after walking a distance ξ.

The flux $\mathcal{J}$ through the surface $z = 0$ or t is proportional to the normal derivative:

$$\mathcal{J}(\xi; z) = \pm D \frac{\mathrm{d}}{\mathrm{d}z} P_z(\xi; z) \quad \Bigg|_{z=0,t} \tag{1}$$

where $+$ is for $z = 0$ and $-$ is for $z = t$, and the diffusion coefficient is $D = l^{*2}/2\Delta t$, with $\Delta t =$ the average time between scatters, which for simplicity is set to 1. One writes D as:

$$D = \frac{l^{*2}}{2}. \tag{2}$$

If the medium is absorptive, however, the flux will be reduced, according to the Bouguer law, by the factor $\exp(-\sigma_a \xi)$ where σ_a is the absorption coefficient, so that:

$$\mathcal{J}(\xi; z) = \pm D \, \frac{\mathrm{d}}{\mathrm{d}z} P_z(\xi; z) \exp(-\sigma_a \xi) \quad \Bigg|_{z=0,t}. \tag{3}$$

The total transmission through the boundary is found by summing over all path lengths ξ:

$$\mathcal{J}(z) = \int_0^\infty \mathcal{J}\xi; z)\mathrm{d}\xi. \tag{4}$$

The reflectance is equal to the probability flux through the boundary at $z = 0$ and the transmittance is the probability flux through $z = t$:

$$R = \mathcal{J}(0), \qquad T = \mathcal{J}(t). \tag{5}$$

2.1 Path Length Probability Density

The probability flux at any point within the turbid slab is obtained as the gradient of the photon path-length probability density at the point (Fick's law). The probability density at the point $\mathbf{r}$ is proportional to the probability that a photon is located at $\mathbf{r}$ within the volume $\mathrm{d}^3\mathbf{r}$. Because the multiple-path model uses Bouguer law to determine the absorption, one is interested in the probability density of photons that have traveled a distance ξ within the slab before arriving at point $\mathbf{r}$. In the following, the path-length probability is obtained by considering a random walk. One first considers the case of no internal reflection at the slab boundaries, in Sect. 6 below the results are generalized to include internal reflection.

The photon random walk begins at $z = z_0$. The walk ends when the z-coordinate is $z < 0$, which case the photon is reflected, or when the z-coordinate is $z > t$ in which case the photon is transmitted. The total distance the photon has traveled after n scatterings, L_n is equal to the sum of distances traveled between each scattering: $L_n = \sum_k^n l_k$, where l_k is the magnitude of the photon displacement between the $k-1$ and k scatterings. The l_k are independent, identically distributed random variables with probability density

$$w(l) = \gamma_s \exp(-\gamma_s l) \tag{6}$$

where γ_s is the scattering coefficient and its inverse: $\gamma_s^{-1} = l^* =$ scattering mean free path—the average distance traveled between scatterings:

$$l^* = \langle l \rangle = \int_0^\infty l\, w(l)\, \mathrm{d}l = \gamma_s^{-1}. \tag{7}$$

One identifies the average distance traveled after n scatterings with the path length ξ. In the following one obtains the probability of traveling a distance L after taking n scatters (steps) using Eq. (6). The probability that the walker, having started at the origin is located at r after one step is:

$$p_1(r) = \gamma_s \exp(-\gamma_s r)$$

The probability the walker is located at r after 2 steps is

$$\begin{aligned} p_2(r) &= \int_0^r p_1(r-r')p_1(r')\,\mathrm{d}r' \\ &= \gamma_s^2 \int_0^r \exp(\big[-\gamma_s(r-r')\big]\exp(-\gamma_s r')\,\mathrm{d}r' \\ &= \gamma_s^2\, r \exp(-\gamma_s r) \end{aligned} \tag{8}$$

The probability the walker is located at r after 3 steps is

$$\begin{aligned} p_3(r) &= \int_0^r p_1(r-r')p_2(r')\,\mathrm{d}r' \\ &= \gamma_s^3 \int_0^r \exp(\big[-\gamma_s(r-r')\big]\, r' \exp(-\gamma_s r')\,\mathrm{d}r' \\ &= \gamma_s^3\, \frac{r^2}{2} \exp(-\gamma_s r) \end{aligned} \tag{9}$$

Proceeding in a similar way, the probability the walker is located at r after n steps is

$$\begin{aligned} p_n(r) &= \int_0^r p_1(r - r')p_{n-1}(r')\,\mathrm{d}r' \\ &= \gamma_s^n \,\frac{r^{n-1}}{(n-1)!}\exp(-\gamma_s r) \end{aligned} \tag{10}$$

It follows from Eq. (10) that the probability density for a photon to travel a distance L after n scatters is:

$$w_n(L) = \frac{\gamma_s^n L^{n-1}}{(n-1)!}\,\exp(-\gamma_s L). \tag{11}$$

One finds

$$\langle L_n \rangle = \int_0^\infty L w(L)\mathrm{d}L \tag{12}$$

which evaluates as

$$\langle L_n \rangle = n\gamma_s^{-1} \tag{13}$$

One finds the path length probability density by first calculating the probability for a photon to undergo n scatters before leaving the medium, then setting the path length ξ equal to $\langle L_n \rangle$.

Since the walk ends when the photon reaches $z = 0$ or $z = t$ and passes through the surface, the number of steps taken is determined by motion along the z-axis. Thus, one can treat the problem as a one dimensional random walk. The distance traveled is through three dimensions, depends on the number of steps n, and is given by Eq. (13). However the number of steps n depends only on motion along the z-axis: the number of steps taken before reaching a boundary, which in turn depends on step size along the z-axis:

$$l_z = \mathbf{l} \cdot \hat{\mathbf{z}} = l \cos\theta \tag{14}$$

where $\mathbf{l}$ is the displacement after scattering, $\hat{\mathbf{z}}$ is a unit vector along the z-axis and θ is the angle $\mathbf{l}$ makes with the z-axis. The problem is a symmetric one dimensional random walk with variable step size l_z and boundaries at $z = 0$ and $z = t$. The boundary can be either absorbing or partially reflecting, corresponding to the case of whether or not there is internal reflection at the slab surfaces. An absorbing boundary means there is zero probability that the photon is reflected back into the medium, i.e. there is no internal reflection. This is the case if the turbid slab is fabric or paper.

One first obtains the probability density that the photon is located at position z after n steps, having started at z_0, for an *unbounded* walk, $W_n(z, z_0)$, and then modifies this result to account for the boundaries (Chandrasekhar 1960). The photon walks along the z-axis with variable step size l_z. A random walk is an additive random process, so by the central limit theorem the probability density $W_n(z, z_0)$ is a normal distribution with variance $\sigma_n^2 = n\sigma^2$, where σ^2 is the variance of a single step. For the unbounded walk:

$$W_n(z, z_0) = \mathcal{N}(z, z_0, \sigma_n^2) \tag{15}$$

where and $\mathcal{N}$ is a normal distribution with mean z_0 and σ_n^2 is the variance after n steps, so that:

$$W_n(z, z_0) = \frac{1}{\sqrt{2\pi\sigma_n^2}} \exp\big[-(z - z_0)^2/2\sigma_n^2\big] \tag{16}$$

The variance of a single step is:

$$\sigma^2 = \langle l_z^2 \rangle \tag{17}$$

where since it is a symmetric walk, $\langle l_z \rangle = 0$.

To get $\langle l_z^2 \rangle$ one first obtains the probability density for $l_z = l \cos\theta$. Isotropic scattering is assumed: the angle θ is a random variable with uniform probability density, so the probability for $\cos\theta = u$ is

$$f(u) = \frac{1/\pi}{\sqrt{1 - u^2}}, \quad -1 \le u \le 1. \tag{18}$$

That this is the probability density for $u = \cos\theta$ with θ uniformly distributed between $[0\ \pi]$ is shown in the following.

For $X \in [0\ \pi]$:

$$P(X \le \theta) = \frac{\theta}{\pi}$$

and the distribution function for $U = \cos X$ is:

$$\begin{aligned} F_U(u) &= P(U \le u) \\ &= P(\cos X \le u) \\ &= P(X \ge \cos^{-1}(u)) \\ &= P(X \le \cos^{-1}(-u)) \\ &= \frac{\cos^{-1}(-u)}{\pi} \end{aligned} \tag{19}$$

The probability density for u is the derivative of $F_U(u)$:

$$\begin{aligned} f(u) &= \frac{\mathrm{d}}{\mathrm{d}u} F_U(u) \\ &= \frac{1/\pi}{\sqrt{1 - u^2}} \end{aligned} \tag{20}$$

which is precisely Eq. (18). One notes that $f(u)$ is normalized over the range $[-1\ 1]$:

$$\int_{-1}^{1} f(u)\,\mathrm{d}u = 1.$$

Using Eq. (6) for $w(l)$ and Eq. (18) for $f(u)$ one obtains the probability density for step size l_z, using $l = l_z/u$:

$$\begin{aligned} p(l_z) &= \int_0^\infty w(l_z/u)\, f(u)\, \frac{\mathrm{d}u}{|u|} \\ &= \frac{1}{\pi l^*} \int_0^\infty \frac{\exp[-(l_z/u)/l^*]}{\sqrt{1-u^2}}\, \frac{\mathrm{d}u}{|u|} \end{aligned} \tag{21}$$

which can be written with $x = l_z/u$, as:

$$p(l_z) = \frac{1}{\pi l^*} \int_{l_z}^\infty \frac{\exp(-x/l^*)}{x\sqrt{1-(l_z/x)^2}} \mathrm{d}x. \tag{22}$$

The lower limit on the integral is l_z because $\cos\theta \le 1$. This can be written, with $y = x/l_z$ as:

$$p(l_z) = \frac{1}{\pi l^*} \int_1^\infty \frac{\exp(-l_z y/l^*)}{\sqrt{y^2-1}} \mathrm{d}y. \tag{23}$$

This integral can be evaluated (G&R 3.387.3) (Gradshteyn and Ryzhik 2007) to get the probability density for step size l_z:

$$p(l_z) = \frac{1}{\pi l^*} K_0(l_z/l^*) \tag{24}$$

where K_0 is a modified Bessel function of the first kind. One finds the variance for a single step is (G&R 6.521.10) (Gradshteyn and Ryzhik 2007):

$$\begin{aligned} \sigma^2 &= \int_0^\infty z^2 p(z)\mathrm{d}z \\ &= \frac{1}{\pi l^*} \int_0^\infty z^2 K_0(z/l^*)\mathrm{d}z \\ &= \frac{1}{2} l^{*2} \\ &= \frac{1}{2\gamma_s^2} \end{aligned} \tag{25}$$

and the variance after n steps is:

$$\begin{aligned} \sigma_n^2 &= n\sigma^2 \\ &= \frac{n}{2\gamma_s^2} \end{aligned} \tag{26}$$

The average step size along the z-axis can be obtained from Eq. (24):

$$\begin{aligned}\langle |l_z| \rangle &= \int_0^\infty x\ p(x)\mathrm{d}x \\ &= \frac{1}{\pi l^*}\int_0^\infty x\ K_0(x/l^*)\mathrm{d}x \\ &= \frac{1}{\pi}\ l^*\end{aligned} \tag{27}$$

where $l^* = \gamma_s^{-1}$ is the scattering mean free path, the average distance traveled between scatters.

Using the results of Eq. (25) for σ^2 the probability for the walker's position after n steps in an unbounded walk is:

$$W_n(z, z_0) = \frac{\gamma_s}{\sqrt{\pi n}} \exp[-\gamma_s^2 (z - z_0)^2/n] \tag{28}$$

To get the path-length probability density one identifies:

$$nl^* = \xi, \qquad \mathrm{d}n = \gamma_s \mathrm{d}\xi, \qquad W_n(z, z_0) \rightarrow P_z(\xi; z) \tag{29}$$

where ξ = path length, and the path length probability for an unbounded walk is:

$$P_z(\xi; z)\mathrm{d}\xi = \frac{1}{\sqrt{\pi l^{*3}\xi}} \exp[-(z - z_0)^2/(l^*\xi)]\ \mathrm{d}\xi \tag{30}$$

where $l^* = \gamma_s^{-1}$ = scattering mean free path. This expression for $P_z(\xi; z)$ is the probability that a walker is located at z after walking a distance ξ having started at the "source" point z_0. The model assumes that an incident photon travels a distance into the slab equal to one mean free path, so $z_0 = l^*$.

2.2 Boundary Conditions

For a bounded walk, the path length probability $P_z(\xi; z)$ must satisfy boundary conditions at $z = 0$ and $z = t$. In order to satisfy the boundary conditions, one expands $P_z(\xi; z)$ using the method of images (Haskell et al. 1994; Rogers 2016; Chandrasekhar 1960). In the method of images, the probability density is a linear superposition of solutions of the form of Eq. (28) or Eq. (30). A number of point sources (images) are constructed such that a sum of the probability densities of these point sources satisfy the boundary conditions. Expanding $P_z(\xi; z)$:

$$P_z(\xi; z) = \sum_{n=-\infty}^{\infty} a_n \gamma_n(\xi; z) \tag{31}$$

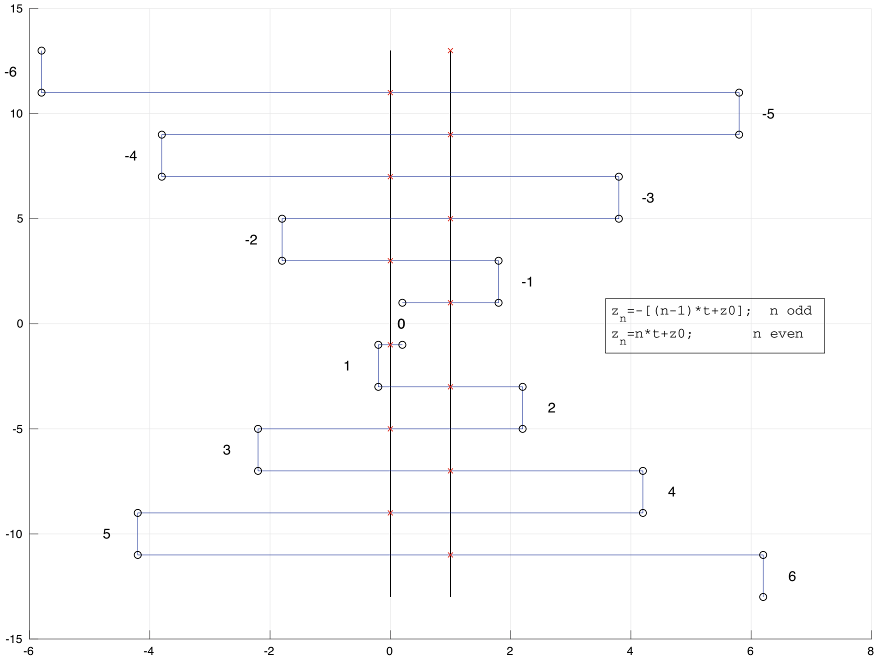

Fig. 1 Location of the nth image

where γ_n is the probability density of the nth image located at z_n:

$$\begin{aligned}\gamma_n(\xi; z) &= \mathcal{N}(z, z_n, l^*\xi/2) \\ &= \frac{1}{\sqrt{\pi\xi l^*}}\exp[-(z-z_n)^2/(l^*\xi)]\end{aligned} \tag{32}$$

with the position of the nth image:

$$z_n = (-1)^n\left[\left(n - \frac{1}{2}\right)t + l^*\right] + \frac{t}{2} \tag{33}$$

where t = thickness of the slab, as shown in Fig. 1. The expansion coefficients a_n in Eq. (31) are determined by the boundary conditions.

For purely absorbing boundaries (Singer et al. 2008; Rogers 2016) P_z has the boundary condition:

$$P_z(\xi; z)\Big|_{z=0,t} = 0, \tag{34}$$

A purely absorbing boundary means that when a walker reaches the boundary, the walker exits the slab and the walk is ended. In this case one finds that $a_n = (-1)^n a_0$

for all n, where a_0 is determined by normalization. For simplicity of notation one sets $a_0 = 1$.

Equation (33) shows that $z_{2k+1} = -z_{2k}$ so for absorbing boundaries $P_z(\xi; z)$ can be written:

$$P_z(\xi; z) = \frac{1}{\sqrt{\pi \xi l^{*\,3}}} \sum_{k=-\infty}^{\infty} \left\{ \exp\left[-(z - z_{2k})^2/\xi l^* \right] - \exp\left[-(z + z_{2k})^2/\xi l^* \right] \right\}, \tag{35}$$

By Eq. (33) one sees by inspection that indeed the boundary conditions Eq. (34) are satisfied i.e., that $P_z(\xi; z)$ vanishes at $z = 0, t$ (see Eq. (33)). This is the case for fabric or paper (Rogers et al. 2017, 2019).

If there is internal reflection at the slab boundaries, each boundary is partially reflective and partially absorptive. For a random walk with a partially absorbing/reflecting boundary, the probability density for the walker's position satisfies a Robin or mixed boundary condition (Erban and Chapman 2007; Singer et al. 2008; Collins and Kimball 1949):

$$D \frac{\mathrm{d}}{\mathrm{d}z} P_z(\xi; z) = \pm K\, P_z(\xi; z) \quad \Big|_{z=0,t}. \tag{36}$$

where + sign for $z = 0$, the − sign for $z = t$, and K depends upon the probability of absorption at the boundary (Singer et al. 2008). A partially absorbing boundary means that when the walker reaches a boundary there is a probability that the walker steps back into the slab and continues its walk. This case is treated in Sect. 6, below. One notes that if $K \to 0$, the BC are that of total reflection, and for $K \to \infty$, the BC is for purely absorptive boundaries.

3 Reflection and Transmission—No Internal Reflection

One first calculates the reflection from and transmission through a slab with no internal reflection. This is the case for fabric or paper, as indicated above. The case of internal reflection at the slab boundaries is treated below.

The reflection of light from and the transmission through a turbid slab is obtained from the probability flux through each surface, given by Eq. (5). The probability flux through a surface is obtained from taking the derivative normal to the surface—Fick's law. The case treated first is for no internal reflection at the slab boundaries. As shown below, one obtains simple intuitive expressions for reflection and transmission of a turbid slab.

3.1 Reflection

Using Eqs. (3)–(5) the reflectance is

$$R = D \int_0^\infty \frac{\mathrm{d}}{\mathrm{d}z} P_z(\xi; 0) \exp(-\sigma_a \xi)\, \mathrm{d}\xi \tag{37}$$

and using Eq. (35)

$$\begin{aligned} \frac{\mathrm{d}}{\mathrm{d}z} P_z(\xi; z) = - \sum_{k=-\infty}^{\infty} \Bigg\{ & \frac{z - z_{2k}}{\sqrt{\pi l^{*\,5}\, \xi^3}} \exp\left[- (z - z_{2k})^2/(l^* \xi) \right] \\ & - \frac{z + z_{2k}}{\sqrt{\pi l^{*\,5}\, \xi^3}} \exp\left[- (z + z_{2k})^2/(l^* \xi) \right] \Bigg\} \end{aligned} \tag{38}$$

For reflection, $z = 0$ and this can be written:

$$\frac{\mathrm{d}}{\mathrm{d}z} P_z(\xi; 0) = \sum_{k=-\infty}^{\infty} \frac{4 z_{2k}}{\sqrt{\pi l^{*\,5}\, \xi^3}} \exp\left[- z_{2k}^2/(l^* \xi) \right] \tag{39}$$

The reflectance then becomes:

$$R = \frac{2D}{l^{*\,2}} \sum_{k=-\infty}^{\infty} \frac{z_{2k}}{\sqrt{\pi l^*}} \int_0^\infty \xi^{-3/2} \exp\left[- z_{2k}^2/(l^* \xi) - \sigma_a \xi \right] \mathrm{d}\xi \tag{40}$$

The integral is evaluated (Gradshteyn and Ryzhik 2007) (Grad&Ryzh 3.471.9):

$$\begin{aligned} \int_0^\infty x^{-3/2} \exp(-b/x - cx) \mathrm{d}x &= 2 \left[\frac{c}{b} \right]^{1/4} K_{1/2}(2\sqrt{bc}) \\ &= \sqrt{\frac{\pi}{b}} e^{-2\sqrt{bc}} \end{aligned} \tag{41}$$

With $b = z_{2k}^2/l^*$ and $c = \sigma_a$ and using $D = l^{*\,2}/2$ one writes

$$\begin{aligned} R &= \sum_{k=-\infty}^{\infty} \frac{z_{2k}}{\sqrt{\pi l^*}} \frac{\sqrt{\pi l^*}}{|z_{2k}|} e^{-2|z_{2k}|\sqrt{\sigma_a/l^*}} \\ &= \sum_{k=-\infty}^{\infty} \frac{z_{2k}}{|z_{2k}|} e^{-2|z_{2k}|\sqrt{\sigma_a/l^*}} \end{aligned} \tag{42}$$

One notes by Eq. (33) that $z_{2k} = 2kt + l^*$ and that $l^* < t$. Thus for $k < 0$ it follows that $z_{2k} < 0$, so $z_{2k}/|z_{2k}| = -1$ and for $k > 0$, $z_{2k}/|z_{2k}| = 1$, so that:

$$
\begin{aligned}
R &= e^{-2z_0\sqrt{\sigma_a/l^*}} + \sum_{k=1}^{\infty}\left[e^{-2|z_{2k}|\sqrt{\sigma_a/l^*}} - e^{-2|z_{-2k}|\sqrt{\sigma_a/l^*}}\right] \\
&= e^{-2l^*\sqrt{2\sigma_a/l^*}} + \sum_{k=1}^{\infty}\left[e^{-2\sqrt{\sigma_a/l^*}\,(2kt+l^*)} - e^{-2\sqrt{\sigma_a/l^*}\,(2kt-l^*)}\right] \\
&= e^{-2\sqrt{\sigma_a l^*}} + \sum_{k=1}^{\infty}\left[e^{-2\sqrt{\sigma_a l^*}\,(2k\tau+1)} - e^{-2\sqrt{\sigma_a l^*}\,(2k\tau-1)}\right] \\
&= e^{-2\sqrt{\sigma_a l^*}} - \sinh 2\sqrt{\sigma_a l^*}\,\sum_{k=1}^{\infty} e^{-2\sqrt{\sigma_a l^*}\,2k\tau}
\end{aligned}
\tag{43}
$$

where $\tau = t/l^*$ is the optical thickness and $z_0 = l^*$.

The sum in Eq. (43) is an infinite geometric series in $(r^2)^k$ with $r = \exp(-2\tau\sqrt{\sigma_a l^*})$ starting at $k = 1$:

$$
\begin{aligned}
\sum_{k=1}^{\infty} r^{2k} &= \sum_{k=0}^{\infty}(r^2)^k - 1 \\
&= \frac{1}{1-r^2} - 1 \\
&= \frac{r}{r^{-1}-r}
\end{aligned}
\tag{44}
$$

so that

$$
\sum_{k=1}^{\infty}\left[e^{-2\tau\sqrt{\sigma_a l^*}}\right]^{2k} = \frac{\exp(-2\tau\sqrt{\sigma_a l^*}\,)}{2\sinh(2\tau\sqrt{\sigma_a l^*}\,)}
\tag{45}
$$

One obtains for R:

$$
R = \exp(-2\sqrt{\sigma_a l^*}) - \frac{\sinh(2\sqrt{\sigma_a l^*}\,)}{\sinh(2\tau\sqrt{\sigma_a l^*}\,)}\exp(-2\tau\sqrt{\sigma_a l^*})
\tag{46}
$$

3.2 Transmission

Calculation of the transmission proceeds in a similar way to that of reflection—taking the derivative of the path-length probability: but at the surface $z = t$. The transmission is obtained from Eqs. (1) to (5) and is given by:

$$
T = -D\int_0^{\infty}\frac{\mathrm{d}}{\mathrm{d}z}P_z(\xi;\,t)\exp(-\sigma_a\xi)\,\mathrm{d}\xi
\tag{47}
$$

Evaluating the derivative of $P_z(\xi;\,z)$ at $z = t$ using Eq. (35), one obtains:

$$\frac{\mathrm{d}}{\mathrm{d}z}P_z(\xi;t) = -\sum_{k=-\infty}^{\infty}\left\{\frac{t-z_{2k}}{\sqrt{\pi l^{*\,5}\,\xi^3}}\exp\Big[-(t-z_{2k})^2/(l^*\xi)\Big] - \frac{t+z_{2k}}{\sqrt{\pi l^{*\,5}\,\xi^3}}\exp\Big[-(t+z_{2k})^2/(l^*\xi)\Big]\right\} \tag{48}$$

Note that from Eq. (33)

$$t - z_{2k} = t - (2kt + l^*) = -\Big[(2k-1)t + l^*\Big] \tag{49}$$

and

$$t + z_{2k} = t + (2kt + l^*) = (2k+1)t + l^* \tag{50}$$

so that

$$\frac{\mathrm{d}}{\mathrm{d}z}P_z(\xi;t) = \sum_{k=-\infty}^{\infty}\left\{\frac{l^* + (2k-1)t}{\sqrt{\pi l^{*\,5}\,\xi^3}}\exp\Big[-[l^* + (2k-1)t]^2/(l^*\xi)\Big] + \frac{l^* + (2k+1)t}{\sqrt{\pi l^{*\,5}\,\xi^3}}\exp\Big[-[l^* + (2k+1)t]^2/(l^*\xi)\Big]\right\} \tag{51}$$

Re-ordering the terms in the summation of the first term in curly brackets by letting $k \to k+1$, this can be written:

$$\frac{\mathrm{d}}{\mathrm{d}z}P_z(\xi;t) = \frac{2}{\sqrt{\pi l^{*\,5}\,\xi^3}}\sum_{k=-\infty}^{\infty}[l^* + (2k+1)t]\exp\Big[-[l^* + (2k+1)t]^2/(l^*\xi)\Big] \tag{52}$$

Inserting this into Eq. (47):

$$T = \frac{-1}{\sqrt{\pi l^*}}\sum_{k(\mathrm{odd})=-\infty}^{\infty}\big(kt + l^*\big) \times \int_0^{\infty}\xi^{-3/2}\exp\Big[-[kt+l^*]^2/(l^*\xi) - \sigma_a\xi\Big]\,\mathrm{d}\xi \tag{53}$$

where, again $D = l^{*\,2}/2$, and k(odd) means only odd values of k are summed over.

The integral in Eq. (53) is evaluated using Eq. (41), and one finds for T:

$$\begin{aligned}
T &= -\sum_{k(\text{odd})=-\infty}^{\infty} \frac{kt+l^*}{\sqrt{\pi l^*}} \frac{\sqrt{\pi l^*}}{|kt+l^*|} e^{-2|kt+l^*|\sqrt{\sigma_a/l^*}} \\
&= -\sum_{k(\text{odd})=1}^{\infty} \left\{ \frac{kt+l^*}{|kt+l^*|} e^{-2|kt+l^*|\sqrt{\sigma_a/l^*}} + \frac{-kt+l^*}{|-kt+l^*|} e^{-2|-kt+l^*|\sqrt{2\sigma_a/l^*}} \right\} \\
&= -\sum_{k(\text{odd})=1}^{\infty} \left\{ \frac{kt+l^*}{|kt+l^*|} e^{-2|kt+l^*|\sqrt{\sigma_a/l^*}} - \frac{kt-l^*}{|-kt+l^*|} e^{-2|-kt+l^*|\sqrt{\sigma_a/l^*}} \right\} \\
&= -\sum_{k(\text{odd})=1}^{\infty} \left\{ e^{-(kt+l^*)2\sqrt{\sigma_a/l^*}} - e^{-(kt-l^*)2\sqrt{\sigma_a/l^*}} \right\} \qquad (54) \\
&= -\sum_{k(\text{odd})=1}^{\infty} e^{-2kt\sqrt{\sigma_a/l^*}} \left\{ e^{-2l^*\sqrt{\sigma_a/l^*}} - e^{2l^*\sqrt{\sigma_a/l^*}} \right\} \\
&= 2\sinh(2\sqrt{\sigma_a l^*}) \sum_{k(\text{odd})=1}^{\infty} e^{-2k\tau\sqrt{\sigma_a l^*}} \\
&= 2\sinh(2\sqrt{\sigma_a l^*}) \sum_{k=0}^{\infty} e^{-(2k+1)2\tau\sqrt{\sigma_a l^*}}
\end{aligned}$$

or

$$T = 2\sinh(2\sqrt{\sigma_a l^*}) e^{-2\tau\sqrt{\sigma_a l^*}} \sum_{k=0}^{\infty} e^{-4k\tau\sqrt{2\sigma_a l^*}} \qquad (55)$$

Again, the sum is a geometric series in r^k with $r = e^{-4\tau\sqrt{\sigma_a l^*}}$ starting at $k = 0$, so:

$$\begin{aligned}
e^{-2\tau\sqrt{\sigma_a l^*}} \sum_{k=0}^{\infty} e^{-4k\tau\sqrt{\sigma_a l^*}} &= \frac{e^{-2\tau\sqrt{\sigma_a l^*}}}{1 - e^{-4\tau\sqrt{\sigma_a l^*}}} \\
&= \frac{1}{2\sinh(2\tau\sqrt{\sigma_a l^*})}
\end{aligned} \qquad (56)$$

One obtains for the transmittance:

$$T = \frac{\sinh(2\sqrt{\sigma_a l^*})}{\sinh(2\tau\sqrt{\sigma_a l^*})} \qquad (57)$$

3.3 Summary—No Internal Reflection

The results of this section are simple expressions for the reflection and transmission of a turbid slab, in terms of the physical quantities that characterize the slab: the scattering mean free path, the absorption coefficient, and the thickness of the slab. The simple expressions are:

$$R = R_\infty - T\ \exp(-2\tau\sqrt{\sigma_a l^*}) \tag{58}$$

where

$$R_\infty = \exp(-2\sqrt{\sigma_a l^*}) \tag{59}$$

is the reflectance for an infinitely thick slab and

$$T = \frac{\sinh(2\sqrt{\sigma_a l^*})}{\sinh(2\tau\sqrt{\sigma_a l^*})} \tag{60}$$

is the transmittance.

Figure 2 shows the reflection and transmission, Eqs. (58) and (60), for the case of no internal reflection. Also shown in Fig. 2 is a Monte-Carlo simulation. In the plots, $l^* = 0.2t$ and σ_a is in units of t^{-1}. In the Monte-Carlo simulation, there are

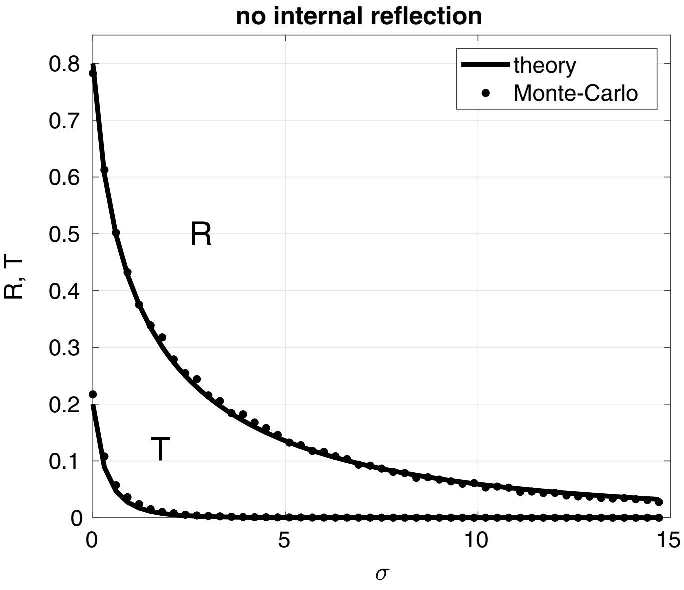

Fig. 2 Monte-Carlo versus theory for no internal reflection. $l^* = 0.2t$, so that $\tau = 5$, and σ_a is in units of mm^{-1} (with $t = 1\,\text{mm}$)

4×10^3 walks for each value of σ_a. The walk begins at $z = 2l^*/\pi$ (the distance of two z steps into the slab) and ends when the walker's z coordinate is either $z > 1$, in which case it is transmitted, or when $z < 0$, in which case it is reflected. The walker carries a "payload" which is initially equal to 1 and decreases exponentially with the distance traveled. When the walker crosses a boundary, it deposits its payload. The reflectance or transmittance is the sum of the payloads deposited at each boundary, divided by the total number of walks. Each step Δl_z is obtained by $\Delta l_z = l \cos\theta$ with l a random number with distribution given by Eq. (6), and θ a random number uniformally distributed over $[0\ \pi]$.

It is interesting to find the reflection and the transmission for the case of no absorption: $\sigma_a = 0$. From Eq. (58) one gets in the limit $\sigma_a \to 0$:

$$R = 1 - \frac{l^*}{t}$$

and for transmission, Eq. (60) in the limit $\sigma_a \to 0$:

$$T = \frac{l^*}{t}$$

These are the splitting probabilities and one sees

$$R + T = 1$$

as expected since, with no absorption, the probability is conserved.

It is interesting to compare the expressions for reflectance and transmittance obtained here using the multiple path model (MP) with the equations that follow from the asymptotic analysis of the radiative transfer equation (RTE), as obtained by Kokhanovsky (Kokhanovsky 2006). The diffuse reflectance for an infinitely thick turbid slab, Eq. (59), is essentially the same as that derived by Kokhanovsky for a thick snow pack (Kokhanovsky 2006). The expression for the reflectance, Eq. 3.95 in Ref. (Kokhanovsky 2006) is

$$\mathcal{R} = \exp\Big[-2\sqrt{v\beta}\Big]$$

where v is a constant dependent on the process under consideration (here $v = 1$), and $\beta = 1 - \omega_0$ is the probability of absorption with ω_0 the albedo. This formula is obtained in Ref. (Kokhanovsky 2006) for $\beta \ll 1$. To connect this formula with the results obtained here, one notes that the albedo can be expressed as:

$$\omega_0 = \frac{\gamma_s}{\sigma_a + \gamma_s}$$

where γ_s is the scattering coefficient and σ_a is the absorption coefficient. Noting that $\gamma_s^{-1} = l^*$ this can be written:

$$\omega_0 = \frac{1}{1 + \sigma_a l^*}$$

and the probability of absorption $\beta = 1 - \omega_0$ is:

$$\beta = \frac{\sigma_a l^*}{1 + \sigma_a l^*}.$$

For weak absorption $\beta \ll 1$ this can be written as:

$$\beta = \sigma_a l^*.$$

Putting this into the expression for $\mathcal{R}$ above one obtains:

$$\mathcal{R} = \exp\left[- 2\sqrt{\sigma l^*} \right]$$

which is precisely the expression obtained for R_∞, Eq. (59), above.

The expressions obtained by Kokhanovsky for a finite thickness slab are similar but not exactly the same as the expressions obtained here. Equations 3.169 and 3.170 of Ref. (Kokhanovsky 2006) for the reflectance and transmittance of a turbid slab are:

$$r = \frac{\sinh(x)}{\sinh(x + y)} \tag{61}$$

and

$$t = \frac{\sinh(y)}{\sinh(x + y)} \tag{62}$$

with x and y defined below. Doing some algebra on Eq. (61), the reflectance r can be written:

$$r = r_\infty - te^{-x-y} \tag{63}$$

or

$$r = e^{-y} - \frac{\sinh(y)}{\sinh(x + y)} e^{-x-y} \tag{64}$$

The parameter y is defined in Ref. (Kokhanovsky 2006) to be

$$y = - \ln R_\infty$$

which is:

$$y = 2\sqrt{\sigma_a l^*}$$

The parameter x as defined in Ref. (Kokhanovsky 2006) is

$$x = k\tau$$

with k the diffusion exponent. Equation (3.172) of Ref. (Kokhanovsky 2006) shows that for isotropic scattering the diffusion exponent k is:

$$k = \sqrt{3(1-\omega_0)} \tag{65}$$

which can be written:

$$\begin{aligned} k &= \sqrt{3\beta} \\ &= \sqrt{3\sigma_a l^*} \end{aligned} \tag{66}$$

so that the parameter $x = k\tau$ is

$$x = \tau\sqrt{3\sigma_a l^*}. \tag{67}$$

Using these values in the multiple-path expression for reflectance Eq. (58) one obtains:

$$R = e^{-y} - \frac{\sinh(y)}{\sinh(x')}\, e^{-x'} \tag{68}$$

where

$$x' = \frac{2x}{\sqrt{3}}$$

Comparison with the RTE diffuse reflectance, Eq. (64), shows similarity. There are two difference between the diffuse reflectance as obtained by RTE and MP: (a) Factor of $2/\sqrt{3}$ in x', and (b) $x \rightarrow x' + y$.

One notes that for large optical depths y can be dropped compared to x': for $\tau \gg 1$, $x' \gg y$, and so $x' + y \approx x'$:

$$\begin{aligned} x' + y &= 2\tau\sqrt{\sigma_a l^*} + 2\sqrt{\sigma_a l^*} \\ &= 2\sqrt{\sigma_a l^*}(\tau + 1) \\ &\approx 2\tau\sqrt{\sigma_a l^*} \\ &= x'. \end{aligned} \tag{69}$$

This can be understood in terms of the derivation of MP. In MP, the random walk must begin within the slab, so it is necessary that $l^* < t$ or $\tau > 1$.

With the conditions $\tau \gg 1$ and $\omega_0 \approx 1$, one sees that there is fair agreement between diffuse reflectance as predicted by MP and RTE.

4 Experiment—Dyed Fabric

The multiple-path model has been used to predict the spectral reflectance curve of a dyed fabric (Rogers et al. 2017). The experiment involved dyeing cotton fabric with magenta and cyan dyes and measuring the spectral reflectance of the dyed fabric.

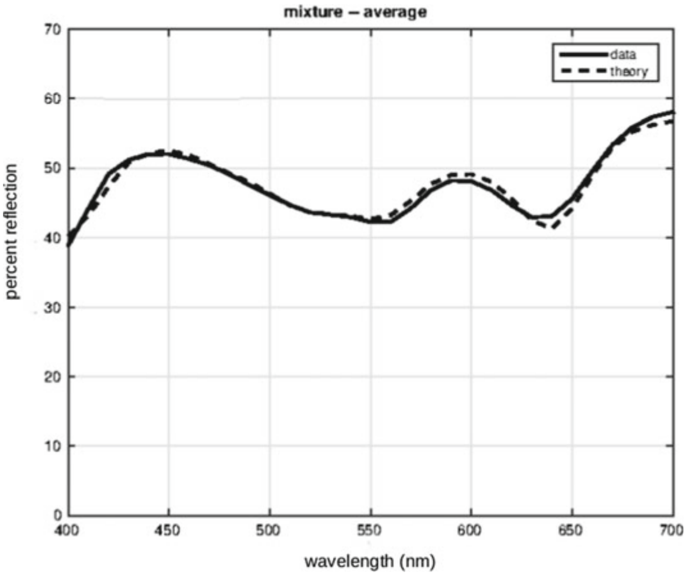

Fig. 3 Percent reflection as a function of wavelength of fabric dyed with a mixture of cyan and magenta dyes

There were three parts to experiment: First, the scattering coefficient of the fabric was determined by measuring the reflectance and transmittance of the undyed fabric and fitting the data to Eqs. (46) and (57). This measurement also provided the absorption coefficient of the undyed fabric. Second, the extinction coefficients of the dyes were determined by measuring the spectral transmission of the dye solutions. The absorption coefficient is obtained from the extinction coefficient. Third, the model was fit to the reflectance measurements by adjusting the (unknown) dye concentrations within the fabric, again using Eqs. (46) and (57). The comparison of model prediction and experimental data is shown in Fig. 3.

5 Diffusion of Light in Paper

Another experiment in which the multiple-path model was used to predict the outcome was the measurement of the diffusion of light within paper (Rogers et al. 2019). Light diffusing in paper affects the color of halftone images printed on the paper, the Yule–Nielsen effect (Yule and Neilsen 1951; Hebert and Hersch 2004, 2015; Coppel et al. 2011), so the quantification of light diffusion within paper allows better control of printed colors.

The modulation transfer function (MTF) of the paper is calculated from the multiple-path model. The MTF is the (spatial) frequency response to light incident at a single point (the impulse response). The MTF is the Fourier transform of the paper's line spread function (LSF) which in turn is obtained from the point spread function (PSF) (Dainty 1974). The PSF is the probability that a photon exits the paper at some distance ρ from which it entered the paper. Because of diffusion a reflected photon having entered the slab at a certain point will probably exit the slab at a different point. The PSF is the probability that the exit point is at the distance ρ from the entrance point. The line spread function is obtained from the PSF by setting $\rho = \sqrt{x^2 + y^2}$ and integrating over y.

The PSF is calculated using the multiple-path model (Rogers 2018) by calculating a two dimensional path length probability density: $P(\xi; z, \rho)$ where ρ is the radial coordinate in a cylindrical coordinate system with azimuthal symmetry. Because there are no boundaries in the x, y plane, the radial path length probability density is a normal distribution and:

$$\begin{aligned} P(\xi; z, \rho) &= W(\xi; \rho)\; P_z(\xi; z) \\ &= \frac{1}{2\pi l^* \xi} \exp\left[-\rho^2/(2l^*\xi) \right]\; P_z(\xi; z) \end{aligned} \tag{70}$$

where the walk begins in the x, y plane at $\rho = 0$. The point spread function is the normalized probability flux through the $z = 0$ surface as a function of ρ:

$$\mathcal{J}(\xi; \rho) = -DW(\xi; \rho)\, \frac{\mathrm{d}}{\mathrm{d}z} P_z(\xi, z)\bigg|_{z=0} \tag{71}$$

where again, all path lengths are summed over, i.e. Eq. (71) is integrated over ξ.

One obtains a simple expression for the PSF, $H(\rho)$:

$$H(\rho) = \frac{l^*/2\pi}{\left[l^{*2} + \rho^2\right]^{3/2}} \tag{72}$$

The line spread function is:

$$L(x) = \frac{l^*/\pi}{l^{*2} + x^2} \tag{73}$$

and the Fourier transform of $L(x)$ is the MTF:

$$\tilde{L}(\omega) = \exp(-l^*|\omega|) \tag{74}$$

The experiment consisted of photographing a bar-target on paper. The bar-target is a rectangular plate consisting of bars with 0% transmission, and between the bars, regions' with 100% transmission. Incident light is transmitted through the bar-target,

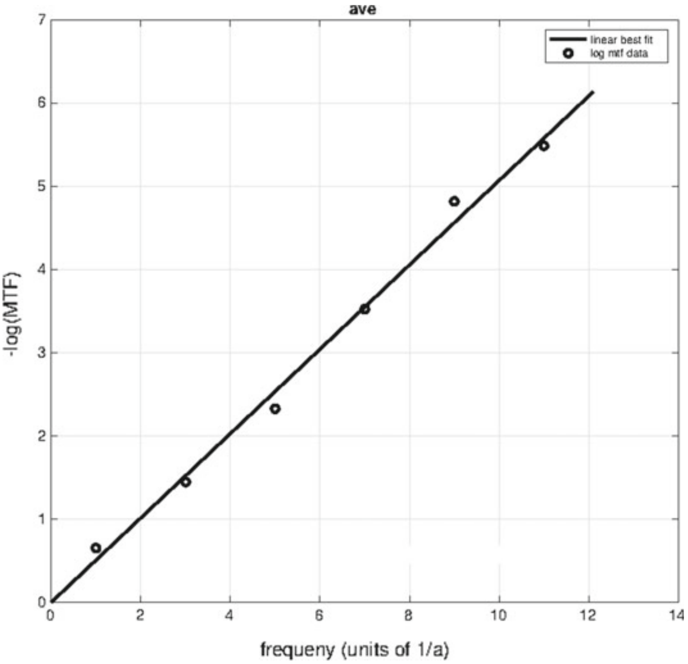

Fig. 4 Log of modulation transfer function. The bar-target has period a, so the x-axis is the spatial frequency in units of $2\pi/a = 8.85\,\text{mm}^{-1}$ since $a = 0.71\,\text{mm}$

diffuses within the paper, and is reflected out, again transiting the bar-target again on reflection. The transmission through the target in the direction perpendicular to the bars is a square-wave with period a. In the photograph, the regions on either side of the bars are "fuzzy" because of light diffusion within the paper. This "fuzziness" is analyzed to quantify the diffusion—one obtains experimental data for the paper MTF.

Figure 4 shows the log of $\tilde{L}(\omega)$ for Eq. (74) and the experimental data. The multiple path model predicts that the log of the MTF is a straight line, and one sees that the experimental data indicates that the log of the MTF is indeed a straight line. The slope of the line is the scattering mean free path l^* for the paper.

6 Reflection and Transmission—Internal Reflection

In this section the reflectance and transmittance are obtained for when there is internal reflection at the slab boundaries. Each boundary is partially reflective and partially absorptive. In terms of the random walk, there is a probability that upon reaching a boundary the walker steps back into the slab. For a random walk with a partially absorbing/reflecting boundary, the probability density for the walker's position satisfies a Robin or mixed boundary condition (Erban and Chapman 2007; Singer et al. 2008):

$$D\frac{\mathrm{d}}{\mathrm{d}z}\;P_z(\xi;z) = \pm K\;P_z(\xi;z)\quad\Big|_{z=0,t}. \tag{75}$$

where $+$ sign for $z = 0$, the $-$ sign for $z = t$, D is the diffusion coefficient, and K depends upon the probability of absorption at the boundary (Singer et al. 2008). The boundary condition on $P_z(\xi; z)$ can be written:

$$\frac{\mathrm{d}}{\mathrm{d}z}P_z(\xi;z) \mp S\;P_z(\xi;z)\Big|_{z=0,t} = 0. \tag{76}$$

where $S = K/D$. With $D = l^{*2}/2$ and $K = (1-r)/(rl^*)$ (Erban and Chapman 2007; Singer et al. 2008):

$$S = \frac{2(1-r)}{r\,l^*} \tag{77}$$

with $r =$ the probability that a photon is reflected when it hits the boundary, i.e. an effective Fresnel reflectance (Rogers 2015). One notes that if $S \to 0$ $(r = 1)$, there is no absorption and the BC are that of total reflection, and for $S \to \infty$ $(r = 0)$, there is no reflection, and the BC is for purely absorptive boundaries.

The quantity $P_z(0, \xi)$ is the probability that a photon is located at the boundary $z = 0$ after having traveled a distance ξ, and similarly for $P_z(t, \xi)$. By Fick's law, the probability current through the boundary is:

$$\mathcal{J}(\xi;z) = \pm D\frac{\mathrm{d}}{\mathrm{d}z}P_z(\xi;z)\quad\Big|_{z=0,t} \tag{78}$$

where $+$ is for the $z = 0$ boundary and $-$ for the $z = t$ boundary. If the medium is absorptive, however, the flux will be reduced, according to Bouguer law, by the factor $\exp(-\sigma_a\xi)$ where σ_a is the absorption coefficient.

$$\mathcal{J}(\xi;z) = \pm D\;\frac{\mathrm{d}}{\mathrm{d}z}P_z(\xi;z)\exp(-\sigma_a\xi)\quad\Big|_{z=0,t}. \tag{79}$$

The total transmission through the boundary is found by summing over all path lengths ξ:

$$\mathcal{J}(z) = \frac{1}{l^*}\int_0^\infty \mathcal{J}(\xi;z)\mathrm{d}\xi.$$

From Eqs. (31) and (32),

$$\mathcal{J}(\xi;z)\Big|_{z=0,t} = \pm D\sum_{n=-\infty}^{\infty} a_n(\xi)\frac{\mathrm{d}}{\mathrm{d}z}\gamma_n(\xi;z). \tag{80}$$

Using Eq. (31) this is, with $D = l^{*2}/2$:

$$\mathcal{J}(z)\Big|_{z=0,t} = \pm \frac{l^*}{2} \sum_{n=-\infty}^{\infty} \int_0^{\infty} a_n(\xi)\, \frac{\mathrm{d}}{\mathrm{d}z}\gamma_n(\xi; z) \exp\big[-\sigma_a \xi\big]\mathrm{d}\xi \tag{81}$$

One notes that

$$\frac{\mathrm{d}}{\mathrm{d}z}\gamma_n(\xi; z) = -2\, \frac{z - z_n}{\sqrt{\pi(\xi l^*)^3}} \exp[-(z - z_n)^2/l^*\xi] \tag{82}$$

so that

$$\mathcal{J}(z)\Big|_{z=0,t} = \mp \frac{1}{\sqrt{\pi l^*}} \sum_{n=-\infty}^{\infty} (z - z_n) \times \int_0^{\infty} a_n(\xi)\xi^{-3/2} \exp\big[-(z - z_n)^2/l^*\xi - \sigma_a\xi\big]\mathrm{d}\xi \tag{83}$$

The reflectance is equal to the probability flux through the boundary at $z = 0$ and the transmittance is the probability flux through $z = t$:

$$R = \mathcal{J}(0), \qquad T = \mathcal{J}(t). \tag{84}$$

One writes $\mathcal{J}(z)$, Eq. (83), as:

$$\mathcal{J}(z) = \mp \sum_{n=-\infty}^{\infty} (z - z_n)\, \mathcal{I}_n(z) \tag{85}$$

where

$$\mathcal{I}_n(z) = \frac{1}{\sqrt{\pi l^*}} \int_0^{\infty} a_n(\xi)\xi^{-3/2} \exp\big[-(z - z_n)^2/l^*\xi - \sigma_a\xi\big]\mathrm{d}\xi \tag{86}$$

In order to evaluate $\mathcal{I}_n$ is necessary to obtain expressions for the a_n using the boundary conditions, Eq. (76).

6.1 Boundary Conditions

To obtain the expansion coefficients for the probability density $P_z(\xi; z)$, Eq. (31), one applies the boundary conditions Eq. (76). Defining

$$p_n(\xi; z) = a_n\gamma_n(\xi; z) + a_{n+1}\gamma_{n+1}(\xi; z) \tag{87}$$

One sees that

$$\begin{aligned} P_z &= \sum_{k=-\infty}^{\infty} p_{2k+1}, \quad \text{(sum odd terms)} \\ &= \sum_{k=-\infty}^{\infty} p_{2k}, \quad \text{(sum even terms)} \\ &= \frac{1}{2} \sum_{n=-\infty}^{\infty} p_n. \end{aligned} \tag{88}$$

One writes P_z in this form because the BC on P_z, Eq. (76), are satisfied if the individual odd terms satisfy the BC at $z = t$:

$$\frac{\mathrm{d}}{\mathrm{d}z} p_{2k+1}(\xi; t) + S\ p_{2k+1}(\xi; t) = 0. \tag{89}$$

and the individual even terms satisfy the BC at $z = 0$:

$$\frac{\mathrm{d}}{\mathrm{d}z} p_{2k}(\xi; 0) - S\ p_{2k}(\xi; 0) = 0. \tag{90}$$

To obtain a recurrence relation for the a_n one inserts Eq. (87) into Eq. (76), using Eqs. (89) and (90):

$$a_n[\gamma_n' - (-1)^n S\gamma_n] + a_{n+1}[\gamma_{n+1}' - (-1)^n S\gamma_{n+1}] = 0 \tag{91}$$

to get

$$a_{n+1} = -\frac{\gamma_n' - (-1)^n S\gamma_n}{\gamma_{n+1}' - (-1)^n S\gamma_{n+1}}\ a_n \tag{92}$$

where the γ_n, γ_n' are evaluated at $z = 0$ for n even and at $z = t$ for n odd.

With n even, Eq. (92) is:

$$a_{n+1} = -\frac{\gamma_n' - S\gamma_n}{\gamma_{n+1}' - S\gamma_{n+1}}\ a_n. \tag{93}$$

On the boundary $z = 0$ the derivative of γ_n, by Eq. (82), is:

$$\begin{aligned} \gamma_n'(0) &= 2\frac{z_n}{\xi l^*}\gamma_n(0) \\ &= 2\frac{nt + l^*}{\xi l^*}\gamma_n(0) \end{aligned} \tag{94}$$

where Eq. (33) for n even is used, and it is easily shown that for $n + 1$ odd:

$$\begin{aligned}\gamma'_{n+1}(0) &= -\gamma'_n(0)\\ &= -2\frac{nt+l^*}{\xi l^*}\gamma_n(0).\end{aligned} \tag{95}$$

It is also easily shown that for $n+1$ odd:

$$\gamma_{n+1}(0) = \gamma_n(0) \tag{96}$$

Using Eqs. (94)–(96) in Eq. (93)

$$a_{n+1} = -\frac{2(nt+l^*)\gamma_n(0) - S\xi l^*\gamma_n(0)}{-2(nt+l^*)\gamma_n(0) - S\xi l^*\gamma_n(0)}\ a_n \tag{97}$$

or:

$$a_{n+1} = -\frac{nt+l^* - S\xi l^*/2}{-nt-l^*-S\xi l^*/2}\ a_n \tag{98}$$

Using Eq. (77), one defines

$$q = \frac{Sl^*}{2} = \frac{1-r}{r}, \tag{99}$$

and the recursion relation for the a_n can be written:

$$a_{n+1} = \frac{nt+l^*-q\xi}{nt+l^*+q\xi}\ a_n \tag{100}$$

Although the recurrence relation Eq. (100) was obtained for n even, it is easily shown, by carrying out a similar analysis as Eqs. (93)–(100) with n odd, that the recurrence relation is the same for odd values of n, as one would expect.

It follows that

$$a_n = \prod_{k=0}^{n-1}\frac{kt+l^*-q\xi}{kt+l^*+q\xi}\ a_0, \qquad n \geq 1. \tag{101}$$

where a_0 is determined by normalization.

For negative summation index, $n < 0$, the recurrence relation Eq. (100) is inverted:

$$a_n = \frac{nt+l^*+q\xi}{nt+l^*-q\xi}\ a_{n+1} \tag{102}$$

and one finds

$$a_n = \prod_{k=1}^{|n|}\frac{kt-l^*-q\xi}{kt-l^*+q\xi}\ a_0, \qquad n \leq -1. \tag{103}$$

The quantity q is a measure of internal reflection. One sees from Eqs. (101) and (103) Eq. (99) that if there is no internal reflection $r \to 0$ then $q \to \infty$, and $a_n = (-1)^n$. This is the case treated in Sect. 3.

6.2 Evaluation of Integral

The probability flux through a surface, Eq. (83), is the sum of integrals of the form:

$$\mathcal{I}_n(z) = \frac{1}{\sqrt{\pi l^*}} \int_0^\infty a_n(\xi)\xi^{-3/2} \exp\big[-(z-z_n)^2/l^*\xi - \sigma_a \xi\big]\mathrm{d}\xi \tag{104}$$

or, using Eqs. (101), (103):

$$\mathcal{I}_n(z) = \frac{a_0}{\sqrt{\pi l^*}} \int_0^\infty \xi^{-3/2} \prod_{k=0}^{n-1} \frac{kt + l^*_\pm - q\xi}{kt + l^*_\pm + q\xi} \exp\big[-(z-z_n)^2/l^*\xi - \sigma_a \xi\big]\mathrm{d}\xi. \tag{105}$$

where $l^*_+ = l^*$ if $n > 0$ and $l^*_- = t - l^*$ if $n < 0$, as can be seen from Eq. (103). Again, for ease of notation, one sets the normalization factor $a_0 = 1$.

For $n = 0$:

$$\mathcal{I}_0 = \frac{1}{\sqrt{\pi l^*}} \int_0^\infty \xi^{-3/2} \exp\big[-(z-z_0)^2/l^*\xi - \sigma_a \xi\big]\mathrm{d}\xi. \tag{106}$$

Equation (106) is evaluated using:

$$\int_0^\infty x^{-3/2} \exp(-\beta/x - \alpha x)\mathrm{d}x = \sqrt{\frac{\pi}{\beta}} e^{-2\sqrt{\beta\alpha}} \tag{107}$$

(Grad&Ryzh 3.471.9) (Gradshteyn and Ryzhik 2007), to obtain:

$$\begin{aligned} \mathcal{I}_0(z) &= \frac{1}{\sqrt{\pi l^*}} \int_0^\infty x^{-3/2} \exp\big[-(z-l^*)^2/l^*x - \sigma_a x\big]\mathrm{d}x \\ &= \frac{1}{\sqrt{\pi l^*}} \sqrt{\frac{\pi l^*}{(z-l^*)^2}} \exp\big[-2|z-l^*|\sqrt{\sigma_a/l^*}\big] \\ &= \frac{1}{|z-l^*|} \exp\left(-2|z-l^*|\sqrt{\sigma_a/l^*}\right) \end{aligned} \tag{108}$$

For $n \neq 0$:

$$\mathcal{I}_n(z) = \frac{1}{\sqrt{\pi l^*}} \int_0^\infty \xi^{-3/2} \prod_{k=0}^{n-1} \frac{(kt + l^* - q\xi)}{(kt + l^* + q\xi)} \times \exp[-(z-z_n)^2/l^*\xi - \sigma_a\xi]\,\mathrm{d}\xi \tag{109}$$

In Appendix 1, it is shown that the partial fraction expansion of the finite product in Eq. (109) is

$$\prod_{k=0}^{n-1} \frac{(kt + l^* - q\xi)}{(kt + l^* + q\xi)} = (-1)^n + \sum_{m=0}^{n-1} \frac{A_{nm}}{mt + l^* + q\xi} \tag{110}$$

with A_{nm} defined in the Appendix 1. The integral $\mathcal{I}_n$, Eq. (109), can be written:

$$\begin{aligned}\mathcal{I}_n(z) = \frac{(-1)^n}{\sqrt{\pi l^*}} \int_0^\infty \xi^{-3/2} \quad \exp[-(z - z_n)^2/l^*\xi - \sigma_a\xi]\, \mathrm{d}\xi \\ + \sum_{m=0}^{n-1} \frac{A_{nm}}{\sqrt{\pi l^*}} \int_0^\infty \xi^{-3/2} \frac{\exp[-(z - z_n)^2/l^*\xi - \sigma_a\xi]}{mt + l^* + q\xi}\, \mathrm{d}\xi\end{aligned} \tag{111}$$

Since A_{nm} depends only on n, m, t and l^*, one sees that for $q \to \infty$, (i.e. no internal reflection) the the second term above (the sum) goes to zero. The first term is the result for the case of no internal reflection, and the second term is the correction when there is internal reflection.

One writes $\mathcal{I}_n$ as the sum of two terms:

$$\mathcal{I}_n + \mathcal{I}_n^{(1)} + \mathcal{I}_n^{(2)} \tag{112}$$

where $\mathcal{I}_n^{(1)}$ is the first term on the right side of Eq. (111) and $\mathcal{I}_n^{(2)}$ is the second term (the sum). The first term $\mathcal{I}_n^{(1)}$ is the the solution for the case of no internal reflection and $\mathcal{I}_n^{(2)}$ is the correction for internal reflection.

The first term $\mathcal{I}_n^{(1)}(z)$ can be evaluated using Eq. (108) to be:

$$\begin{aligned}\mathcal{I}_n^{(1)} &= \frac{(-1)^n}{\sqrt{\pi l^*}} \sqrt{\frac{\pi l^*}{(z - z_n)^2}} \; \exp[-2\sqrt{\sigma_a (z - z_n)^2/l^*}] \\ &= \frac{(-1)^n}{|z - z_n|} \; \exp\Big[-2|z - z_n|\sqrt{\sigma_a/l^*}\Big]\end{aligned} \tag{113}$$

The second term is

$$\mathcal{I}_n^{(2)} = \sum_{m=0}^{n-1} \frac{A_{nm}}{\sqrt{\pi l^*}} \int_0^\infty \xi^{-3/2} \frac{\exp[-(z - z_n)^2/l^*\xi - \sigma_a\xi]}{mt + l^* + q\xi}\, \mathrm{d}\xi \tag{114}$$

For the values of l^* and q used in this investigation, the value of the integral in the above equation for terms $n \neq 1$ are very small compared to the $n = 1$ term and so can be neglected. With $A_{10} = 2l^*$ and $z_1 = -z_0 = -l^*$

$$\mathcal{I}_1^{(2)}(z) = 2\sqrt{\frac{l^*}{\pi}} \int_0^\infty \xi^{-3/2} \frac{\exp[-(z + l^*)^2/l^*\xi - \sigma_a\xi]}{l^* + q\xi}\, \mathrm{d}\xi \tag{115}$$

In Appendix 2, this integral is evaluated and it is shown that

$$\mathcal{I}_1^{(2)} = \frac{2}{1+\bar{z}}\ \exp\big(-2(1+\bar{z})\sqrt{\sigma_a l^*}\big) \times \left\{1-(1+\bar{z})\ \sqrt{\pi q}\ \exp\left[\frac{1}{q}\Big((1+\bar{z})q+\sqrt{\sigma_a l^*}\Big)^2\right] \times \operatorname{erfc}\left(\frac{1}{\sqrt{q}}\Big[(1+\bar{z})q+\sqrt{\sigma_a l^*}\Big]\right)\right\} \tag{116}$$

where erfc (x) is the complementary error function, and $\bar{z} = z/l^*$, so that

$$\bar{z} = \begin{cases} 0, & z = 0 \\ \tau, & z = t \end{cases} \tag{117}$$

where $\tau = t/l^*$ is the optical thickness.

6.3 Reflection and Transmission

The reflection and transmission is the probability flux through the surface: the $z = 0$ surface for reflection and the $z = t$ surface for transmission. Both the reflection, R, and the transmission, T, can be separated into two parts: the first part $R^{(1)}$, $T^{(1)}$ is the case for no internal reflection and the second part $R^{(2)}$, $T^{(2)}$ the correction due to internal reflection. Each part is given by the flux through the boundary:

$$\mathcal{J} = \mathcal{J}^{(1)} + \mathcal{J}^{(2)} \tag{118}$$

The probability flux through the surface is given by Eq. (85):

$$\begin{aligned} \mathcal{J}(z) &= \mp\frac{1}{2}\sum_{n=-\infty}^{\infty}(z-z_n)\,\mathcal{I}_n(z) \\ &= \mp\frac{1}{2}\left\{\sum_{n=-\infty}^{\infty}(z-z_n)\,\mathcal{I}_n^{(1)}(z) + (z-z_1)\,\mathcal{I}_1^{(2)}(z)\right\} \end{aligned} \tag{119}$$

where the negative sign for reflection and $z = 0$; for transmission the positive sign and $z = t$. The quantity $\mathcal{I}_n(z)$ is given in Eqs. (113) and (116).

6.4 *Reflection*

Reflection from the slab is given by Eq. (119) for $z = 0$:

$$R = \mathcal{J}(0)$$

and

$$\mathcal{J}(0) = \frac{1}{2} \sum_{n=-\infty}^{\infty} z_n \, \mathcal{I}_n(0) \tag{120}$$

so that from Eqs. (112) to (116)

$$\mathcal{J}(0) = \frac{1}{2} \left\{ \sum_{n=-\infty}^{\infty} (-1)^n \, z_n \, \mathcal{I}_n^{(1)}(0) + z_1 \mathcal{I}_1^{(2)}(0) \right\} \tag{121}$$

The flux, and therefore the reflectance, consists of two terms, the first for the case of no internal reflection, the second a correction to account for internal reflection.

First term:

The first term is given by Eqs. (121) and (113) with $z = 0$:

$$\mathcal{J}^{(1)} = \frac{1}{2} \sum_{n=-\infty}^{\infty} (-1)^n \frac{z_n}{|z_n|} \; \exp\left[-2|z_n|\sqrt{\sigma_a/l^*} \right] \tag{122}$$

Separating the even and odd terms:

$$\mathcal{J}^{(1)}(0) = \frac{1}{2} \sum_{k=-\infty}^{\infty} \left\{ \frac{z_{2k}}{|z_{2k}|} \exp\left[-2|z_{2k}|\sqrt{\sigma_a/l^*} \right] \right. \\ \left. - \frac{z_{2k+1}}{|z_{2k+1}|} \exp\left[-2|z_{2k+1}|\sqrt{\sigma_a/l^*} \right] \right\} \tag{123}$$

Noting that by Eq. (33) $z_{2k+1} = -z_{2k}$ this can be written:

$$\mathcal{J}^{(1)}(0) = \frac{1}{2} \sum_{k=-\infty}^{\infty} \left\{ \frac{z_{2k}}{|z_{2k}|} \exp\left[-2|z_{2k}|\sqrt{\sigma_a/l^*} \right] \right. \\ \left. + \frac{z_{2k}}{|z_{2k}|} \exp\left[-2|z_{2k}|\sqrt{\sigma_a/l^*} \right] \right\} \tag{124}$$

which is

$$\mathcal{J}^{(1)}(0) = \sum_{k=-\infty}^{\infty} \frac{z_{2k}}{|z_{2k}|} \exp\left[-2|z_{2k}|\sqrt{\sigma_a/l^*} \right] \tag{125}$$

This is precisely the relation found in Eq. (42) and indicates that the first term in Eq. (121) is the result for reflection without internal reflection. Noting that

$$R^{(1)} = \mathcal{J}^{(1)}(0),$$

one uses the result Eq. (46) to obtain

$$R^{(1)} = \exp\left(-2\sqrt{\sigma_a l^*}\right) + \frac{\sinh\left[2\sqrt{\sigma_a l^*}\right]}{\sinh\left[2\tau\sqrt{\sigma_a l^*}\right]}\exp\left(-2\tau\sqrt{\sigma_a l^*}\right) \tag{126}$$

which is the reflectance for the case of no internal reflection.

Second term:

Noting that $R^{(2)} = \mathcal{J}^{(2)}$, and using Eq. (121)

$$\begin{aligned} \mathcal{J}^{(2)}(0) &= z_1 \mathcal{I}_1^{(2)}(0) \\ &= -l^*\, \mathcal{I}_1^{(2)}(0) \end{aligned} \tag{127}$$

since $z_1 = -l^*$. One obtains the second term in Eq. (121) from Eq. (119) and Eq. (116) to get:

$$\begin{aligned} R^{(2)} &= -\exp\left(-2\sqrt{\sigma_a l^*}\right) \\ &\times \left\{1 - \sqrt{\pi q}\ \exp\left[\frac{1}{q}\left(q + \sqrt{\sigma_a l^*}\right)^2\right]\operatorname{erfc}\left(\frac{1}{\sqrt{q}}\left[q + \sqrt{\sigma_a l^*}\right]\right)\right\} \end{aligned} \tag{128}$$

6.5 *Transmission*

The transmission through the slab is given by Eq. (119) for $z = t$:

$$T = \mathcal{J}(t)$$

and

$$\mathcal{J}(t) = \frac{1}{2}\sum_{n=-\infty}^{\infty}(t - z_n)\,\mathcal{I}_n(t) \tag{129}$$

which is

$$\mathcal{J}(t) = \frac{1}{2}\sum_{n=-\infty}^{\infty}(-1)^n\,(t - z_n)\,\mathcal{I}_n^{(1)}(t) + (t - z_1)\mathcal{I}_1^{(2)}(t) \tag{130}$$

Again, the flux consists of two terms, the first for the case of no internal reflection, the second a correction to account for internal reflection.

First term:

From Eq. (113):

$$\mathcal{I}_n^{(1)}(t) = \frac{(-1)^n}{|t - z_n|}\ \exp\Big[-2|t - z_n|\sqrt{\sigma_a/l^*}\Big] \tag{131}$$

so that:

$$\mathcal{J}^{(1)}(t) = \frac{1}{2}\sum_{n=-\infty}^{\infty}(-1)^n\frac{t - z_n}{|t - z_n|}\ \exp\Big[-2|t - z_n|\sqrt{\sigma_a/l^*}\Big] \tag{132}$$

Separating the odd and even terms in Eq. (132) one obtains

$$\begin{aligned}\mathcal{J}^{(1)}(t) = \frac{1}{2}\sum_{k=-\infty}^{\infty}\Bigg\{&\frac{t - z_{2k}}{|t - z_{2k}|}\ \exp\Big[-2|t - z_{2k}|\sqrt{\sigma_a/l^*}\Big]\\ &-\frac{t - z_{2k+1}}{|t - z_{2k+1}|}\ \exp\Big[-2|t - z_{2k+1}|\sqrt{\sigma_a/l^*}\Big]\Bigg\}\end{aligned} \tag{133}$$

which is, noting that $z_{2k+1} = -z_{2k}$ by Eq. (33):

$$\begin{aligned}\mathcal{J}^{(1)}(t) =&\frac{1}{2}\sum_{k=-\infty}^{\infty}\Bigg\{\frac{t - z_{2k}}{|t - z_{2k}|}\ \exp\Big[-2|t - z_{2k}|\sqrt{\sigma_a/l^*}\Big]\\ &-\frac{t + z_{2k}}{|t + z_{2k}|}\ \exp\Big[-2|t + z_{2k}|\sqrt{\sigma_a/l^*}\Big]\Bigg\}\end{aligned} \tag{134}$$

Again by Eq. (33) one sees that:

$$t + z_{2k} = t + 2kt + l^* = (2k+1)t + l^*$$

and

$$t - z_{2k} = t - 2kt - l^* = -\Big[(2k-1)t + l^*\Big]$$

so that

$$\begin{aligned}\mathcal{J}^{(1)}(t) = -\frac{1}{2}\sum_{k=-\infty}^{\infty}\Bigg\{&\frac{(2k-1)t + l^*}{|(2k-1)t + l^*|}\ \exp\Big[-2|(2k-1)t + l^*|\sqrt{\sigma_a/l^*}\Big]\\ &+\frac{(2k+1)t + l^*}{|(2k+1)t + l^*|}\ \exp\Big[-2|(2k+1)t + l^*|\sqrt{\sigma_a/l^*}\Big]\Bigg\}\end{aligned} \tag{135}$$

In the first term in curly brackets, re-order terms in the summation: $k \to k+1$, so

$$\mathcal{J}^{(1)}(t) = -\sum_{k=-\infty}^{\infty} \frac{(2k+1)t + l^*}{|(2k+1)t + l^*|} \exp\Big[-2|(2k+1)t + l^*|\sqrt{\sigma_a/l^*}\Big] \tag{136}$$

or

$$\mathcal{J}^{(1)}(t) = -\sum_{k(\text{odd})=-\infty}^{\infty} \frac{kt + l^*}{|kt + l^*|} \exp\Big[-2|kt + l^*|\sqrt{\sigma_a/l^*}\Big] \tag{137}$$

where k(odd) indicates only odd values of k are summed. This equation is the same as Eq. (54), which indicates that the first term in Eq. (132) is the transmission for the case that there is no internal reflection.

Noting that $T^{(1)} = \mathcal{J}^{(1)}(t)$ and using Eq. (57), one can write:

$$T^{(1)} = \frac{\sinh\Big[2\sqrt{\sigma_a l^*}\Big]}{\sinh\Big[2\tau\sqrt{\sigma_a l^*}\Big]} \tag{138}$$

which is the transmission through the slab for the case of no internal reflection.

Second term:

The second term in Eq. (130) is

$$T^{(2)} = \mathcal{J}^{(2)}(t) = \frac{t + l^*}{2}\, \mathcal{I}_1^{(2)}(t) \tag{139}$$

where $z_1 = -l^*$ and $\mathcal{I}_1^{(2)}(t)$ is obtained in Appendix 2, Eq. (178). One finds:

$$\begin{aligned} T^{(2)} = \exp\big(-(\tau+1)\sqrt{2\sigma_a l^*}\big) \\ \times \Bigg\{1 - (\tau+1)\sqrt{\pi q}\, \exp\Bigg[\frac{1}{q}\Big((\tau+1)q + \sqrt{\sigma_a l^*}\Big)^2\Bigg] \\ \times \operatorname{erfc}\Bigg(\frac{1}{\sqrt{q}}\Big[(\tau+1)q + \sqrt{\sigma_a l^*}\Big]\Bigg)\Bigg\} \end{aligned} \tag{140}$$

where $\tau = t/l^*$ is the optical thickness.

For the values of q and τ of interest in this investigation, it is found that

$$T^{(2)} \ll T^{(1)}.$$

Internal reflection has negligible effect on the transmission of light through the turbid slab, so one sets:

$$T^{(2)} = 0.$$

6.6 Normalization

The expressions for reflection and transmission are proportional to a normalization factor a_0 that was set to 1 for ease in notation Eq. (105). The normalization factor should be set such that for $\sigma_a = 0$:

$$a_0 R + a_0 T = 1 \tag{141}$$

or

$$R + T = \frac{1}{a_0} \tag{142}$$

so that

$$R \to a_0 R, \qquad T \to a_0 T$$

where $R = R^{(1)} + R^{(2)}$ and $T = T^{(1)}$. The probability is conserved if there is no absorption. From Eqs. (126) and (138), one finds for $\sigma_a = 0$:

$$R^{(1)} = 1 - \frac{1}{\tau}, \qquad T^{(1)} = \frac{1}{\tau}$$

so that using Eq. (142) one sees that:

$$a_0 = \frac{1}{1 + R^{(2)}}$$

From Eq. (128) for $\sigma_a = 0$:

$$R^{(2)} = \sqrt{\pi q}\ \exp(q)\,\mathrm{erfc}\left(\sqrt{q}\right) - 1 \tag{143}$$

so that

$$a_0 = \left\{\sqrt{\pi q}\ \exp(q)\,\mathrm{erfc}\left(\sqrt{q}\right)\right\}^{-1} \tag{144}$$

For $q \gg 1$, one can use the asymptotic expansion (Abram&Steg 7.1.23) (Abramowitz and Stegun 1972)

$$e^{x^2}\,\mathrm{erfc}(x) = \frac{1}{x\sqrt{\pi}} \sum_{k=0}^{\infty} (-1)^k \frac{(2k-1)!!}{(2x^2)^k} \tag{145}$$

to obtain:

$$\sqrt{\pi q}\ \exp(q)\,\mathrm{erfc}\left(\sqrt{q}\right) = \sum_{k=0}^{\infty} (-1)^k \frac{(2k-1)!!}{(2q^2)^k} \tag{146}$$

Fig. 5 Reflectance from slab: first term, second term, and total. The absolute value of the second term is shown. $l^* = 0.2t$, so that $\tau = 5$, and σ_a is in units of mm^{-1}, (with $t = 1\,mm$). The average internal reflectance is $r = 0.25$ so $q = 3$

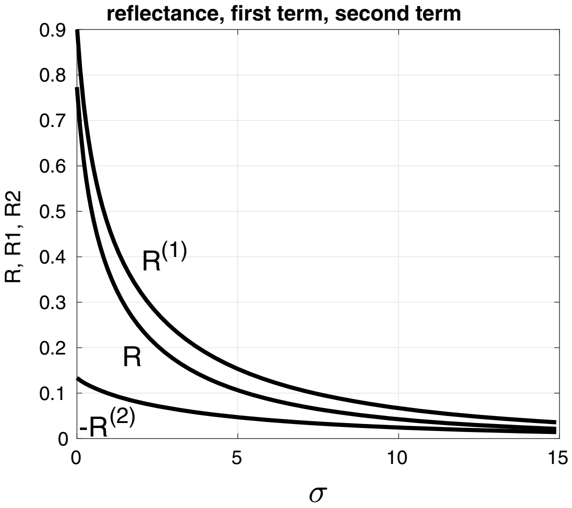

6.7 Plots of Reflectance and Transmittance—Internal Reflection

Figure 5 shows reflection for the slab with and without internal reflection as a function of the absorption coefficient σ_a, which is in units of t^{-1}. The curve labeled $R^{(1)}$ is the reflectance with no internal reflection, Eq. (126), the curve $R^{(2)}$ is the correction due to internal reflection, Eq. (128), and the curve R is the sum: the total reflection when there is internal reflection:

$$R = R^{(1)} + R^{(2)}$$

One sees that internal reflection can significantly affect reflection from the slab. As one would expect, the reflectance is decreased when internal reflection is included. Because of internal reflection, photons have a greater path length within the slab and therefore the absorption is greater.

Figure 6 shows the theory and Monte-Carlo where internal reflection is included. Again, in the Monte-Carlo simulation, there are 4×10^3 walks for each value of σ_a. The walk begins at $z = l^*/\pi$ (an average z step size into the slab). The walker carries a "payload" which is initially equal to 1 and decreases exponentially with the distance traveled. The walk ends when the payload is less than 10^{-4}. When the walker reaches a boundary, it deposits its payload reduced by the factor $1 - r$, and continues its walk with the payload reduced by the factor r. The reflectance or transmittance is the sum of the payloads deposited by the walker at each boundary, divided by the total number of walks. Each step l_z is obtained by $l_z = l \cos\theta$ with l a

Fig. 6 Monte-Carlo versus theory with internal reflection included. $l^* = 0.2t$, so that $\tau = 5$, and σ_a is in units of mm^{-1}, (with $t = 1$ mm. The average internal reflectance is $r = 0.25$ so $q = 3$

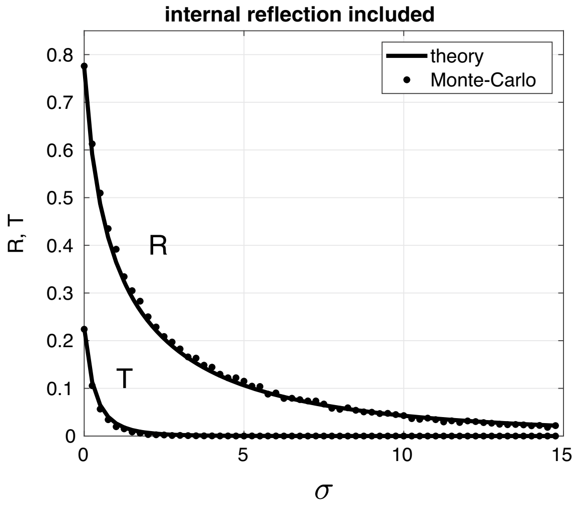

random number with distribution given by Eq. (6), and θ a random number uniformly distributed over $[0\ \pi]$.

In Fig. 6 one sees that there is good agreement between prediction made by the multiple-path model and the Monte-Carlo simulation.

7 Conclusion

Presented here is the reflection and transmission of a turbid slab as predicted by the multiple-path model. The multiple-path model treats photon interaction with disordered media as a random walk: the walk begins at a point that is one scattering mean free path from the surface of incidence, and the walk ends when the photon steps through one of the slab surfaces. It is a reflected photon if it steps through the surface of incidence; it is a transmitted photon if it steps through the opposite surface. If there is internal reflection at the slab boundaries, there is a probability that when the photon reaches a boundary, the photon steps back into the slab and continues its walk. An advantage of the multiple-path model over other models of light interacting with a slab is this simple treatment of boundaries.

A key quantity is the path length probability density, the probability that the photon has coordinate z after having walked a distance ξ. The gradient of this probability normal to the slab surface is the reflection or transmission. The form of the path length probability depends on the boundary conditions at the slab surface: if there is no internal reflection, the probability is zero at the boundary and if there is internal reflection the probability is proportional to the its normal gradient at the boundary, i.e.it has mixed or Robin boundary conditions.

Predictions of the multiple-path model are compared to experimental results for the case of no internal reflection, and there is seen to be good agreement. The reflection and transmission with internal reflection included are compared to a Monte-Carlo simulation, and again, there is found to be good agreement.

Appendix 1

One makes a partial fraction expansion of the finite product:

$$\prod_{k=0}^{n-1} \frac{(kt + l^* - x)}{(kt + l^* + x)} = B_n + \sum_{m=0}^{n-1} \frac{A_{nm}}{mt + l^* + x} \tag{147}$$

for $n \geq 1$. In the following the expansion coefficients B_n, A_{nm} are obtained using Eq. (147).

One first lets $x \to \infty$ in Eq. (147) to get

$$B_n = (-1)^n. \tag{148}$$

To get A_{nm} multiply both sides of Eq. (147) by $(ht + l^* + x)$ with $h = 0, 1, 2 \ldots n - 1$.

$$\begin{aligned} &\prod_{k=0}^{n-1} \frac{(kt + l^* - x)}{(kt + l^* + x)} (ht + l^* + x) \\ &\qquad = B_n (ht + l^* + x) + \sum_{m=0}^{n-1} \frac{A_{nm}}{mt + l^* + x} (ht + l^* + x) \end{aligned} \tag{149}$$

On the left side, the $k = h$ factor in the denominator cancels. Let $x = -(l^* + ht)$, then on the right side all terms, except $m = h$ vanish. One obtains:

$$A_{nm} = \frac{\prod_{k=0}^{n-1} (k + m + 2l^*/t)}{t^{-1} \prod_{\substack{k=0 \\ k \neq m}}^{n-1} (k - m)}$$

with $m = 0, 1, 2 \ldots n - 1$.

A similar result is found for $n < 0$ with $m \to m + 1$ and $2l^* \to -2l^*$.

Appendix 2

In the following the integral $\mathcal{I}_1^{(2)}$, Eq. (115), is evaluated. One first evaluates the integral $H(\beta, \alpha)$:

$$H(\beta, \alpha) = \int_0^\infty x^{-3/2} \, \frac{1}{1+x} \, \exp(-\beta/x - \alpha x) \, \mathrm{d}x, \tag{150}$$

then uses that solution to obtain $\mathcal{I}_1^{(2)}$.

The derivative of $H(\beta, \alpha)$ with respect to α is:

$$\begin{aligned} \frac{\mathrm{d}}{\mathrm{d}\alpha} H(\beta, \alpha) &= \int_0^\infty x^{-3/2} \frac{-x}{1+x} \exp(-\beta/x - \alpha x)\mathrm{d}x \\ &= \int_0^\infty x^{-3/2} \, \frac{-1-x+1}{1+x} \exp(-\beta/x - \alpha x)\mathrm{d}x \\ &= -\int_0^\infty x^{-3/2} \exp(-\beta/x - \alpha x)\mathrm{d}x + H(\beta, \alpha) \\ &= -\sqrt{\frac{\pi}{\beta}} e^{-2\sqrt{\beta\alpha}} + H(\beta, \alpha) \end{aligned} \tag{151}$$

where one uses:

$$\int_0^\infty x^{-3/2} \exp(-\beta/x - \alpha x)\mathrm{d}x = \sqrt{\frac{\pi}{\beta}} e^{-2\sqrt{\beta\alpha}} \tag{152}$$

Gradshteyn and Ryzhik (2007) (Grad&Ryzh 3.471.9). It follows that:

$$\frac{\mathrm{d}}{\mathrm{d}\alpha} H(\beta, \alpha) - H(\beta, \alpha) = -\sqrt{\frac{\pi}{\beta}} e^{-2\sqrt{\beta\alpha}} \tag{153}$$

Multiplying both sides by $\exp(-\alpha)$:

$$e^{-\alpha} \, \frac{\mathrm{d}}{\mathrm{d}\alpha} H(\beta, \alpha) - e^{-\alpha} \, H(\beta, \alpha) = -e^{-\alpha} \, \sqrt{\frac{\pi}{\beta}} e^{-2\sqrt{\beta\alpha}} \tag{154}$$

or

$$\frac{\mathrm{d}}{\mathrm{d}\alpha} \left[e^{-\alpha} \, H(\beta, \alpha) \right] = -e^{-\alpha} \, \sqrt{\frac{\pi}{\beta}} e^{-2\sqrt{\beta\alpha}} \tag{155}$$

Integrating both sides between 0 and α:

$$e^{-\alpha} \, H(\beta, \alpha) - H(\beta, 0) = -\sqrt{\frac{\pi}{\beta}} \int_0^\alpha e^{-u} \, e^{-2\sqrt{\beta u}} \, \mathrm{d}u \tag{156}$$

one obtains

$$H(\beta,\alpha) = e^{\alpha}\left[\; H(\beta,0) - \sqrt{\frac{\pi}{\beta}}\int_0^{\alpha} e^{-u}\; e^{-2\sqrt{\beta u}}\,\mathrm{d}u\right] \tag{157}$$

Note that by Eq. (150):

$$H(\beta,0) = \int_0^{\infty} \frac{e^{-\beta/y}}{y^{3/2}(y+1)}\,\mathrm{d}y \tag{158}$$

Substituting $x = 1/y$, this can be written:

$$H(\beta,0) = \int_0^{\infty} \sqrt{x}\;\frac{e^{-\beta x}}{x+1}\,\mathrm{d}x \tag{159}$$

which is (Grad&Ryzh 3.383.6 and Grad&Ryzh 9.254.2) (Gradshteyn and Ryzhik 2007):

$$H(\beta,0) = \sqrt{\frac{\pi}{\beta}} - \pi e^{\beta}\left[1 - \operatorname{erf}\left(\sqrt{\beta}\,\right)\right] \tag{160}$$

The integral in Eq. (157)

$$\mathcal{K}(\beta,\alpha) = \sqrt{\frac{\pi}{\beta}}\int_0^{\alpha} e^{-u-2\sqrt{\beta u}}\,\mathrm{d}u \tag{161}$$

is solved as follows:

Let $u = x^2$, so $\mathrm{d}u = 2x\,\mathrm{d}x$ and

$$\begin{aligned}\mathcal{K}(\beta,\alpha) &= 2\sqrt{\frac{\pi}{\beta}}\int_0^{\sqrt{\alpha}} x\, e^{-x^2-2\sqrt{\beta}x}\,\mathrm{d}x\\ &= 2\sqrt{\frac{\pi}{\beta}}\; e^{\beta}\int_0^{\sqrt{\alpha}} x\, e^{-(x+\sqrt{\beta})^2}\,\mathrm{d}x\end{aligned} \tag{162}$$

Let $u = x + \sqrt{\beta}$:

$$\mathcal{K}(\beta,\alpha) = 2\sqrt{\frac{\pi}{\beta}}e^{\beta}\int_{\sqrt{\beta}}^{\sqrt{\beta}+\sqrt{\alpha}} \left[u - \sqrt{\beta}\,\right]e^{-u^2}\,\mathrm{d}u \tag{163}$$

Dividing the above integral into two terms: $\mathcal{K} = \mathcal{K}_1 - \mathcal{K}_2$, with

$$\mathcal{K}_1 = 2\sqrt{\frac{\pi}{\beta}}e^{\beta}\int_{\sqrt{\beta}}^{\sqrt{\beta}+\sqrt{\alpha}} u\; e^{-u^2}\,\mathrm{d}u \tag{164}$$

and

$$\mathcal{K}_2 = 2\sqrt{\pi}e^{\beta}\int_{\sqrt{\beta}}^{\sqrt{\beta}+\sqrt{\alpha}} e^{-u^2}\ \mathrm{d}u \tag{165}$$

By the definition of the erf () function, the integral $\mathcal{K}_2$ is easily evaluated to obtain:

$$\mathcal{K}_2(\beta,\alpha) = \pi e^{\beta}\left[\mathrm{erf}\left(\sqrt{\beta}+\sqrt{\alpha}\right) - \mathrm{erf}\left(\sqrt{\beta}\right)\right] \tag{166}$$

To evaluate $\mathcal{K}_1$ one notes that

$$\int_0^u xe^{-x^2}\ \mathrm{d}x = \frac{1}{2}\left[1 - e^{-u^2}\right] \tag{167}$$

(Grad&Ryzh 3.321.4) Gradshteyn and Ryzhik (2007), and that

$$\int_{\sqrt{\beta}}^{\sqrt{\beta}+\sqrt{\alpha}} u\ e^{-u^2}\ \mathrm{d}u = \int_0^{\sqrt{\beta}+\sqrt{\alpha}} u\ e^{-u^2}\ \mathrm{d}u - \int_0^{\sqrt{\beta}} u\ e^{-u^2}\ \mathrm{d}u \tag{168}$$

so

$$\begin{aligned}\mathcal{K}_1(\beta,\alpha) &= \sqrt{\frac{\pi}{\beta}}\ e^{\beta}\left\{\exp(-\beta) - \exp\left[-(\sqrt{\beta}+\sqrt{\alpha})^2\right]\right\}\\ &= \sqrt{\frac{\pi}{\beta}}\left\{1 - \exp\left[-(2\sqrt{\beta\alpha}+\alpha)\right]\right\}\end{aligned} \tag{169}$$

One then obtains for $\mathcal{K}$:

$$\begin{aligned}\mathcal{K}(\beta,\alpha) = \sqrt{\frac{\pi}{\beta}}&\left\{1 - \exp\left[-(2\sqrt{\beta\alpha}+\alpha)\right]\right\}\\ &-\pi e^{\beta}\left[\mathrm{erf}\left(\sqrt{\beta}+\sqrt{\alpha}\right) - \mathrm{erf}\left(\sqrt{\beta}\right)\right].\end{aligned} \tag{170}$$

The factor in square brackets on the right side of Eq. (157) can be written using Eqs. (160) and (161) and Eq. (170):

$$\begin{aligned}
H(\beta,0)-\mathcal{K}(\beta,\alpha) &= \sqrt{\frac{\pi}{\beta}}-\pi e^{\beta}\left[1-\operatorname{erf}\left(\sqrt{\beta}\,\right)\right] \\
&\quad -\sqrt{\frac{\pi}{\beta}}\left\{1-\exp\left[-(2\sqrt{\beta c}+\alpha)\right]\right\} \\
&\quad -\pi e^{\beta}\left[\operatorname{erf}\left(\sqrt{\beta}+\sqrt{\alpha}\right)-\operatorname{erf}\left(\sqrt{\beta}\right)\right] \\
&= -\pi e^{\beta}\left[1-\operatorname{erf}\left(\sqrt{\beta}\,\right)\right]+\sqrt{\frac{\pi}{\beta}}\,\exp\left(-2\sqrt{\beta c}-\alpha\,\right) \\
&\quad +\pi e^{\beta}\left[\operatorname{erf}\left(\sqrt{\beta}+\sqrt{\alpha}\right)-\operatorname{erf}\left(\sqrt{\beta}\right)\right] \\
&= -\pi e^{\beta}+\sqrt{\frac{\pi}{\beta}}\,\exp\left(-2\sqrt{\beta\alpha}-\alpha\,\right)+\pi e^{\beta}\left[\operatorname{erf}\left(\sqrt{\beta}+\sqrt{\alpha}\right)\right] \\
&= \sqrt{\frac{\pi}{\beta}}\,\exp\left(-2\sqrt{\beta\alpha}-\alpha\,\right)-\pi e^{\beta}\left[1-\operatorname{erf}\left(\sqrt{\beta}+\sqrt{\alpha}\right)\right]
\end{aligned} \tag{171}$$

so that

$$\begin{aligned}
H(\beta,\alpha) &= e^{\alpha}\left[H(\beta,0)-\mathcal{K}(\beta,\alpha)\right] \\
&= \sqrt{\frac{\pi}{\beta}}\,\exp\left(-2\sqrt{\beta\alpha}\right)-\pi e^{\beta+\alpha}\left[1-\operatorname{erf}\left(\sqrt{\beta}+\sqrt{\alpha}\right)\right] \qquad (172) \\
&= \sqrt{\frac{\pi}{\beta}}\,\exp\left(-2\sqrt{\beta\alpha}\right)-\pi e^{\beta+\alpha}\operatorname{erfc}\left(\sqrt{\beta}+\sqrt{\alpha}\right)
\end{aligned}$$

where erfc (x) is the complementary error function. Completing the square in the second exponential:

$$\begin{aligned}
H(\beta,\alpha) &= \sqrt{\frac{\pi}{\beta}}\,\exp\left(-2\sqrt{\beta\alpha}\right)-\pi\exp\left(-2\sqrt{\beta\alpha}\right)e^{(\sqrt{\beta}+\sqrt{\alpha})^2}\operatorname{erfc}\left(\sqrt{\beta}+\sqrt{\alpha}\right) \\
&= \exp\left(-2\sqrt{\beta\alpha}\right)\left\{\sqrt{\frac{\pi}{\beta}}-\pi e^{(\sqrt{\beta}+\sqrt{\alpha})^2}\operatorname{erfc}\left(\sqrt{\beta}+\sqrt{\alpha}\right)\right\}
\end{aligned} \tag{173}$$

or

$$\begin{aligned}
H(\beta,\alpha) &= \sqrt{\frac{\pi}{\beta}}\exp\left(-2\sqrt{\beta\alpha}\right) \\
&\quad \times\left\{1-\sqrt{\pi\beta}\,e^{(\sqrt{\beta}+\sqrt{\alpha})^2}\operatorname{erfc}\left(\sqrt{\beta}+\sqrt{\alpha}\right)\right\}
\end{aligned} \tag{174}$$

One uses this solution for $H(\beta,\alpha)$ to obtain an expression for $\mathcal{I}_1^{(2)}(z)$.
Note that

$$\mathcal{I}_1^{(2)}(z) = 2\sqrt{\frac{l^*}{\pi}} \int_0^\infty \xi^{-3/2}\ \frac{\exp\big[-(z+l^*)^2/l^*\xi - \sigma_a\xi\big]}{l^* + q\xi}\ \mathrm{d}\xi \tag{175}$$

Let $\xi = yl^*/q$ in Eq. (175), then

$$\begin{aligned}
\mathcal{I}_1^{(2)}(z) &= 2\sqrt{\frac{l^*}{\pi}}(q/l^*)^{1/2} \int_0^\infty y^{-3/2}\ \frac{\exp\big[-q(z+l^*)^2/l^{*2}y - \sigma_a l^* y/q\big]}{l^* + l^* y}\ \mathrm{d}y \\
&= 2\sqrt{\frac{q}{\pi}} \int_0^\infty y^{-3/2}\ \frac{\exp\big[-q(z+l^*)^2/l^{*2}y - \sigma_a l^* y/q\big]}{l^* + l^* y}\ \mathrm{d}y \\
&= 2\sqrt{\frac{q}{\pi l^{*2}}} \int_0^\infty y^{-3/2}\ \frac{\exp\big[-q(z+l^*)^2/l^{*2}y - \sigma_a l^* y/q\big]}{1 + y}\ \mathrm{d}y
\end{aligned} \tag{176}$$

which by Eq. (150) is equal to:

$$\mathcal{I}_1^{(2)} = 2\sqrt{\frac{q}{\pi l^{*2}}}\ H(\beta, \alpha) \tag{177}$$

with $\beta = q(z+l^*)^2/l^{*2}$ and $\alpha = \sigma_a l^*/q$. Using Eq. (174) this can be written:

$$\begin{aligned}
\mathcal{I}_1^{(2)}(z) = {} & 2\sqrt{\frac{q}{\pi l^{*2}}}\sqrt{\frac{\pi l^{*2}}{q(z+l^*)^2}}\ \exp\big(-2|z+l^*|\sqrt{\sigma_a/l^*}\big) \\
& \times \left\{1 - |z+l^*|\ \sqrt{\frac{\pi q}{l^{*2}}}\ \exp\left[\left(|z+l^*|\sqrt{q/l^{*2}} + \sqrt{\sigma_a l^*/q}\right)^2\right]\right. \\
& \left. \times\ \mathrm{erfc}\left(|z+l^*|\sqrt{q/l^{*2}} + \sqrt{\sigma_a l^*/q}\right)\right\}
\end{aligned} \tag{178}$$

or

$$\begin{aligned}
\mathcal{I}_1^{(2)}(z) = {} & \frac{2}{|z+l^*|}\ \exp\big(-2|z+l^*|\sqrt{\sigma_a/l^*}\big) \\
& \times \left\{1 - |z+l^*|\ \sqrt{\frac{\pi q}{l^{*2}}}\ \exp\left[\left(|z+l^*|\sqrt{q/l^{*2}} + \sqrt{\sigma_a l^*/q}\right)^2\right]\right. \\
& \left. \times\ \mathrm{erfc}\left(|z+l^*|\sqrt{q/l^{*2}} + \sqrt{\sigma_a l^*/q}\right)\right\}
\end{aligned} \tag{179}$$

Defining $\bar{z} = z/l^*$, so that

$$\bar{z} = \begin{cases} 0, & z = 0 \\ \tau, & z = t \end{cases} \tag{180}$$

where $\tau = t/l^*$ is the optical thickness. One obtains:

$$\mathcal{I}_1^{(2)}(\bar{z}) = \frac{2/l^*}{1+\bar{z}}\ \exp\big(-2(1+\bar{z})\sqrt{\sigma_a l^*}\big) \times \left\{1-(1+\bar{z})\ \sqrt{\pi q}\ \exp\left[\Big((1+\bar{z})\sqrt{q}+\sqrt{\sigma_a l^*/q}\Big)^2\right] \times \operatorname{erfc}\Big((1+\bar{z})\sqrt{q}+\sqrt{\sigma_a l^*/q}\Big)\right\} \tag{181}$$

or

$$\mathcal{I}_1^{(2)}(\bar{z}) = \frac{2/l^*}{(1+\bar{z})}\ \exp\big(-2(1+\bar{z})\sqrt{\sigma_a l^*}\big) \times \left\{1-(1+\bar{z})\ \sqrt{\pi q}\ \exp\left[\frac{1}{q}\Big((1+\bar{z})q+\sqrt{\sigma_a l^*}\Big)^2\right] \times \operatorname{erfc}\left(\frac{1}{\sqrt{q}}\Big[(1+\bar{z})q+\sqrt{\sigma_a l^*}\Big]\right)\right\} \tag{182}$$

The asymptotic expansion of $\exp(x^2)\ \operatorname{erfc}(x)$ for large x is (Abramowitz and Stegun 1972):

$$e^{x^2}\ \operatorname{erfc}(x) = \frac{1}{x\sqrt{\pi}}\sum_{k=0}^{\infty}(-1)^k\frac{(2k-1)!!}{(2x^2)^k} \tag{183}$$

with

$$x = \frac{1}{\sqrt{2q}}\Big[(1+\bar{z})q+\sqrt{2\sigma_a l^*}\Big] \tag{184}$$

References

Abramowitz M, Stegun IA (eds) (1972) Handbook of mathematical functions with formulas, graphs, and mathematical tables. Government Printing Office, U.S

Chandrasekhar S (1960) Radiative transfer. Dover Publications

Collins FC, Kimball GE (1949) Diffusion-controlled reaction rates. J Colloid Sci 4(4):425–437

Contini D, Martelli F, Zaccanti G (1997) Photon migration through a turbid slab described by a model based on diffusion approximation. I. Theory. Appl Opt 36(19):4587–4599

Coppel LG, Neuman M, Edstrom P (2011) Lateral light scattering in paper - MTF simulation and measurement. Opt Express 19:25181–25187

Dainty JC, Shaw R (1974) Image science. Academic

Erban R, Chapman SJ (2007) Reactive boundary conditions for stochastic simulations of reaction-diffusion processes. Phys Biol 4(1):16–28

Farrell TJ, Patterson MS, Wilson B (1992) A diffusion theory model of spatially resolved, steady-state diffuse reflectance for the noninvasive determination of tissue optical properties in vivo. Med Phys 19(4):879–888

Gandjbakhche AH, Weiss GH (1995a) V: random walk and diffusion-like models of photon migration in turbid media. Prog Opt 34:333–402

Gandjbakhche AH, Weiss GH (1995b) Random walk and diffusion-like models of photon migration in turbid media. Prog Opt 34:333–402

Gradshteyn IS, Ryzhik IM (2007) Table of integrals, series, and products. Elsevier/Academic, Amsterdam

Groenhuis RAJ, Ferwerda HA, Ten Bosch JJ (1983) Scattering and absorption of turbid materials determined from reflection measurements. 1: theory. Appl Opt 22(16):2456–2462

Haskell RC, Svaasand Lars O, Tsong-Tseh Tsay, Ti-Chen Feng, McAdams Matthew S, Tromberg Bruce J (1994) Boundary conditions for the diffusion equation in radiative transfer. J Opt Soc Am A 10:2727–2741

Hebert M, Hersch RD (2004) Classical print reflection models: a radiometric approach. J Imaging Sci Technol 48:363–374

Hebert M, Hersch RD (2015) Review of spectral reflectance models for halftone prints: principles, calibration, and prediction accuracy. Color Res Appl 40:383–397

Ishimaru A (1978) Wave propagation and scattering in random media. Academic

Keijzer M, Star WM, Storchi PRM (1988) Optical diffusion in layered media. Appl Opt 27(9):1820–1824

Kienle A, Lilge L, Patterson MS, Hibst R, Wilson BC (1996) Spatially resolved absolute diffuse reflectance measurements for noninvasive determination of the optical scattering and absorption coefficients of biological tissue. Appl Opt 35(13):2304–2314

Kokhanovsky AA (2006) Cloud optics. Atmospheric and oceanographic sciences library. Springer, Netherlands

Rogers GL (2015) The point spread function and optical dot gain (Chap. 28). In: Kriss M (ed) Handbook of digital imaging. Wiley, NY

Rogers GL (2016) Random walk analysis for reflectance and transmission of turbid media. Color Res Appl

Rogers G (2018) Analysis of the Yule-Nielsen effect with the multiple-path point spread function in a frequency-modulated halftone. J Opt Soc Am A 35:917–922

Rogers G, Dalloz N, Fournel T, Hebert M (2017) Multiple-path model of spectral reflectance of a dyed fabric. J Opt Soc Am A 34:721–725

Rogers G, Corblet O, Fournel T, Hebert M (2019) Measurement of the diffusion of light within paper. J Opt Soc Am A 36:636–640

Singer A, Schussy Z, Holcmanz D, Osipovx A (2008) Partially reflected diffusion. SIAM J Appl Math 844–868

Stamnes K, Tsay S-C, Wiscombe W, Jayaweera K (1988) Numerically stable algorithm for discrete-ordinate-method radiative transfer in multiple scattering and emitting layered media. Appl Opt 27:2502–2509

Wang L, Jacques SL, Zheng L (1995) MCML–Monte Carlo modeling of light transport in multi-layered tissues. Comput Methods Programs Biomed 47

Yule JAC, Neilsen WJ (1951) The penetration of light into paper and its effect on half-tone reproduction. In: TAGA proceedings, pp 65–76

Laboratory Measurements of Multi-spectral, Polarization, and Angular Characteristics of Light Reflected from Particulate Samples

Hao Zhang, Weidong Jin, Te Jiang, Yazhou Yang, and Pei Ma

Abstract Visible and near-infrared reflectance spectroscopy is a powerful technique in remotely identifying the mineralogical and chemical compositions of planetary surface materials. Reflectance spectra measured at varied illumination and viewing conditions may also reveal the physical properties of planetary surfaces. The accurate data interpretation would require quantitative modeling as well as laboratory measurements of analog samples, in particular the granular materials. Here we describe three light scattering facilities constructed at China University of Geosciences used in spectrophotometric measurements of particulate samples. The first one is a three-colour (633, 532, and 473 nm) goniometer capable of measuring the polarized bi-directional reflectance from phase angle 2 to 130 degrees in the principal plane. The second one is a multi-angular imaging device capable of measuring reflectance in the upper hemisphere at discrete wavelengths (typical values include 458, 633, 750, and 905 nm). The third one is a bi-directional reflectance spectrometer that covers the wavelength range from 350 to 2500 nm. For each instrument, we first introduce the instrument concept and system descriptions, followed by the calibration and characterizations. Typical measurement results with applications to planetary remote sensing are then presented.

H. Zhang (✉) · W. Jin · T. Jiang · Y. Yang · P. Ma
China University of Geosciences, Wuhan, China
e-mail: zhanghao@cug.edu.cn

H. Zhang
CAS Center for Excellence in Comparative Planetology, Hefei, China

W. Jin
University of Alabama, Tuscaloosa, AL, USA

Y. Yang
National Space Science Center, Chinese Academy of Sciences, Beijing, China

A. Kokhanovsky (ed.), *Springer Series in Light Scattering*, Springer Series in Light Scattering, https://doi.org/10.1007/978-3-031-10298-1_2

1 Introduction

Visible and near-infrared (0.4–2.5 μm) reflectance spectroscopy is one of the most powerful tools in remotely detecting the chemical and mineralogical compositions of planetary surfaces because of the presence of diagnostic absorption features caused by crystal filed transitions in planetary materials (e.g., Adams and Filice 1967; Burns 1993) and the atmospheric transparency within this spectral range. Due to the rarity of returned planetary samples, the quantitative interpretation of planetary spectra depends heavily on laboratory measurements on analog materials (e.g., Clark et al. 2003; Pieters 1983; Pieters and Hiroi 2004). However, the illumination and viewing conditions of remote sensing spectra usually vary greatly in contrast to the limited configurations of library spectral measurements. For example, most library spectra hosted at the Reflectance Laboratory (RELAB) facility (Pieters and Hiroi 2004) were measured at the "RELAB configuration" with incident zenith 30° and viewing zenith 0° in the principal plane (see definitions in Sect. 2 below), while space mission spectra are rarely measured in the principal plane due to spacecraft safety concerns. Such a discrepancy in reflectance configurations may lead to disparate reflectance spectra of similar or identical sample surfaces and may obscure any direct comparisons for the following reasons.

Most solar system bodies including the terrestrial planets, dwarf planets, small bodies (asteroids and comets), and planetary moons are covered by a layer of fine regolith particles produced by long-term space weathering processes. Since most particulate layers reflect light anisotropically, and this scattering anisotropy is usually wavelength-dependent, the spectral features including albedo, absorption depth, and spectral slope of the same surface may be dependent on scattering geometry. For example, many airless bodies exhibit an increased spectral slope at larger phase angles, the so-called phase reddening effect (e.g., Abe et al. 2006; Johnson et al. 2013; Schröder et al. 2014). Such an angular dependence of spectral features complicates the interpretations of remote sensing spectra.

On the other hand, the directional spectral features contain rich information of the physical properties of regolith grains including the particle shape, grain transparency, particle size distribution, and packing conditions. This is because the angular scattering behavior of small particles is mostly controlled by particle physical properties, in contrast to that the absorption features are mostly controlled by chemical and mineralogical properties. For example, the well-known opposition effect which is the pronounced brightness enhancement toward the opposition is strongly dependent on particle size, transparency, and porosity of the packed layer (e.g., Muinonen et al. 2002; Shkuratov et al. 2011). These physical conditions of the regolith layers are direct consequences of the geological evolution and the space environment of the planetary surface. Therefore, a thorough understanding of light reflection by packed particulate layers would not only enable us to calibrate remote sensing spectra to the standard library spectra and help interpret planetary data, but also help us infer the physical and geological properties of planetary surfaces (e.g., Jin et al. 2015; Ma et al. 2020; Jiang et al. 2021).

To study light reflection by surfaces of planetary analogues, research groups around the world have built a multitude of multi-angular spectro-goniometric devices that are capable of measuring reflectance from particulate surfaces (e.g., Sandmeier 2000; Voss et al. 2000; Shepard 2001; Brissaud et al. 2004; Pieters and Hiroi 2004; Coburn and Peddle 2006; Gunderson et al. 2006, 2007; Shkuratov et al. 2007; Sun et al. 2014; Pommerol et al. 2019). Just like any scientific apparatus, no light scattering device can be made omnipotent in having a wide spectral coverage, high angular resolution, a thorough coverage of the incident and viewing directions, polarization capabilities, while at the same time with moderate complexity and cost. Instead, people have designed and constructed instruments with different specialized capabilities for different goals. Here we describe the three light scattering devices constructed at China University of Geosciences used in the study of reflectance properties of planetary analog materials. The first one is a three-wavelength (633, 532, and 473 nm) goniometer capable of measuring the polarized bi-directional reflectance from phase angle 2–130° in the principal plane. The second one is a multi-angular imaging system capable of measuring the bi-directional reflectance at various wavelengths. The third one is a bi-directional reflectance spectrometer that covers the spectral range from 350 to 2500 nm. We first introduce the basic definitions including the scattering geometry and polarized reflectance. Then we present the instrument descriptions for each device followed by its calibration and characterization procedures. Typical measurement results of various particulate layers are then presented.

2 Basic Definitions and Design Tradeoffs

2.1 Reflectance Configuration and Nomenclature

The reflectance configuration for a disk-resolved surface is shown in Fig. 1. In this plot, the collimated light beam with zenith angle i and azimuth angle $\phi = 0°$ is incident onto a flat surface with local surface normal $\boldsymbol{n}$. The detector views the surface from the direction with a viewing zenith angle e and azimuth angle ϕ. The solar phase angle α is the angle between the incident and viewing directions. The plane containing the incident and viewing directions is the scattering plane, and the plane containing the incident direction, viewing direction, and surface normal is the principal plane.

To quantify the measured reflectance value, the radiance factor *I/F* (Hapke 2012), defined as the ratio of the reflected radiance *I* to the incident flux *F*, has been extensively used in the planetary science community. The *I/F* is related to the reflectance factor (REFF) as

$$I/F \equiv \frac{I}{J/\pi} = \mu_0 \mathrm{REFF} = \pi \frac{I}{J} \tag{1}$$

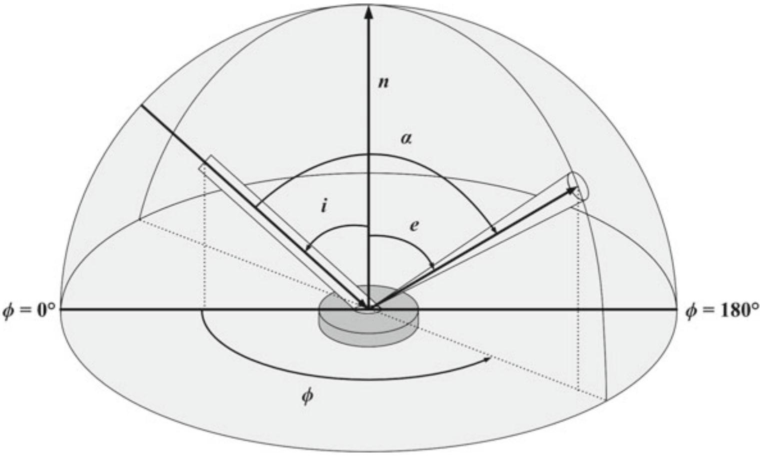

Fig. 1 Schematics of the reflectance geometry that shows the incident zenith angle i, viewing zenith angle e, solar phase angle α, and azimuth angle ϕ. The plane containing the incident direction, viewing direction, and the local zenith or surface normal $\boldsymbol{n}$ is the principal plane

where J is the incident irradiance with $J = \pi F$ and $\mu_0 = \cos i$. The REFF can be easily measured in laboratory (e.g., Zhang and Voss 2005, 2008) by first taking the ratio of the sample radiance and the calibration plaque (e.g., Labsphere Spectralon) radiance, then taking into account the non-Lambertian behavior of the plaque, and then normalizing the plaque reflectance to the widely accepted absolute values (e.g., Bruegge et al. 2001). Then *I/F* is obtained by multiplying the REFF by μ_0. Since a Lambertian surface has a constant REFF or *I/F*, using either of them can easily quantify how a sample surface reflectance deviates from a perfect diffuse surface. Detailed examples of the REFF measurement will be given in the following sections.

Upon reflection from the surface of an airless body, the unpolarized sunlight becomes weakly polarized that may contain both linearly and circularly polarized components. As shown in Fig. 2, by observing the reflected intensity with polarizations parallel and perpendicular to the scattering plane, the degree of linear polarization (DOP) can be obtained as

$$\mathrm{DOP} = \frac{I_\perp - I_\parallel}{I_\perp + I_\parallel}, \tag{2}$$

where $I_\perp$ and $I_{//}$ are the intensity components perpendicular and parallel to the scattering plane, respectively. Figure 3 shows the typical intensity and polarization phase curves of an airless body (e.g., Muinonen et al. 2002). As α increases from 0° (the opposition), the intensity decreases and the DOP first decreases from 0 to a minimum value $\mathrm{DOP}_{\min}$, and then increases to 0 at the inversion angle α_{inv}. At $\alpha_{\max}$ (typically ~100°), the *DOP* reaches a maximum value $\mathrm{DOP}_{\max}$. These parameters, together with the slope h at α_{inv}, contain rich information of the mineralogical and physical properties of the regolith (e.g., Mishchenko et al. 2010; Shkuratov et al.

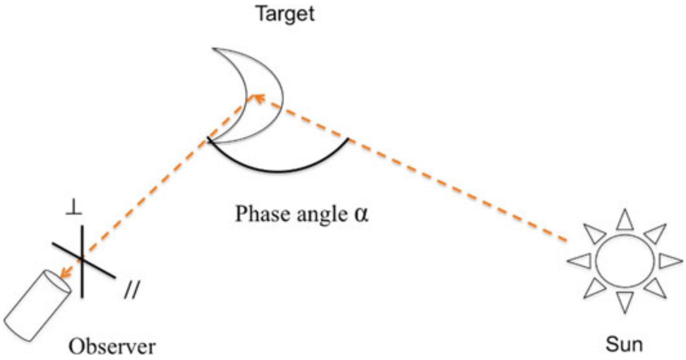

Fig. 2 Schematics of polarized remote observations of a planetary surface. Upon reflection from the surface of an airless target body, the unpolarized sunlight becomes weakly polarized

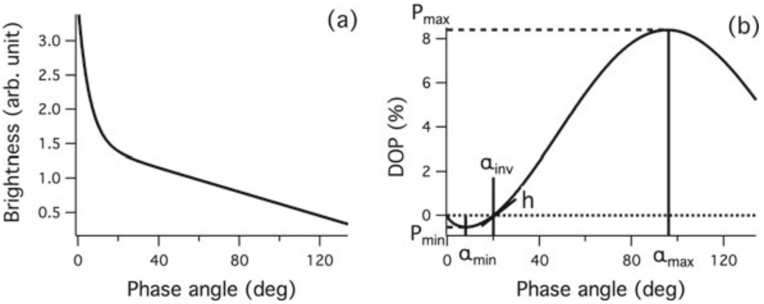

Fig. 3 Schematics of the intensity phase curve (**a**) and polarization phase curve (**b**)

2015; Kaydash et al. 2011; Levasseur-Regourd et al. 2015; Belskaya et al. 2017). Unfortunately, our current understanding of the physical mechanisms responsible for negative polarization (NEP) is still far from complete. Thus, extensive laboratory measurements on analog samples with diverse optical properties are desired to dig out the quantitative information that the NEP may contain.

2.2 *Instrument Design Tradeoffs*

The relevant specifications of a spectro-goniometric system include phase angle coverage, angular resolution, dynamic range, polarization capabilities, wavelength range coverage, level of automation, and so forth. Compromises must be made in order to ensure the instrument has dedicated functionalities, and often times multiple systems with complementary functionalities are needed to make comprehensive measurements. In the following, we give a brief discussion on several trade-offs that constrained the designs of our instruments.

2.2.1 Over-Illumination Versus Over-View

For field goniometers using solar radiation as the light source (e.g., Sandmeier 2000; Coburn and Peddle 2006), the detector always views a small portion of the illuminated area of the sample surface. This so-called over-illumination scheme has the advantages that the detected signal is insensitive to the distance between the detector and the sample surface, and the detected signal does not fall off as the cosine of the viewing zenith angle. For a laboratory goniometric device, however, the over-illumination scheme may waste a large portion of the lighting budget and thus may lead to a low signal-to-noise (SNR) level. Moreover, this scheme would require a very precise sensor alignment, or inconsistent viewed areas at different viewing angles would result, especially for heterogeneous surfaces. In contrast, the over-view scheme has a field of view (FOV) that is larger than the illuminated spot at all viewing directions and as a result, the detector alignment is less critical and the incident energy is fully utilized. The major con of the over-view scheme is the cosine behavior of the collected radiance versus viewing zenith angle and hence the low collection efficiency at large viewing angles. Even though this design has the above-mentioned disadvantages, it is still favored by most laboratory goniometer designers because it can make full use of the incident energy, so that the measurement can have a higher SNR. In addition, the over-view scheme would allow us to use a small incident beam size and thus works for precious planetary materials such as returned lunar samples and rare carbonaceous chondrite meteorites that are only available in very small amount.

It is imperative to realize that one of the two schemes mentioned above should be adopted in the design of a goniometer. Otherwise, if the size of the detector FOV is comparable to the size of the incident light spot, the detector will view different portions of the illuminated area at different viewing zenith angles, and this artificial change in the measured radiance will be mixed with the real angular scattering behavior of the sample surface. This issue can be better understood by looking at the plots shown in Fig. 4 below. When a measurement is made in the principal plane (Fig. 4a, b), the detector FOV (dashed ellipse) may be smaller or larger than the incident spot (solid ellipse) for $i > e$ and $i < e$, respectively. When a measurement is carried out outside of the principal plane (Fig. 4c), the detector FOV may or may not cover the illuminated area, depending on the specific configurations. As a result, the measured bi-directional reflectance properties of the sample surface cannot be real.

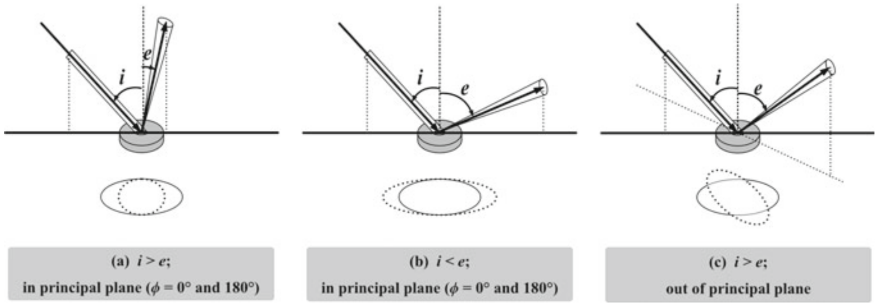

(a) $i > e$; in principal plane ($\phi = 0°$ and 180°)

(b) $i < e$; in principal plane ($\phi = 0°$ and 180°)

(c) $i > e$; out of principal plane

Fig. 4 Schematics showing the relative sizes of the incident spot (the ellipse with a solid line) and the detector field of view (the ellipse of a dashed line)

2.2.2 Phase Angle Coverage and Spectral Coverage Versus Signal-to-Noise Ratio

For airless bodies, their optical properties of great scientific interests are often found to occur near the opposition (Fig. 3). Therefore, it is desirable that a goniometric system can get close to 0° phase angle as much as possible with a high angular resolution. The angular resolution of a goniometer is determined by the ratio of the aperture stop to the distance between the stop and the sample surface (e.g., McGuckin et al. 1996). Therefore, high resolution requires a small aperture stop or a large detector-sample distance (e.g., Psarev et al. 2007), and either of these options will inevitably result in a drop in the SNR. In addition to the small phase angle and high angular resolution capabilities, a wide coverage of phase angles is also required for any multi-angle reflection measurement to accurately retrieve the correct photometric parameters of a measured surface (e.g., Mishchenko 1994; Hapke 1996). In order to meet these requirements, people often use multiple instruments with complementary phase angle capabilities. For example, the Karazin Kharkiv National University light scattering laboratory has built several photo-polarimeters with phase angle capabilities of 0.008–1.6°, 0.2–3.5°, 0.2–17°, and 2–170° to cover a wide range of phase angles (Ovcharenko et al. 2006; Shkuratov et al. 2006, 2008; Psarev et al. 2007).

In order to make angular scattering measurements with sufficient SNR, lasers are often used because of their high power and high level of collimation. The monochromaticity of lasers also makes them suitable for measurements to be compared with model calculations at some specific wavelengths. However, the spatial coherence of lasers will easily cause a large number of speckles in the incident light spot, which may affect the angular measurement results. Also, as mentioned in Sect. 1, the directional scattering and spectroscopic properties of most particulate surfaces are generally intertwined with each other, and thus angular scattering measurements made at limited discrete wavelengths may not reveal the full scattering properties of the samples. For example, the coherent backscattering effect which occurs in micron particles with weak absorptions (e.g., Mishchenko et al. 2006) may appear at wavelengths that the material is weakly absorbing but may not appear near its absorption bands. As many planetary materials including water ice that have absorption features in the visible and near-infrared, multi-angular reflectance measurements made in broadband wavelength are needed. To achieve this goal, a broadband light source such as the halogen lamp is often used. However, most broadband sources have low spatial coherence and thus the detector-sample distance has to be kept small and a low angular resolution will result.

In short, various light sources with complementary characteristics are often needed in different systems to make comprehensive measurements.

2.2.3 Levels of Automation

It is always desirable to have a system make measurements automatically. For example, in order to keep the instrument at a certain degree of automation while avoiding the use of any rotating parts, optic fibers fixed at various angular positions and imaging CCD have been used to make angular reflectance measurements (e.g., Voss et al. 2000). While this design can only have limited angular resolutions and thus may miss features for scattering media with sharp angular patterns, it has the advantage of being very compact with very good measurement precisions. For angular measurements with rotating booms (bars), a high level of automation will unavoidably increase the system complexity and construction cost, and may reduce the functionality of other aspects of the system performance. For example, for goniometers with motorized booms carrying optical elements, great care must be taken to avoid any potential collision/entanglement hazards. To make a compromise, we used both motor-driven and manual controls for our systems described below.

3 The Three-Colour Goniometer

3.1 Construction Motivations

The three-colour goniometer was constructed with the original motivation of performing controlled laboratory measurements on light scattering by regular grains with various albedos to test the performance of various photometric models (Zhang and Voss 2005, 2009, 2011). Since grains with regular shapes such as spheres have sharp scattering features such as the first and higher order rainbows, glory, and diffraction corona (Grandy 2005), this instrument is expected to have high angular resolution, high SNR, and polarization capabilities (Zhang et al. 2014).

3.2 System Descriptions

The overall design of the instrument is shown in Fig. 5 with the numbered parts listed in Table 1, and the pictures of the system are shown in Fig. 6. We use a CVI Melles Griot 633 nm HeNe laser with a nominal output power of 35 mW and two Spectra-Physics DPSS lasers of 532 and 473 nm with output powers of 50 mW as the red, green, and blue light sources, respectively. Laser light is inserted into a 20-m-long Newport custom fiber through a 5-axis fiber coupler and is then collimated by a collimator before incident onto the sample surface (Fig. 6a). The fiber coupler consists of a 5-dimensional lens positioner and a 5-dimensional fiber optic positioner and such a combination can effectively couple light from free space into the fiber. The reflected light is collected by viewing optics assembly including an aperture stop, an interference filter for the appropriate laser wavelength, a focusing lens, and a photodiode. The incident collimator and the viewing optics assembly are mounted on the incident bar and viewing bar with lengths of 2.2 m. Such a long bar was initially designed to allow for a high angular resolution and a small minimum phase angle. However, in most measurements, both the fore optics of the incident and viewing optics are positioned about 1 m from the sample surface to allow for a sufficient SNR and a smaller incident spot. With an aperture stop of 2.5 cm, such a distance gives an angular resolution is 1.4°. With these configurations, the minimum phase angle is 2.7°. At an incident zenith angle of 60°, the maximum phase angle could be 150° (90° viewing zenith angle). However, as the collection efficiency drops significantly above 70° zenith angle, measurements at phase angles larger than 130° are seldomly made. We have made sample holders with varying diameters and depths for samples with different available amounts. The most often used one is the sample holder with a diameter of 35 mm and a depth of 20 mm, so the elliptical spot ($15 * 7.5$ mm) on the sample surface at 60° incident zenith can have sufficiently large scattering volume.

Since the conventional lasers are notorious for power fluctuations and the commercially available power stabilized lasers have very limited output powers (<1 mW), some stabilizing measure must be taken to ensure a constant incident irradiation during a measurement. To achieve this goal, it is common practice to use a beam splitter to direct part of the beam exiting the laser onto a monitor detector and divide the reflected signal from the sample surface by the monitor signal. In the past years, however, we have found that this scheme does not work well for our systems as the signal channel and the monitor channel have power fluctuations with different frequencies and thus their ratio is not a constant. So, we set the monitor channel to look at the sample surface directly (Fig. 6a). This solution has the advantage that any fluctuations of the irradiance incident on the sample surface can be accounted for by the monitor channel and the ratio is highly stable (see Sect. 3.3.1). Although the surface albedo information is lost upon doing the ratio in this way, the surface brightness information can be retrieved by averaging the monitor channel signals during the measurements (see Sect. 3.4.1 below).

Both the viewing and the monitor sensors are Hamamatsu silicon S8745 photodiodes with internal amplifiers. Since the viewing optics assembly is 100 cm away

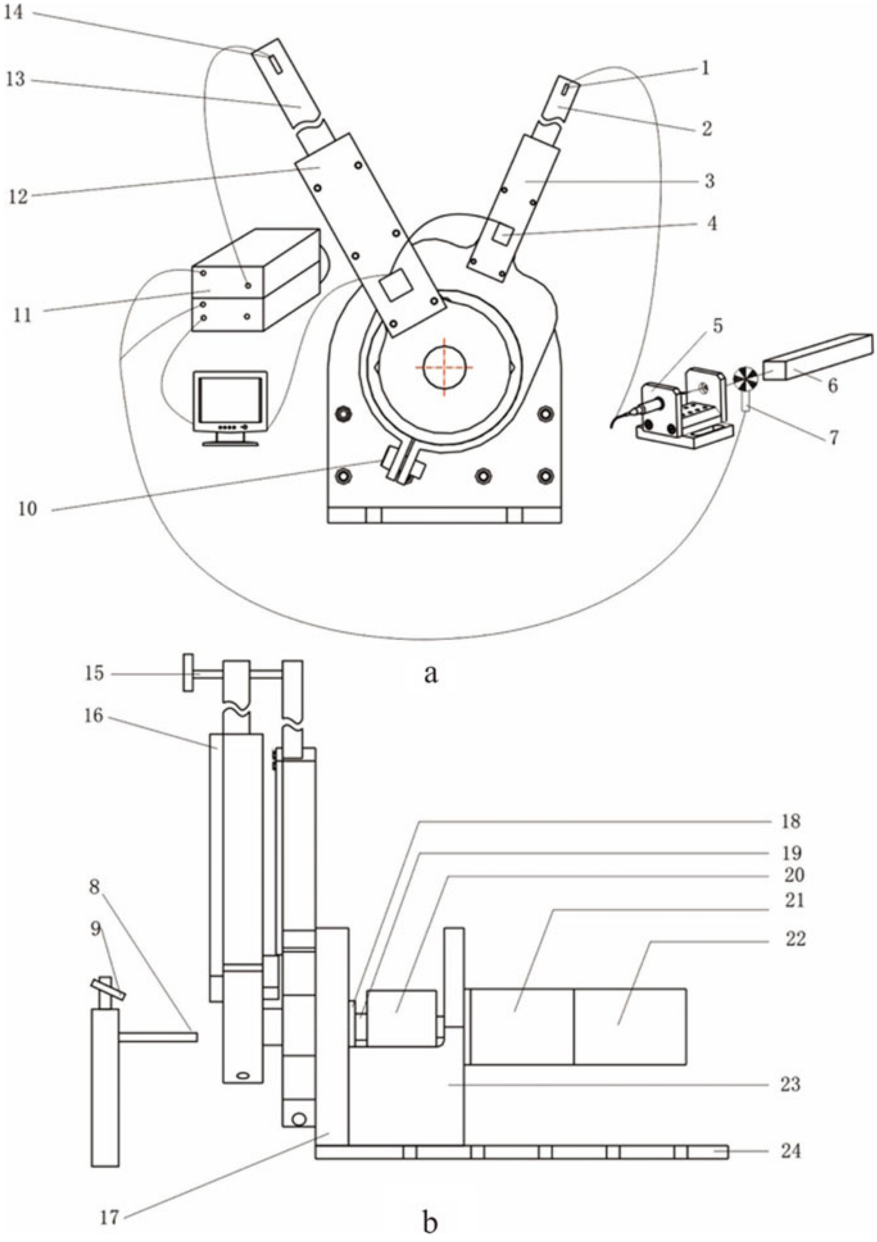

Fig. 5 Schematics of the three-colour goniometric system, **a** front view, **b** side view. The numbered parts are listed in Table 1

Table 1 Specific part names shown in Fig. 5. The inclinometer installed on the incident bar is not numbered here but can be seen in Fig. 6b

Part #	Part name	Note
1	Incident optics assembly	Collimator included
2	Incident bar	Custom
3	Incident bar holder	Custom
4	Inclinometer for incident bar	Rion SCA116T
5	Fiber coupler	Newport five-axis
6	Laser	CVI Melles Griot He-Ne (633 nm), Spectra-Physics Solid State 532 and 473 nm
7	Optical chopper	SR 540
8	Sample holder	Custom
9	Monitor detector	Hamamatsu S8745
10	Fastening screw	–
11	Lock-in amplifier	SR-830 dual phase lock-in
12	Viewing bar holder	Custom
13	Viewing bar	Custom
14	Viewing optics assembly	Hamamatsu S8745
15	Post	Custom
16	Hold down plate	Custom
17	Bezel	Custom
18	Bearing	Custom
19	Main shaft	Custom
20	Coupler	KBK KB4/300-105-32-40
21	Gear reducer	Shimpo VRB-115-60-K3
22	Servo motor	Panasonic MDME102GCH
23	Pedestal	Custom
24	Base plate	Custom

from the sample surface, the detected signal is quite weak due to the inverse square law of light propagation. In order to improve the SNR level, we used the phase sensitive detection method. The voltages output from both the viewing channel and the monitor channel are fed into two Stanford Research SRS830 lock-in amplifiers. A Stanford Research SR540 optical chopper is placed in front of the laser to chop the beam at a certain frequency and only signals with this frequency are detected. With this measure, the SNR is greatly improved and measurements can be carried out even with the fluorescent lights on in the dark room.

The bar carrying the incident optics assembly (Part 2 in Fig. 5a) can be manually adjusted within the range of 0 ~ 180° in the principal plane. The viewing bar is controlled by a Panasonic servo motor that can rotate in the principal plane with an angular resolution of 0.1°. The motor is connected to a 60: 1 gear reducer through

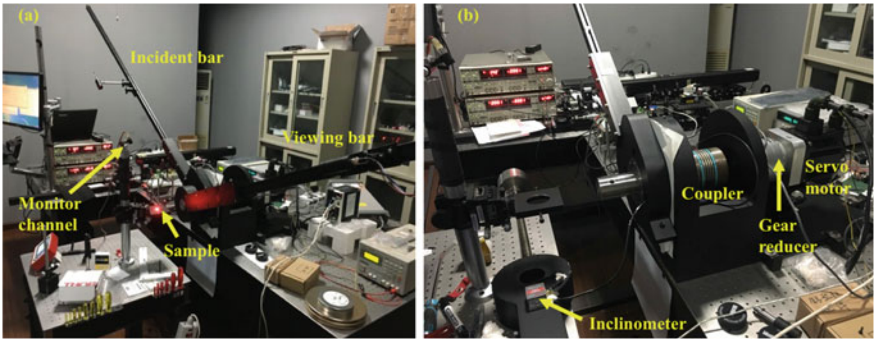

Fig. 6 Pictures of the three-colour goniometric system: **a** The overall look of the system including the incident and viewing bars, **b** a view of the electric drive system including the servo motor, gear reducer, and the coupler. In (**b**), the viewing bar with counterweight is removed for maintenance and the inclinometer on the viewing bar can be seen

a main shaft and a coupler that is attached to the viewing bar. The whole set of the device is fixed on a mechanical box seat that is fixed to the optical bench through threaded holes. Both the incident and viewing bars are equipped with one-axis digital inclinometers (SCA 116T from Shenzhen Rion Technology) that can output the angular positions of the bars. Both output signals from the lock-in amplifiers and the digital inclinometers are fed into a laptop computer through serial ports and the whole system is controlled by C++ software which also performs data acquisition.

3.3 System Characterizations

3.3.1 Stability Test

Figure 7 shows a typical stability test result of the incident beam power. During this ~80 min test period, the He-Ne laser power incident onto the sample surface varied by ~3%, yet the ratio signal has a fluctuation smaller than 0.2%, as the monitor channel fluctuation closely follows the viewing channel. This has demonstrated the good stability of the system.

3.3.2 System Linearity

To test the system linearity, eight neutral density filters with optical density (OD) values from 0.1 to 3.0 were placed in front of the viewing optics tube and measurements at four incident zenith angles were made. The OD is related to transmission T as

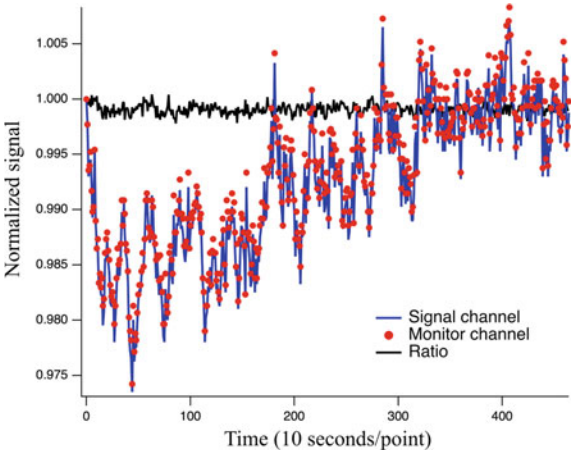

Fig. 7 A stability test of the three-colour goniometer's incident light beam power

$$\mathrm{OD} = \log_{10}\frac{1}{T}. \tag{3}$$

The results shown in Fig. 8 demonstrate that the system linearity is very good.

3.3.3 Laser Speckle Reduction

Because lasers have a high level of spatial coherence, the light spot exiting from an optic fiber has a non-uniform granular pattern and this speckle may distort the angular scattering measurement results in different levels, depending on the structure of the sample surface to be measured. By adding a laser speckle reducer (Optotune LSR-3005-6D-VIS) in the optical layout (Fig. 9), the quality of the incident spot is greatly improved (Fig. 10).

3.3.4 Mechanical Stability

The stability of the mechanical system is also crucial for a goniometric system. During the measurement process, the mechanical vibration caused by the rotation of the motor may cause changes in the optical path and affect the goniometer measurement, and a motor-controlled rotating bar may experience overshooting. To check this, we ran a measurement test using Spectralon plaque illuminated at 45° incident zenith by rotating the viewing bar in forward and reverse directions. In Fig. 11, positive and negative zenith angles stand for backward and forward scattering directions, respectively, and the ordinate is the measured intensity divided by the cosine of the viewing zenith. From this test one can see that the two sets of measured signals almost overlap with each other, and the maximum difference is less than 1%. Note,

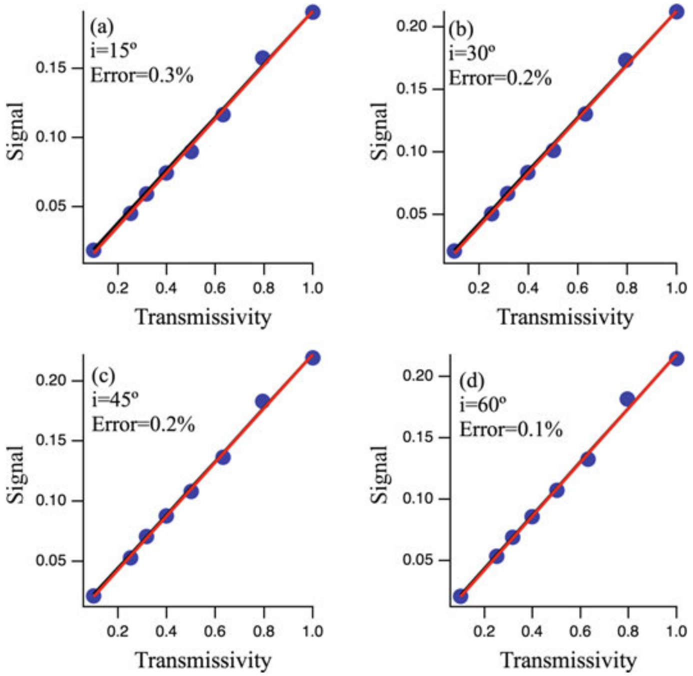

Fig. 8 The linearity test results at four different incident zenith angles

the difference in measured signals also includes fluctuations in laser power and electronics. Thus, the mechanical system of the instrument has good stability.

3.3.5 Effects of Tilting and Rotating of the Sample Holder

Since the accuracy of multi-angular reflectance measurements critically depends on the angular accuracy of the system including the sample surface levelness, it is important to understand the effects of sample surface tilting on measurement results. In an early version of the system, the sample holder was installed on a mounting post assembly (Fig. 12a) and a digital angle checker with an accuracy of ±0.1° was used to level the sample plane before any measurement was started. We used a Labsphere Spectralon with a nominal 99% reflectance to test the sample plane yawing on measurement results. Specifically, we rotated the sample stage around the R1 direction (yaw) to three positions relative to the horizontal plane, −0.5°, + 0.5° and 0° (when facing the front of the instrument, counterclockwise is positive, clockwise is negative) and measured the reflectance in REFF at four incident zenith angles: 8, 40, 45, 50, and 55°. Figure 13 shows measurement results with comparisons to the multi-angle imaging spectroradiometer (MISR) results (McGuikin et al. 1996, 1997; Bruegge et al. 2001). In each of the plot shown in Fig. 13, positive and negative

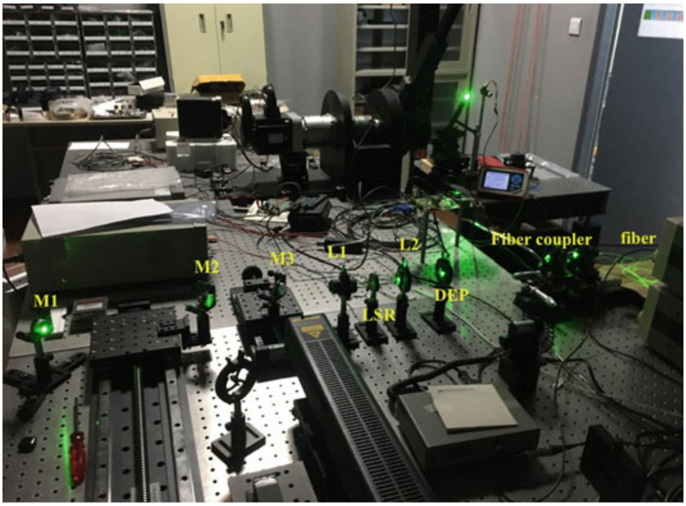

Fig. 9 Layout of the incident optics. M1–M3 are mirrors, L1 and L2 are focusing and collimating lenses, LSR and DEP laser are laser speckle reducer and depolarizer, respectively

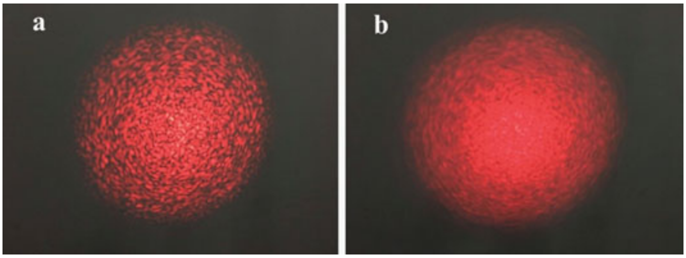

Fig. 10 Effects of using a laser speckle reducer on laser spot quality: **a** With LSR off, **b** with LSR on. The images are laser spots incident on the dark room wall after exiting the fiber

viewing zenith angles correspond to backward and forward scattering directions, and the ordinate is the normalized REFF value.

The results show that, when the sample plane is horizontal (0°), the relative difference from the MISR data is smaller than 3% within 70° viewing zenith. When the sample plane is rolled −0.5°, our 8°-incidence measurement has the smallest deviation from that of the MISR, with a maximum relative difference around 0.5%, and our 55°-incidence has the largest deviation from that of the MISR, with a maximum difference of 6%. For the +0.5° roll, our 8°-incidence again has the smallest difference from that of the MISR with a maximum 0.5% difference, and our 55°-incidence has the largest deviation with a maximum relative difference of 1.5%. Overall, these differences are within the acceptable range.

To check the effects of sample yawing (R2 rotation shown in Fig. 12a), we again used the Spectralon as the test sample and made four measurements and rotated

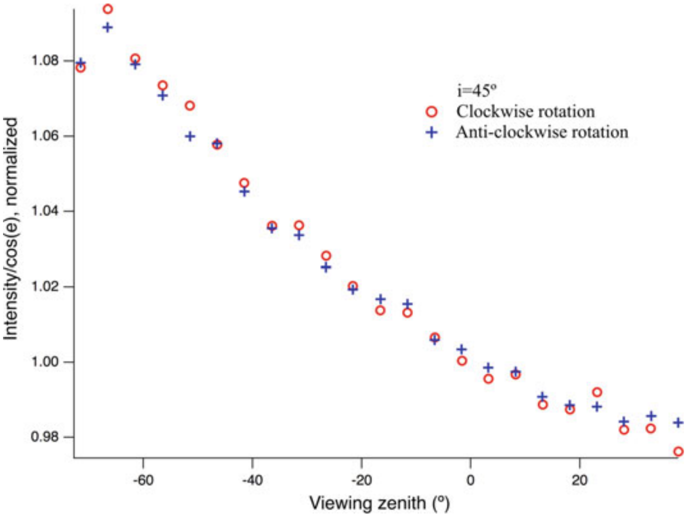

Fig. 11 Mechanical stability test of the goniometric test. The sample is a 99% reflectance Spectralon plaque illuminated at 45° zenith

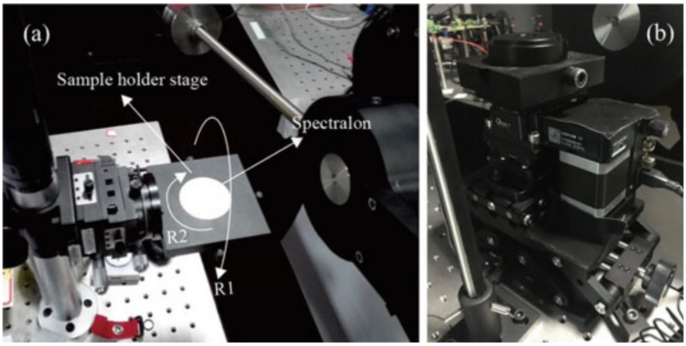

Fig. 12 The sample holder plate in an early version of the system (**a**) and in the improved version with a motorized sample rotation mechanism (**b**). The effects of sample holder stage roll (R1) and yaw (R2) are shown in Figs. 13 and 14, respectively

the plaque 90° between each measurement, and the results are shown in Fig. 14 for two incident zenith angles, $i = 8°$ and $i = 45°$. Since the viewing zenith angles are not identical between different measurements, we use the division of the measured signals by the cosine of the viewing zenith as the ordinates in Fig. 14. It can be seen that the maximum difference (~4%) between the 4 measurements occurred at $i = 45°$ and $e = 60°$.

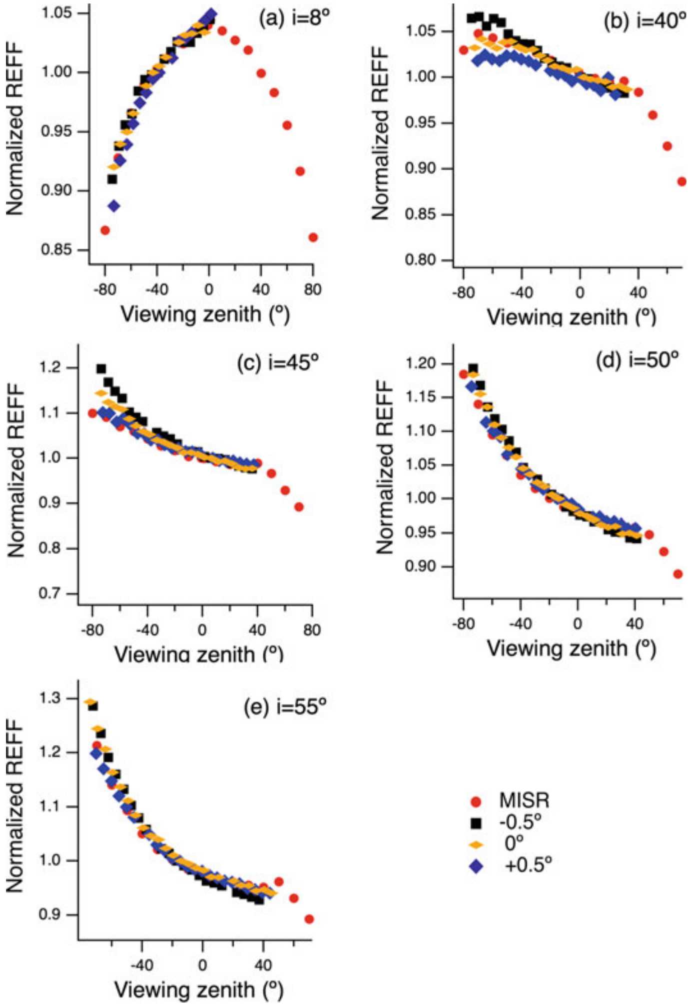

Fig. 13 Effects of sample surface roll on Spectralon REFF accuracies. −0.5, 0.5 and 0° indicate the sample plate plane is rolled −0.5, 0.5, and 0°, respectively, in R1 direction (roll) shown in Fig. 12a

Since many particulate layers have a more inhomogeneous and heterogeneous surface than the Spectralon plaque, the errors caused by sample plane yawing may be larger. Therefore, we upgraded the sample holder plate with motorized rotation capabilities, as shown in Fig. 12b. Measurements made on such a rotating sample have greatly reduced the errors caused by the yawing of the sample.

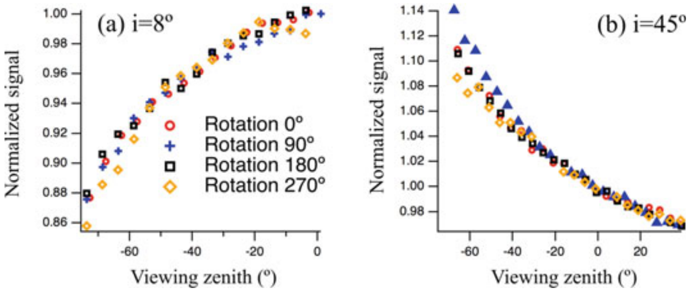

Fig. 14 Effects of rotating the Spectralon plaque 90° between four measurements (yaw or R1 in Fig. 12a)

3.3.6 Polarization Capabilities

By adding linear polarizers and quarter wave plates to the incident and viewing optics assemblies using rotation mounts, both linear and circular polarization ratios can be measured (e.g., Hapke et al. 1993). However, such measurements are time-consuming. A liquid crystal retarder scheme that can make faster measurements was proposed (Zhang et al. 2014) but has not been fully characterized.

3.4 Typical Measurement Results

3.4.1 Data Reductions

We use the relative calibration method described in Zhang and Voss (2005, 2008) to obtain the REFF from intensity measurements. For measurements made at a specific wavelength, the relative reflectance is obtained by

$$R(i, e) = \frac{I_{\text{sample}}(i, e)}{I_{\text{spectralon}}(i, e)}, \tag{4}$$

where I_{sample} (i, e) and $I_{\text{Spectralon}}$ (i, e) are the intensity from the sample and the 99% reflectance Spectralon (calibration target) measured at the same incident zenith i and viewing zenith e. As described in Sect. 3.2, the ratio of the viewing signal and the monitor signal is used to suppress the power fluctuations of the light source, and thus the surface albedo information is lost. To retrieve the surface albedo information, Eq. (4) is multiplied by the ratio C given in Eq. (5) below,

$$C(i) = \frac{\overline{M}_{\text{sample}}(i)}{\overline{M}_{\text{Spectralon}}(i)}, \tag{5}$$

where $\overline{M}_{\text{sample}}(i)$ and $\overline{M}_{\text{Spectralon}}(i)$ are the average of the monitor signals of the sample and the Spectralon during the measurement, respectively. To account for the non-Lambertian behavior of the Spectralon plaque, Eq. (4) is multiplied by a "roll-off" correction factor,

$$\text{Corr}^{\text{roll-off}}(i, e) = \frac{I_{\text{Spectralon}}(i, e)}{\cos(e)} \times f(e^0), \tag{6}$$

where $f(e^0)$ is a normalization constant that brings $I_{\text{Spectralon}}$ (i, e)/cos(e) to the absolute REFF value at a specified viewing angle e^0 measured by the MISR team (Bruegge et al. 2001). Equation (6) is necessary to obtain the absolute REFF value because ideally the quantity $I_{\text{Spectralon}}(i, e)$/cos(e) should be a flat line, but in practice it was found to fall off about 15% at larger viewing zenith angles (Voss and Zhang 2006). Summing up, the measured REFF is

$$\text{REFF}(i, e) = R(i, e) * C(i) * \text{Corr}^{\text{roll-off}}(i, e). \tag{7}$$

Since the angular reflectance pattern of the Spectralon plaque is a smooth curve with an approximate cosine behavior, Eq. (6) is fitted to three-term polynomials that can be used in the calibration procedures (Voss and Zhang 2006).

3.4.2 Sample Measurements

The three-colour goniometer has been used in our study of light scattering by planetary analog materials before and after simulated space weathering alterations (Jiang et al. 2019). Here we present our recent measurements on Allende meteorite in four different forms: a slab of cut surface (Fig. 15a), a porous layer of fine grains formed by pouring the powders into the sample holder with no compressions (Fig. 15b), a compact layer of fine grains formed by pouring the powders into the sample holder following by compression (Fig. 15c), and fine grains scattered on the slab surface (Fig. 15d). These four types of "samples" were made to simulate a realistic asteroidal surface (e.g., Belskaya et al. 2017).

The reflectance and DOP measurements under 60°-incidence are shown in Fig. 16, with the full phase angle range and small phase angle region in (a)(c) and (b)(d), respectively. Each curve is the average of 4 measurements, and the error bars for reflectance measurements are much smaller than that of the polarization measurements. From Fig. 16a, b one can see that all four types of samples exhibit a strong opposition effect, and the strongest oppositions appear in porous samples ("Porous powders" and "Powders on slab"). In fact, obvious inter-particle shadows can be seen by naked eyes in Fig. 15b, d, and thus may explain their stronger backscattering nature. Both slab samples ("Slab" and "Powders on slab") show specular reflections centered around the specular angle, or phase angle 120° in this case. All four samples have shown strong negative polarization effect below ~30° phase angle, with the smallest inversion angle for "Porous powders" (Fig. 15b) and largest

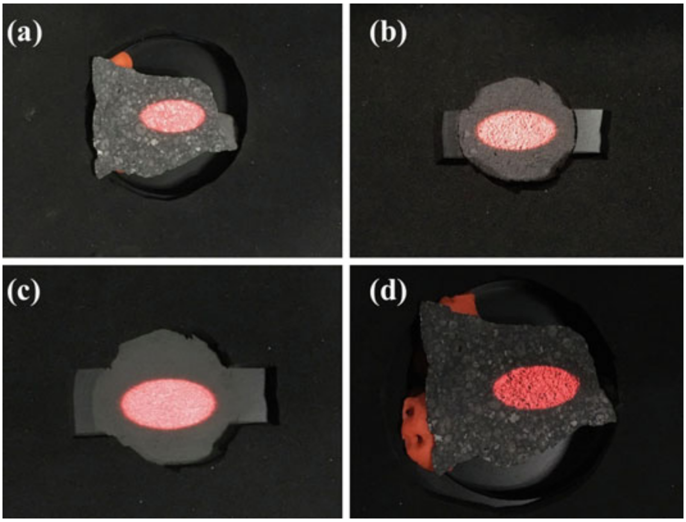

Fig. 15 Allende meteorite and its powders under measurement. **a** A slab of the sample, **b** a porous surface of Allende powders, **c** a compact surface of Allende powders, **d** Allende powders scattered on the slab. In these plots, the incident spot has a major axis of 1.5 cm at 60° incident zenith. A piece of red Plasticine used to fix the chunk meteorite can be seen in (**a**) and (**d**). Shadows cast by porous layers in (**b**) and (**d**) can be observed

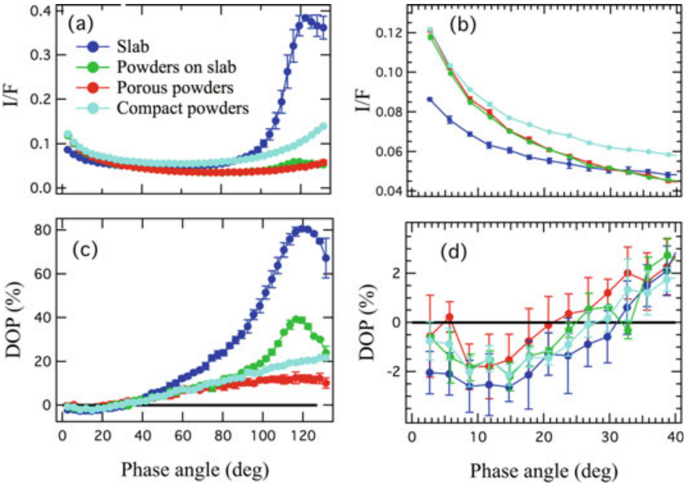

Fig. 16 Measured radiance factors (**a**) and (**b**) and degree of (linear) polarization (DOP) of the four samples shown in Fig. 15. Both (**b**) and (**d**) are the small phase angle region of (**a**) and (**c**)

for Slab (Fig. 15a). Compared with the intensity measurement, the DOP curve for "Powders on slab" shows a stronger specular peak. These results show that, the physical condition of the sample has a significant effect on both the I/F curve feature and the polarization parameters.

4 The Bi-directional Reflectance Imaging System

4.1 Construction Motivations

The construction of this apparatus was mainly motivated by applications of the phase ratio imagery method in detecting surface features of planetary surfaces (e.g., Kreslavsky et al. 2000; Shkuratov et al. 2011; Kaydesh et al. 2011; Blewett et al. 2014; Yuffa et al. 2017). By looking at the ratio image of two images of the same region but measured at two different phase angles, one can qualitatively extract the strength of past resurfacing events on a planetary surface. Specifically, if R(α1) and R(α2) are reflectance images measured at two different phase angles α1 and α2, the ratio image R(α1)/R(α2) is dependent on the physical properties of the surface including the porosity and surface roughness. The major advantage of using the ratio image is that it can greatly suppress the surface albedo effect and thus can enhance surface texture features that may be suppressed in brightness images. Similarly, the ratio of images measured at different wavelengths, or the colour ratio (e.g., McCord 1969; Rava and Hapke 1987; Lucey et al. 2000), may enhance the compositional differences in the imaged area. Thus, the major motivations for the construction of this device were to perform laboratory phase ratio and colour ratio measurements on various analogue samples to better understand the mechanisms for these remote sensing techniques.

4.2 Overall Description

The picture of the system including the camera lens system is shown in Fig. 17. To image the sample surface from various angular directions, an imaging radiometer is mounted on a vertical semicircular rail which is installed on a horizontal circular rail (both from HepcoMotion). The sled carrying the camera system can slide from −55 to 65° zenith angle, where the negative sign indicates the sensor is on the opposite side of the light source. The relative viewing azimuth angle can be changed from 0 to 360° by rotating the horizontal circular rail. A stabilized fiber-coupled light source (Thorlabs SLS201L) with a spectral coverage of 360–2600 nm and a removable filter holder serves as the light source. Light coupled into an optic fiber is collimated at the other end and then incident onto the sample surface. The spot size can be adjusted by changing the aperture size in the optical cage system. The incident optics assembly

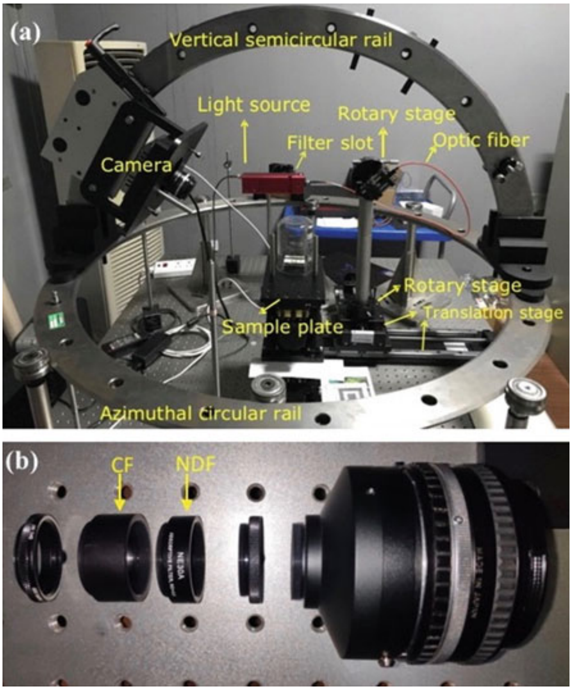

Fig. 17 The bi-directional reflectance imaging system: **a** the overall layout, **b** the camera lens system including the color filter (CF), neutral density filter (NDF), camera and the adapters. The color filter can also be inserted into the filter slot in the light source shown in (**a**). Light reflected from the sample surface enters the lens system from the far right of the lens system in (**b**)

is installed on a rotary stage mounted on an adjustable column which is installed on a two-dimensional translation stage. The imaging radiometer consists of a Nikon zoom lens with adjustable aperture and focal length as the telescope and a 512 × 512-pixel Apogee F260 CCD camera with a 16-bit analog-to-digital converter which has a maximum digital value of 65,535.

4.3 Calibration and Characterizations

4.3.1 Dark and Bias Image Subtractions

A typical sample measurement includes the acquisition of a dark frame before the sample measurement, the sample frame, and another dark frame after the sample measurement. Both the sensor temperature and the exposure time of the dark image were set to be the same as that for the sample images. Since each image contains the bias frame, when the average of the two dark frames is subtracted from the sample image, the bias frame is also removed.

4.3.2 Flat Fielding and Image Registrations

Since different pixels in the CCD sensor have different sensitivities, a flat fielding correction is needed in the data reduction procedure. We normally illuminated a 5 by 5 inch (12.5 by 12.5 cm) square Spectralon plaque with a nominal 99% reflectance and imaged the plaque from various directions with a 15° viewing zenith and symmetrically distributed azimuth angles, and used the average of these images as the flat field image. This flat fielding data has been used as a reference of the pixel-pixel variations, but is not needed in phase ratio or colour ratio imagery method, as any ratio image would eliminate such common factors.

To obtain the desired phase ratio or colour images in remote sensing applications, image registration is needed to correct the stretching and distortion caused by phase angle changes. In laboratory measurements, however, we have found the images of powdery samples lack the controlling points needed by image registrations. To avoid doing the image registration procedure, we fixed the viewing positions and only varied the incident zenith angle during the measurements.

4.3.3 Spectral Filters and Linearity Test

Since a broadband light source is used, colour filters are needed in the study of phase ratios or colour ratios at some specific wavelength. As shown in Fig. 18, the selected filters have high transmission values and span the range from visible to near-infrared, so they can represent the typical wavelengths used in phase ratio or colour ratio studies in planetary remote sensing. By performing image acquisitions with different exposure durations, the linearity of the system was found to be very satisfactory, as shown in Fig. 19.

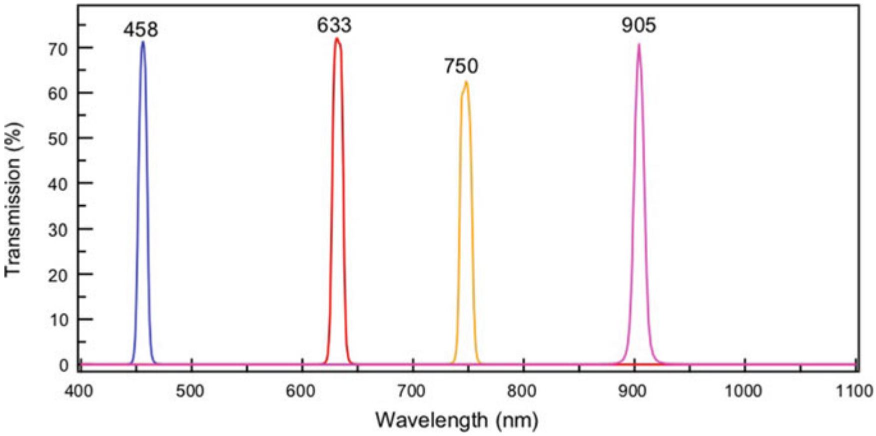

Fig. 18 Transmission curves for the four colour filters

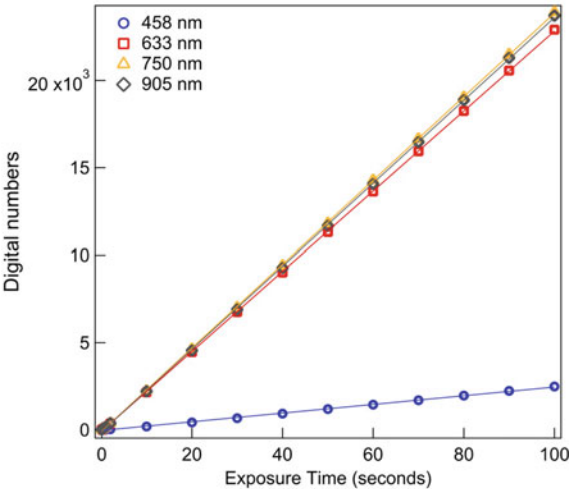

Fig. 19 Linearity test for the four colour filters. Straight lines are line fittings

4.3.4 Bi-directional Reflectance Characterizations

To characterize the angular reflectance behavior of the system, we measured the bi-directional reflectance of the 5 by 5 inch Spectralon at 4 different incident zenith angles: 8, 40, 45, and 55°, and compared the results with that of the MISR. To obtain the Spectralon REFF, we first averaged the DN values of the 512*512 pixels after performing the calibration procedures described above. Then the averaged DN values were divided by the cosine of the corresponding viewing zenith angles to get the un-normalized REFF (Zhang and Voss 2005, 2008). Finally, a normalization constant is applied to the un-normalized REFF to get the absolute REFF. For this case, we brought our un-normalized REFF value at $i = 8°$ and $e = -20°$ (a minus sign in viewing zenith indicates the forward scattering direction) to that of the MISR measurement (Fig. 20a) and this scaling constant is also applied to data measured as the other three incident angles. The two typical measurement results shown in Fig. 20 show that the overall match to the MISR data is very good with a maximum relative difference ~4%. Therefore, the photometric measurement feature of this device is well-behaved.

4.4 Example Measurements

In this chapter, we present our colour ratio measurements made on four types of lunar-related minerals, olivine (OLV), ortho-pyroxene (OPX), plagioclase (PLG), and ilmenite (ILM), as the example measurement results (Yang et al. 2020). The goal of this study was to understand if the colour ratio images measured at different phase angles can be used to discriminate surface types and/or particle size distributions.

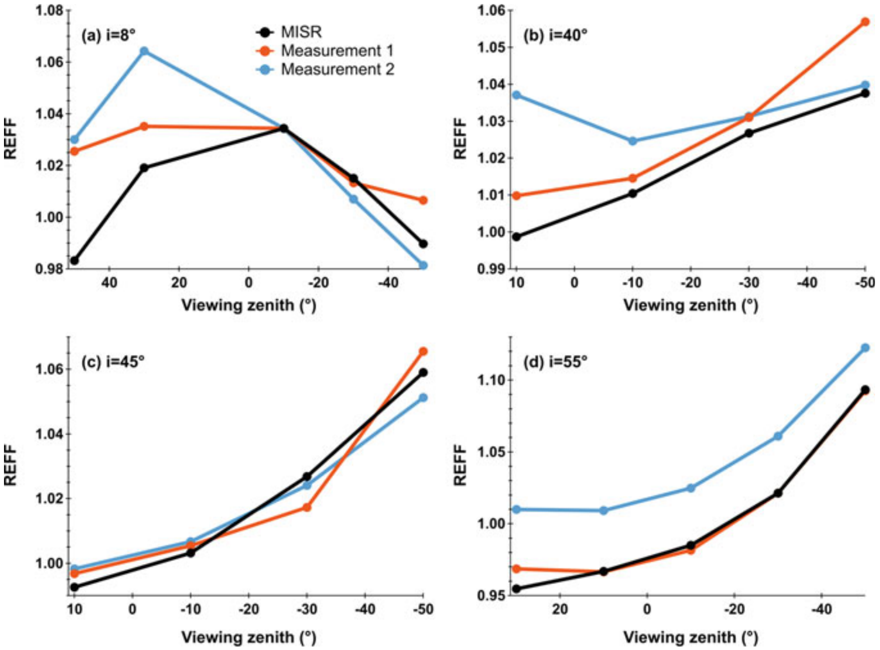

Fig. 20 Comparisons with REFF measurements on Spectralon done by the MISR team and by the bi-directional reflectance imaging system at four incident zenith angles

Figure 21 shows the samples with five size distributions in sample holders and the selected sample reflectance spectra from 400 to 1100 nm. To obtain colour ratio images at different phase angles, measurements were made at a fixed incident zenith angle of 45° and viewing zenith angles at 35° (10°), 20° (25°), 10° (35°), 0° (45°), −10° (55°), −20° (65°), −30° (75°), −45° (90°), and −55° (100°), where the negative sign in viewing zenith indicates the forward scattering direction and the angles in parenthesis are phase angles. Figure 22 shows the intensity images in 633 nm taken at 4 viewing zenith angles. These minerals have varied albedos and the finer grains are brighter except for ILM.

Among the four colour images of intensity, six image pairs can be generated to make colour ratio images. In Fig. 23 we show one of the ratio images, R(905 nm)/R(750 nm), measured at nine different phase angles. Obviously, the ratio images are dependent on compositions and phase angle. The “bluest” (meaning the smallest spectral slope) sample is OPX, and the “reddest” (meaning the largest spectral slope) sample is ILM. This feature is controlled by the spectral reflectance values at these two wavelengths (Fig. 21b): the OPX’s strongest absorption at 905 nm makes its R(905 nm)/R(750 nm) the smallest. All 4 samples show an increased R(905 nm)/R(750 nm) as phase angle increase (phase reddening), and this ratio slightly increases as the particle size decreases.

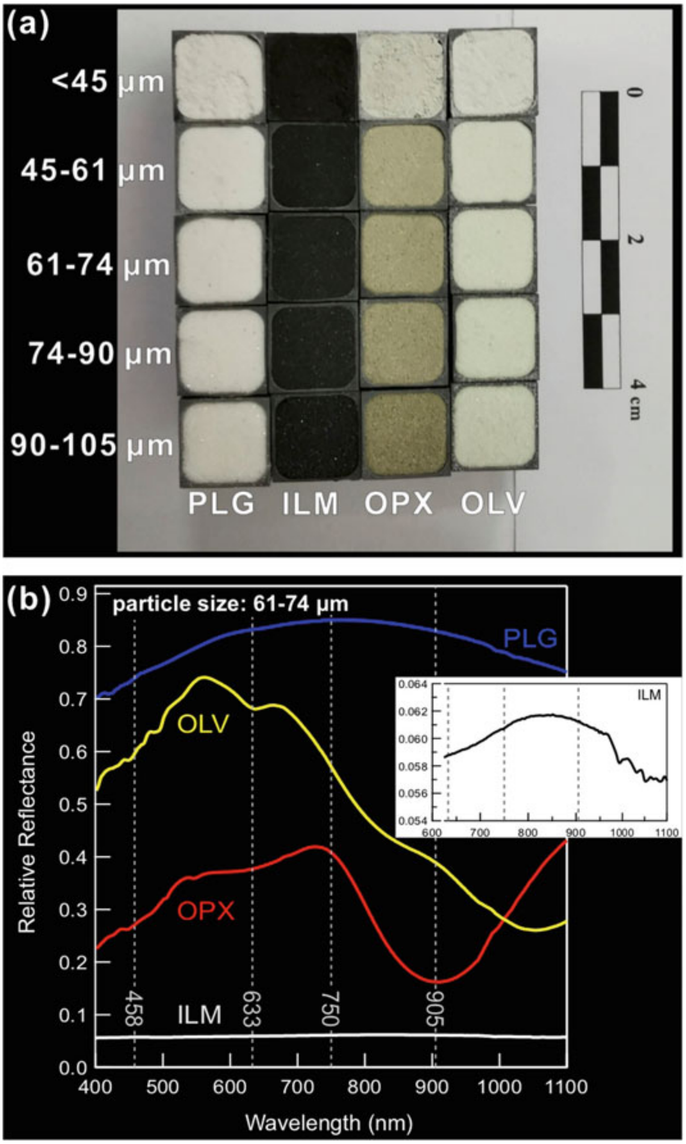

Fig. 21 Photos and the visible-near-infrared reflectance spectra of the samples used in the colour ratio measurements: **a** sample images: from left to right, the four columns are plagioclase (PLG), ilmenite (ILM), orthopyroxene (OPX), and olivine (OLV) grains with different particle sizes, respectively. Samples in the same row have the same size distribution; for example, the four samples in the top row all have a size distribution of 0–45 μm. **b** reflectance spectra of the four mineral samples with a particle size distribution of 61–74 μm measured at $i = 30°$, $e = 0°$, $\alpha = 30°$. The dashed lines indicate the central wavelengths of the four filters used in this study. The inset plot shows the enlarged view of the ILM spectrum, which has a reflectance peak around 850 nm. Adopted from (Yang et al. 2020)

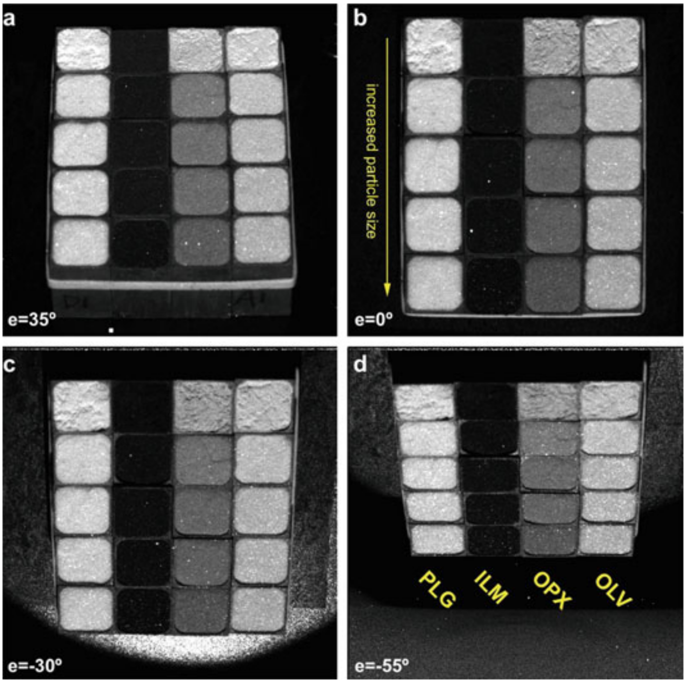

Fig. 22 Sample images at a fixed incident zenith 45º and various viewing zeniths of 35º (**a**), 0º (**b**), −30º (**c**), and −55º (**d**), all in 633 nm wavelength. The sample positions are the same as those shown in Fig. 21. Pixel values are relative reflectance and the scales are the same in all four plots. Adopted from (Yang et al. 2020)

Similar phase-angle and size-distribution dependences for all four minerals can be found in ratio images of R(905 nm)/R(633 nm) and R(905 nm)/R(458 nm) (Yang et al. 2020). In the forward scattering directions (negative viewing zenith) in ratio images R(905 nm)/R(750 nm), R(905 nm)/R(633 nm), and R(905 nm)/R(458 nm), ILM has its unique patterns clearly different from the three silicates (OLV, OPX, and PYX). In contrast, grain size has a limited effect on the phase angle dependence of the colour ratios. Yang et al. (2020) concluded that, with a priori knowledge of the phase angle dependence of the colour ratios of different types of minerals, one can find the best combination of the colour ratio and phase angle to distinguish the compositions of a target surface.

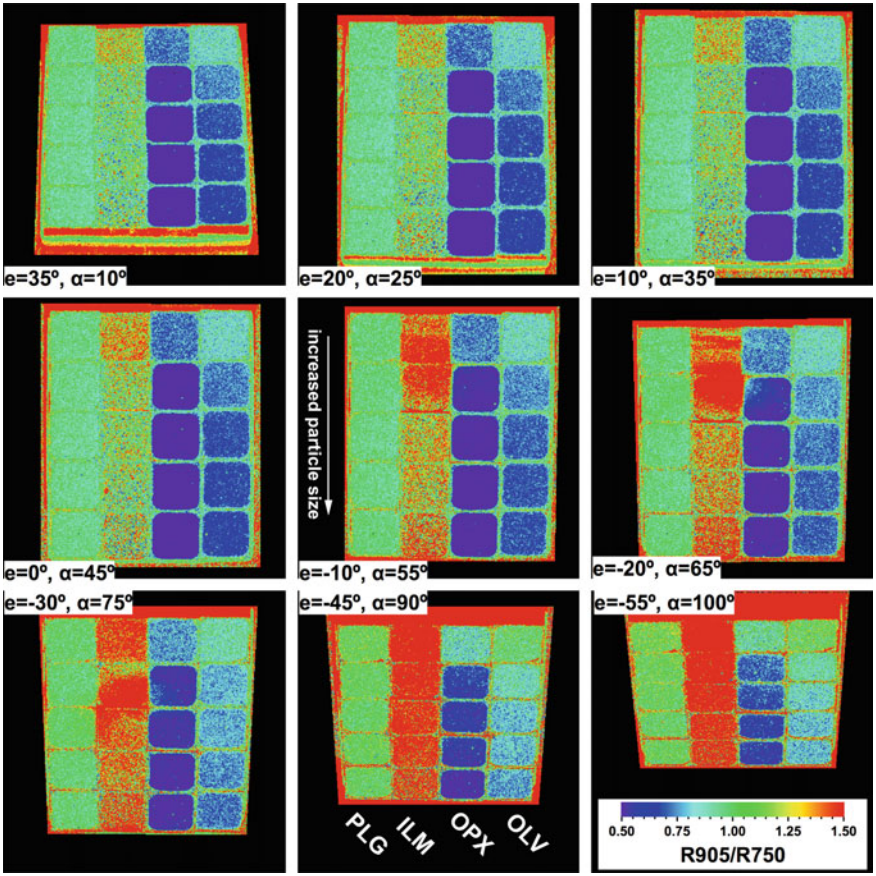

Fig. 23 Colour ratio images of R(905 nm)/R(750 nm) measured at nine phase angles. Adopted from (Yang et al. 2020)

5 The Bi-directional Reflectance Spectrometer

5.1 Construction Motivations

The two instruments described above that can make bi-directional reflectance measurements at several discrete wavelengths are unable to make spectroscopic measurements. To measure the spectral properties of particulate surfaces under various illumination and viewing conditions, a radiometer with high spectral resolutions is needed. In order to achieve flexible illumination and viewing at various angular positions, fiber optic cables were used to transmit the incident and scattered light. As a result, potential fiber entanglement at some angular positions may occur and thus we opted a manual design instead of a motorized one to reduce system complexity and construction cost. We have constructed this measurement system mainly using commercially available components.

5.2 System Descriptions

A detailed description of the system including calibration, characterization, and measurement procedures can be found in a recent journal paper (Jiang et al. 2022), so only a brief description is given here. As shown in Fig. 24, the system consists of three major parts: a quartz tungsten halogen (QTH) light source (Newport 66,502-250Q-R1), a goniometer, and a spectrometer. The QTH uses a lamp (Newport 6334NS) with a maximum flux of 10,000 Lumens, a 3400 K colour temperature, and an output power adjustable from 0 to 250 W. Light from the source is coupled into a Newport 77,576 fiber optic cable with a numerical aperture of 0.22. This fiber has a ~50% transmittance over the spectral range between 260 and 2200 nm except at two absorption regions around 1200 nm (~40%) and 1400 nm (~5%). Light exiting from the other end of the fiber is collimated by a collimator (Newport 77,646) which is mounted on the incident bar. The radial distance from the collimator's aperture stop to sample surface is 8 cm and the incident spot size is 1.5 cm at normal incidence and increases to 2.6 cm at 55° incidence. Light reflected by the sample surface is collected by another optic fiber with its tip placed 15 cm from the sample surface. Such a configuration allows a 14 cm-diameter field of view at nadir viewing so a

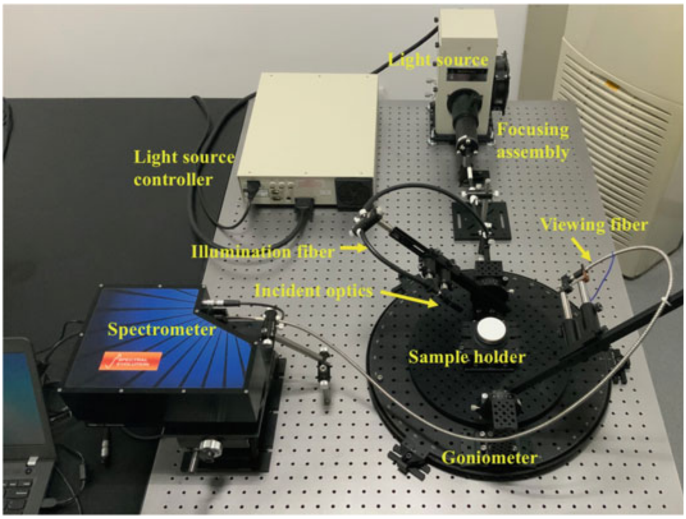

Fig. 24 The bi-directional reflectance spectrometer including the light source, the spectrometer, and the goniometer. A Spectralon plaque is placed at the sample holder position in this picture

particulate sample filled into a 3.5 cm-diameter sample holder can be comfortably viewed (the over-view scheme).

The goniometer consists of a 30 cm-long incident bar and a 60 cm-long viewing bar, both mounted on rotary stages (Edmund Optics 66,516) connected to mounting blocks (Thorlabs TS240) which are installed on a rotatable breadboard. The zenith angles of the incident and viewing bars are manually adjustable from 0 to 90°, but for most measurements they are limited to 55 and 70°, respectively, due to the elongation of the incident light spot and the lower collection efficiency at large viewing zenith angles. The relative azimuth angle ϕ (Fig. 1) is mechanically adjustable from 0 to 360°. However, some angular positions between 270 and 360° are not reachable due to the mechanical interference between the incident and viewing bars/fibers. The minimum phase angle can be reached is 10°, and the angular precisions of the zenith and azimuth angles are 10' and 5', respectively (Jiang et al. 2022).

The spectrometer (Spectral Evolution SR-2500) covers the spectral range from 350–2500 nm with spectral resolutions of 5 nm at 350–1000 nm and 22 nm at 1500–2100 nm. The spectrometer uses a 512-element UV-enhanced silicone array in 350–1000 nm and a 256-element thermal electrically-cooled extended InGaAs array in the 1000–2500 nm region. When used with a 1.2-m-long optic fiber, the typical noise equivalence radiances are $0.8*10^{-9}$ W/cm^2/nm/Sr at 400 nm, $1.5*10^{-9}$ W/cm^2/nm/Sr at 1500 nm, and $1.8*10^{-9}$ W/cm^2/nm/Sr at 2100 nm, respectively.

5.3 Characterizations and Calibrations

5.3.1 Signal-to-Noise Level Evaluations

We used a 2-inch diameter Spectralon with 99% nominal reflectance and the volcanic sand collected from the Big Island with very low albedo to evaluate the noise levels in different samples. For this measurement system, stray light in the dark room, electrical noise from the spectrometer circuits, and spurious light signals produced by multiple reflections of light from various components in the system are the major sources of noises. To estimate the contributions from these unwanted signals, we made four combinations of measurements. First, we made a measurement on the Spectralon with the light source off and the viewing fiber blocked by a plastic block. In this measurement, the dominant noise is the electrical noise as shown as the green curves in Fig. 25a, b. It turned out the electrical noise is on the level of ~0.01% in the visible and less than 0.5% above 1 μm except at the overlapping region of the two detectors (~0.9 μm). In the second test, the light source is turned on while the viewing fiber is still being blocked by the plastic block, and a measurement was made on Spectralon. The signal measured in this test (blue curves in Fig. 25a, b) mainly consists of electrical noise and ambient noise, and a comparison with Test 1 shows the ambient light level can be ignored. The third test was also made on Spectralon with the light source on and the viewing fiber unblocked. This test included all three noises and the stray light is also found to be negligibly small. The fourth test is the

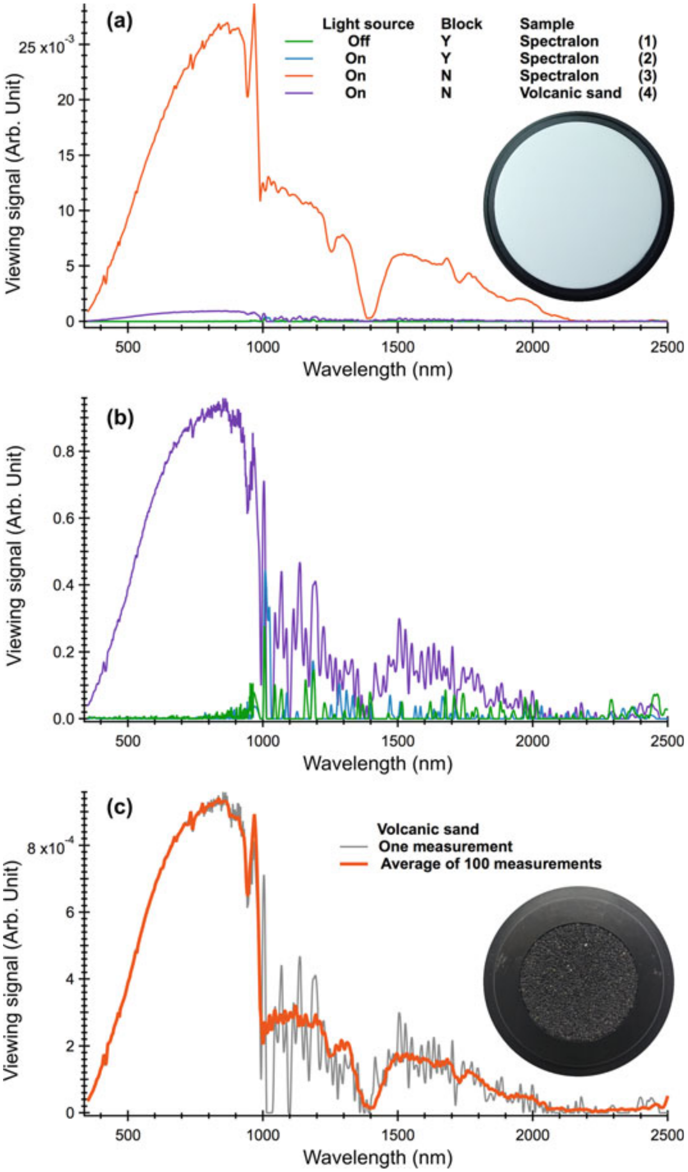

Fig. 25 The noise and stray light evaluation test results. Numbers in parenthesis in (**a**) correspond to the test numbers described in Sect. 5.3. The diameter of the sample holder in (**c**) is 3.5 cm

same as Test 3, but with the Spectralon replaced by the volcanic sand (purple curves in Fig. 25a, b, and the grey curve in Fig. 25c). This is the worst scenario that the spectrum above 1000 nm is dominated by huge fluctuations. However, for this very dark sample, the average of 100 measurements has reduced the noise level to 5% and the overall SNR values over the full spectral region are quite satisfactory. This has demonstrated the importance of repeated measurements for very dark samples.

5.3.2 System Linearity

The linearity test was performed by setting the power of the light source at five different levels, 25, 50, 100, 150, 200, and 225 W, and measuring the intensities reflected from the Spectralon at a fixed incident zenith 30° and viewing zenith 0° in the principal plane. Both the integration time and the number of measurements were fixed during the measurements. Nine laser line and bandpass filters (Fig. 26) were placed between the incident collimator and the sample and the power incident onto the sample surface was measured by a power meter. The signals reflected by the Spectralon were measured by the spectrometer and the results are shown in Fig. 27. Obviously, the system has an excellent linearity response.

5.3.3 Data Reduction and Calibration

The detailed data reduction procedures to obtain REFF from measured radiances can be found in Yang et al. (2019) and Jiang et al. (2022), and thus only a simple outline is given here. Similar to the procedures outlined in Sect. 3.4.1, we first take the ratio of the measured sample radiance (I_{sample} (i, e, ϕ, λ)) and the Spectralon radiance

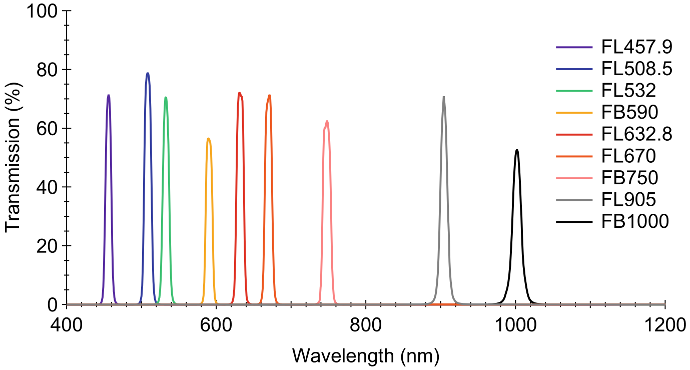

Fig. 26 The transmission curves of the colour filters used in the linearity test. FL and FB indicate laser line and bandpass filters, respectively. The numbers following FL and FB are the central wavelengths in nm and all filers have a full width at half maximum of 10 nm. Redrawn from (Jiang et al. 2022)

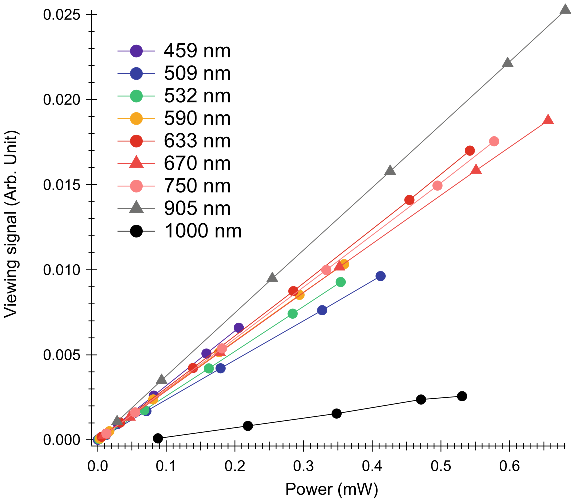

Fig. 27 Linearity performance of the system. The output power of the lamp was set to 25, 50, 100, 150, 200, and 225 W. The power (horizontal axis) was measured by an optical power meter with its sensor placed between the incident collimator and the sample surface, and the viewing signal reflected from Spectralon (vertical axis) was measured by the spectrometer. The incident and viewing zenith angles were fixed at $i = 30°$ and $e = 0°$ in the principal plane, and the number of averages was 30. The wavelengths were selected based on the central wavelengths of the filters shown in Fig. 26. Redrawn from (Jiang et al. 2022)

($I_{\text{spectralon}}$ (i, e, ϕ, λ)) (both in arbitrary units since the spectrometer has not undergone frequent in-factory absolute calibrations) measured at the same configuration to obtain the relative reflectance as

$$R(i, e, \phi, \lambda) = \frac{I_{\text{sample}}(i, e, \phi, \lambda)}{I_{\text{spectralon}}(i, e, \phi, \lambda)}, \tag{8}$$

where λ is the radiation wavelength. The sample REFF can then be obtained as

$$\text{REFF}_{\text{sample}}(i, e, \phi, \lambda) = R(i, e, \phi, \lambda)\text{REFF}_{\text{Spectralon}}(i, e, \phi, \lambda), \tag{9}$$

where $\text{REFF}_{\text{Spectralon}}(i, e, \phi, \lambda)$ is the absolute REFF of Spectralon measured by the MISR team (McGuckin et al. 1996, 1997; Bruegge et al. 2001) and can be obtained using the following normalization as (using 633 nm as an example)

$$\text{REFF}_{\text{Spectralon}}(i, e, \phi, 633\text{nm}) = \frac{I_{\text{spectralon}}(i, e, \phi, 633\text{nm})}{\text{Cos}(e)}A, \tag{10}$$

where A is a normalization factor at a specific viewing position (here $e = 1°$ and $\phi = 0°$) that scales our measurement data to that of the MISR REFF, $\text{REFF}^{\text{MISR}}_{\text{Spectralon}}$. Then, the REFF of the sample in 633 nm can be obtained. We used different

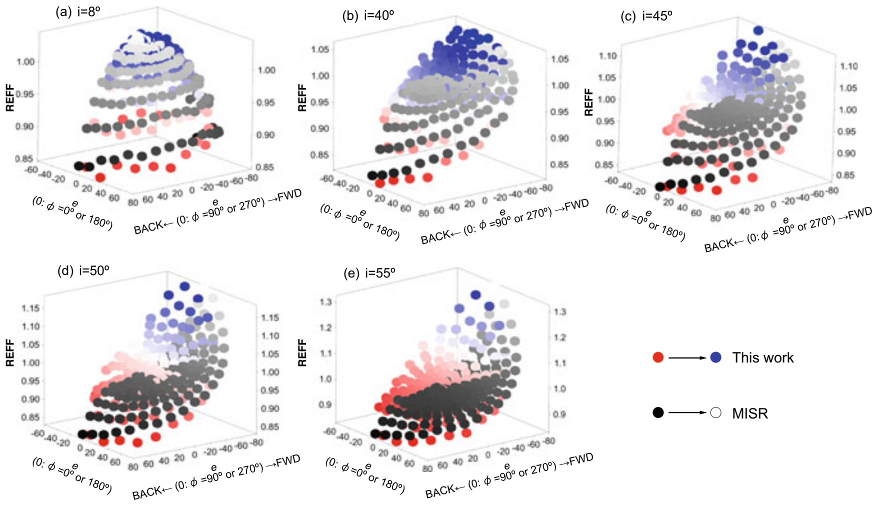

Fig. 28 Comparisons of the Spectralon REFF measured by MISR and our instrument at various incident zenith angles. Adopted from (Jiang et al. 2022)

A's for different incident zeniths, but their relative differences are less than 1%. Since the MISR $\text{REFF}_{\text{Spectralon}}^{\text{MISR}}$ in three wavelengths (442, 633, and 866 nm) have nearly identical photometric properties, we assumed the Spectralon has similar photometric behavior in the visible and near-infrared regions and this assumption allowed us to scale our REFF data to MISR's data through one simple constant at 633 nm. Next, the Spectralon spectrum measured by RELAB (Yang et al. 2019), $\text{REFF}_{\text{Spectralon}}^{\text{RELAB}}(i = 30°, \text{e} = 0°, \phi = 0°, \lambda)$, is used to calibrate the wavelength dependence of the Spectralon reflectance as

$$\begin{aligned}\text{REFF}_{\text{spectralon}}(i, e, \phi, \lambda) &= \text{REFF}_{\text{Spectralon}}(i, e, \phi, 633\text{nm}) \\ &\quad * \text{REFF}_{\text{Spectralon}}^{\text{RELAB}}(i = 30°, \text{e} = 0°, \phi = 0°, \lambda) * B, \quad (11)\end{aligned}$$

where B is a constant that normalizes the RELAB REFF, $\text{REFF}_{\text{Spectralon}}^{\text{RELAB}}(i = 30°, e = 0°, \phi = 0°, \lambda)$, to MISR's REFF,$\text{REFF}_{\text{Spectralon}}^{\text{MISR}}(i, e = 0°, \phi = 0°, \lambda)$.

The Spectralon REFF obtained through the above procedure and that of the MISR are displayed in Fig. 28. The good agreements between the two datasets indicate our system has the correct photometric behavior.

5.4 Typical Measurement Results

Figure 29 shows the comparison measurements on a 2-inch diameter Spectralon plaque and Orbitech's JSC-1A Martian Soil Simulant (Sibille et al. 2006) made by

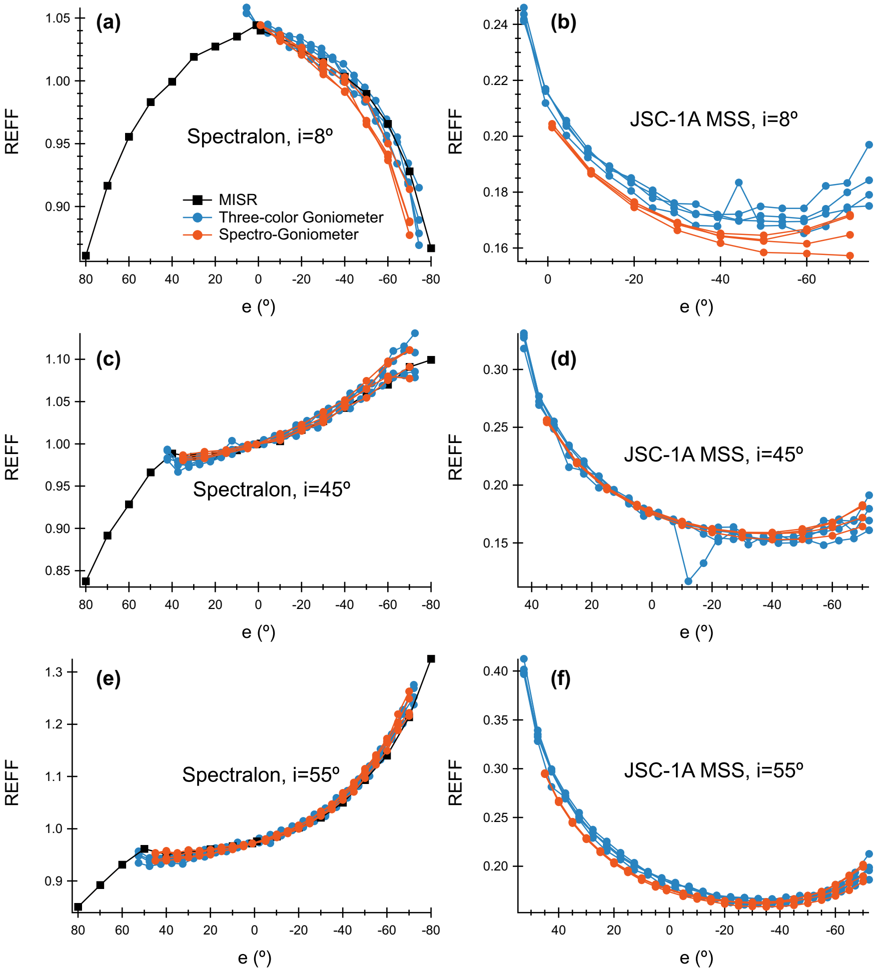

Fig. 29 *REFF* of the Spectralon (**a**, **c**, **e**) and the JSC-1A Martian Soil Simulant (**b**, **d**, **f**) measured by the three-color goniometer and the bi-directional spectro-goniometer in 633 nm. The MISR Spectralon data is also included for comparisons. Adopted from (Jiang et al. 2022)

the three-colour goniometer and the bi-directional reflectance spectrometer at three incident zenith angles, $i = 8$, 45, and 55°. Since both instruments can use the same sample holder, the same sample can be easily switched between the two devices. For each sample, four measurements were made and the sample surface was rotated 90° (the R2 rotation in Fig. 12a) between the adjacent measurements. The results shown in Fig. 29 indicate that the measurements made by the two instruments agree with each other very well except for JSC-1A at $i = 8°$ (Fig. 29b). In this worst case, a maximum ~6% relative difference exists, possibly caused by sample surface setting during the transfer of the sample holder from one instrument to the other. The

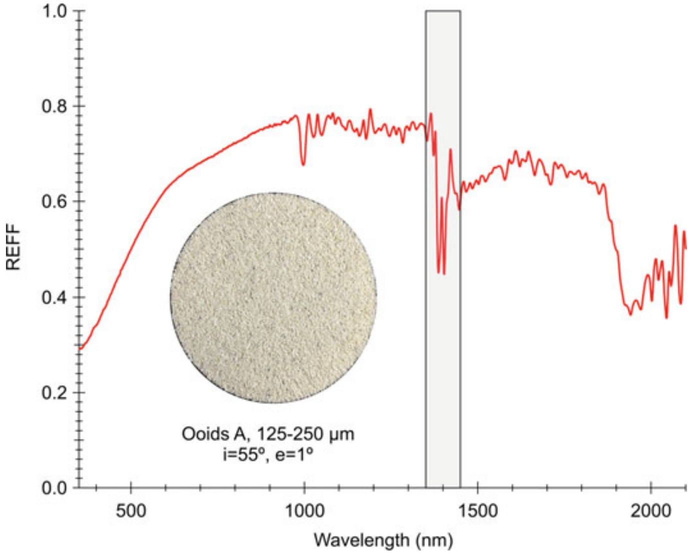

Fig. 30 Reflectance spectrum of shallow water sediment ooids at $i = 55°$ and $e = 1°$. The grey area indicates the spectral region with strong fiber absorptions. The diameter of the sample holder is 3.5 cm

sample-rotation incurred spreads are also largest in this case, implying the larger surface heterogeneities. But for all other measurements, the influence of surface heterogeneity is better than 3% in REFF values, and the maximum spreads mostly occur in the forward scattering direction.

Another sample measurement was carried out on a shallow water sediment ooids that were extensively measured by other bi-directional reflectance devices (Zhang and Voss 2006, 2009; Zhang et al. 2003). Figure 30 shows the reflectance spectrum at a specific scattering configuration and Fig. 31 shows the REFF at 658 nm. Due to this sample's high surface albedo, the spectrum has good SNR except in the fiber absorption region indicated by the grey box in Fig. 30. The REFF pattern shown in Fig. 31 indicates that the surface reflectance is very anisotropic at $i = 55°$ illumination, with both an enhanced backscattering and forward scattering lobes. Both the angular pattern and the absolute REFF values agree with the previous measurements made on other instruments very well.

6 Summary

We have described three angular light scattering systems constructed at China University of Geosciences during the past decade. The three-colour goniometric system has the widest phase angle coverage (2–130°), highest angular resolution (1.4°), and finest angular step (0.1°), polarization measurement capabilities, and thus is capable

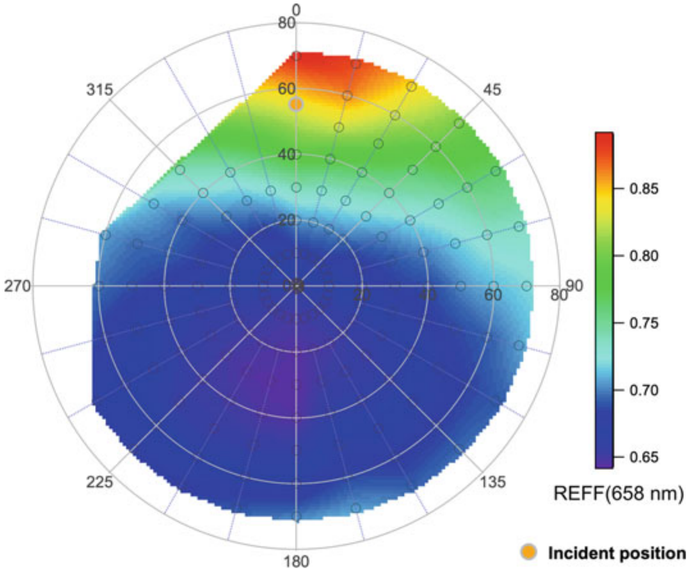

Fig. 31 The bi-directional reflectance in REFF in 658 nm of shallow water sediment ooids with grain size 0.125–0.25 μm. The incident zenith was $i = 55°$ and is indicated by an orange circle in the plot

of measuring scattering patterns with fine angular structures of regular particles in controlled measurements. The system works in the principal plane with three excitation wavelengths, 633, 532, and 473 nm. The multi-angular imaging system can measure the bi-directional reflectance of a particulates surface in the upper hemisphere with imaging capability and can be operated at discrete wavelengths from 400 to 1000 nm by using the appropriate spectral filters. This device can be used to perform the colour ratio and phase ratio measurements on particulate layers. The bi-directional reflectance spectrometer works in the wavelength range from 350 to 2400 nm and can measure the multi-directional reflectance in the upper hemisphere. All three instruments have very good performance of stability, system linearity, and the correct angular scattering behavior, as demonstrated by comparison measurements made on standard samples by various instruments. Extensive measurements on various types of particulate samples are being carried out to help us understand the many outstanding questions in light scattering by closely packed particulate media.

Acknowledgements We thank Kenneth Voss, Yuriy Shkuratov, Robert Nelson, Ralph Milliken, and Sana Kassalenen for helpful discussions. We are also indebted to CUG's Office of Laboratory and Equipment Management led by Siping Xu for generous support. Continuous support from the National Natural Science Foundation of China through grants 12073024, 11941001, 11773023, 41071229, 41276180, U1631124, and the support from the Pre-research Project on Civil Aerospace Technologies funded by Chinese National Space Administration (D 020302), are gratefully acknowledged.

References

Abe M, Takagi Y, Kitazato K, Abe S, Hiroi T, Vilas F et al (2006) Near-infrared spectral results of asteroid Itokawa from the Hayabusa spacecraft. Science 312(5778):1334–1338

Adams JB, Filice AL (1967) Spectral reflectance 0.4 to 2.0 microns of silicate rock powders. J Geophys Res 72(22): 5705–5715

Belskaya IN, Fornasier S, Tozzi GP, Gil-Hutton R, Cellino A, Antonyuk K, Krugly YN, Dovgopol AN, Faggi S (2017) Refining the asteroid taxonomy by polarimetric observations. Icarus 284:30–42

Bhandari A, Hamre B, Frette Ø, Zhao L, Stamnes JJ, Kildemo M (2011) Bidirectional reflectance distribution function of Spectralon white reflectance standard illuminated by incoherent unpolarized and plane-polarized light. Appl Opt 50(16):2431–2442

Blewett DT, Levy CL, Chabot NL, Denevi BW, Ernst CM, Murchie SL (2014) Phase-ratio images of the surface of mercury: evidence for differences in sub-resolution texture. Icarus 242:142–148

Brissaud O, Schmitt B, Bonnefoy N, Doute´S, Rabou P, Grundy W, Fily M (2004) Spectrogonio radiometer for the study of the bidirectional reflectance and polarization functions of planetary surfaces. 1. Design and tests. Appl Opt 43(9):1926–1937

Bruegge C, Chrien N, Haner D (2001) A Spectralon BRF data base for MISR calibration applications. Remote Sens Environ 77(3):354–366

Burns RG (1993) Mineralogical applications of crystal field theory. Cambridge University Press, Cambridge, UK

Clark RN, Swayze GA, WiseR, Livo KE, Hoefen1 TM, Kokaly RF, Sutley SJ (2003) USGS Digital Spectral Library splib05a. https://pubs.usgs.gov/of/2003/ofr-03-395/ofr-03-395.html

Coburn C, Peddle D (2006) A low-cost field and laboratory goniometer system for estimating hyperspectral bidirectional reflectance. Can J Remote Sens 32:244–253

Grandy WT (2005) Scattering of waves from large spheres. Cambridge University Press, Cambridge, UK

Gunderson K, Thomas N, Whitby JA (2006) First measurements with the Physikalisches Institut Radiometric Experiment (PHIRE). Planet Space Sci 54(11):1046–1056

Gunderson K, Lüthi B, Russell P, Thomas N (2007) Visible/NIR photometric signatures of liquid water in Martian regolith simulant. Planet Space Sci 55:1272–1282

Hapke BW, Nelson RM, Smyth WD (1993) The opposition effect of the moon: the contribution of coherent backscatter. Science 260(5107):509–511

Hapke B (1996) Are planetary regolith particles backscattering? Response to a paper by M. Mishchenko. J Quant Spectrosc Radiat Transfer 55:837–848

Hapke B (2012) Theory of reflectance and emittance spectroscopy. Cambridge University Press, Cambridge, UK

Jiang T, Zhang H, Yang Y, Hu X, Ma P, Sun Y, Britt D et al (2019) Bi-directional reflectance and polarization measurements of pulse-laser irradiated airless body analog materials. Icarus 331:127–147

Jiang T, Hu XY, Zhang H, Ma P, Li C, Ren X et al (2021) In situ lunar phase curves measured by Chang'E-4 in the Von Kármán Crater, South Pole-Aitken basin. Astron Astrophys 646:A2

Jiang T, Zhang H, Yang YZ, Ma P, Sun YX (2022) A non-motorized spectro-goniometric system to measure the bi-directional 2 reflectance spectra of particulate surfaces in the visible and near-infrared. Rev Sci Instrum 93:024504. https://doi.org/10.1063/5.0071621

Jin W, Zhang H, Yuan Y, Yang Y, Shkuratov YG, Lucey PG et al (2015) In situ optical measurements of Chang'E-3 landing site in Mare Imbrium: 2. Photometric properties of the regolith. Geophys Res Lett 42(20):8312–8319

Johnson JR, Shepard MK, Grundy WD, Paige DA, Foote EJ (2013) Spectrogoniometry and modelling of martian and lunar analog samples and Apollo soils. Icarus 223(1):383–406

Kaydash V, Shkuratov Y, Korokhin V, Videen G (2011) Photometric anomalies in the Apollo landing sites as seen from the Lunar Reconnaissance Orbiter. Icarus 211:89–96

Kreslavsky M, Shkuratov Y, Velikodsky Y, Kaydash V, Stankevich D, Pieters C (2000) Photometric properties of the lunar surface derived from clementine observations. J Geophys Res 105(E8):20281–20296

Levasseur-Regourd AC, Renard JB, Shkuratov Y, Hadamcik E (2015) Laboratory studies. In: Kolokolova L, Hough J, Levasseur-Regourd AC (eds) Polarimetry of stars and planetary systems. Cambridge University Press, pp 62–80

Lucey PG, Blewett DT, Jolliff BL (2000) Lunar iron and titanium abundance algorithms based on final processing of clementine ultraviolet-visible images. J Geophys Res-Planets 105(E8):20297–20305

Ma P, Sun YX, Zhu MH, Yang YZ, Hu XY, Jiang T, Zhang H et al (2020) A plagioclase-rich rock measured by Yutu-2 Rover in Von Karman crater on the far side of the Moon. Icarus 350:113901

McCord TB (1969) Color differences on the lunar surface. J Geophys Res 74(12):3131–3142

McGuckin BT, Haner DA, Menzies RT, Esproles C, Brothers AM (1996) Directional reflectance characterization facility and measurement methodology. Appl Opt 35(24):4827–4834

McGuckin BT, Haner DA, Menzies RT (1997) Multiangle Imaging Spectroradiometer: optical characterization of the calibration panels. Appl Opt 36(27):7016–7022

Mishchenko MI (1994) Asymmetry parameters of the phase function for densely packed scattering grains. J Quant Spectrosc Radiat Transfer 52:95–110

Mishchenko MI, Travis LD, Lacis AA (2006) Multiple scattering of light by particles: radiative transfer and coherent backscattering. Cambridge University Press, Cambridge

Mishchenko MI et al (2010) Polarimetric remote sensing of solar system objects. Kyiv, Akadem-periodyka

Muinonen K, Piironen J, Shkuratov YG, Clark BE (2002) Asteroid photometric and polarimetric phase effects. In: Bottke WF et al (eds) Asteroids III. University of Arizona Press

Ovcharenko AA, Bondarenko SY, Zubko ES, Shkuratov YG, Videen G, Nelson RM, Smythe WD (2006) Particle size effect on the opposition spike and negative polarization. J Quant Spectrosc Radiat Transfer 101:394–403

Pieters CM (1983) Strength of mineral absorption features in the transmitted component of near-infrared reflected light: first results from RELAB. J Geophys Res: Solid Earth 88(B11):9534–9544

Pieters CM, Hiroi T (2004) RELAB (reflectance experiment laboratory): a NASA multiuser spectroscopy, Version 2

Pommerol A, Jost B, Poch O, Yoldi Z, Brouet Y, Gracia-Berná A et al (2019) Experimenting with mixtures of water ice and dust as analogues for icy planetary material: recipes from the ice laboratory at the University of Bern. Space Sci Rev 215(5):article #37

Psarev V, Ovcharenko A, Shkuratov Yu, Belskaya I, Videen G (2007) Photometry of surfaces with complicated structure at extremely small phase angles. J Quant Spectrosc Radiat Transf 106:455–463

Rava B, Hapke B (1987) An analysis of the Mariner 10 color ratio map of mercury. Icarus 71(3):397–429

Sandmeier SR (2000) Acquisition of bidirectional reflectance factor data with field goniometers. Remote Sens Environ 73:257–269

Shepard MK (2001) The Bloomsburg University Goniometer (BUG) Laboratory: an integrated laboratory for measuring bidirectional reflectance functions. Lunar and Planetary Science XXXII

Shkuratov Y, Bondarenko S, Ovcharenko A, Pieters C, Hiroi T, Volten H, Munoz O, Videen G (2006) Comparative studies of the reflectance and degree of linear polarization of particulate surfaces and independently scattering particles. J Quant Spectrosc Radiat Transfer 100:340–358

Shkuratov Y, Bondarenko S, Kaydash V, Videen G, Muñoz O, Volten H (2007) Photometry and polarimetry of particulate surfaces and aerosol particles over a wide range of phase angles. J Quant Spectrosc Radiat Transfer 106:487–508

Shkuratov Y, Ovcharenko A, Psarev V, Bondarenko S (2008) Laboratory photopolarimetric measurements of particulate surfaces. In: Kokhanovsky A (eds) Light scattering reviews III. Springer-Praxis

Shkuratov Y, Kaydash V, Korokhin V, Velikodsky Y, Opanasenko N, Videen G (2011) Optical measurements of the Moon as a tool to study its surface. Planet Space Sci 59:1326–1371

Shkuratov Y, Opanasenko N, Korokhin V, Videen G (2015) The moon. In: Kolokolova L, Hough J, Levasseur-Regourd AC (eds) Polarimetry of stars and planetary systems. Cambridge University Press, pp 303–319

Schröder SE, Ye G, Pommerol A, Keller HU, Thomas N, Roush TL (2014) Laboratory observations and simulations of phase reddening. Icarus 239:201–216

Sibille L et al. (2006) Lunar regolith simulant materials: recommendations for standardization, production, and usage. NASA Technical Reports 2006–214605.

Sun ZQ, Wu ZF, Zhao YS (2014) Semi-automatic laboratory goniospectrometer system for performing multi-angular reflectance and polarization measurements for natural surfaces. Rev Sci Instrum 85(1):014503

Voss KJ, Chapin AL, Monti M, Zhang H (2000) Instrument to measure the bidirectional reflectance distribution function of surfaces. Appl Opt 39:6197–6206

Voss KJ, Zhang H (2006) Bidirectional reflectance of dry and submerged Labsphere Spectralon plaque. Appl Opt 45:7924–7927

Yang Y, Li S, Milliken RE, Zhang H, Robertson K, Hiroir T (2019) Phase functions of typical lunar surface minerals derived for the Hapke model and implications for visible to near-infrared spectral unmixing. J Geophys Res-Planets 124:31–60

Yang Y, Ma P, Qiao L, Zhang H, Jin W, Jiang T, Liu Y, Zou Y (2020) Phase-angle dependence of colour ratios and potential implications for lunar remote sensing. Astron Astron 644:A30

Yuffa AJ, Kaydash V, Korokhin V, Shkuratov Y, Zubko E, Videen G (2017) Phase-ratio imaging as applied to desert sands for tracking human presence. Appl Opt 56(3):B184–B190

Zhang H, Voss KJ, Reid RP (2003) Determining the influential depth for surface reflectance of sediment by BRDF measurements. Opt Express 11:2654–2665

Zhang H, Voss KJ (2005) Comparisons of bidirectional reflectance distribution function measurements on prepared particulate surfaces and radiative-transfer models. Appl Opt 44:597–610

Zhang H, Voss KJ (2006) Bidirectional reflectance study on dry, wet and submerged particulate layers: effects of pore liquid refractive index and translucent particle concentrations. Appl Opt 45:8753–8763

Zhang H, Voss KJ (2008) Bi-directional reflectance measurement of closely packed natural and prepared particulate layers. In: Kokhanovsky A (eds) Light scattering reviews III. Springer-Praxis

Zhang H, Voss KJ (2009) Bi-directional reflectance and polarization measurements on packed surfaces of benthic sediments and spherical particles. Opt Express 17:5217–5231

Zhang H, Voss KJ (2011) On Hapke photometric model predictions on reflectance of closely packed particulate surfaces. Icarus 215:27–33

Zhang H, Jin WD, Xu WB, Wang ZW, Yang YZ, Sun H (2014) A goniometric system to measure the incomplete mueller matrices of packed layers. In: 45th Lunar and planetary science conference 2872. The Woodlands, TX

Spectropolarimetry of Snow and Ice Surfaces: Measurements and Radiative Transfer Calculation

Tomonori Tanikawa

Abstract The properties of light reflected from snow and ice surfaces are important for the interpretation of remote sensing of the cryosphere. They can be explained in terms of snow physical and external parameters. These parameters are snow grain size and shape, snow density and light absorbing snow impurities, snow depth, layer structure, and surface conditions. The external parameters are parameters related to atmospheric conditions (cloud cover, aerosols, air pressure and atmospheric gases) and solar zenith angle. The presented results are based on a large number of observational and simulation studies on snow albedo and reflectance related to the total intensity of reflected light. Light reflected from the surface can also be described in terms of its polarization properties. Polarimetric observations have recently attracted much attention and there has been an extensive effort to investigate the polarization of light reflected from snow and ice surfaces. The polarization state of light contains valuable information about the optical properties of snow and ice. The majority of research into the polarimetric properties of snow is concerned with the degree of linear polarization (DoLP). In recent years, spectral features of each element of the Stokes vector that makes up the DoLP have also been clarified and the existence of neutral points in the DoLP of snow and ice surfaces was revealed. The elements of Stokes vector are related to the magnitude and orientation of the semi-major axis of the polarization ellipse, which is expected to contain additional information concerning snow properties. This paper gives a review of polarimetric properties of snow and ice surfaces based on measurements and radiative transfer simulations. The effects of snow physical parameters and external parameters on the polarimetric properties are discussed.

Keywords Polarization · Light scattering · Neutral points · DoLP · Reflectance · Snow · Bare ice · Polarized radiative transfer model

---

T. Tanikawa (✉)
Meteorological Research Institute, Japan Meteorological Agency,
Tsukuba 305-0052, Ibaraki, Japan
e-mail: tanikawa@mri-jma.go.jp

A. Kokhanovsky (ed.), *Springer Series in Light Scattering*, Springer Series
in Light Scattering, https://doi.org/10.1007/978-3-031-10298-1_3

1 Introduction

National Snow & Ice Data Center reported that on August 14, 2021, rain was observed at the highest point, National Science Foundation's Summit Station (3216 m a.s.l) on the Greenland ice sheet for several hours (National Snow & Ice Data Center 2021). There is no previous report of rainfall at this station (72.58°N, 38.46°W). Warm condition led to an estimated 7 billion tons of rainfall on the ice sheet. Due to heavy rainfall, widespread surface melting has been confirmed. The heavy rainfall was also observed in 2012, and a historical surface melting event has been occurred (Nghiem et al. 2012; Aoki et al. 2014). Recently, meltwater runoff into the ocean and ice-mass loss of the glacier has been dramatically increasing on the Greenland ice sheet. The mass of the ice sheet has begun to decrease in the latter half of the 1990s s and has decreased significantly since 2000 (Shepherd et al. 2012). In addition, due to the progress of ice sheet surface melting in recent years, satellite observations have revealed a decrease in the surface albedo over the entire ice sheet (Box et al. 2012). The decrease in the snow surface albedo is one of the main contributor to ice-mass loss because it increases the absorption of solar radiation and promotes surface melting (Box et al. 2012). The IPCC Special Report on the Ocean and Cryosphere in a Changing Climate summarized that ongoing glacier/ice sheet mass loss and the reduction of sea ice area in the Arctic region will continue with further warming (IPCC 2019). The cryosphere is a region that is vulnerable to climate change and where changes are most prominent. Thus, it is necessary to further strengthen the monitoring system in order to respond quickly and appropriately to the cryosphere changes.

Satellite observations are indispensable for the wide area snow-cover monitoring. Optical remote sensing has expanded from the use of panchromatic and multispectral sensors to imaging spectrometers with multi-viewing capability. Operational satellites such as Advanced Very High Resolution Radiometer (AVHRR), Moderate Resolution Imaging Spectroradiometer (MODIS), Second-generated Global Imager (SGLI), and Sentinel-series are capable of high-resolution observation on spatial and temporal scales which give the opportunity to investigate large-scale changes of the cryosphere in response to climate changes. For example, snow coverage was monitored by satellite data acquired from the 1980s to the present and changes in snow coverage were analyzed (Hori et al. 2017; Armstrong and Brodzik 2001; Brown et al. 2010). In addition, retrievals of snow parameters such as snow grain size, mass concentration of light absorbing particles in snow, which are the primary parameters controlling spectral and broadband albedo, and snow/ice surface temperature were attempted (Nolin and Dozier 2000; Li et al. 2001; Tanikawa et al. 2002). These snow parameters were retrieved by Global Imager (GLI) in the Northern Hemisphere (Stamnes et al. 2007; Aoki et al. 2007; Hori et al. 2007). Afterwards, the snow grain size in the Antarctic and Greenland ice sheets has been monitored by many researchers and its spatial and temporal variations have been revealed (Scambos et al. 2007; Jin et al. 2008; Lyapustin et al. 2009; Zege et al. 2011; Wiebe et al. 2013; Chen et al. 2021). These results are based on a large number of observational and simulation studies on spectral albedo and reflectance of snow related to the intensity of reflected light (Wiscombe and Warren 1980; Warren and Wiscombe 1980; Grenfell and Warren 1999; Aoki et al. 2000; Painter and Dozier 2004; Tanikawa et al. 2006a; Marks et al. 2015; Kokhanovsky et al. 2018; Tanikawa et al. 2020).

Light reflected from the surface can also be described in terms of its polarization properties (Hansen and Travis 1974; Talmage and Curran 1986; Mishchenko et al. 2006). Polarimetric observations have recently attracted much attention and their use is accelerating especially in the atmospheric and oceanic communities. The space-borne POLarization and Directionality of the Earth's Reflectances (POLDER) instrument, which was launched in 1996 on the Advanced Earth Observing Satellite (ADEOS) platform, provided the first quantitative measurements of the reflectance and polarization characteristics in atmosphere, land and ocean surface (Deschamps et al. 1994). The POLDER instrument measured polarization that was used for cloud and aerosol microphysics retrievals (Bréon and Goloub 1998; Deuzé et al. 2000). NASA/GISS airborne Research Scanning Polarimeter (RSP) based on polarimetric and multi-angular measurements, provided accurate polarimetric measurements from land and ocean surfaces and retrieved various geophysical parameters (Cairns et al. 2003; Ottaviani et al. 2015).

On the other hand, for the land surface use, despite more than 30 years of experiments, practical applications have remained few. Though very few studies and limited information have been reported on the polarization properties of the snow surface, useful knowledge about the polarization is now emerging and being established. Goloub et al. (1992) confirmed that a few percent of snow polarization were observed in the forward direction of POLDER data. From a comparison between the degree of linear polarization (DoLP) of snow and that of clouds, they suggested that the polarization may be useful for snow and cloud discrimination even though the rainbow feature present in the clouds was not detected. After that, the reflectance properties of snow were examined under the POLDER project (Leroux et al. 1998). The field measurement revealed that total and polarized reflectance at wavelength $\lambda = 1.6$ μm were sensitive to both snow grain size and shape. In addition, the radiative transfer simulation confirmed the same effect (Leroux et al. 1999). The performance of the spectrometer was enhanced at the beginning of this century. The spectrum range has been extended to the solar spectrum between $\lambda = 0.35$ and 2.5 μm with high spectral resolution and the portability and the operability has also been improved. Various optical measurements have been conducted as a routine part of many observation campaigns. Field and laboratory measurements of various surfaces were reported by Peltoniemi et al. (2009), who investigated various spectral reflection and polarization features in detail through many intensive field campaigns. Light reflected from dry and wet snow has different features, and significant reduction of the polarization for wet snow was confirmed in the forward direction while significant increase was found in the nadir. Angular dependence of snow DoLPs was measured in a cold laboratory, in a systematic experiment using a homogeneous incident light source (Sun and Zhao 2011). The effects of the snow grain size on the DoLP were spectrally confirmed. Furthermore, the contribution of the U component of Stokes vector (described in the next section) to the DoLP was found to be quite small. Similar results were obtained during intensive field campaigns in a snowfield in Hokkaido, Japan, and on the northwest Greenland ice (Tanikawa et al. 2014). Measurement results revealed that the polarization is quite sensitive to not only optical properties of snow but also the solar incident angle and illumination condition. The effect of a densely packed medium in snow polarization was theoretically studied based on ray-tracing simulations (Peltoniemi 2007), and it was later confirmed by Lv and Sun (2014) that the changes of the negative degree of linear polarization in the backward direction, which is a most remarkable observation phenomenon, were related to the packing density of snow. More recently it has been shown that the measurements revealed for the first time the existence of neutral points of Q and U in the snow surface (Tanikawa et al. 2021). The angular dependence of the neutral points especially in the shortwave infrared regions was linked exclusively to the measurement geometry regardless of snow particle size and shape.

Regarding the polarization properties of sea ice surface, relatively few studies have been reported. The first indication was probably reported by Perovich (1994), who conducted spectral measurements of the DoLP for sea ice surfaces at Resolute Bay in the Canadian Arctic Archipelago. Spectral measurement indicated a big change in the reflectance and polarization occurred in the forward direction. Especially, any specularly reflected light would be highly polarized under the condition that the solar zenith angle is close to the Brewster angle (Perovich 1998). The effects of air bubbles and brine pockets on the DoLP were examined in the cold laboratory (Sun et al. 2013). The volume scattering by the air bubbles and the brine pockets contributed to the reduction of DoLP in the visible regions while a specular reflection contributed to the strong polarization in the near infrared regions. Angular dependence of DoLP, Q and U for the sea ice surface was reported (Tanikawa et al. 2021) and Q component contributed to the high specular reflection in the forward direction while the surface roughness of the sea ice could contribute to the moderate polarization in the backward direction. Furthermore, the neutral points of Q and U in sea ice surface as well as snow surface were confirmed (Tanikawa et al. 2021).

There has been an extensive effort to investigate the area of the polarization of snow and ice surfaces described above. The majority of research into the polarimetric properties of snow and ice is concerned with the DoLP and the polarization properties of DoLP have been intensively studied. Recently, each element of Stokes vector that makes up the DoLP has been reported for the polarization properties of snow and ice surfaces. The elements of Stokes vector are related to the magnitude and orientation of the semi-major axis of the polarization ellipse, which is expected to contain additional information concerning snow and ice properties.

This paper reviews the spectral properties of light polarization by snow and ice surfaces based on the results of spectral measurements and radiative transfer calculations. In Sect. 2, definitions of terms and explanations of spectral measurements are presented. Section 3 covers spectral measurement conditions about location, snow and atmospheric conditions. In Sect. 4, spectral DoLP and related parameters that make up the DoLP for various snow types and bare ice surfaces are reported. The angular dependence on these parameters including viewing and azimuth angles were reviewed. Section 5 presents conclusions and future work.

2 Definition of Radiant Quantities Concerning the Polarization State of Light

The polarization state of light can be described by a set of four parameters specified by the symbols $I_{\|}$, $I_{\perp}$, U and V, which are elements of the Stokes vector $\mathbf{I}(\lambda) = [I_{\|}(\lambda)\ I_{\perp}(\lambda)\ U(\lambda)\ V(\lambda)]^T$. The Stokes parameters $I_{\|}(\lambda)$ and $I_{\perp}(\lambda)$ are the intensity components that are parallel and perpendicular to the scattering plane, respectively. $U(\lambda)$ is the degree of linear polarization in 45° and 135° planes to the reference plane, and $V(\lambda)$ is the degree of circular polarization which is usually negligible after reflection, and the superscript T denotes the transpose (Talmage and Curran 1986; Hovenier and van der Mee 1983; Stamnes and Stamnes 2015). This Stokes vector is related to the more common one, $\mathbf{I}_S(\lambda) = [I(\lambda)\ Q(\lambda)\ U(\lambda)\ V(\lambda)]^T$, by $I(\lambda) = I_{\|}(\lambda) + I_{\perp}(\lambda)$ and $Q = I_{\|}(\lambda) - I_{\perp}(\lambda)$, where $I(\lambda)$ is the total intensity of the reflected light. The Stokes vector's first three elements are the most important ones determining the polarization state. The degree of linear polarization (DoLP) is described by

$$\mathrm{DoLP}(\lambda) = \sqrt{P_q^2(\lambda) + P_u^2(\lambda)}, \tag{1}$$

where $P_q(\lambda)$ and $P_u(\lambda)$ are polarization-related parameters normalized by $I(\lambda)$ as follows:

$$P_q(\lambda) = -\frac{Q(\lambda)}{I(\lambda)}, \quad P_u(\lambda) = \frac{U(\lambda)}{I(\lambda)}. \tag{2}$$

In case Stokes parameter U equals 0, an alternative definition of DoLP can be used as follows:

$$\mathrm{DoLP}_q(\lambda) = -\frac{Q(\lambda)}{I(\lambda)}. \tag{3}$$

In this review, we used the DoLP properly in accordance with the purposes. These above quantities depend on the solar-target-sensor geometry, i.e. on the solar zenith and azimuth angles (θ_0, ϕ_0) and the sensor's viewing and azimuth angles (θ_v, ϕ_v) respectively, so DoLP, DoLP_q, P_q and P_u depend on θ_0, θ_v, ϕ_0 and ϕ_v.

The hemispherical-directional reflectance factor (HDRF) is provided in order to examine the relation between DoLP and HDRF. The HDRF is defined by

$$\mathrm{HDRF}(\theta_0, \theta_v, \phi_0, \phi_v; \lambda) = \frac{\pi I(\theta_0, \theta_v, \phi_0, \phi_v; \lambda)}{F(\theta_0; \lambda)}, \tag{4}$$

where I is the upward radiance reflected from the surface and F is the downward solar irradiance for the surface which includes radiation from the entire hemisphere.

3 Spectral Measurements and Instrumentation Device

The spectral measurements have been conducted by various researchers. They used self-developed goniometers in accordance with the target and measured the spectral radiant quantities by spectrometers with goniometers. In general, there are two types of goniometers used for the spectral measurement of snow and ice surfaces: tripod-based (mast-based) goniometer and ring-based one. Figure 1 shows the two types of goniometers developed in Meteorological Research Institute (MRI) (Tanikawa et al. 2014, 2021). The former observes the area around the goniometer instead of observing the same point based on the assumption that the surface is homogeneous around the goniometer. This goniometer is simple and easy-use for the field measurement (Aoki et al. 2000; Tanikawa et al. 2006b, 2014; Kuchiki et al. 2011). The mast-based measurement system which is the same concept as the tripod-based one is useful for the large area with surface roughness such as sastrugi (Hudson et al.

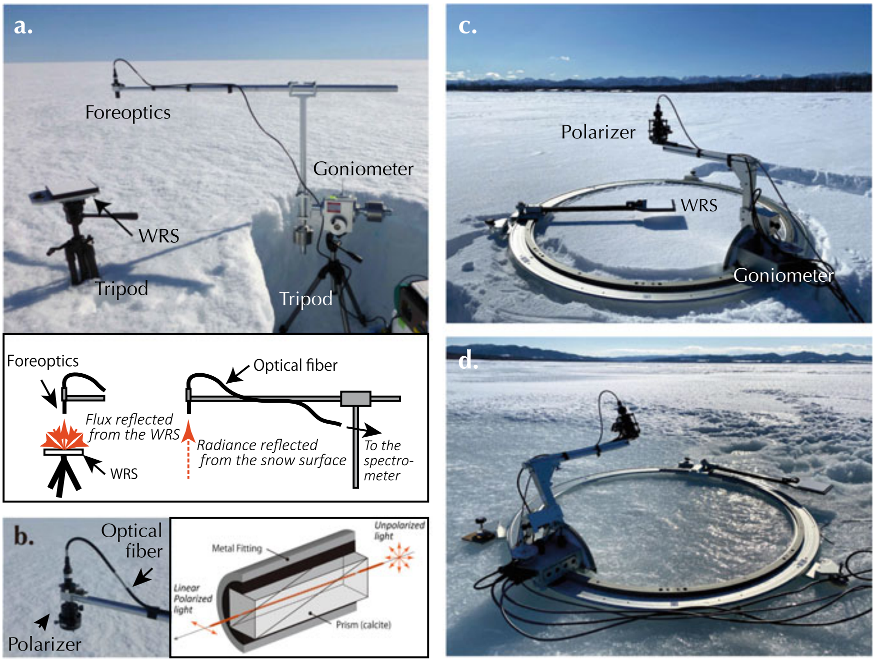

Fig. 1 Photographs of observation setup and schematic illustration of the setup for the spectral measurements using MRI goniometer: **a** tripod-based goniometer and **c**–**d** ring-based goniometer. **b** Glan–Thomson prism attached to the foreoptics to measure the polarized radiance and illustration of the prism. The upward polarized radiance was directly measured by the optical fiber through the foreoptics with polarizer. The downward solar flux was measured by directing the optical fiber through the fore optics to the upper surface of the WRS. Photographs were taken at the snow surface at SIGMA-A, Greenland (**a**) and Nakasatsunai, Hokkaido (**c**) and at the bare ice surface at Saroma-ko Lagoon, Hokkaido (**d**) (see Table 1)

2006). The later, the ring-based measurement system, observes the same point of the target from any polar and azimuth angle. The field goniometers of various size were created and used in accordance with the target and the purpose (Marks et al. 2015; Peltoniemi et al. 2009; Tanikawa et al. 2021; Perovich 1994, 1998; Sandmeier and Itten 1999; Painter et al. 2003; Peltoniemi et al. 2005). Automated goniometer was also developed because many measurement points are needed for the HDRF and DoLP (Marks et al. 2015; Peltoniemi et al. 2009; Tanikawa et al. 2021; Painter et al. 2003; Bourgeois et al. 2006). This is a significant development, improving the accuracy of measurement data.

We have worked on the development of the tripod-based goniometer (Aoki et al. 2000) and then upgraded it gradually (Tanikawa et al. 2006b, 2014; Kuchiki et al. 2011). Even in a manual operating system, the viewing and azimuth angles have an error of less than 1°. We put the goniometer in a snow pit and kept the rotation axis on the same level as the snow surface. The polarized radiance reflected from the surface was measured on the south side area of the snow pit (toward the solar direction). The measurement was made for the principal plane $\Delta\phi = 0°$ and 180° with the viewing angle of every 5° from 0° to 80°. Although the foreoptics keeps pointing to the same snow surface from any viewing angle, the precise area of the measured snow surface varies with the viewing angle. The field of view of the calcite Glan–Thomson prism is 7°. Thus, since we set the distance between the sensor and target point to be 50 cm, the footprint of the DoLP measurement was an circle with a diameter of 6.1 cm at nadir and an ellipse with a major axis of 12.3 cm at $\theta_v = 60°$. Note that the footprint of the HDRF measurement was the same as that of DoLP. The downward flux F was measured with a white reference standard (WRS) of a Spectralon panel, SRT-99 (Labsphere Inc., North Sutton, New Hampshire). The WRS was set on a tripod and placed on the east side of the snow pit to avoid the shadowing effect of the WRS on the upward radiance measurements. The average uncertainties of the DoLP and HDRF measured in the field were within 6 and 2% in this system, based on the error analysis process (Suomalainen et al. 2009).

MRI ring-based goniometer was developed in 2012 and upgraded gradually. The goniometer shown in Fig. 1c was completed in 2019. Because this system doesn't require the tripod, it is now possible to conduct the spectral measurement over the ice surface (Fig. 1d). The polar and azimuth angles can be set with an accuracy better than 1° by a machine control device. The polarized radiance reflected from the snow and ice surfaces was brought into the spectrometer by the same calcite Glan–Thomson prism installed in the fore optics. By machine control devices, the calcite Glan–Thomson prism was rotated in an increment of 1° to measure the polarized radiation of different directions. A quartz-wedge depolarizer was inserted between the optical fiber and polarizer in order to prevent a linearly polarized radiation entering the spectrometer. The field of view of this system is 7°. The Stokes vector's first three elements are derived by measuring the reflected polarized radiance at different polarizer directions as follows:

$$I(\lambda) = \{L_{0^\circ}(\lambda) + L_{45^\circ}(\lambda) + L_{90^\circ}(\lambda) + L_{135^\circ}(\lambda)\}/2, \tag{5}$$

$$Q(\lambda) = L_{0^\circ}(\lambda) - L_{90^\circ}(\lambda), \tag{6}$$

$$U(\lambda) = L_{45^\circ}(\lambda) - L_{135^\circ}(\lambda), \tag{7}$$

where $L_x(\lambda)$ is the polarized radiance at different polarizer directions x ($x = 0^\circ, 45^\circ, 90^\circ$ and 135°). For the HDRF measurement, the downward solar irradiance was observed by directing of optical fiber through the foreoptics with polarizer to the upper surface of the WRS placed on the plate.

The measurement was made for various planes including the principal and the perpendicular plane with the viewing angle θ_v of basically every 10° from 0° (nadir) to 70°. During the measurement, the fore optics holds pointing to the same target of the snow/bare ice surface from any polar and azimuth angle, but the footprint of the measured surface varies with the polar angle. The configuration of this goniometer is the same as that of the tripod-based goniometer. So, the footprint was a circle with a diameter of 6.1 cm at $\theta_v = 0^\circ$ and an ellipse with a major axis of 12.3 cm at $\theta_v = 60^\circ$. The average measurement uncertainty of this system was estimated within 3% based on the error analysis process (Suomalainen et al. 2009). Comparing to the tripod-based goniometer, the measurement uncertainty was reduced due to mainly the power angle adjustments of the goniometer and the polarizer direction, and the wedge depolarizer installed in the measurement system.

The spectral measurements were made using grating spectrometers, ASD FieldSpec 3 and 4 (Malvern Panalytical, UK). The scanning spectral range of the instrument is from the ultraviolet to the near infrared wavelength region between $\lambda = 0.35$ and 2.5 μm with a spectral resolution of 3 nm for $\lambda = 0.35 - 1.0$ μm and 10 nm for $\lambda = 1.0 - 2.5$ μm, and a spectral sampling (bandwidth) of 1.4 nm for $\lambda = 0.35 - 1.0$ μm and 1.1 nm for $\lambda = 1.0 - 2.5$ μm. The scanning time employed was 0.1 s with a sampling interval of 1 nm for the full spectral range.

4 Spectral Polarization Properties of Light Reflected from Snow and Ice Surfaces

This section reviews the spectral properties of polarization by snow and ice surfaces based mainly on results by Tanikawa et al. (2014, 2021). First, spectral features of polarization in snow surface are discussed, and then the snow grain size dependence and a unique case of the specular reflection with completely polarized light are described. The angular dependence of DoLP, P_q and P_u for snow and ice surfaces which are important for satellite observations is discussed in detail. The clear differences between these polarimetric parameters for snow surface and those of ice surface are pointed out. Spectral measurements revealed for the first time the existence of the neutral points of P_q and P_u. The behavior of the neutral points are introduced using a simple scattering theory and the radiation transfer model. Finally, an application of the use of polarization-information for the optical remote sensing is discussed.

The spectral measurements were carried out for various snow and ice field at Hokkaido, Japan and at northwest Greenland ice sheet. For the observation site in Hokkaido, one is seasonally snow covered flat-farms, where there were no shadows caused by surface roughness and forest near the site. The other is smooth bare ice fields at Saroma-ko Lagoon (surface area, 151.59 km^2 and maximum depth, 22 m) where is located on the northeast coast of Hokkaido and is connected to the southern part of the Sea of Okhotsk through two inlets (Nomura et al. 2020). The site in Greenland is at the SIGMA-A Camp in an accumulation area at a height of 1,490 m a.s.l, which is located along the ridge line in Hayes Peninsula about 70 km north-east of Qaanaaq village (Aoki et al. 2014). There were no shadows caused by surface roughness such as sastrugi or dunes, although the snow surface was slightly inclined ($<1^\circ$). The all spectral data showing in this review were obtained under clear sky conditions near local solar noon when θ_0 was close to $\theta_0 = 53^\circ - 61^\circ$ for each observation, and the snow surface was illuminated by direct solar radiation and diffuse skylight.

Snow pit work was conducted together with spectral measurements in order to explain various spectral data quantitatively. The snow physical parameters measured here were as follows: snow depth, snow grain size and shape, snow temperature, snow density and mass concentration of light absorbing particles in snow. The snow grain shape is according to “The International Classification for Seasonal Snow on the Ground” (Fierz et al. 2009). The snow grain size is the optically equivalent snow grain size defined by Aoki et al. (2000), who noted that the grain size was defined as half the branch width of dendrites, as half of the width of the narrower portion of broken crystals, or the radius of each spherical particle. This dimension corresponds to r_2 defined by Aoki et al. (2000) (see an illustration of Fig. 1 in Aoki et al. 2007).[1] Table 1 summarized field campaign sites with a short summary of snow condition. The snow form and the snow grain size summarized in Table 1 indicated measurement results of a surface (top) snow layer in snow vertical profiles. Detail explanations of snow vertical profiles are described by Tanikawa et al. (2014, 2021).

---

[1] Recently, the understanding that the spectral snow albedos in the NIR and SWIR regions are well correlated with the specific surface area of snow grains is relatively widespread (Dominé et al. 2006). The measurements of the specific surface area of snow grains instead of snow grain size were reported in the various field experiments. Though measured snow grain sizes r_2 have a wide range (Table 1) due to the visual observations, there is a good correlation between r_2 and the specific surface area of snow grains (Tanikawa et al. 2020). Therefore, to a first approximation, the optically equivalent snow grain size can be recognized as r_2 which is one-half the branch width of dendrites or one-half the dimension of the narrow portion of broken crystals (Aoki et al. 2000).

Table 1 Field campaign sites with the short summary of snow condition. Each site location is as follows: Bihoro, Hokkaido (43°52′07″N, 144°06′45″E), Nakasatsunai, Hokkaido (42°38′40″N, 143°06′36″E), Saroma-ko lagoon, Hokkaido (44°07′21″N, 143°57′59″E), and SIGMA-A, Greenland (78°03′06″N, 67°37′42″W). The grain size is the optically equivalent snow grain size. Minimum, maximum and medium (within brackets) values are described

Data	Location	Measurement item	Snow form	Grain size (μm)
Feb. 13, 2012	Bihoro	DoLP$_q$, HDRF	Precipitation particle	20–100 (40)
Jul. 04, 2012	SIGMA-A	DoLP$_q$, HDRF	Needles	50–530 (100)
Jul. 05, 2012	SIGMA-A	DoLP$_q$, HDRF	Surface hoar	100–580 (180)
Jul. 06, 2012	SIGMA-A	DoLP$_q$, HDRF	Melt form	280–780 (500)
Jul. 08, 2012	SIGMA-A	DoLP$_q$, HDRF	Melt-freeze crust	800–2000 (1000)[a]
Feb. 11, 2020	Nakasatsunai	DoLP, P_q, P_u, HDRF	DF[b]	25–50 (<50)
Feb. 14, 2020	Nakasatsunai	DoLP, P_q, P_u, HDRF	Melt-freeze crust	100–1000 (250)
Feb. 25, 2020	Saroma-ko lagoon	DoLP, P_q, P_u, HDRF	Sea ice	na

[a] Statistics of thickness of melt-freeze crust are indicated

[b] DF means the decomposing and fragmented precipitation particles

4.1 Spectral Dependence on the DoLP, P_q, P_u and HDRF

Figure 2 depicts spectral DoLP and its related polarized parameters P_q and P_u at $\lambda = 0.35 - 2.5$ μm for the decomposing and fragmented precipitation particles taken at Nakasatsunai site on February 11, 2020. Spectral data at several viewing angles in the forward direction ($\Delta\phi = 0°$), sideward direction ($\Delta\phi = 90°$) and backward direction ($\Delta\phi = 180°$) are depicted. In this review, we refer to the directions of $0 \leq \Delta\phi \leq 60°$, $60° < \Delta\phi \leq 120°$ and $120° < \Delta\phi \leq 180°$ as the "forward direction", "sideward direction", and "backward direction", respectively. The solar zenith angles were $\theta_0 = 57°$ corresponding to local solar noon. The spectral data at $\lambda = 1.8 - 2.1$ μm and $\lambda > 2.3$ μm were masked due to low signal-to-noise ratios in absorption bands of atmospheric gases. For a reference, results of spectral HDRF data were depicted.

The spectral DoLPs in the visible region (VIS; $\lambda = 0.4 - 0.7$ μm) were small in the range between 0.0 and 0.03 and spectrally uniform. There was no clear dependence on the relative azimuth angle. Because the light absorption by the ice is particularly weak in VIS regions (Warren and Brandt 2008), multiple scattering is dominant, implying that the light reflected from the snow surface was essentially unpolarized. In the near infrared (NIR; $\lambda = 0.7 - 1.4$ μm) and the shortwave infrared (SWIR; $\lambda = 1.4 - 2.5$ μm) regions, wavelength dependence of the DoLP with unique spectral features was confirmed. Some sharp peaks at $\lambda = 1.5$ μm and ~ 2.1 μm and

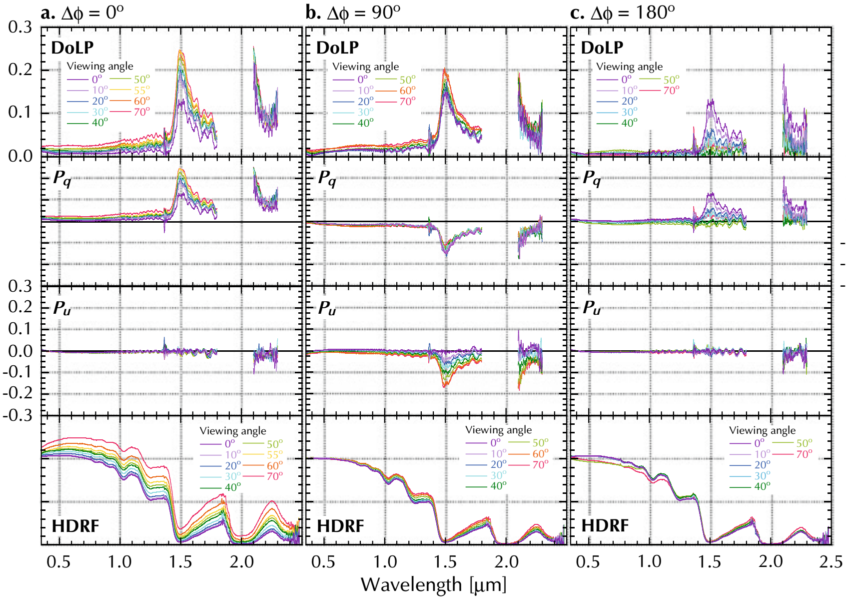

Fig. 2 Spectral DoLP, P_q, P_u and HDRF at several viewing angles in the forward direction ($\Delta\phi = 0°$), sideward direction ($\Delta\phi = 90°$) and backward direction ($\Delta\phi = 180°$), respectively, taken at "Nakasatsunai site on" February 11, 2020. $\theta_0 = 57°$. Note that DoLP, P_q, P_u between $\lambda = 1.8$ μm and 2.1 μm and for $\lambda > 2.3$ μm were masked due to the low signal to noise ratios in the atmospheric gaseous absorption bands. Spectral data for $\theta_v = 60°$ in the backward direction ($\Delta\phi = 180°$) were masked due to the detector shadow

some troughs between each peak corresponded to the light absorption by ice. This result can be explained by the difference of the contribution of volume scattering to the reflected light. The volume scattering originates from the spectral dependence of the absorption coefficient by ice. So, for highly absorbing spectral regions, the volume scattering is relatively low. In other words, scattering processes at surfaces are dominant for the reflected light. Hence, the reflected light is polarized for highly absorbing spectral regions, which explains the characteristic measured spectral features in the NIR and SWIR regions. These features have been reported by several authors conducted in the cold laboratory and the snow field (Peltoniemi et al. 2009; Sun and Zhao 2011; Lv and Sun 2014).

The dependence of the DoLP on the viewing angle was mainly observed in the SWIR regions, but it is interesting to note that the viewing angle dependence was different between the DoLP and the HDRF; the viewing angle corresponding to the maximum values were different from each other. Similar results for other cases were obtained. This result will be discussed in the Sect. 4.5.

Regarding the linear polarization parameters P_q and P_u, the DoLP in the principal plane ($\Delta\phi = 0°$ and $180°$) is determined by $P_q > 0$ and $P_u \sim 0$, respectively (Fig. 2a, c). In general, the U Stokes parameter would be 0 in the principal plane, so that Q is dominant in the DoLP. In contrast, the DoLP in the perpendicular plane (sideward direction; $\Delta\phi = 90°$) depends on both $P_q < 0$ and $P_u < 0$ (Fig. 2b). So, the DoLP is the result of combining the polarizations of both Q and U. Furthermore, we found that the weak dependence of the DoLP on viewing angle was mainly due to P_u, since P_q would be independent of the viewing angle. In summary, the behavior in Q and U was different even in the same DoLP, depending on the azimuth angle, and besides that, the viewing angle dependence in Q and U was different in the azimuth angle. In the Sect. 4.5, the effect of the viewing and azimuth angles on the DoLP and related parameters P_q and P_u will be further discussed.

4.2 *Snow Grain Size Dependence on the DoLP*

Effects of snow grain size on the polarization properties have been intensively studied in the cold laboratory and the snowfield (Peltoniemi et al. 2009; Sun and Zhao 2011; Tanikawa et al. 2014; Lv and Sun 2014) and in the radiative transfer model (Peltoniemi 2007). This section reviewed the measurement results taken at Bihoro, Japan and Greenland based on the result by Tanikawa et al. (2014).

Figure 3 presents the spectral DoLP$_q$ at $\lambda = 0.35 - 2.5$ µm for the five snow types. The solar zenith angles were in the range $\theta_0 = 55° - 58°$ for all cases which is close to the Brewster angle $\theta_B = 52° - 53°$ (depending on the wavelength). We masked the spectral data at $\lambda = 1.35 - 1.4$ µm, $\lambda = 1.8 - 2.0$ µm and $\lambda > 2.4$ µm, respectively, due to the same reason described in the previous section. Although the spectral signals in $\lambda = 2.0 - 2.4$ µm were quite noisy, we present the results at $\lambda = 2.0 - 2.4$ µm to illustrate the relative tendency of the DoLP inferred from the spectral signals.

The spectral DoLP$_q$ in the forward direction in the NIR and SWIR regions changes in a wide range between 0.2 and 0.97, and increases with an increase in snow grain size. For example, the DoLP$_q$ at $\lambda = 1.5$ µm for $\theta_v = 55°$ in the forward direction ($\Delta\phi = 0°$) was 0.21 for the precipitation particle, 0.29 for the needles, 0.37 for the surface hoar, 0.75 for the granular snow, and 0.912 for the melt-freeze crust, respectively. Figure 4a depicts the spectral DoLP$_q$ at $\theta_v = 55°$ for five types of snow. A clear increase in the spectral DoLP$_q$ associated with the snow grain size can be seen in the NIR and SWIR regions. This can be explained by the relative contribution of surface versus volume scattering to the reflected light. The surface scattering contribution is typically due to specular reflection implying that light polarization is governed by Fresnel reflection whereas the volume scattering contribution is typically due to multiple scattering. In addition, the volume scattering contribution depends on the snow grain size: small grain size, high-order scattering; large grain size, low-order scattering because the light absorption by the ice is strong. Thus, the volume scattering contribution results in a reduction in the DoLP$_q$ depending on the snow grain size. In other words, a relatively large DoLP$_q$ results from both specular reflection and low-order scattering by the larger particles whereas a small DoLP$_q$

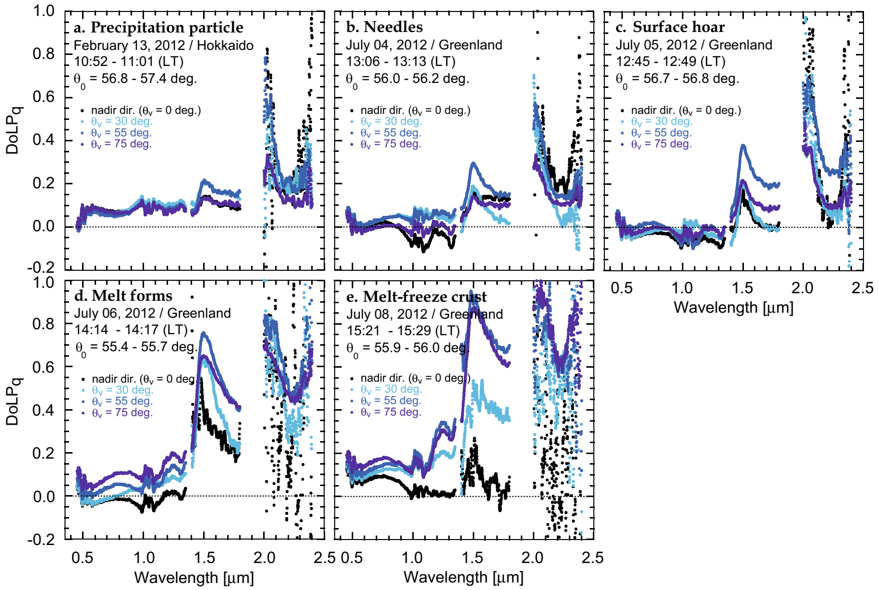

Fig. 3 Spectral DoLP_q curves at the four viewing angles of $\theta_v = 0°, 30°, 55°, 75°$ in the forward direction ($\Delta\phi = 0°$) for five types of snow. Note that the spectral data for $\lambda = 1.35$ and $1.4\ \mu\mathrm{m}$, $\lambda = 1.8$ and $2.0\ \mu\mathrm{m}$ and $\lambda > 2.4\ \mu\mathrm{m}$ are masked because of the low signal to noise ratios in the atmospheric gaseous absorption bands

is caused by high-order (multiple) scattering because the large particles (mm-scale) would appear much more flat than small (fresh) snow particles.

In order to further validate the grain size dependence of the snow DoLP_q, we investigate the relation between the spectral HDRF and the DoLP_q for the five types of snow. Figure 4b shows spectral HDRF at $\theta_v = 55°$ for five types of snow. As the snow grain size increases, the HDRF in the NIR and SWIR decreases whereas the DoLP_q increases (Fig. 4b), implying that there is a negative correlation between the DoLP_q and the HDRF. This negative correlation is consistent with previous studies (Peltoniemi et al. 2009; Sun and Zhao 2011). This result indicates that it should be possible to retrieve the snow grain size at the snow surface by making use of the spectral DoLP_q in the NIR and SWIR. More detailed discussion of this issue is provided in Sect. 4.7.

4.3 High DoLP for the Melt-Freeze Crust

The spectral DoLP_q for the melt-freeze crust has a maximum at $\theta_v = 55°$ (Fig. 3e). The melt-freeze crust is a thin, glittering ice layer, which is sometimes visible on the

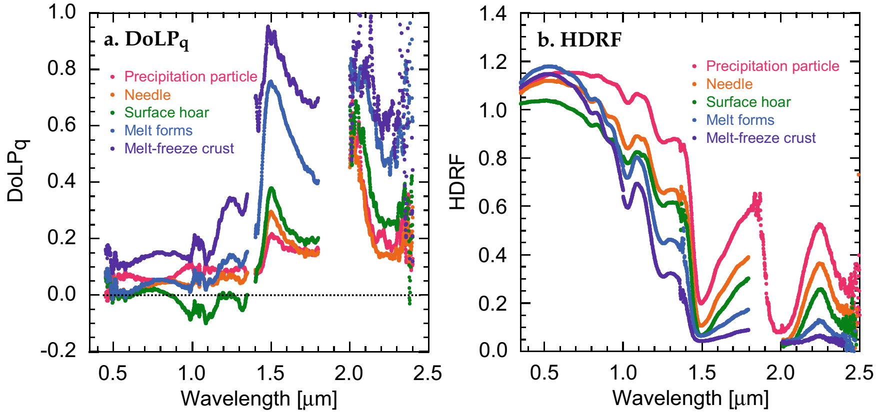

Fig. 4 Spectral DoLP$_q$ and HDRF at $\theta_v = 55°$ and $\Delta\phi = 0°$ for five types of snow. Note that the spectral data for $\lambda = 1.35$ and 1.4 μm (only DoLP$_q$), $\lambda = 1.8$ and 2.0 μm and $\lambda > 2.4$ μm (only DoLP$_q$) are masked because of the low signal to noise ratios in the atmospheric gaseous absorption bands. The mask for $\lambda < 0.45$ μm (only DoLP$_q$) is due to the noise of the polarimetric calibration

snow surface on sunny days (Ozeki and Akitaya 1998). The upper surface was flat compared with the bottom.

The DoLP$_q$ in the SWIR spectral range has two peaks at the wavelength close to $\lambda = 1.5$ and 2.0 μm corresponding to extreme values close to 1.0. These extreme values occur when these two conditions are satisfied: (1) the incident angle is approximately equal to the Brewster angle, and (2) no radiation is propagated from the inside of the ice. When the incident radiation at $\theta_0 = \theta_B$ is traveling to the boundary surface of the ice, the reflected light component in the direction perpendicular to the principal plane at $\theta_v = \theta_B$ vanishes, implying that only the reflected light in the parallel component can be measured. Thus, if the surface is completely flat and smooth with no radiation propagated from the inside of the ice due to the strong light absorption by the ice, the DoLP$_q$ will be expected to be 1.0. Because the melt-freeze crust creates almost specular reflection of solar illumination with completely polarized light even though the surface is not really flat, and because the ice absorbs strongly in the SWIR region especially for these wavelengths, high values of the DoLP$_q$ were measured in the glint region around $\theta_v = 55°$ at $\Delta\phi = 0°$. This result suggests that the melt-freeze crust behaves like a glittering ice layer that acts as a specularly reflecting surface material.

The wavelength dependence of the DoLP$_q$ for $\theta_0 = \theta_B$ can also be explained by the same reason described in the previous section. It is due to the wavelength dependence of the volume scattering contribution to the reflected light, which occurs regardless of the incident angle being the Brewster angle. Hence, the measurements at the Brewster angle provide the optimum conditions for obtaining the maximum DoLP$_q$ of 1.0 at $\theta_v = \theta_B$ and also for indicating whether the surface is smooth.

4.4 *Viewing Angle Dependence on the DoLP*

Figure 5 shows the viewing angle dependence of the spectral DoLP_q for five snow types taken at Hokkaido, Japan and Greenland and selected wavelengths $\lambda = 0.55$, 0.86, 1.24 and 1.64 μm. We selected these wavelengths employed in the snow parameter retrievals (Stamnes et al. 2007; Aoki et al. 2007; Hori et al. 2007). These wavelengths roughly correspond to the spectral bands of satellite sensors such as POLDER, MODIS, GLI, SGLI and RSP. The wavelength at $\lambda = 1.5$ μm is also used to demonstrate the impact of snow grain size on the reflected light as an extreme case. This wavelength corresponds to one of the local maxima in the DoLP_q (Fig. 4) in which light absorption by the ice is relatively strong (Warren and Brandt 2008). The measurements shown in Fig. 5 were obtained under clear skies for solar zenith angles in the range $\theta_0 = 55 - 58°$, which are close to the Brewster angle.

The DoLP_q for precipitation particles, needles and surface hoar (Figs. 5a–c) exhibit a small dependence on viewing angle both in the VIS and NIR. The maximum difference between the nadir ($\theta_v = 0°$) and off-nadir angle ($\theta_v = 55°$ and $\Delta\phi = 0°$) falls within 0.1 except for the SWIR. For these snow particles, multiple scattering is the dominant contributor to the DoLP_q at VIS and NIR wavelengths. In the SWIR

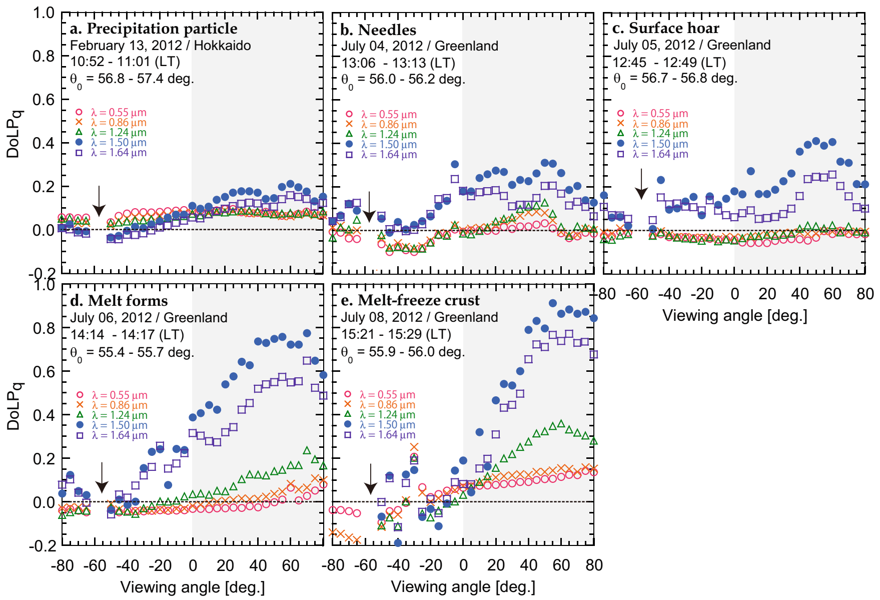

Fig. 5 Viewing angle dependence of the DoLP_q at five selected wavelengths. Positive viewing angles correspond to the forward direction ($\Delta\phi = 0°$) and negative ones correspond to the backward direction ($\Delta\phi = 180°$). The arrow in each figure means the incident zenith angle. The illumination from the sun comes from the backward direction along the principal plane. So the data of this angle was masked due to the shading by the optical fiber arm

region, the DoLP$_q$ appears to exhibit a broad peak around $\theta_v = 40° - 60°$ in the forward direction ($\Delta\phi = 0°$). The DoLP$_q$ of melt forms (Fig. 5d) in the VIS and NIR regions shows that the angular dependence near nadir angles ($|\theta_v| < 20°$) is small and similar to that of precipitation particle, needles and surface hoar (Figs. 5a–c), whereas the angular dependence at off-nadir angles in $\Delta\phi = 0°$ is moderate in the NIR and strong in the SWIR. The DoLP$_q$ of melt-freeze crust has the strongest angular dependence of the five selected snow types (Fig. 5e). The spectral DoLP$_q$ at $\lambda = 1.5$ and 1.64 μm clearly indicates a dispersed reduction from the broad peak around the $\theta_v = 40° - 60°$.

In general, we note that the DoLP$_q$ exhibits a broad peak around $\theta_v = 40° - 60°$ in $\Delta\phi = 0°$ in the NIR and SWIR, but not in the VIS. This result can be explained in terms of two basic reasons: (1) the relative contribution of surface versus volume scattering to the reflected light and (2) the ratio of direct/diffuse components in the incident solar radiation. The primary reason is the same as described previously in Sect. 4.1 that the surface scattering contribution is typically due to specular reflection so that the reflected light is polarized, whereas the volume scattering contribution is typically due to multiple scattering that leads to unpolarized reflected light. Another reason is that atmospheric scattering is also an important factor in determining the DoLP. Under clear sky conditions, the diffuse sky light due to Rayleigh scattering is nearly one quarter of the total downward solar radiation in the VIS, whereas this component becomes negligibly small at NIR and SWIR wavelengths due to the $1/\lambda^4$ dependence of the Rayleigh scattering cross section, implying that the direct component is dominant in the NIR and SWIR regions. Therefore, in the VIS, because the illumination of the sky arrives from a multitude of directions and weak light absorption by the ice leads to multiple scattering by the snow grains, the small viewing angle dependence on the DoLP can be seen as a result of unpolarized light reflected from the snow surface. In contrast, in the NIR and SWIR, because the direct component of the solar radiation is much larger than the diffuse one, and light absorption by the ice is strong, the broad peak around the $\theta_v = 40° - 60°$ can be seen as mainly a consequence of both specular reflection and low-order scattering by the snow particles. It is concluded that the angular distribution of the spectral DoLP results from the direct/diffuse partitioning of the incident solar radiation as well as the snow optical properties. Next section provides further explanations for the angular distribution of the DoLP and its snow grain size dependence based on the scattering properties of snow grains.

4.5 Viewing and Azimuth Angle Dependence on the DoLP and Related Parameters P_q and P_u

This section discusses the effect of the viewing and azimuth angles on the DoLP and its related parameters P_q and P_u for snow and ice surfaces. Figures 6, 7 and 8 show polar contour plots of measured HDRF, DoLP, P_q and P_u for the snow and bare ice

a. λ = 0.443 μm

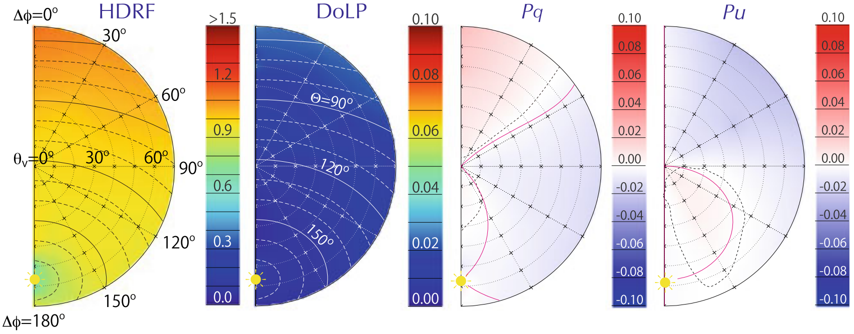

b. λ = 0.869 μm

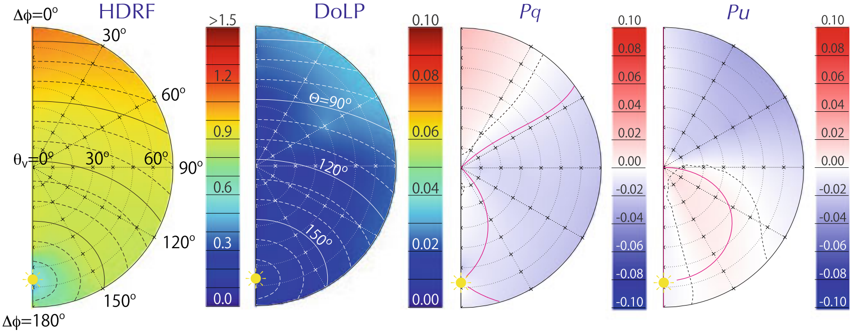

c. λ = 1.63 μm

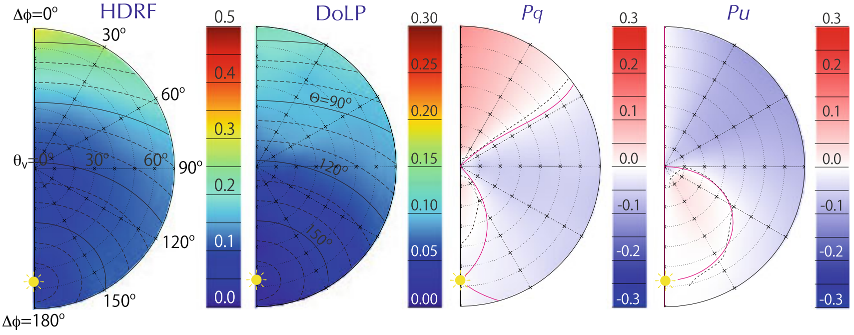

Fig. 6 Polar contour plots of HDRF, DoLP, P_q and P_u at three selected SGLI channels as obtained from spectral measurements for the decomposing and fragmented precipitation particles on February 11, 2020. The small cross signs on each contour plot indicate observation points. The radial coordinate is proportional to the viewing angle θ_v. The centre of the half-circle is $\theta_v = 0°$ (nadir) and the outer half-circle is $\theta_v = 70°$. The illumination from the sun comes from the lower half of each map, indicated by the yellow sun mark. The solar zenith angle is $\theta_0 = 57°$. The solid and dashed lines in the HDRF and DoLP plot the scattering angle Θ with 10° interval, while the black dash and red solid lines in the P_q and P_u indicate observed and calculated neutral points, respectively. The top of each contour map is the forward scattering direction. The values around the yellow sun mark in the HDRF are low because of the detector shadow

a. λ = 0.443 μm

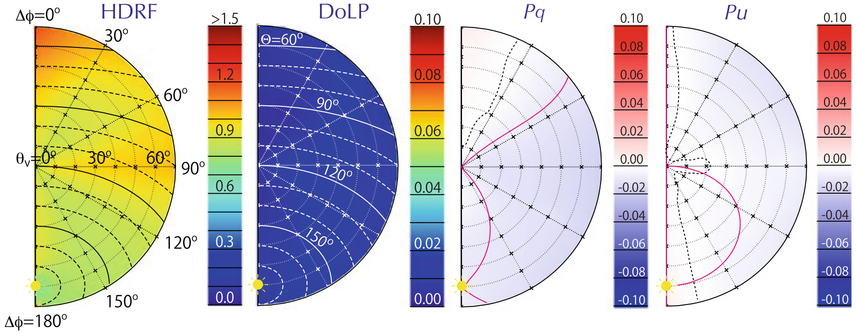

b. λ = 0.869 μm

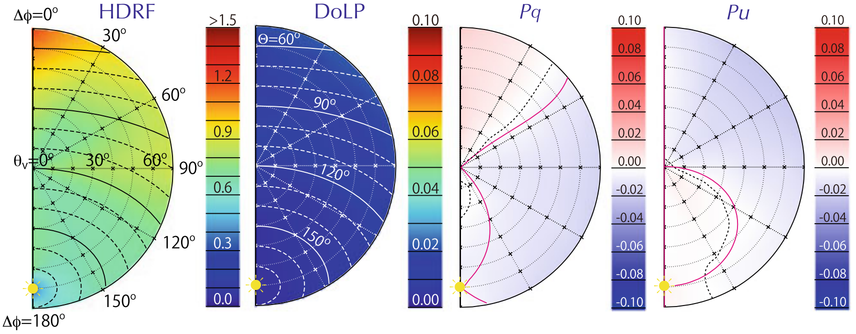

c. λ = 1.63 μm

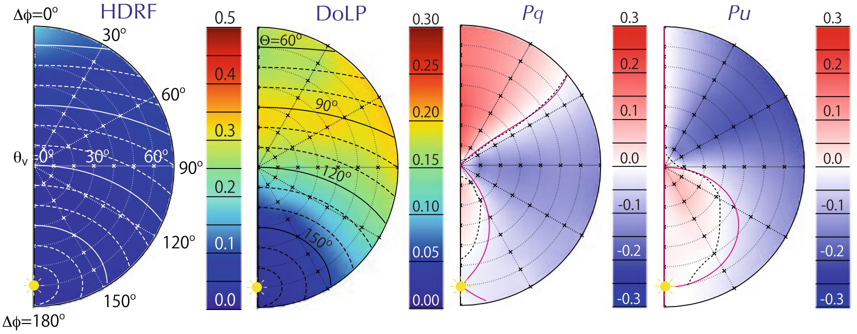

Fig. 7 Same as Fig. 6, but for the melt forms on February 14, 2020. $\theta_0 = 58° - 61°$

a. λ = 0.443 μm

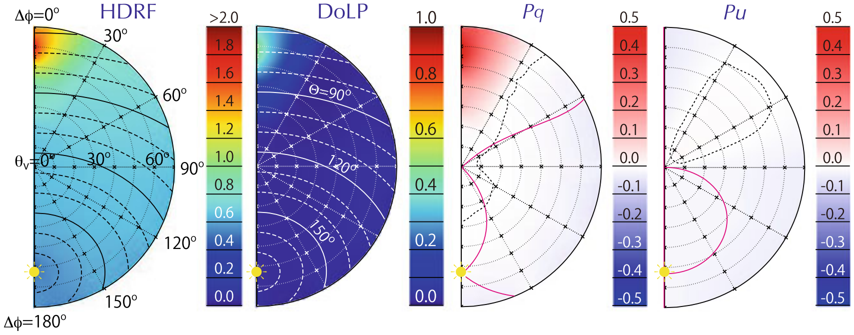

b. λ = 0.869 μm

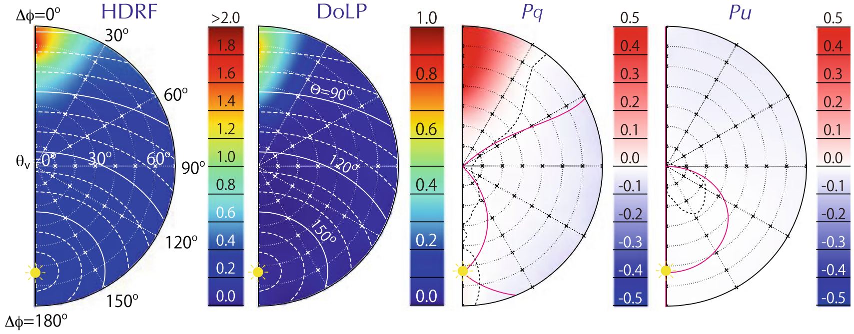

c. λ = 1.63 μm

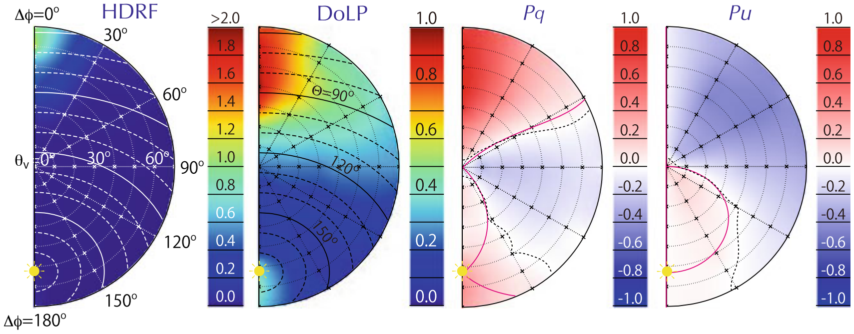

Fig. 8 Same as Fig. 6, but for the bare ice surface on February 25, 2020. $\theta_0 = 53^\circ - 54^\circ$

surfaces in SGLI selected channels at $\lambda = 0.443$, 0.869 and 1.63 μm. These wavelengths are used in the snow parameter retrievals adopted for the SGLI snow/ice products (Chen et al. 2021), and actually SGLI has two polarization channels at $\lambda = 0.674$ and 0.869 μm that can measure polarization (Imaoka et al. 2010). These three wavelengths selected here were similar to the spectral channels of satellite instruments such as MODIS and POLDER as well as RSP. All measurements were conducted under clear sky condition for $\theta_0 = 52° - 62°$. For the bare ice measurements, θ_0 was almost equal to the Brewster angle ($\theta_B \sim 52°$).

4.5.1 DoLP

Snow surface. At first, we discuss the DoLP of snow surface. Figure 6 shows results for the decomposing and fragmented precipitation particles on February 11, 2020, while Fig. 7 depicts results for the melt forms on February 14, 2020. The DoLP plots were characterized by high values in the forward direction ($\Delta\phi = 0°$) that gradually decreased toward the side and backward directions even at $\lambda = 0.443$ and 0.869 μm. The angular dependence of the DoLP on the viewing geometry at these three wavelengths was commonly very small and the DoLP in the forward direction was less than 0.03. Because multiple scattering is dominant due to relatively weak light-absorption by ice at these wavelengths (Warren and Brandt 2008), the reflected radiances were almost unpolarized.

In contrast, the dependence of the DoLP on viewing angle was clearly seen at $\lambda = 1.63$ μm. The DoLP appears to exhibit a broad peak in the forward and sideward directions of $\Delta\phi < 90°$. This polarization feature can be seen in both cases (Figs. 6 and 7); as a general trend, the DoLPs of the melt forms were higher than those of the decomposing and fragmented precipitation particles. This is the same polarization feature as described in the previous section, i.e. snow grain size dependence on the DoLP. These results can be explained in terms of single scattering properties of snow particles using the simple scattering theory. In the SWIR regions where the light absorption by ice is relatively strong, the scattering process will be dominated by the single scattering at the surface layer. So, for unpolarized incident solar radiation $\mathbf{I}_0 = [I_0\ 0\ 0\ 0]^T$ where I_0 is the unpolarized intensity, the scattered radiation after one scattering event $\mathbf{I}_1 = [I_1\ Q_1\ U_1\ V_1]^T$ can be described as follows:

$$\mathbf{I}_1(\Theta, \sigma_1, \sigma_2) = \mathbf{L}(-\sigma_2)\mathbf{F}(\Theta)\mathbf{L}(\pi - \sigma_1)\mathbf{I}_0 \tag{8}$$

$$= \begin{bmatrix} a_1(\Theta)I_0 \\ \cos 2\sigma_2 b_1(\Theta)I_0 \\ -\sin 2\sigma_2 b_1(\Theta)I_0 \\ 0 \end{bmatrix}, \tag{9}$$

where $\mathbf{F}(\Theta)$ is the normalized scattering matrix, $\mathbf{L}$ is the rotation matrix, and Θ is the scattering angle. a_1 and b_1 are elements of $\mathbf{F}$, and σ_1 and σ_2 are the angles of rotation (see in Fig. 11.3.1(a) in Mishchenko et al. 2006). The normalized scattering matrix $\mathbf{F}$

generated by electromagnetic scattering theory provides a complete characterization of the angular distribution and polarization state of the light scattered by an ensemble of dielectric particles (Mishchenko et al. 2002). These three angles of Θ, σ_1 and σ_2 are connected with measurement geometries of θ_0, θ_v, and $\Delta\phi(= \phi_v - \phi_0)$ based on spherical trigonometry (Mishchenko et al. 2006) (see Appendix 1). Thus, $\mathbf{I}_1$ can be represented using the measurement geometries, that is $\mathbf{I}_1(\theta_0, \theta_v, \Delta\phi)$. Details of the normalized scattering matrix $\mathbf{F}$ and its related coordinate system are described in Mishchenko et al. (2006). From the Stokes parameters of $\mathbf{I}_1$, we obtain the DoLP as follows:

$$\mathrm{DoLP} = \mid b_1(\Theta)/a_1(\Theta) \mid . \tag{10}$$

Figure 9 shows the ratio $-b_1/a_1$ of elements of normalized scattering matrix for various snow grain sizes and shapes calculated by the geometrical optics approximation (Masuda et al. 2012; Ishimoto et al. 2018) and the Mie theory. In general, this ratio indicates the degree of the linear polarization of scattered light for unpolarized incident light in a single grain and is a function of a scattering angle Θ. From the results, the ratio reveals a broad peak at side scattering and $\lambda = 1.63$ µm regardless of the shape and size of the particles. This means that the scattered light in this range of scattering angles would be polarized. Based on this result, we investigated the relationship between the broad peak of the DoLP and the scattering angle Θ calculated from θ_0, θ_v and $\Delta\phi$ (Appendix 1) and found that the broad peak of the DoLP corresponds to around $\Theta = 60° - 120°$ (Figs. 6d and 7d). It is concluded that the broad peak of the DoLP results from the polarimetric properties of the single light scattering by snow particles. Regarding the difference between DoLP of the decomposing and fragmented precipitation particles and that of the melt forms, it is considered from Fig. 9 that the dependence on the snow grain size would be reflected in the measured DoLP.

As can be seen in the Sect. 4.1, the dependence on viewing angle was different between the DoLP and the HDRF; the viewing angle corresponding to the maximum values were different from each other, and the maximum values were at $\theta_v = 30° - 60°$ for the DoLP, but at $\theta_v = 70°$ for the HDRF. Both features can be explained by the single scattering properties of snow particles. Since the reason for the DoLP has already been described above, the reason for the HDRF can be discussed below. From the relationship between the particle size and the wavelength, the scattered light intensity is dominant in the forward direction (see in Fig. 3 in Tanikawa et al. 2020); the smaller the scattering angle, the higher the scattered intensity. Therefore, the HDRF has a relatively higher value in the forward direction with the larger viewing angle where the scattering angle is small. This is the reason why the angular distribution was different between the DoLP and the HDRF.

Bare ice surface. Next, we discuss the DoLP of the bare ice surface shown in Fig. 8. The DoLP had strong peaks around $\theta_v = 40° - 60°$ in the forward direction for all three wavelengths. The DoLP at $\lambda = 1.63$ µm was almost 1.0. This result is caused by a large specular reflection component plus strong polarization near the

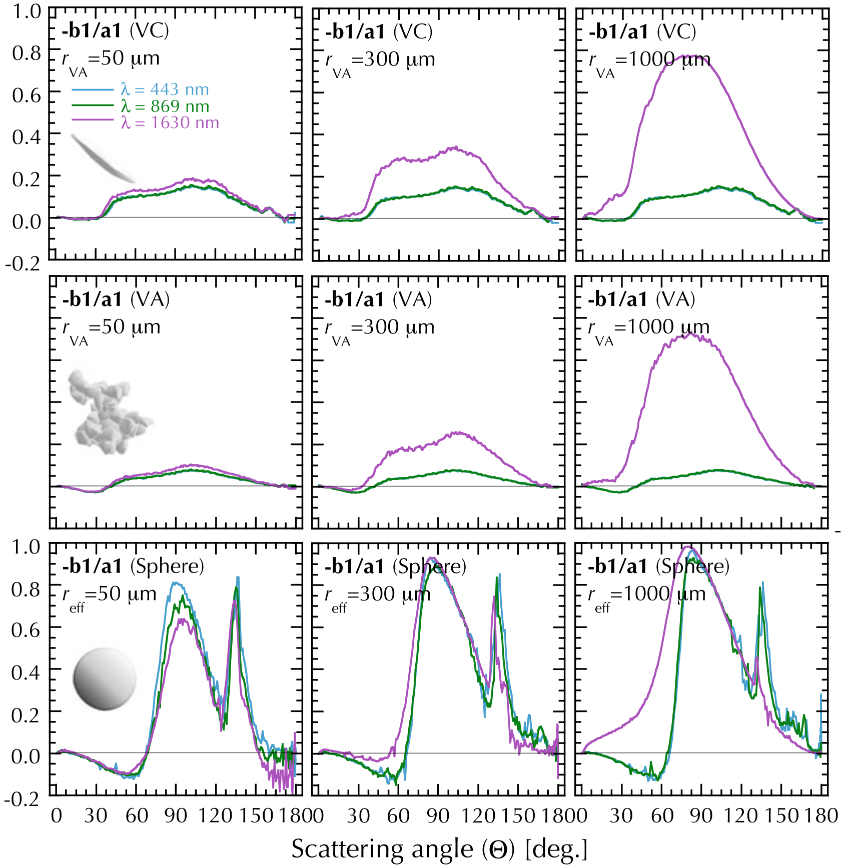

Fig. 9 The ratio $-b_1(\Theta)/a_1(\Theta)$ of the elements of normalized Stokes scattering matrix for the various snow grain sizes and shapes: Voronoi column (VC), Voronoi aggregate (VA) and spherical particles, respectively. r_{VA} is the effective snow grain radius of Voronoi particles defined as radius of sphere that has an equal volume/area ratio (Grenfell and Warren 1999), and r_{eff} is the effective radius of spherical particles. For the Voronoi particles, the ratios at $\lambda = 0.443$ and 0.869 μm are almost the same

Brewster angle. Under the measurement condition of $\theta_0 = 53° - 54°$, the viewing angle $\theta_v = 40° - 60°$ along the principal plane was approximately equal to the angle of reflection, where there is a large specular component in the reflected light. Also, near Brewster's angle the specularly reflected light is strongly horizontally polarized. Thus, the high DoLP was mainly a result of specular reflection at $\theta_0 \sim \theta_B$. At other angles away from Brewster's angle, where the specular reflection was smaller, there was much less linear polarization of the reflected light. The reason is that the reflected light mainly consists of the volume scattering component which is largely unpolarized. However, surface reflection is essentially independent of wavelength, while the volume component is reduced at longer wavelength due to increased light absorption by the ice, implying that a noticeable polarization can be measured at $\lambda = 1.63$ μm even at angles away from Brewster's angle. We note that the viewing angle corresponding to the maximum DoLP was different between the two wavelengths ($\lambda = 0.443$ and 0.869 μm) and $\lambda = 1.63$ μm. This might be due to the surface roughness in the bare ice surface (Fig. 1d). If the bare ice surface was to be perfectly smooth, one would expect to measure high DoLP values at almost the same viewing angle at $\lambda = 0.443$ and 0.869 μm.

4.5.2 P_q and P_u

Snow surface. We focus on the angular dependence of P_q and P_u for light reflected from a snow surface (Figs. 6 and 7). By definition, both values were measured to be in the range below the DoLP. So, P_q and P_u were close to zero at $\lambda = 0.443$ and 0.869 μm but they showed a remarkable dependence on the viewing geometry. P_q had positive values in the forward direction and then the sign was inverted from the side to the backward directions, and P_q exhibited zero and negative values except for some angles. In contrast, P_u was almost zero in the principal plane, had negative values in the forward direction except for the principal plane, and had positive values in the backward direction. The neutral points ($P_q = 0$ and $P_u = 0$) were continuously observed. For P_q, neutral points were observed in the forward and backward directions, while for P_u, neutral points were observed in the backward direction. An even more interesting result is that the signs and neutral points of P_q and P_u are almost independent of viewing geometry especially for NIR and SWIR wavelengths, though they are not completely the same positions. This result can be seen in both snow surface measurements of the decomposing and fragmented precipitation particle and melt form: the snow conditions have little effect on the position of the signs and the neutral points. This circumstance would be indicative of a universal property of the polarization. These measurements represent the first known confirmation of these unique snow polarization features.

We now examine the position of the signs and the neutral points of P_q and P_u for the snow case. First, we consider the wavelength of $\lambda = 1.63$ μm using a same approach as for the DoLP. If the single scattering in the surface layer is assumed to be dominant, then P_q and P_u can be represented from $\mathbf{I}_1$ (Eq. 9) as follows:

$$P_q = -\cos 2\sigma_2 \cdot b_1(\Theta)/a_1(\Theta), \tag{11}$$

$$P_u = -\sin 2\sigma_2 \cdot b_1(\Theta)/a_1(\Theta), \tag{12}$$

where b_1/a_1 is again the ratio of elements of the normalized scattering matrix. Thus, the signs and the neutral points of each P_q and P_u would be determined by Eqs. (11) and (12). From this equation, the neutral points in P_q ($P_q = 0$) can be seen to require a measurement angle corresponding to the following condition: (i) principal plane ($\phi_v - \phi_0 = 0$): $\sigma_2 = 0$ or π (see Fig. 13), so $\cos 2\sigma_2 = 1$, implying that the measurement angle must satisfy $-b_1(\Theta)/a_1(\Theta) = 0$, and (ii) the others ($\phi_v - \phi_0 \neq 0$):

$\cos 2\sigma_2 = 0$ regardless of $-b_1(\Theta)/a_1(\Theta)$. An important point here is that the neutral point is independent to the snow grain size and shape. For $P_u = 0$, the following condition is required: (i) principal plane ($\phi_v - \phi_0 = 0$): $\sigma_2 = 0$ or π, so $\sin 2\sigma_2 = 0$, implying that P_u would be everywhere zero in the principal plane, and (ii) the others ($\phi_v - \phi_0 \neq 0$): $\sin 2\sigma_2 = 0$ regardless of $-b_1(\Theta)/a_1(\Theta)$. The neutral point in P_u is also independent of the snow grain size and shape.

Figures 6d and 7d show polar contour plots of P_q and P_u and calculated neutral points at $\lambda = 1.63$ μnm. Each neutral point is seen to be consistent with the measured one. Also, each sign of P_q and P_u was consistent with the measured one, respectively, under the following condition: $P_q > 0$ ($P_u > 0$) for positive sign and $P_q < 0$ ($P_u < 0$) for negative sign in Eqs. (11) and (12). It is concluded that in the SWIR regions where the single scattering at the surface is dominant, the signs of P_q and P_u and the neutral points can be determined from the measurement geometric conditions irrespective of the snow grain size and the shape.

On the other hand, the angular dependence of P_q and P_u in the VIS and NIR regions was weak, but not cancelled completely. A weak dependence on the viewing geometry was still confirmed. This reason could be that the contribution to the reflected radiation of the surface scattering is higher than that of the volume scattering. But, the signs and neutral points of P_q and P_u did not completely match in all three wavelengths. For example, there exists a slight difference of the neutral points among them. Comparing to the neutral points at $\lambda = 1.63$ μm, the neutral points for P_q at other two wavelengths seemed to be shifted forward, while the neutral points for P_u seemed to be broad in the backward direction. This difference may be related to the scattering properties at each wavelength. Because scattering by larger particles such as snow is characterized by strong forward scattering with a diffraction in the forward direction, and because the multiple (volume) scattering component is increased at shorter wavelength such as VIS, the scattered light penetrates in the forward direction, resulting in the difference among all three wavelengths. This could be the reason why the calculated neutral points based on the single scattering were not consistent with the measured ones in the VIS and NIR regions. According to radiative transfer calculations in the atmosphere-ocean system, the position of the neutral points indicated the difference in atmospheric conditions due to multiple scattering (Takashima and Masuda 1985). Thus, we conjecture that the snow layer structure and the atmospheric condition are related to the position of the signs and the neutral points. The effects of the snow and the atmospheric condition on the polarization features are briefly discussed in the Sect. 4.6.

Bare ice surface. We next investigate the P_q and P_u for the bare ice surface (Fig. 8). The angular dependence on the signs of P_q were mostly the same as for the snow case: P_q had positive values in the forward direction and then the sign was inverted from the side to the backward directions, and P_q exhibited zero and negative values except for some angles. But, the P_q in the forward direction was high in all three wavelengths comparing to the snow. In contrast, P_u was almost zero in the principal plane, and had positive values in the forward direction at $\lambda = 0.443$ μm and in the backward direction at $\lambda = 0.869$ and 1.63 μm. The neutral points each were continuously observed. But, the positions of the neutral points of P_q and P_u were different between the bare ice and snow except for those at $\lambda = 1.63$ µm.

The position in the signs and the neutral points at $\lambda = 1.63$ µm are examined using the same approach as for the snow case. In the SWIR regions, the scattering process will also dominate reflection at the bare ice surface. However, the surface condition is different between the snow and the bare ice because the bare ice is not an aggregate of ice particles but a smooth surface. So, we applied a Fresnel reflection matrix **R** instead of the scattering matrix **F** in the simple scattering calculations. If $r_\parallel$ and $r_\perp$ are Fresnel reflection coefficients due to the change in refractive index n at the air-ice interface, P_q and P_u would be expected as follows:

$$P_q = -\cos 2\sigma_2 \cdot (r_\parallel r_\parallel^* - r_\perp r_\perp^*)/(r_\parallel r_\parallel^* + r_\perp r_\perp^*), \tag{13}$$

$$P_u = -\sin 2\sigma_2 \cdot (r_\parallel r_\parallel^* - r_\perp r_\perp^*)/(r_\parallel r_\parallel^* + r_\perp r_\perp^*), \tag{14}$$

where

$$r_\parallel = \frac{n\cos\theta_0 - \cos\theta_t}{n\cos\theta_0 + \cos\theta_t}, \tag{15}$$

$$r_\perp = \frac{\cos\theta_0 - n\cos\theta_t}{\cos\theta_0 + n\cos\theta_t}, \tag{16}$$

and θ_0 is connected with θ_t by Snell's law: $\sin\theta_0 = n\sin\theta_t$ where θ_t is the refraction angle in the bare ice. From these equations, each neutral point, for example, can be seen in the measurement angle corresponding to the angle under the condition of $P_q = 0$ and $P_u = 0$ in Eqs. (13) and (14), respectively.

Figure 8d depicts polar contour plots of P_q and P_u and measured and calculated neutral points at $\lambda = 1.63$ µm. The calculated neutral points were roughly consistent with the measured ones. However, there was a difference in the backscattering regions ($\Theta > 150°$). This could be due to the contribution of the surface roughness in the bare ice. In this calculation, the Fresnel reflection matrix **R** in which the surface is an idealized surface that is perfectly smooth, was employed. However, the bare ice surface was not perfectly smooth as shown in Fig. 1d. As a result, a moderate polarization was observed in the backscattering regions, showing a difference between the calculations and the measurements.

In the VIS and NIR regions, a weak angular dependence was observed in P_q (except for the forward direction) and P_u. In the forward direction in P_q, the surface reflection did contribute. Since the surface reflection is essentially independent of wavelength, the angular dependence can be seen commonly for all three wavelengths. At other angles except for the forward direction, multiple (volume) scattering would be dominated. The existence of air bubbles and brine pockets in the sea ice gives rise to changes in DoLP (Sun et al. 2013). Regarding the neutral points, they did not completely match calculated ones based on the surface scattering process. From Fig. 8a–c, the observed neutral points in P_q were shifted to the forward direction and there is a difference of the neutral points between calculations and measurements.

In addition, the neutral points in P_u were quite different at different wavelengths. Although the reason for the difference is not clear at this moment, this difference could be related to the multiple (volume) scattering, the surface roughness and the illumination conditions that determine the polarization magnitude and the plane of the polarization. Regarding the neutral points in P_u, there is a possibility that these differences are due to the measurement uncertainty since the magnitude of the P_u is rather small at $\lambda = 0.443$ and 0.869 μm. It is desirable to clarify the reason through a quantitative analysis using a radiative transfer model of atmosphere-snow/ice system.

4.6 Atmosphere Effects on the Polarization Properties of Snow Surface by Use of the Radiative Transfer Model

In the previous section, the calculated neutral points based on the simple scattering theory were not consistent with the measured ones in the VIS and NIR regions. This result suggests that the snow and the atmospheric conditions related to the multiple scattering concern the position of the signs and the neutral points. This section discusses the effect of the snow and the atmospheric conditions on the spectral polarization properties of snow surface by use of the radiative transfer model.

A multiple-scattering radiative transfer model for the atmosphere-snow/ice system was used for calculating the angular distribution of polarization properties of snow surface. This model is based on the doubling and adding method for the multiple scattering with the polarization in the the atmosphere-ocean system (Masuda and Takashima 1988) and is extended to the atmosphere-snow/ice system. Single scattering properties of snow particles were computed from a ray-tracing technique based on a geometrical-optics approximation (Masuda et al. 2012; Yang and Liou 1998). Snow grain shapes were assumed to be Voronoi column and aggregate particles (Fig. 9) which were numerically determined by extraction of the X-ray micro-CT data of snow samples (Ishimoto et al. 2018, 2010) and were validated with ground-based optical measurement (Tanikawa et al. 2020). For the atmospheric model, a standard mid-latitude winter model (Hess et al. 1998) was adopted. Atmospheric transmittance due to gaseous absorption was calculated for water vapor, carbon dioxide, oxygen and ozone. In addition, we used OPAC continental average aerosol model (Hess et al. 1998) and set the aerosol vertical distribution from 0 to 2 km in this model. The effect of snow depth and atmosphere on the spectral P_q and P_u was examined for three cases: (i) snow optical thickness $\tau_s = 0.01$ (very thin case), (ii) $\tau_s = 5000$ (semi-infinite snow depth) and (iii) Atmosphere over the semi-infinite snow layer. The snow layer was assumed to be homogeneous and the underlying surface albedo was assumed to be zero. The effective snow grain radius of $r_{\text{eff}} = 1000$ μm was used. The database of wavelength dependent refractive indices of ice were used in the calculation (Warren and Brandt 2008).

Figure 10 depicts polar contour plots of simulated P_q and P_u at $\lambda = 0.443$, 0.869 and 1.63 μm for three test cases. At first, when (i) $\tau_s = 0.01$, there were no significant

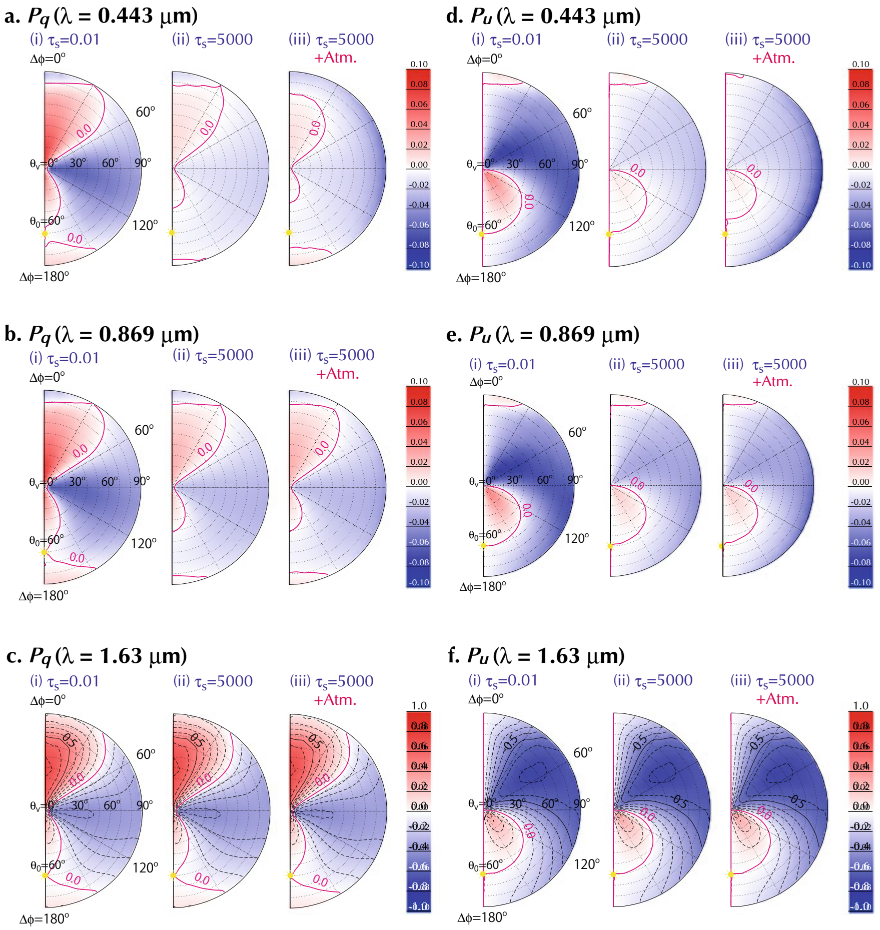

Fig. 10 Polar contour plots of simulated P_q and P_u at three selected SGLI channels for three test cases: (i) $\tau_s = 0.01$, (ii) $\tau_s = 5000$, and (iii) atmosphere over the snow (τ_s = 5000+Atm.). $\theta_0 = 60°$. The red solid lines in the P_q and P_u indicate the neutral points. Contour interval for P_q and P_u values is 0.1

differences of the angular distribution of signs and neutral points in P_q and P_u among three wavelengths. Since the optical thickness of snow is sufficiently thin and the underlying surface albedo is set to be zero, these results were attributed to the surface scattering component in the reflected light for each wavelength. Based on the results, the effects of the snow depth and the existence of atmosphere concerning to the multiple scattering are examined. Results at $\lambda = 1.63$ μm showed that the positions of the sign and the neutral point of P_q and P_u did not change in any case regardless of the snow and the atmosphere, and they were equal to the case (i) where the optical thickness is sufficiently thin ($\tau_s = 0.01$). As has been described in the previous section, the main reason is that the single scattering at the surface is dominant and the diffuse sky light due to Rayleigh scattering becomes negligibly small in the SWIR regions.

In contrast, the values of P_q and P_u at $\lambda = 0.443$ µm in the VIS regions decreased and the positions of the neutral point moved as the snow optical thickness increased in the case (ii). Relatively weak light absorption by the ice in the VIS regions results in the increase of the multiple scattering by ice particles, and hence the decrease in P_q and P_u, and the change in the position of the neutral point. When the atmosphere was present over the snow surface in the case (iii), some of the signs in P_q and P_u changed and the positions of the neutral point moved further. Moreover, negative values in P_q and P_u increased.[2] This is due principally to the multiple reflections between the atmosphere and the snow surface because of downward multiple Rayleigh scattering in the atmosphere.

The effects of the snow and atmosphere on P_q and P_u at $\lambda = 0.869$ µm were approximately between $\lambda = 0.443$ µm and $\lambda = 1.63$ µm. Since the light absorption by ice is relatively stronger (weaker) than that at $\lambda = 0.443$ µm (1.63 µm) and the downward diffuse radiation is lower (larger) than that at $\lambda = 0.443$ µm (1.63 µm), the effects of the snow and atmosphere is considered to be between $\lambda = 0.443$ µm and $\lambda = 1.63$ µm. These features on P_q, P_u and neutral point do not vary even if the solar zenith angle is changed and the atmospheric aerosol is considered (not shown in this review). The neutral points in P_q and P_u in the VIS and NIR regions are attributed to the multiple scattering by snow particles and multiple reflections between the atmosphere and the snow surface.

Based on the simulation results described above, comparisons between measured P_q and P_u and simulated ones using the radiative transfer model were made. Figure 11 presents an example of measured P_q and P_u for the melt forms on February 14, 2020 (same as Fig. 7) and theoretically calculated ones by the radiative transfer model for the atmosphere-snow/ice system. Snow grain size, density and layer structure required in the radiative transfer calculations were determined from the results of snow pit works (Tanikawa et al. 2021). For the atmospheric model, since analysis is confined to the Hokkaido in Japan, the standard mid-latitude winter model (Hess et al. 1998) was adopted. Continental average aerosol model (Hess et al. 1998) was used and aerosol optical thickness was set to be 0.3 at $\lambda = 0.5$ µm based on the atmospheric measurement (Tanikawa et al. 2021). The position of the neutral points calculated by the simple scattering theory (see Sect. 4.5.2) are also drawn in order to see the difference between single scattering effect and multiple scattering one. The calculated results show the differences between two neutral points, which can be clearly seen at $\lambda = 0.443$ µm and appears at any wavelengths even in $\lambda = 1.63$ µm. The simulated neutral points in P_q by the radiative transfer model shifted forward and those of P_u shrank. Both P_q and P_u simulated by the radiative transfer model were roughly consistent with the measured ones. These comparisons between the simulated neutral points and the measured ones indicate that the radiative transfer model

---

[2] The sign of P_u is reversed in the case at $\Delta\phi = 0° - 180°$ and $\Delta\phi = 180° - 360°$ so that the positive values in P_u increased at $\Delta\phi = 180° - 360°$ (not shown in this review).

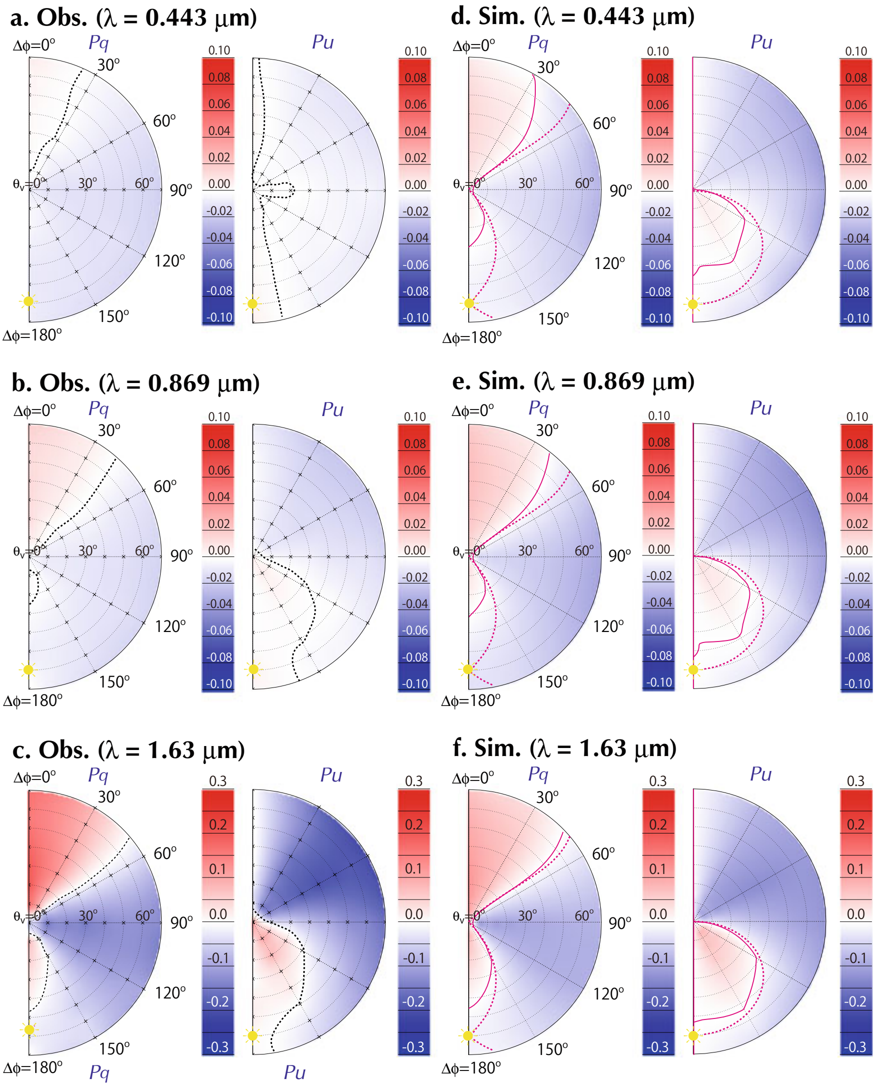

Fig. 11 Polar contour plots of measured P_q and P_u (**a**–**c**) and theoretically calculated ones by the radiative transfer model for the atmosphere-snow/ice system (**d**–**f**) at three selected SGLI channels. Measurements data are for the melt forms on February 14, 2020 (Fig. 7). The black dash lines (**a**–**c**) in the P_q and P_u indicate the measured neutral points. The red dash and solid lines (**d**–**f**) indicate simulated ones by the simple scattering theory (see Sect. 4.5.2) and the radiative transfer model, respectively

for the atmosphere-snow/ice system simulates the measurement of polarization features better than the simple scattering theory. It was confirmed that the neutral points in VIS regions result from the multiple scattering by snow particles and multiple reflections between the atmosphere and the snow surface.

4.7 Possibility of the Use of Polarization Information for the Remote Sensing

In this section we finally discuss the possibility of using polarization-information to retrieve snow grain size from remote sensing measurements. As already shown in Fig. 4, the largest effect of snow grain size is seen in the NIR and SWIR where the DoLP at $\lambda = 1.6$ µm may fall from 0.8 to 0.2 between the snow grain size $r_2 = 50$ µm and 1000 µm. Figure 12a shows the nadir reflectance versus measured snow grain size (r_2) for three selected wavelengths that are typical and useful ones for airborne/satellite remote sensing of snow grain size (Tanikawa et al. 2002; Stamnes et al. 2007; Lyapustin et al. 2009; Mary et al. 2013). It is clear from this figure that the nadir reflectance at these wavelengths decreases as the grain size increases. This feature is similar to that of the off-nadir reflectance. The wavelength dependence can be seen in the decrease of the nadir reflectance as the grain size increases. The largest effect of grain size is seen at $\lambda = 1.24$ µm where the nadir reflectance at $\lambda = 1.24$ µm is moderately decreased as the grain size increases. By comparison, the reduction of the nadir reflectance at $\lambda = 1.64$ µm is rapid for $r_2 < 300$ µm whereas the reflectance for the larger grain radii $r_2 > 300$ µm almost does not change . This result provides a plausible reason why the satellite-derived snow surface grain size is underestimated as a whole when employing the channel at $\lambda = 1.64$ µm. The underestimation of satellite-retrieved grain sizes have been reported (Aoki et al. 2007; Fily et al. 1997; Kay et al. 2003). As an important finding here, we note another and essential possible reason for the underestimation of the larger grain size; the sensitivity to the larger grain size is too small because of the strong light absorption by the ice. This finding implies that the channel at $\lambda = 1.64$ µm is not suitable for retrieval of large snow grains. From the previous results (Tanikawa et al. 2006b; Kuchiki et al. 2009), we infer that microstructures on the snow crystal surface has a significant impact on the reflected light at $\lambda = 1.64$ µm. Therefore, one should note that the reflectance (or reflected radiance) at $\lambda = 1.64$ µm can be used for remote sensing of small snow grains in the surface snow layer.

Figure 12b shows the measured DoLP$_q$ ($\theta_v = 55°$ and $\Delta\phi = 0°$) versus the snow grain size measured at the snow pit works. In contrast to the reflectance shown in Fig. 12a, the DoLP$_q$ at $\lambda = 1.64$ µm gradually increases with increasing snow grain size up to $r_2 \sim 1000$ µm while the increase of the DoLP$_q$ with increasing snow grain size at $\lambda = 0.86$ µm is much weaker. The DoLP$_q$ at $\lambda = 1.24$ µm is also sensitive to the snow grain size but the DoLP$_q$ sensitivity is somewhat smaller than that of the reflectance. It is evident from Fig. 12b that the DoLP$_q$ at $\lambda = 1.64$ µm implies the

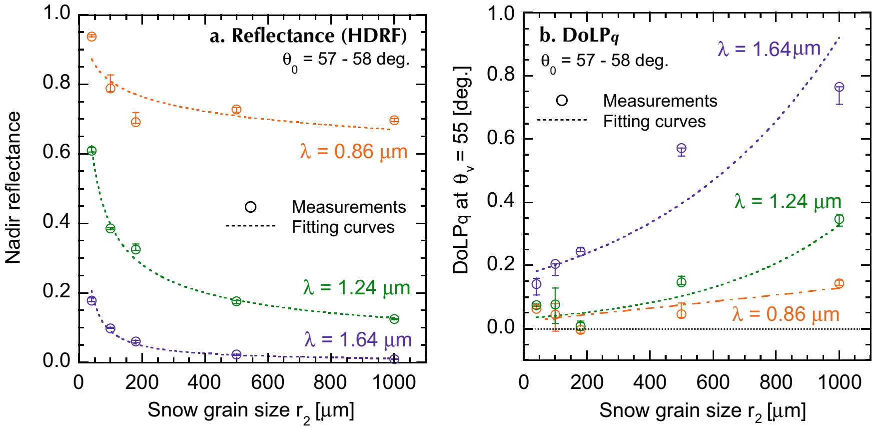

Fig. 12 **a** Nadir reflectance (HDRF at $\theta_v = 0°$) and **b** DoLP$_q$ ($\theta_v = 55°$) versus measured snow grain size for three selected wavelengths. The error bar for each plot shows the maximum and minimum values of HDRF within $|\theta_v| \leq 5°$ and DoLP$_q$ at $50° \leq \theta_v \leq 60°$, respectively. The dashed lines are the result of a fit to the reflectance and DoLP$_q$ by the exponential function, respectively. The dot-and-dash line is the result by the linear function due to the negative value at $\lambda = 0.86$ µm

possibility of snow grain size retrievals especially for the large grains. Therefore, if polarization data at $\lambda = 1.64$ µm were available, they could be used for retrieval of snow grain size at the surface snow, and also help improve the accuracy of snow grain size retrievals based on intensity-only measurements. Especially it will be effective for data obtained at larger viewing angle $\theta_v > \theta_B$.

In addition, as a polarimetric remote sensing, it may be possible to retrieve information on the snow particle shape. The DoLP depends on the snow particle size and shape (Leroux et al. 1998, 1999). In fact, attempts have been made to estimate snow grain size, snow particle shape, asymmetry factor of snow grains from polarimetric measurements (Ottaviani et al. 2015). Furthermore, a specific wetness effect was investigated and there is a difference in the DoLP between wet and dry snow (Peltoniemi et al. 2009). This makes it possible to retrieve liquid water content in snow from the polarimetric remote sensing with specific channels and multi-angle measurements. Focusing on the atmosphere, application of snow/cloud discrimination by polarimetric measurements was proposed (Goloub et al. 1992). The usefulness of polarimetric measurements to separate surface and atmospheric contributions of remote sensing data was investigated (Ottaviani et al. 2012). Though limited information have been reported on the potential of the polarimetric remote sensing, useful knowledge about the polarimetric remote sensing is now emerging and being gradually established.

5 Conclusion and Closing Remarks

Spectral properties of light polarization reflected from snow and ice surfaces based on the spectral measurements and the radiative transfer model for atmosphere-snow/ice system were reviewed in this chapter. The spectral properties of P_q and P_u that make up DoLP were considered in this review. The neutral points of P_q and P_u in snow and ice surfaces that revealed from recent studies were introduced. The spectral properties of polarization of light reflected from snow and ice surfaces have not been completely explained yet, compared to non-polarized information (e.g. spectral reflectance and albedo). Especially, spectral properties of light polarization for the bare ice, including sea ice and glacier ice, are very limited. Therefore, further measurements for different snow/ice types as well as additional surface features are needed to enhance our understanding of light scattering properties.

The development of the radiation transfer model with account for the light polarization is important for the quantitative interpretation of optical properties of snow and ice. For example, the optical properties of non-spherical particles in snow have been investigated based on the spectral albedo and BRDF, i.e. non-polarized information. In other words, it has not yet been done based on the polarization which is sensitive to the snow grain shape. Consequently, highly accurate radiative transfer models are needed and more detailed spectral measurements including the polarization would be useful for improvement and validation of the radiative transfer models of atmosphere-snow/ice systems. The radiative transfer model would be helpful for indicating the possibility of snow parameter retrievals and for the practical application to the polarimetric remote sensing of the snow surface.

The challenge for the future is to extract quantitative information regarding snow and ice physical parameters from polarimetric measurement data. The SGLI is an imaging sensor onboard GCOM-C satellite, having two polarization channels at $\lambda = 0.674$ and $0.869\ \mu\text{m}$. Though the measured polarization features were weak at these channels, the neutral points were detectable based on the measurements of the plane of polarization position. The polarimetric measurements are expected to be useful for the retrieval of new snow and ice physical parameters and help improve the accuracy of snow retrievals based on the intensity-only measurements.

Acknowledgements This review mainly summarized the results of field measurements during intensive field campaigns at Hokkaido, Japan and at northwest Greenland ice sheet. I would like to thank T. Aoki, M. Hori, A. Hachikubo, M. Niwano, K. Sugiura, S. Matoba, T. Toyota and N. Ohkawara for supporting field measurements during field campaigns, K. Masuda, H. Ishimoto and K. Stamnes for the development and implementation of the radiative transfer model in the coupled atmosphere-snow/ice system and T. Yamasaki, S. Tomioka and K. Fukuhara for their dedicated logistic support. These works were conducted as part of the Experimental Research Fund for Global Environment Conservation, the Ministry of the Environment of Japan, Grant Number MLIT1753, the Japan Society for the Promotion of Science, Grants-in-Aid for Scientific Research, Grant Number 16H01772, 17K00534, 18H03363, 20K12142 and 20H00206, the GCOM-C research project of Japan Aerospace Exploration Agency (JAXA), and the Arctic Challenge for Sustainability II (ArCS II), Grant Number JPMXD 1420318865.

Appendix 1: The Phase and Scattering Matrices

The phase matrix **M** can be calculated with the scattering matrix **F** and two rotation matrices **L**:

$$\begin{aligned}
\mathbf{M}(\Theta,\sigma_1,\sigma_2) &= \mathbf{L}(-\sigma_2)\mathbf{F}(\Theta)\mathbf{L}(\pi-\sigma_1) \\
&= \begin{bmatrix} 1 & 0 & 0 & 0 \\ 0 & \cos 2\sigma_2 & \sin 2\sigma_2 & 0 \\ 0 & -\sin 2\sigma_2 & \cos 2\sigma_2 & 0 \\ 0 & 0 & 0 & 1 \end{bmatrix} \\
&\times \begin{bmatrix} a_1(\Theta) & b_1(\Theta) & 0 & 0 \\ b_1(\Theta) & a_2(\Theta) & 0 & 0 \\ 0 & 0 & a_3(\Theta) & b_2(\Theta) \\ 0 & 0 & -b_2(\Theta) & a_4(\Theta) \end{bmatrix} \\
&\times \begin{bmatrix} 1 & 0 & 0 & 0 \\ 0 & \cos 2\sigma_1 & \sin 2\sigma_1 & 0 \\ 0 & -\sin 2\sigma_1 & \cos 2\sigma_1 & 0 \\ 0 & 0 & 0 & 1 \end{bmatrix}
\end{aligned} \tag{17}$$

where a_i $(i = 1, 2, 3, 4)$ and b_i $(i = 1, 2)$ are elements of normalized scattering matrix, Θ is the scattering angle between incident and scattering angles and σ_1 and σ_2 are angles of rotation that can be calculated from the measurement geometries θ_0, θ_v, ϕ_0 and ϕ_v using spherical trigonometry (Mishchenko et al. 2006):

$$\cos\Theta = -\cos\theta_v\cos\theta_0 + \sin\theta_v\sin\theta_0\cos(\phi_v-\phi_0), \tag{18}$$

$$\cos\sigma_1 = \frac{\cos\theta_v + \cos\theta_0\cos\Theta}{\sin\theta_0\sin\Theta}, \tag{19}$$

$$\cos\sigma_2 = -\frac{\cos\theta_0 + \cos\theta_v\cos\Theta}{\sin\theta_v\sin\Theta}. \tag{20}$$

The angles of σ_1 and σ_2 are illustrated in Fig. 13.

Fig. 13 Illustration of the relationship between the phase and scattering matrices. This illustration is the same as Fig. 11.3.1 (a) in Mishchenko et al. (2006). $\hat{\mathbf{n}}^{\mathrm{inc}}$ and $\hat{\mathbf{n}}^{\mathrm{sca}}$ are the direction of incident and scattering waves

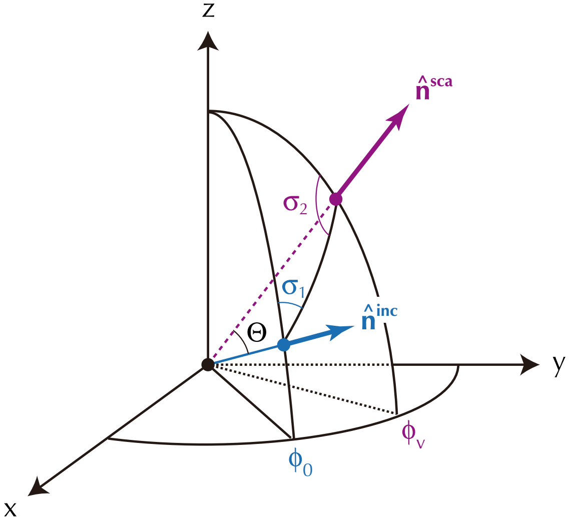

References

Aoki T, Aoki T, Fukabori M, Hachikubo A, Tachibana Y, Nishio F (2000) Effects of snow physical parameters on spectral albedo and bi-directional reflectance of snow surface. J Geophys Res 105(D8):10219–10236. https://doi.org/10.1029/1999JD901122

Aoki T, Hori M, Motoyohi H, Tanikawa T, Hachikubo A, Sugiura K, Yasunari TJ, Storvold R, Eide HA, Stamnes K, Li W, Nieke J, Nakajima Y, Takahashi F (2007) ADEOS-II/GLI snow/ice products: part II - validation results using GLI and MODIS data. Remote Sens Environ 111:274–290. https://doi.org/10.1016/j.rse.2007.02.035

Aoki T, Matoba S, Yamaguchi S, Tanikawa T, Niwano M, Kuchiki K, Adachi K, Uetake J, Motoyama H, Hori M (2014) Light-absorbing snow impurity concentrations measured on northwest Greenland ice sheet in 2011 and 2012. Bull Glaciol Res 32:21–31. https://doi.org/10.5331/bgr.32.21

Armstrong RL, Brodzik MJ (2001) Recent northern hemisphere snow extent: a comparison of data derived from visible and microwave satellite sensors. Geophys Res Lett 28:3673–3676. https://doi.org/10.1029/2000GL012556

Bourgeois CS, Calanca P, Ohmura A (2006) A field study of the hemispherical directional reflectance factor and spectral albedo of dry snow. J Geophys Res 111(D20):2. https://doi.org/10.1029/2006JD007296

Box JE, Fettweis X, Stroeve JC, Tedesco M, Hall DK, Steffen K (2012) Greenland ice sheet albedo feedback: thermodynamics and atmospheric drivers. Cryosphere 6:821–839. https://doi.org/10.5194/tc-6-821-2012

Bréon FM, Goloub P (1998) Cloud droplet effective radius from spaceborne polarization measurements. Geophys Res Lett 25:1879–1882. https://doi.org/10.1029/98GL01221

Brown RD, Derksen C, Wang L (2010) Amulti-data set analysis of variability and changes in arctic spring SNWO cover extent, 1967–2008. J Geophys Res 115:D16111. https://doi.org/10.1029/2010JD013975

Cairns B, Russell EE, LaVeigne JD, Tennant PMW (2003) Research scanning polarimeter and airborne usage for remote sensing of aerosols. In: Proceedings of SPIE, vol 5158. Polarization science and remote sensing. https://doi.org/10.1117/12.518320

Chen N, Li W, Fan Y, Zhou Y, Aoki T, Tanikawa T, Niwano M, Hori M, Shimada R, Matoba S, Stamnes K (2021) Snow parameter retrieval (SPR) algorithm for GCOM-C/SGLI. Remote Sens Environ (under review)

Deschamps P, Breon F, Leroy M, Podaire A, Bricaud A, Buriez J, Seze G (1994) The polder mission: instrument characteristics and scientific objectives. IEEE Trans Geosci Remote Sens 32(3):598–615. https://doi.org/10.1109/36.297978

Deuzé JL, Goloub P, Herman M, Marchand A, Perry G, Susana S, Tanre D (2000) Estimate of the aerosol properties over the ocean with POLDER. J Geophys Res 105:15329–15346. https://doi.org/10.1029/2000JD900148

Dominé F, Salvatori R, Legagneux L, Salzano R, Fily M, Casacchia R (2006) Correlation between the specific surface area and the short wave infrared (swir) reflectance of snow. Cold Regions Sci Technol 46:60–68. https://doi.org/10.1016/j.coldregions.2006.06.002

Fierz C, Armstrong RL, Durand Y, Etchevers P, Greene E, McClung DM, Nishimura K, Satyawali PK, Sokratov SA (2009) The international classification for seasonal snow on the ground. Technical report, IHP-VII Technical Documents in Hydrology No. 83, IACS Contribution No.1, UNESCO-IHP, Paris, 90pp

Fily M, Bourdelles B, Dedieu JP, Sergent C (1997) Comparison of in situ and Landsat Thematic Mapper derived snow grain characteristics in the alps. Remote Sens Environ 59:452–460. https://doi.org/10.1016/S0034-4257(96)00113-7

Goloub P, Herman M, Deuze JL (1992) Contrast between polarization properties of snow/ice and clouds. Antarct J Unit States 27:199–202

Grenfell TC, Warren SG (1999) Representation of a nonspherical ice particle by a collection of independent spheres for scattering and absorption of radiation. J Geophys Res 104(D24):31,697–31,709. https://doi.org/10.1029/1999JD900496

Hansen JE, Travis LD (1974) Light scattering in planetary atmosphere. Space Sci Rev 16:527–610. https://doi.org/10.1007/BF00168069

Hess M, Koepke P, Schult I (1998) Optical properties of aerosols and clouds: the software package OPAC. Bull Am Meteorol Soc 79:831–844

Hori M, Aoki T, Stamnes K, Li W (2007) ADEOS-II/GLI snow/ice products: part III - retrieved results. Remote Sens Environ 111:291–336. https://doi.org/10.1016/j.rse.2007.01.025

Hori M, Sugiura K, Kobayashi K, Aoki T, Tanikawa T, Kuchiki K, Niwano M, Enomoto H (2017) A 38-year (1978–2015) northern hemisphere daily snow cover extent product derived using consistent objective criteria from satellite-borne optical sensors. Remote Sens Environ 191:402–418. https://doi.org/10.1016/j.rse.2017.01.023

Hovenier JW, van der Mee CVM (1983) Fundamental relationships relevant to the transfer of polarized light in a scattering atmosphere. Astron & Astrophys 196:287–295

Hudson SR, Warren SG, Brandt RE, Grenfell TC, Six D (2006) Spectral bidirectional reflectance of Antarctic snow: measurements and parameterization. J Geophys Res 111:D18106. https://doi.org/10.1029/2006JD007290

Imaoka K, Kachi M, Fujii H, Murakami H, Hori M, Ono A, Igarashi T, Nakagawa K, Oki T, Honda Y, Shimoda H (2010) Global Change Observation Mission (GCOM) for monitoring carbon, water cycles, and climate change. Proc IEEE 98:717–734. https://doi.org/10.1109/JPROC.2009.2036869

IPCC (2019) Summary for policymakers. In: IPCC special report on the ocean and cryosphere in a changing climate. IPCC

Ishimoto H, Zaizen Y, Uchiyama A, Masuda K, Mano Y (2010) Shape modeling of mineral dust particles for light-scattering calculations using the spatial Poisson-Voronoi tessellation. J Quant Spectrosc & Radiat Transf 111:2434–2443. https://doi.org/10.1016/j.jqsrt.2010.06.018

Ishimoto H, Adachi S, Yamaguchi S, Tanikawa T, Aoki T, Masuda K (2018) Snow particles extracted from X-ray computed microtomography imagery and their single-scattering properties. J Quant Spectrosc & Radiat Transf 209:113–128. https://doi.org/10.1016/j.jqsrt.2018.01.021

Jin Z, Charlock TP, Yang P, Xie Y, Miller W (2008) Snow optical properties for different particle shapes with application to snow grain size retrieval and MODIS/CERES radiance comparison over Antarctica. Remote Sens Environ 112:3563–3581. https://doi.org/10.1016/j.rse.2008.04.011

Kay JE, Gillespie AR, Hansen GB, Pettit EC (2003) Spatial relationship between snow contaminant content, grain size, and surface temperature from multispectral images of Mt. Rainier, Washington (USA). Remote Sens Environ 86:216–231. https://doi.org/10.1016/S0034-4257(03)00102-0

Kokhanovsky A, Lamare M, Mauro BD, Picard G, Arnaud L, Dumont M, Tuzet F, Brockmann C, Box JE (2018) On the reflectance spectroscopy of snow. The Cryosphere 12:2371–2382. https://doi.org/10.5194/tc-12-2371-2018

Kuchiki K, Aoki T, Tanikawa T, Kodama Y (2009) Retrieval of snow physical parameters using a ground-based spectral radiometer. Appl Opt 48(29):5,567–5,582. https://doi.org/10.1364/AO.48.005567

Kuchiki K, Aoki T, Niwano M, Motoyoshi H, Iwabuchi H (2011) Effect of sastrugi on snow bidirectional reflectance and its application to MODIS data. J Geophys Res 116. https://doi.org/10.1029/2011JD016070

Leroux C, Deuzé J, Goloub P, Sergent C, Fily M (1998) Ground measurements of the polarized bidirectional reflectance of snow in the near-infrared spectral domain: Comparisons with model results. J Geophys Res 103(D16):19,721–19,731. https://doi.org/10.1029/98JD01146

Leroux C, Lenobel J, Brogniez G, Hovenier JW, Haan JFD (1999) A model for the bidirectional polarized reflectance of snow. J Quant Spectrosc & Radiat Transf 61(3):273–285

Li W, Stamnes K, Chen B (2001) Snow grain size retrieved from near-infrared radiances at multiple wavelengths. Geophys Res Lett 28(9):1,699–1,702. https://doi.org/10.1029/2000GL011641

Lv Y, Sun Z (2014) The reflectance and negative polarization of light scattered from snow surface with different grain size in backward direction. J Quant Spectrosc & Radiat Transf 113:472–481. https://doi.org/10.1016/j.jqsrt.2013.09.010

Lyapustin A, Tedesco M, Wang Y, Aoki T, Hori M, Kokhanovsky AA (2009) Retrieval of snow grain size over Greenland from MODIS. Remote Sens Environ 113:1976–1987. https://doi.org/10.1016/j.rse.2009.05.008

Marks A, Fragiacomo C, MacArthur A, Zibordi G, Fox N, King MD (2015) Characterisation of the HDRF (as a proxy for BRDF) of snow surfaces at Dome C, Antarctica, for the inter-calibration and inter-comparison of satellite optical data. Remote Sens Environ 158:407–416. https://doi.org/10.1016/j.rse.2014.11.013

Mary A, Dumont M, Dedieu JP, Durand Y, Sirguey P, Milhem H, Mestre O, Negi HS, Kokhanovsky AA, Lafaysse M, Morin S (2013) Intercomparison of retrieval algorithms for the specific surface area of snow from near-infrared satellite data in mountainous terrain, and comparison with the output of a semi-distributed snowpack model. The Cryosphere 7:741–761. https://doi.org/10.5194/tc-7-741-2013

Masuda K, Takashima T (1988) Dependence of the radiation just above and below the ocean surface on atmospheric and oceanic parameters. Appl Opt 27(23):4891–4898

Masuda K, Ishimoto H, Mano Y (2012) Efficient method of computing a geometric optics integral for light scattering by nonspherical particles. Pap Meteorol Geophys 63:15–19. https://doi.org/10.2467/mripapers.63.15

Mishchenko MI, Travis LD, Lacis AA (2002) Scattering, absorption, and emission of light by small particles. Cambridge University Press, Cambridge

Mishchenko MI, Travis LD, Lacis AA (2006) Multiple scattering of light by particles: radiative transfer and coherent backscattering. Cambridge University Press, Cambridge

National Snow & Ice Data Center, Rain at the Summit of Greenland (2021) https://nsidc.org/greenland--today/2021/08/rain--at--the--summit--of--greenland

Nghiem SV, Hall DK, Mote TL, Tedesco M, Albert MR, Keegan K, Shuman CA, DiGirolamo NE, Neumann G (2012) The extreme melt across the Greenland ice sheet in 2012. Geophys Res Lett 39:L20502. https://doi.org/10.1029/2012GL053611

Nolin AW, Dozier J (2000) A hyperspectral method for remotely sensing the grain size of snow. Remote Sens Environ 74:207–216. https://doi.org/10.1016/S0034-4257(00)00111-5

Nomura D, Wongpan P, Toyota T, Tanikawa T, Kawaguchi Y, Ono T, Ishino T, Tozawa M, Tamura TP, Yabe IS, Son EY, Vivier F, Lourenco A, Lebrun M, Nosaka Y, Hirawake T, Ooki A, Aoki S, Else B, Fripiat F, Inoue J, Vancoppenolle M (2020) Saroma-ko lagoon observations for sea ice physico-chemistry and ecosystems 2019 (SLOPE2019). Bull Glaciol Res 38:1–12. https://doi.org/10.5331/bgr.19R02

Ottaviani M, Cairns B, Ferrare R, Rogers R (2012) Iterative atmospheric correction scheme and the polarization color of alpine snow. J Quant Spectrosc & Radiat Transf 123:789–804. https://doi.org/10.1016/j.jqsrt.2012.03.014

Ottaviani M, van Diedenhoven B, Cairns B (2015) Photopolarimetric retrievals of snow properties. The Cryosphere 9:1933–1942. https://doi.org/10.5194/tc-9-1933-2015

Ozeki T, Akitaya E (1998) Energy balance and formation of sun crust in snow. Ann Glaciol 26:35–38

Painter TH, Dozier J (2004) Measurements of the hemispherical-directional reflectance of snow at fine spectral and angular resolution. J Geophys Res 109:D18115. https://doi.org/10.1029/2003JD004458

Painter TH, Dozier J, Roberts DA, Davis RE, Greene RO (2003) Retrieval of subpixel snow-covered area and grain size from imaging spectrometer. Remote Sens Environ 85:64–77. https://doi.org/10.1016/S0034-4257(02)00187-6

Peltoniemi J (2007) Spectropolarised ray-tracing simulations in densely packed particulate medium. J Quant Spectrosc & Radiat Transf 108(2):180–196. https://doi.org/10.1016/j.jqsrt.2007.05.009

Peltoniemi J, Kaasalainen S, Naranen J, Matikainen L, Piironen J (2005) Measurement of directional and spectral signatures of light reflectance by snow. IEEE Trans Geosci Remote Sens 43:2294–2304. https://doi.org/10.1109/TGRS.2005.855131

Peltoniemi J, Hakala T, Suomalainen J, Puttonen E (2009) Polarised bidirectional reflectance factor measurements from soil, stones, and snow. J Quant Spectrosc & Radiat Transf 110:1940–1953. https://doi.org/10.1016/j.jqsrt.2009.04.008

Perovich DK (1994) Light reflection from sea ice during the onset of melt. J Geophys Res 99(C2):3351–3359. https://doi.org/10.1029/93JC03397

Perovich DK (1998) Observation of the polarization of light reflected from sea ice. J Geophys Res 103(C3):5563–5575. https://doi.org/10.1029/97JC01615

Sandmeier SR, Itten KI (1999) A field goniometer system (FIGOS) for acquisition of hyperspectral BRDF data. IEEE Trans Geosci Remote Sens 37:978–986. https://doi.org/10.1109/LGRS.2012.2196753

Scambos T, Haran T, Fahnestock M, Painter TH, Bohlander J (2007) MODIS-based mosaic of Antarctica (MOA) data sets: continent-wide surface morphology and snow grain size. Remote Sens Environ 111(2–3):242–257. https://doi.org/10.1016/j.rse.2006.12.020

Shepherd A, Ivins ER, Geruo A, Barletta VR, Bentley MJ, Bettadpur S, Briggs KH, Bromwich DH, Forsberg R, Galin N, Horwath M, Jacobs S, Joughin I, King MA, Lenaerts JTM, Li J, Ligtenberg SRM, Luckman A, Luthcke SB, McMillan M, Meister R, Milne G, Mouginot J, Muir A, Nicolas JP, Paden J, Payne AJ, Pritchard H, Rignot E, Rott H, Sørensen LS, Scambos TA, Scheuchl B, Schrama EJO, Smith B, Sundal AV, van Angelen JH, van de Berg WJ, van den Broeke MR, Vaughan DG, Velicogna I, Wahr J, Whitehouse PL, Wingham DJ, Yi D, Young D, Zwally HJ (2012) A reconciled estimate of ice-sheet mass balance. Science 338(6111):1183–1189. https://doi.org/10.1126/science.1228102

Stamnes K, Stamnes J (eds) (2015) Radiative transfer in coupled environmental systems. Wiley-VCH

Stamnes K, Li W, Eide H, Aoki T, Hori M, Storvold R (2007) ADEOS-II/GLI snow/ice products: part I - scientific basis. Remote Sens Environ 111:258–273. https://doi.org/10.1016/j.rse.2007.03.023

Sun Z, Zhao Y (2011) The effects of grain size on bidirectional polarized reflectance factor measurements of snow. J Quant Spectrosc & Radiat Transf 112:2372–2383. https://doi.org/10.1016/j.jqsrt.2011.05.011

Sun Z, Zhang J, Zhao Y (2013) Laboratory studies of polarized light reflection from sea ice and lake ice in visible and near infrared. IEEE Geosci Remote Sens Lett 10(1):170–173. https://doi.org/10.1109/LGRS.2012.2196753

Suomalainen J, Hakala T, Peltoniemi J, Puttonen E (2009) Polarised multiangular reflectance measurements using the Finnish Geodetic Institute field gonio spectrometer. Sensors 9:3891–3907. https://doi.org/10.3390/s90503891

Takashima T, Masuda K (1985) Degree of radiance and polarization of the upwelling radiation from an atmosphere-ocean system. Appl Opt 24(15):2423–2429. https://doi.org/10.1364/AO.24.002423

Talmage DA, Curran PJ (1986) Remote sensing using partially polarized light. Int J Remote Sens 7:47–64. https://doi.org/10.1080/01431168608954660

Tanikawa T, Aoki T, Nishio F (2002) Remote sensing of snow grain size and snow impurities from Airborne Multispectral Scanner data using a snow bidirectional reflectance distribution function model. Ann Glaciol 34:74–80. https://doi.org/10.3189/172756402781817437

Tanikawa T, Aoki T, Hori M, Hachikubo A, Abe O, Aniya M (2006) Monte Carlo simulations of spectral albedo for artificial snowpacks composed of spherical and nonspherical particles. Appl Opt 45(21):5310–5319. https://doi.org/10.1364/AO.45.005310

Tanikawa T, Aoki T, Hori M, Hachikubo A, Aniya M (2006) Snow bidirectional reflectance model using non-spherical snow particles and its validation with field measurements. EARSeL eProceedings 5(2):137–145

Tanikawa T, Hori M, Aoki T, Hachikubo A, Kuchiki K, Niwano M, Matoba S, Yamaguchi S, Stamnes K (2014) In situ measurements of polarization properties of snow surface under the Brewster geometry in Hokkaido, Japan, and northwest Greenland ice sheet. J Geophys Res 119:13946–13964. https://doi.org/10.1002/2014JD022325

Tanikawa T, Kuchiki K, Aoki T, Ishimoto H, Hachikubo A, Niwano M, Hosaka M, Matoba S, Kodama Y, Iwata Y, Stamnes K (2020) Effects of snow grain shape and mixing state of snow impurity on retrieval of snow physical parameters from ground-based optical instrument. J Geophys Res 125:e2019JD031858. https://doi.org/10.1029/2019JD031858

Tanikawa T, Masuda K, Ishimoto H, Aoki T, Hori M, Niwano M, Hachikubo A, Matoba S, Sugiura K, Toyota T, Ohkawara N, Stamnes K (2021) Spectral degree of linear polarization and neutral points of polarization in snow and ice surfaces. J Quant Spectrosc & Radiat Transf 273:107845. https://doi.org/10.1016/j.jqsrt.2021.107

Warren SG, Wiscombe WJ (1980) A model for the spectral albedo of snow. II: snow containing atmospheric aerosols. J Atmos Sci 37(12):2735–2745. https://doi.org/10.1175/1520-0469(1980)037<2734:AMFTSA>2.0.CO;2

Warren SG, Brandt RE (2008) Optical constants of ice from the ultraviolet to the microwave: a revised compilation. J Geophys Res 113:D14220. https://doi.org/10.1029/2007JD009744

Wiebe H, Heygster G, Zege E, Aoki T, Hori M (2013) Snow grain size retrieval SGSP from optical satellite data: validation with ground measurements and detection of snow fall events. Remote Sens Environ 128(21):11–20. https://doi.org/10.1016/j.rse.2012.09.007

Wiscombe WJ, Warren SG (1980) A model for the spectral albedo of snow. I: pure snow. J Atmos Sci 37(12):2712–2733. https://doi.org/10.1175/1520-0469(1980)037<2712:AMFTSA>2.0.CO;2

Yang P, Liou KN (1998) Single-scattering properties of complex ice crystals in terrestrial atmosphere. Contrib Atmos Phys 71(2):223–248

Zege EP, Katsev IL, Malinka AV, Prikhach AS, Heygster G, Wiebe H (2011) Algorithm for retrieval of the effective snow grain size and pollution amount from satellite measurements. Remote Sens Environ 115(10):2674–2685. https://doi.org/10.1016/j.rse.2011.06.001

Light Scattering by Large Densely Packed Clusters of Particles

Yevgen Grynko, Yuriy Shkuratov, Samer Alhaddad, and Jens Förstner

Abstract We review our results of numerical simulations of light scattering from different systems of densely packed irregular particles. We consider spherical clusters, thick layers and monolayers with realistic topologies and dimensions much larger than the wavelength of light. The maximum bulk packing density of clusters is 0.5. A numerically exact solution of the electromagnetic problem is obtained using the Discontinuous Galerkin Time Domain method and with application of high- performance computing. We show that high packing density causes light localization in such structures which makes an impact on the opposition phenomena: backscattering intensity surge and negative linear polarization feature. Diffuse multiple scattering is significantly reduced in the case of non-absorbing particles and near-field interaction results in a percolation-like light transport determined by the topology of the medium. With this the negative polarization feature caused by single scattering gets enhanced if compared to lower density samples. We also confirm coherent double scattering mechanism of negative polarization for light scattered from dense absorbing slabs. In this case convergent result for the scattering angle polarization dependency at backscattering can be obtained for a layer of just a few tens of particles if they are larger than the wavelength.

1 Introduction

Light scattering in discrete disordered media is a multidisciplinary problem that is solved in different fields from optics and photonics to remote sensing and planetary science. This includes study of light transport in disordered photonic structures (Burgess et al. 2016), crystal powders for random lasers (Wiersma 2008; Jeong et al.

Y. Grynko (✉) · S. Alhaddad · J. Förstner
Department of Theoretical Electrical Engineering, Paderborn University, Warburger Str. 100, 33102 Paderborn, Germany
e-mail: yevgen.grynko@uni-paderborn.de

Y. Shkuratov
Institute of Astronomy of V.N. Karazin, Kharkiv National University, Sumska Str. 35, Kharkiv 61022, Ukraine

A. Kokhanovsky (ed.), *Springer Series in Light Scattering*, Springer Series in Light Scattering, https://doi.org/10.1007/978-3-031-10298-1_4

2018), and biological tissues (Jacques 2013) as well as light reflection from natural powder surfaces consisting of mineral particles like sands, soils, including planetary regoliths, and snow (Videen et al. 2004; Kokhanovsky and de Leeuw 2009; Mishchenko et al. 2010; Belskaya et al. 2019). The solution of the problem can be obtained with experimental and theoretical methods depending on the properties of the target media that can be categorized into sparse and dense types. In the first case, the free path length of light is much larger than the wavelength which approximately corresponds to the volume fraction of the material smaller than 0.1. Far-field scattering properties of individual scatterers and analytical radiative transfer approach can be applied in this case (e.g., Mishchenko et al. 2015). If particles are densely packed, e.g., in powders, the distances between them become smaller than the wavelength. In this case near-field interactions between the neighbors become important and complex transport phenomena like weak and strong (Anderson) localization (Aegerter and Maret 2009; Segev et al. 2013) may take place. The light scattering problem taking into account these effects in a dense random medium is not solved at present analytically. It can be handled, however, with numerical simulations and numerically exact methods.

We are interested in geophysical and planetary science optical remote sensing applications. In this field a problem of data retrieval from photopolarimetric and spectroscopic measurements is solved (e.g., Mishchenko et al. 2010; Nelson et al. 2018; Shkuratov et al. 2007a, b). The surfaces of the Solar System bodies such as the Moon, Mars, giant planet satellites, asteroids, and cometary nuclei are covered with debris material called regolith. It is formed by long-time meteoroid bombardment of primordial compositionally heterogeneous surfaces and consists of dust, broken rocks and glasses. Similarly, icy bodies in the Kuiper Belt objects as well as polar regions on Earth are covered with ice particles. Solar light scattered from such objects carries information and physical properties of the upper layer of their surfaces. Measuring intensity and linear polarization as functions of the scattering θ or phase angle α ($\alpha = \pi - \theta$) one can characterize them and extract the information about the complex refractive index of the material, particles size, packing density and the surface microrelief (e.g., Shkuratov et al. 2002; Videen et al. 2004; Shkuratov et al. 2004; Ovcharenko et al. 2006; Shkuratov et al. 2007a, b; Mishchenko et al. 2010; Kolokolova et al. 2015; Levasseur-Regourd et al. 2015; Nelson et al. 2018; Poch et al. 2018; Muinonen et al. 2015a, b). This method potentially can be applied for characterization of the surfaces of solid exoplanets with no substantial atmospheres if such polarimetric observations are realized (Wiktorowicz and Stam 2015).

Solar System objects are usually observed at relatively small phase angles and near opposition. In this range the so-called backscattering optical phenomena like intensity surge (IS) and negative polarization (NP) are characteristic for powder-like surfaces (Shkuratov et al. 2002; Levasseur-Regourd et al. 2015; Ovcharenko et al. 2006; Nelson et al. 2018). Examples of the IS and NP profiles for the Moon are shown in Fig. 1. In the first case this is an enhancement of intensity which can become strongly nonlinear. It is caused by shadowing, if constituent particles or aggregates of them are absorbing, and the coherent backscattering mechanism in the narrow

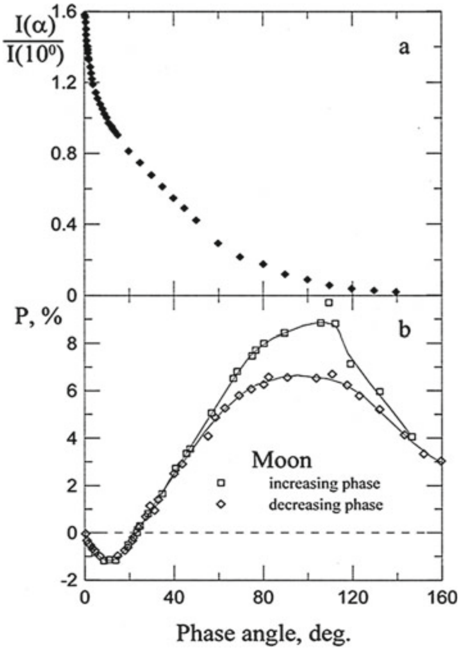

Fig. 1 **a** Phase-angle curves of normalized integral albedo and **b** linear polarization degree measured for Moon. The plots are adapted from Shkuratov et al. (2011) in which data by Lyot (1929) and Muinonen et al. (2002) were used

range of a few degrees near exact backscattering due to constructive interference of the counterpropagating waves (e.g., Shkuratov et al. 2011). The coherent component is also known as a weak localization of light and is studied in the other fields of optics of discrete media (e.g., Fazio et al. 2017). The angular dependence of linear polarization in the definition $P = \left(I_{\perp} - I_{\parallel}\right)/\left(I_{\perp} + I_{\parallel}\right)$, where $I_{\perp}$ and $I_{\parallel}$ are intensities at corresponding orientations of polarizer follows from the positive maximum to the zero level and changes its sign typically in the range of 10–25 degrees of the phase angle with a minimum value up to a few percent. The origin of NP may have different sources depending on the structure and albedo of the surface. At high albedo we deal with contributions of single and multiple scattering that influence the total response in different ways. For instance, denser packing creates conditions for weak localization of light and one can expect a wider backscattering surge in this case. Single non-absorbing particles produce strong NP in a wide range of sizes (Shkuratov et al. 2006; Grynko et al. 2020) and, therefore, they can be considered as the main sources of NP. The multiple scattering component has low polarization due to randomization of local planes of polarization at scattering in particulate media. After many scatterings the information about the initial polarization is quickly lost and light leaves such a medium almost unpolarized. Thus, one can expect a depolarization effect suppressing the NP feature produced by single particles in the very upper layer. Generally, the relative contributions of single and multiple scattering and the exact role of the coherent multiple scattering component in the formation of NP in the non-absorbing case remains unclear.

Absorbing particles larger than the wavelength do not produce NP as it is formed by internal scattering and the external component of single scattering is always positively polarized. At the same time low-albedo objects often exhibit a noticeable NP feature. It has been measured for the Moon and dark asteroids (Shkuratov et al. 1992; Belskaya et al. 2005, 2019). For powder samples with albedo of as low as several percents it also has been found in the laboratory experiments (Shkuratov et al. 2002; Ovcharenko et al. 2006). At such conditions multiple scattering is reduced to a few orders and the NP effect is apparently caused by coherent double scattering. Higher orders are unlikely to contribute here as their intensity exponentially drops with every scattering event and the degree of polarization as well. Analytical solutions in approximate models that consider interference of waves at counterpropagating paths show that the NP effect can be explained with such a mechanism (Shkuratov 1985, 1989; Muinonen 1989; Shkuratov et al. 1994). Solutions for a pair of Fresnel scatterers (Shkuratov 1985, 1989), particles with Rayleigh polarization phase functions (Shkuratov 1991), random distribution of electric dipoles (Muinonen, 1989) or clouds of randomly oriented reflecting facets (Videen 2002) produce the NP feature that is generally consistent with observations. However, the problem is not solved for realistic geometries like dense packings of irregular particles larger than the wavelength.

The width of the IS and the slope of the intensity curve, the inversion angle of polarization and the position and depth of the NP feature depend on the physical properties of such powder-like surfaces. From the multi-wavelength and multi-angle photopolarimetry of a scattering object one can assess these properties if an adequate theoretical model is applied. However, the problem of interpretation appears to be hard due to complexity of the light scattering solution for a target like a system of many densely packed irregular particles. One has to consider very large model samples, much larger than the wavelength, and with distances between particles smaller than the wavelength. This makes the problem multi-scale which is always a challenge for numerical methods. In addition, random irregular constituent shapes should be considered because scatterers with perfect geometries like spheres or ellipsoids cannot be representative due to their peculiar optical properties. Therefore, laboratory photopolarimetric measurements of powder samples remain the only reliable reference at present.

In theoretical modeling various approximations are usually applied. For instance, the geometrical optics (GO) approach allows modeling very large systems of particles of arbitrary shape (e.g., Shkuratov and Grynko 2005; Grynko and Shkuratov 2007; Schröder et al. 2014), but it does not take into account the wave effects. The hybrid or physical optics models accounting for diffraction of light beams and their coherent summation have been applied to single scattering by isolated particles (Shishko et al. 2019; Yang et al. 2007) but no results for particulate clusters have been reported so far. Markkanen et al. (2018) suggest an approximate ray tracing model that combines incoherent scattering with interference of rays propagating along conjugate trajectories is presented. In (Väisänen et al. 2020) it has been validated and the simulation results were compared with photopolarimetric measurements of large deposits of densely packed of silica spheres. In some cases, even far-field characteristics of the scatterers are used in the formulations of light scattering models for dense media (Muinonen et al 2015a, b; Petrova et al. 2019; Kolokolova et al. 2019).

The popular superposition T-matrix method allows simulation of light scattering from very large dense clusters providing a numerically exact solution (Pattelli et al. 2018; Egel et al. 2017; Pitman et al. 2017; Theobald et al. 2021). However, this is possible for spherical constituents only. In the formulation of the method a correct single-scattering solution is obtained at the distance of a radius of a sphere circumscribing a particle. Thus, such spheres should not overlap which reduces the maximum packing density for non-spherical constituents. E.g., for random irregular particles such a limitation restricts the maximum packing density to $\rho \approx 0.1$. However, attempts have been made to overcome this problem (Theobald et al. 2017; Bertrand et al. 2020).

With a full wave solution one can avoid the listed approximations and shed light on the optical mechanisms responsible for the formation of the backscattering phenomena. One can correctly account for the single-scattering phase function, single-scattering polarization properties of particles and near-field effects that control light transport in a dense medium. If no approximations are introduced in a model the input parameters like particle size, complex refractive index and packing density are clearly defined and the analysis of their role in the backscattering properties of a densely packed structure becomes straightforward.

Finite Difference Time Domain, Discrete Dipole Approximation and Pseudo-spectral Time Domain methods have been applied to study light scattering by single particles of different shapes and sizes (e.g., Sun et al. 2003, Sun et al. 2013, Zubko et al. 2013; Liu et al. 2012; Derek et al. 2014). However, there are no works published on their application to large clusters of particles. As we mentioned above, the problem requires large multiscale meshes and, consequently, significant computational resources.

Here we apply high-performance computing (HPC) in order to obtain a numerically exact solution of the problem for dense clusters of irregular particles that have dimensions much larger than the wavelength. Optimal use of HPC hardware implies that the utilized PDE solver code is efficiently parallelized. The users of modern HPC systems can typically allocate jobs on up to a several thousands of CPU cores. Correspondingly, we need a numerical method that can handle simulations distributed over thousands of processes. Considering complex geometry that random clusters of irregular particles may have a method should also be flexible in representation of such structures. Below we list these and additional requirements to a numerical method that could provide such a solution:

- arbitrary geometry and structure of the scatterer with any level of complexity:
- optimal space discretization, unstructured meshing;
- simple implementation of different types of light sources, boundary conditions, and materials;
- possibility of time domain simulations;
- good intrinsic parallel scalability property provided by the numerical scheme.

The formulation of the Discontinuous Galerkin Time Domain method (Hesthaven and Warburton 2002) for solving Maxwell's equations satisfies these conditions. It is based on unstructured meshing and its numerical scheme uses local stencils defined withing a single element. The scheme is free from global matrices and operators and most of the operations are done locally. This makes parallelization of the computer code straightforward. The method has been successfully applied in electromagnetics and photonics (Niegemann et al. 2009; Stannigel et al. 2009; Descombes et al. 2013; Linden et al. 2012; Grynko et al. 2014, 2018, 2020; Grynko and Förstner 2017) showing good parallel performance.

In this work we review our applications of the DGDT method to the problem of light scattering from dense clusters of irregular particles. We study angular dependences of intensity and linear polarization of scattered light and, in addition, address several other questions. Solving a full wave problem one can obtain a reliable estimate of the characteristic transport length of light in a dense medium with realistic structure. At first, it is important to have an estimation of the thickness of the surface layer where multiple scattering concentrates most energy and to determine the characteristic spatial scale of multiple scattering effects at which the backscattering feature are formed. Second, one has to know if an elementary scattering volume can be defined at such a scale as this is a basic element of the radiative transfer theories that are often applied for interpretation of the observational data (Hapke 1981, 2012). With direct time-domain simulations and a realistic structure geometry one can also visualize the exact pattern of the near field interaction for irregular particles larger than the wavelength if they at densely packing. And, generally, we want to evaluate the maximum size of samples that can be considered in systematic simulations with available high-performance computing (HPC) resources and a parallel DGDT Maxwell solver.

In Sect. 2 we present our model, briefly introduce a numerical scheme of the DGTD method and describe our light scattering code. In Sect. 3 we review results of the simulations for large clusters of non-absorbing irregular particles and layers of highly absorbing particles packed with packing densities of $\rho = 0.5$.

2 Model Description

In this section we describe the DGTD method with its implementation in a light-scattering code and a method for generating dense clusters of irregular particles.

2.1 DGTD Method

According to the formulation of the DGDT method a computational domain Ω can be discretized into K elements of generally arbitrary shape and size (Hesthaven and

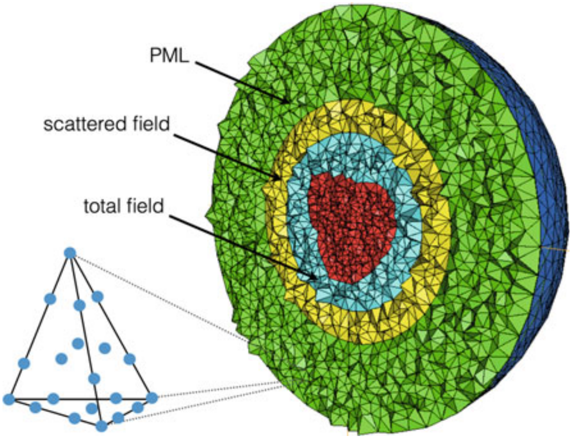

Fig. 2 Example of a discretized computational domain with PML, total field and scattered field regions and an irregular particle

Warburton 2002; Busch et al. 2011). Most often these are tetrahedral cells (Fig. 2) or triangles in a 2D formulation.

If

$$\mathbf{q} = \begin{bmatrix} \mathbf{E} \\ \mathbf{H} \end{bmatrix}$$

is a field state vector defined locally on a k-th element the solution can be expanded as

$$\mathbf{q}^k(\mathbf{r}, t) = \sum_{j=1}^{N} \mathbf{q}^k(\mathbf{r}_j, t) L_j(\mathbf{r})$$

where $L_j(\boldsymbol{r})$ are interpolating Lagrange polynomials. Depending on the expansion order p the number of terms is determined as $N = (p + 1)(p + 2)(p + 3)/6$. The problem is solved for unknown values $\mathbf{q}_k(\mathbf{r}_j, \mathrm{t})$ that are defined in the N nodal points distributed in the element k (see Fig. 2). Using the Galerkin approach one can derive explicit expressions for the Maxwell's equations in the k-th element:

$$\begin{aligned} \varepsilon^k &= \frac{\partial \mathbf{E}^k}{\partial t} = \mathbf{D}^k \times \mathbf{H}^k \\ &\quad + \left(\mathscr{M}^k\right)^{-1} \mathscr{F}^k \left(\frac{\Delta \mathbf{E} - \hat{n} \cdot \left(\hat{n} \cdot \Delta \mathbf{E}\right) + Z^+ \hat{n} \times \Delta \mathbf{H}}{\bar{Z}} \right) \qquad (*) \\ \mu^k \frac{\partial \mathbf{H}^k}{\partial t} &= \mathbf{D}^k \times \mathbf{E}^k \end{aligned}$$

$$+\left(\mathscr{M}^{k}\right)^{-1}\mathscr{F}^{k}\left(\frac{\Delta\mathbf{H}-\hat{n}\cdot\left(\hat{n}\cdot\Delta\mathbf{H}\right)-Y^{+}\hat{n}\times\Delta\mathbf{E}}{\bar{Y}}\right) \qquad (**)$$

The first term in the right side of both equations is the rotor operation where $\overrightarrow{\mathrm{D}^{\mathrm{k}}} = \left(\mathrm{D}_{\mathrm{x}}^{\mathrm{k}}, \mathrm{D}_{\mathrm{y}}^{\mathrm{k}}, \mathrm{D}_{\mathrm{z}}^{\mathrm{k}}\right)$ is a differentiation matrix with $\left(\mathrm{D}_{\mathrm{m}}^{k}\right)_{ij} = \partial_m L_j\left(\overrightarrow{r_i}\right)$ and $m \in \{x, y, z\}$. The second term represents a numerical flux that is calculated over all nodal points located on four faces of the element. For that we map neighbor faces and pairs of the corresponding nodal points (Fig. 3) and for each pair differences of the field values $\Delta\mathbf{E}$ and $\Delta\mathbf{H}$ are computed. Here $\hat{n}$ is is the outward-pointing normal vector, $\left(\mathcal{M}^{\mathrm{k}}\right)_{ij} = \int_{\Omega^k} L_i\left(\overrightarrow{r}\right)L_j\left(\overrightarrow{r}\right)d\overrightarrow{r}$ is the mass matrix and $\left(\mathcal{F}^{\mathrm{k}}\right)_{ij} = \int_{\delta\Omega^k} L_i\left(\overrightarrow{r}\right)L_j\left(\overrightarrow{r}\right)d\overrightarrow{r}$ is the face matrix that is calculated on the element interface $\delta\Omega^k$. Dielectric materials can be characterized through impedances $Z^{\pm}$ and conductances $Y^{\pm}$

$$Z^{\pm} = \frac{1}{Y^{\pm}} = \sqrt{\frac{\mu^{\pm}}{\varepsilon^{\pm}}}$$

and their sums $\overline{\mathrm{Z}} = \mathrm{Z}^{+} + \mathrm{Z}^{-}$ and $\overline{\mathrm{Y}} = \mathrm{Y}^{+} + \mathrm{Y}^{-}$. Thus, by means of the numerical flux term continuity between initially disconnected neighbor elements is recovered preserving locality of the numerical scheme.

Equations (*) and (**) represent an explicit numerical scheme and can be time-integrated using any explicit integration method. Considering the wide variety of existing methods this is an additional flexibility factor in DGTD. Low-storage Runge–Kutta (LSRK) methods appear to be efficient enough in this case yet simple to implement. We use an optimized LSRK scheme (Niegemann et al. 2012) consisting of 14 stages and having 5th order accuracy. We note, that DGTD as any other explicit method is sensitive to the quality of the mesh because of the CFL condition. Here the time step criterion is formulated as follows (Busch et al. 2011)

$$\Delta t_{\max} \le s \cdot d_{\min}(p) \cdot \min_{\Delta}\left(r_{in}^{\Delta}\right)$$

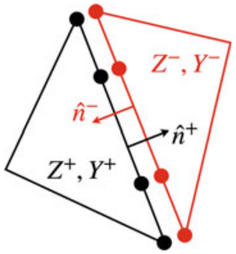

Fig. 3 Nodal points on the interfaces of two neighbor 2D elements for which the field differences $\Delta\mathbf{E}$ and $\Delta\mathbf{H}$ in the equations (*) and (**) are calculated

where r_{in}^{Δ} is the radius of the sphere inscribed in the element Δ, $d_{min}(p)$ is the smallest distance between two nodes among all the elements in the mesh, and s is a factor similar to the Courant number. One can see that bad quality or very small elements in a mesh may result in low performance. Especially, this problem becomes significant if we need to generate large unstructured meshes for multiples samples of irregular particles or random clusters of particles. If the problem is multiscale, we obtain a broad distribution of sizes of the elements in a mesh, in the range of several orders of magnitude, and the probability of accidental appearance of low-quality element quickly increases. Therefore, in each simulation the code analyzes the quality of a particular mesh and estimates the possible maximum time step. The most optimal value can be found empirically. As an alternative, one can use multiple time-stepping techniques that should be more efficient in such situations. Generally, one can split a mesh into groups of small and large elements and use different time steps for them. Various multiple time-stepping schemes developed for the DGTD method are described in the literature (e.g., Demirel et al. 2015; Angulo et al. 2014). With these modifications one can expect a speedup by factors of 2 or 3 if the number of small elements is not very large.

2.2 Parallel Light Scattering Code

Our light scattering code is based on the publicly available implementation of the DGTD method Midg developed by Warburton (2008). Midg is written in the C language and contains a DGTD solver that originally allowed solving an initial value electromagnetic problem. It uses the MPI library functions and can be run on multiple CPUs. Mesh partitioning is done by means of ParMetis library. After reading a mesh from a file, its parts are distributed among the MPI processes. The maps of pairs of the interface nodes for neighbor elements that belong to different processes are created for the simulation-time stage. During time-stepping the field differences $\Delta\mathbf{E}$ and $\Delta\mathbf{H}$ are calculated using MPI messaging for nodal points that belong to different processes (see Fig. 4). For elements that have no faces belonging to the boundary of a partition the field differences and all the other quantities are computed in usual way (sequential regime). The number of MPI calls appears to be small in comparison to the total amount of other tasks and operations. Over 90% of the run time is occupied by execution of local arithmetic operations. It is mostly the differentiation part where the curls of the $\mathbf{E}$ and $\mathbf{H}$ fields are calculated. We note that increasing the number of parallel processes for the same mesh we decrease the size of each partition and, correspondingly, the amount of the communication data. In the simulation time there is only communication between neighbor partitions and there is no global all-to-all messaging. This results in a good parallel scalability of the code. In Fig. 5 one can see that the speedup is close to ideal. We were able to run successful simulations on at least 5000 CPU cores.

Fig. 4 Example of a mesh partitioning showing element face nodal points inside a partition and on the interface between two neighbor partitions

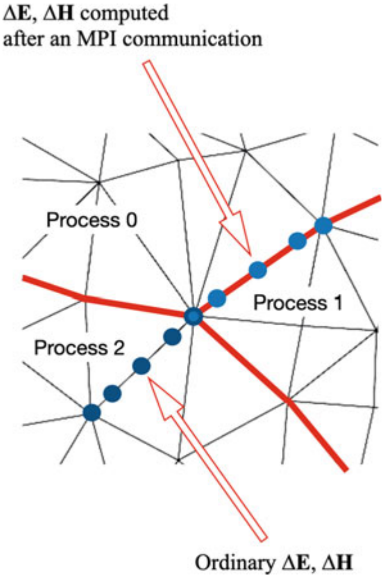

Fig. 5 Parallel scalability of the code normalized at 16 cores as tested on the HPC cluster of the Paderborn University (Grynko and Förstner 2017)

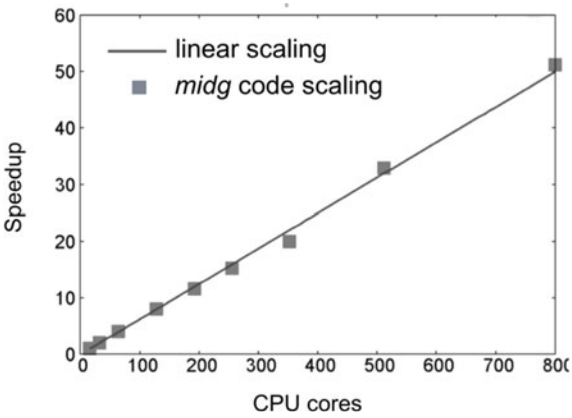

For simulations of light scattering by various target objects we need to implement light sources, efficient absorbing boundary conditions and dielectric and dispersive materials.

In most cases a monochromatic plane wave is used as a standard light source. This can be realized by means of the total field/scattered field (TF/SF) technique (Taflove 1995). Initially it has been formulated for the FDTD method but its application in DGTD is straightforward. One can define a surface around a scatterer and map all nodal points belonging to this surface. Then, light source energy is injected in the field differences $\Delta\mathbf{E}$ and $\Delta\mathbf{H}$ that are included in the flux terms in full accordance with the TF/SF formulation. Gaussian focused beams can be modelled with the extension of the TF/SF technique to the plane wave superposition method (e.g., Capoglu et al. 2008).

To simulate light scattering in an infinite space we apply a Perfectly Matched Layer (PML) boundary condition. Our implementation of PML is similar to that presented in (Niegemann et al. 2009). Infinite layers of particles can be modelled by means of periodic boundary conditions applied to horizontal directions. For that an unstructured mesh with corresponding periodic sides must be generated. Then, the corresponding boundary element interfaces are processed in the code and the neighbor nodal pairs in the opposite sides are mapped accounting for the parallel multi-process environment. After that, computation of fluxes for the elements belonging to the opposite sides becomes straightforward.

Figure 2 shows an example of a computational domain with total field and scattered field regions, PML and a single irregular particle as a target object.

The result of a time domain electromagnetic simulation is the distribution of the electromagnetic near-field around and inside the scatterer. In our case we are interested in the analysis of the scattered field in the far zone. Therefore, in the final stage the scattered near field is measured and then, transformed to the far-field quantities. We apply the surface-integral method (Zhai et al. 2004) for the near to far field transformation. The electric field components on a virtual integrating surface in the scattered field region are Fourier-transformed and a near to far field transformation is applied to obtain the 2×2 Jones matrix elements. Then, a 4×4 Mueller matrix F_{ij} is calculated for a range of scattering angles from 0° to 180°. Unpolarized light source is simulated by means of two simulation runs with linearly polarized plane waves having perpendicular polarizations.

2.3 Generation of Dense Clusters of Irregular Particles

We use Gaussian Random Field (GRF) shapes (Grynko and Shkuratov 2002, 2003; Grynko et al. 2014, 2016, 2018; Grynko and Förstner 2017) for all our simulations. Having a large pre-generated set of particle samples approximated by sets of triangular facets we can apply the particle packing routine to generate dense clusters.

Maximum packing density that can be achieved with random uniform distribution of non-overlapping irregular shapes is $\rho \approx 0.1$ (Grynko and Shkuratov 2008). Therefore, generation of model media with $\rho > 0.1$ requires additional efforts. One can apply, e.g., a Boolean summation of a few pre-generated media samples with $\rho = 0$. Stankevich et al. (2003) are reached the total density of $\rho = 0.3$ with such an approach. Grynko and Shkuratov (2008) and Schröder et al. (2014) applied isometric inflation with Monte Carlo rotation of particles in a system with sparse initial distribution. The maximum packing density obtained was $\rho \approx 0.4$.

Higher packing density for irregular particles can be achieved using any implementation of the Discrete Element method (DEM) or a similar approach (e.g., Xu et al. 2020). Using DEM one can simulate dynamics and collisions of multiple arbitrary 3D shapes in time domain. One can also take into account friction between

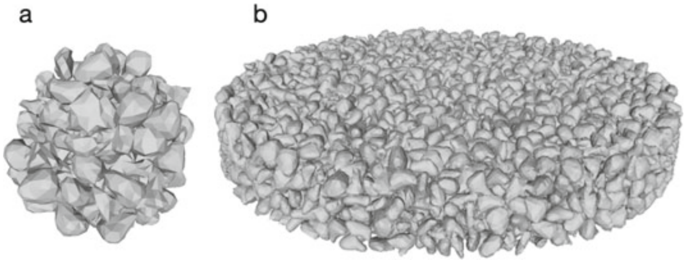

Fig. 6 A spherical cluster (**a**) and a thick layer (**b**) of densely packed GRF particles with bulk packing density $\rho = 0.5$

close particles, gravity and various kinds of attractive potentials. Thus, simulating natural powder mechanics samples with realistic parameters can be created. Here we are interested only in geometrical arrangement of constituents in a system with maximum packing density. For that we apply the Bullet Physics engine (Coumans and Bai 2021). This is an open-source C++ library that can be also used as an add-on in Blender software. Applying a background gravitation force and zero friction we can generate spherical clusters or flat layers of irregular particles with bulk packing density up to $\rho = 0.55$. In the first case we begin with a cloud of sparsely distributed particles in air with a point gravity source in the center of the cloud. In a time-domain simulation such a system evolves into a dense spherical cluster (Fig. 6a).

Similarly, flat layers can be generated simulating free fall of particles on a substrate in a closed cylindrical volume. Controlling the number of particles and the size of the cylinder one can generate dense thick granular layers or monolayers. Figure 6b shows an example of a layer with several thousands of GRF particles.

Neighbor particles in real powders touch each other. However, the problem of generation of such a model geometry would have much higher level of complexity. Moreover, such a 3D structure would have non-manifold edges, which makes tetrahedralization impossible. Thus, we choose a small but non-zero minimum distance between the particles and keep it much smaller than the wavelength. However, too small minimum distance between the particles in a cluster results in the presence of very small elements in a tetrahedral mesh. Consequently, this can reduce the time step in the explicit time integration of Maxwell's equations in the DGTD numerical scheme. We were able to find an optimal value for the minimum distance parameter in the numerical packing that allows both large packing density values and an acceptable time step.

3 Results

3.1 Non-absorbing Clusters

In this section we discuss the results of light scattering simulations done for dense spherical clusters of non-absorbing GRF particles (Grynko et al. 2020). Spherical shape of cluster samples is the simplest geometry allowing simulation of light scattering in the entire range of scattering angles including variation of angles of incidence. Thus, it is a good starting point for studying backscattering properties of dense media.

One of the questions that should be answered is how the backscattering response in intensity and polarization depends on the cluster size and the number of particles in it and how large this number should be for a convergent result. For that we consider three cases with size parameters $X_D = 50$, 100 and 150 ($X_D = \pi D/\lambda$, where D is the cluster diameter and λ is the wavelength) (Fig. 7). With the size of individual particles $X_d = 10$ and bulk packing density $\rho = 0.5$ this makes the numbers of particles N = 200, 1600 and 5000, respectively. The complex refractive index of the material is $m = 1.5 + 0i$ in all cases.

Generally, we are interested in the study of backscattering response to illumination of clusters by unpolarized plane waves. However, we first analyze the light transport pattern inside a dense model structure, probing it with a Gaussian focused beam. The role of the near-field interaction between close neighbors at dense packing is very important and it should be understood. For that, we consider a cluster with 200 particles and size $X_d = 50$ and illuminate it with a portion of wavefronts with cross-section smaller than the cluster size. Thus, its spot on the surface spans just a few particles. With forward scattering by these particles the transport process starts inside a structure. The result of such a simulation is shown in Fig. 8. This is a steady-state distribution of the E_x-component of the electric field. The incident pulse is

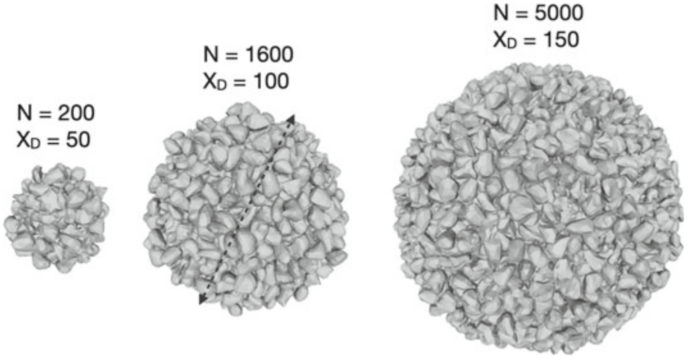

Fig. 7 Samples of spherical cluster with different sizes and numbers of constituent particles. The packing density is $\rho = 0.5$

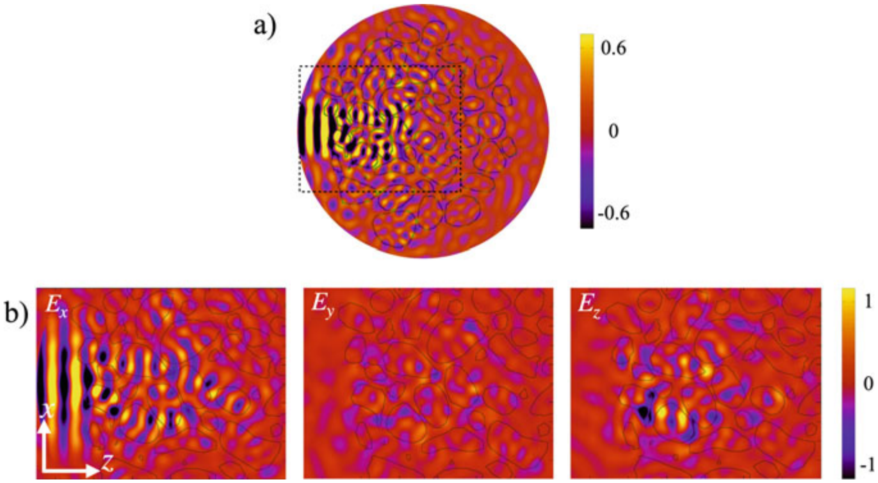

Fig. 8 Steady state distribution of the electric field component E_x inside a dense cluster of 200 particles illuminated by a focused beam propagating along Z axis (**a**) and a zoomed fragment showing all three components (Grynko et al. 2020)

E_x-polarized and propagates in Z direction. One can see that very small distance between neighbor particles plays crucial role in the field propagation. The light transmitted and scattered by particles in the upper layer follows propagation channels formed by particle chains. The main mechanisms of near field interaction are focusing on the neighbor particle after transmission and whispering gallery wave coupling between the surfaces of the neighbors. We note that this pattern is polarization independent and an incident pulse with perpendicular polarization follows the same propagation paths. Interestingly, the E_z components are enhanced in the regions of the near field interaction between close particles (Fig. 8b). This indicates that it also can play an important role in the light transport. It is insignificant in sparse media as radial component decays with distance as $\sim 1/r^3$ but becomes influent at high packing density.

In Fig. 9a we show a logarithm of intensity ($\log(|E|^2)$) of the internal field in frequency domain for the same cluster and the same simulation. Such a volume color map representation better illustrates the result of the described mechanisms of near field interactions. In Fig. 9b, a similar energy distribution for a dense cluster consisting of 200 spherical particles with the same size and material is presented for comparison. Propagation energy threads can accidentally split on the way at certain geometrical conditions forming a fractal-like structure. We found that it spans more that 90% of total energy. This implies high level of light localization and low diffuse scattering. We note that geometrical complexity and the degree of disorder measures, e.g., fractal dimension, for such a field distribution as well as the cluster structure itself can be involved in the analysis in addition to the ordinary parameters of the particle size and packing density. Here one can see how different a field pattern can be if the constituents are spherical. Densely packing of spheres produces mostly

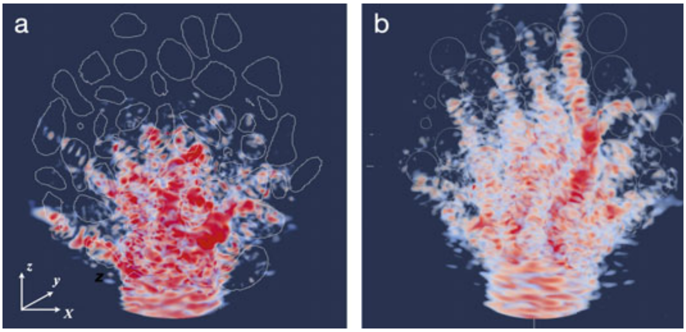

Fig. 9 Frequency domain 3D distributions of logarithm of intensity inside a cluster of GRF particles (**a**) and a cluster of spheres (**b**) of the same size. Clusters are illuminated by a focused beam propagating in Z direction (Grynko et al. 2020)

hyperuniform topology with reduced degree of disorder (Fig. 10). This results in more developed propagation paths and more efficient transmittance. This fact should also be taken into account in the models approximating dense random media by clusters of spheres.

Visualization of the field distribution for a cluster much larger than the wavelength ($X_D = 150$) formed by irregular particles shows that light localization plays role also in the characteristic transport length. Figure 11 shows a steady state distribution of the E_x-field component as a result of illumination of the cluster by a plane wave. Despite zero absorption of the material most energy is confined in a layer with thickness smaller than the cluster diameter, i.e., $X \approx 70$ in size parameter units. As a result of a random walk process light tends to leave the cluster through the rear boundary and does not reach the forward hemisphere. $X \approx 70$ corresponds to the order of 10 μ for the optical wavelength range which is a relatively small scale. The transport length can be larger if a finely powdered surface has a "fairy castle" structure and a

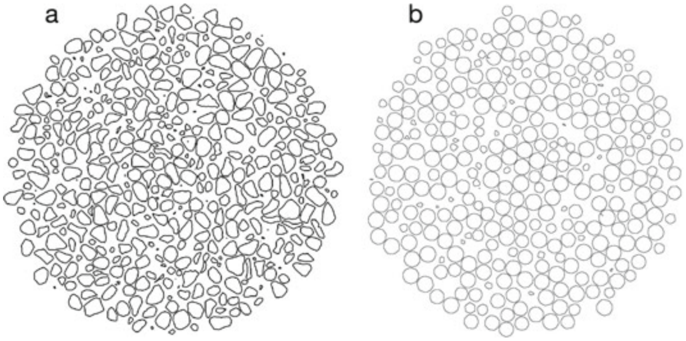

Fig. 10 Cross-sections of large clusters consisting of GRF particles (**a**) and spheres (**b**) at packing density $\rho = 0.5$

Fig. 11 Steady state distribution of the electric field component E_x in a cluster of GRF particles with diameter $X_D = 150$ and $\rho = 0.5$ illuminated by a plane wave

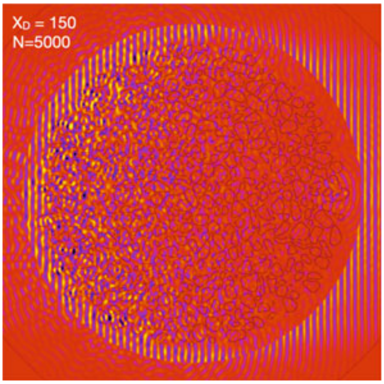

thick transition layer. Also, densely packed clumps of this size are often formed in fine powders. Apparently, they can be optically thick even at this scale and produce shadowing effect. We note that natural fine powders often have complex structure of the upper layer, which obviously makes an impact on their backscattering properties, and theoretical models that are able to reproduce this structure should be considered.

From the above analysis we can conclude that light propagation in a dense particulate medium is more a percolation process than multiple scattering from particle to particle according to a standard concept. We note also that small penetration depth even at zero absorption and the geometrical complexity of the near field distribution makes definition of the elementary scattering volume, a crucial element of the radiative transfer approach, impossible. Thus, widely used conventional radiative transfer theories (Hapke 1981, 2012) cannot be applied in such conditions.

Before we discuss far-field scattering from clusters we recall single scattering by compact irregular particles of different sizes. The contribution of the very upper layer of any particulate surface to backscattering is largely formed by the far field scattering properties of single particles as they are not obscured by anything and can backscatter to the far zone. The questions that should be addressed are how strong this contribution is and how it is affected by the multiple scattering component. In Fig. 12 we show results of systematic study by Grynko et al. (2018) of scattering by isolated GRF particles of different sizes from $X_d = 10$ to 150. We note that the polarization curves do not change qualitatively in a wide range of sizes. The main features are present on all curves, from the size close to the wavelength to the nearly geometrical optics regime. This implies the same mechanisms of their origin. Smaller particles reveal a strong NP branch which should play a role in the case of dense clusters. Such particles produce also a size-dependent backscattering IS (Fig. 12c) which can contribute to the backscattering from clusters as well.

In Fig. 13 we compare the simulated intensities for clusters of different sizes and isolated GRF particles with $X_d = 10$. One can see that the optical thickness grows with size predictably making clusters less transparent. The backscattering IS is present as expected. Apparently, it is caused mainly by coherent multiple scattering. The profile of the IS is determined by the structure of clusters and not their sizes. It is

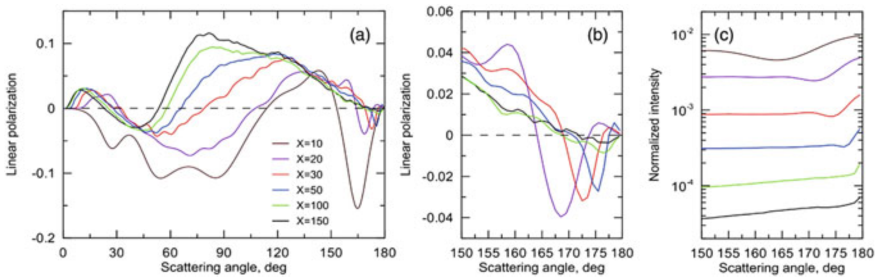

Fig. 12 Scattering angle functions of linear polarization (**a**, **b**) and intensity (**c**) computed for ensembles of isolated GRF particles with different from X = 10 to 150 with complex refractive index $m = 1.5 + 0i$ (Grynko et al. 2018)

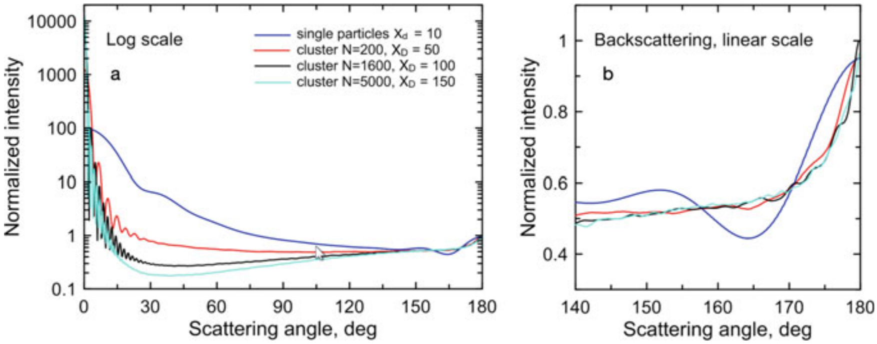

Fig. 13 Scattering angle functions of intensity in logarithmic scale (**a**) and linear scale near backscattering (**b**) for single GRF particles with size parameter $X_d = 10$ and clusters of GRF particles with $X_D = 50$, 100 and 150 and $\rho = 0.5$ (Grynko et al. 2020)

also a statistical phenomenon which can be revealed only after averaging over many samples. It can be weak or even absent for single samples (Fig. 14) in which paths with constructive interference do not exist.

Clusters with $X_D = 100$ and $X_D = 150$ produce closeby curves in Fig. 13b which implies convergence of the solution in this angular range. They appear to be large enough with respect to the wavelength and the size of constituents. Thus, we get an answer to the question of how large the sample should be taken in order to mimic an infinite medium near backscattering.

A similar stability near backscattering is observed for polarization (Fig. 15). The NP branch depends only little on the cluster size and the inversion angle remains constant coinciding with that for isolated particles. This is an indication that single particles are the main sources for NP. Apparently, the particles in the upper layer generate a deep NP which is partially depolarized by the contribution of multiple scattering. Again, it is the size of constituent particles and the cluster structure what determines the angular profile of NP. At the same time, polarization at smaller angles

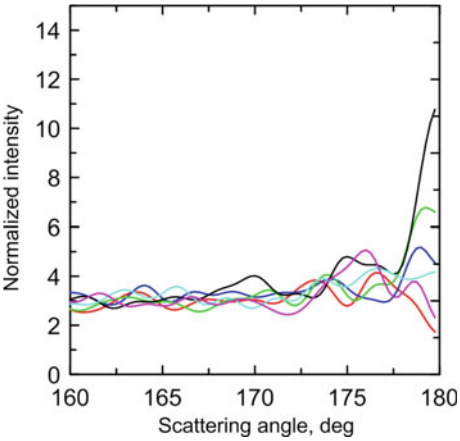

Fig. 14 Scattering angle functions of intensity near backscattering for single samples of clusters with diameter $X_D = 100$ and $\rho = 0.5$

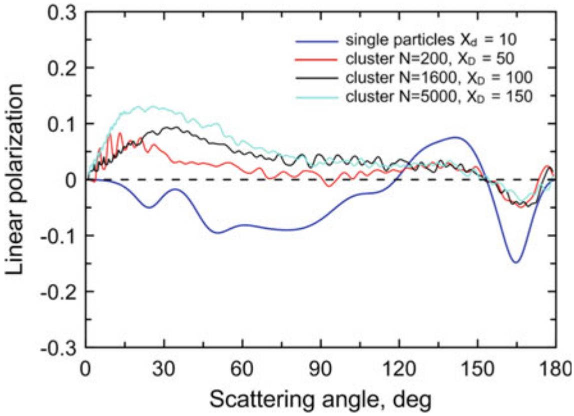

Fig. 15 Scattering angle functions of linear polarization for single GRF particles with size parameter $X_d = 10$ and clusters of GRF particles with $X_D = 50$, 100 and 150 and $\rho = 0.5$ (Grynko et al. 2020)

appears to be size-dependent. In forward scattering (at small scattering angles) the curves are formed mainly by the positively polarized light reflected from the particles at the edges of clusters. A similar effect is observed in the experimental measurements of powders at large angles of incidence (Shkuratov et al. 2007a, b) and our previous GO modeling (Grynko et al. 2006).

To analyze the role of internal structure of clusters in more detail we consider two more cases: sparse packings with the same ρ but different topologies. For the size $X_D = 100$ we take the set of samples with density $\rho = 0.5$ and from each cluster remove 2/3 of constituent particles. With this the packing density becomes $\rho = 0.16$ and internal structure becomes non-uniform. There are still groups of very close particles and voids larger than the particles size and, correspondingly, the wavelength. The second set of samples is represented by clusters of the same diameter and packing density but with simple uniform distribution of constituents.

Examples of both types a given in Fig. 16. In Fig. 17 we compare their backscattering properties. Once can see that sparse structures are able to produce the IS (Fig. 17). The intensity curve corresponding to the non-uniform topology is very close to the one produced with maximum packing density. What is common between dense and sparse non-uniform clusters is the presence of dense groups of particles. Apparently, the conditions for constructive interference producing the IS are created at such a scale and small agglomerates are responsible for the IS. The near-field interaction is reduced if the distances between all the constituents are at least not smaller than the wavelength which is the case in the uniform distribution. This condition reveals backscattering properties of single particles. As a result, the IS from the uniform sparse clusters tends to be similar to the single-scattering one. We note that structures with the same bulk packing density but different topologies may produce IS with different angular profiles. In practice fine-powder surfaces may have a complex structure of the upper layer and the parameter of packing density (filling fraction) is not enough for the topology description and the solution of the retrieval problem. Therefore, other measures like the thickness of the transition layer, the packing density gradient or fractal dimension should be involved.

Compression of powders, i.e., destroying a “fairy castle” structure of the upper layer, increases negative and positive polarization features (Shkuratov et al. 2002; Bondarenko et al. 2006; Shkuratov et al. 2007a, b). Laboratory measurements of dried suspension and compressed powder samples reveal also an effect of packing density in NP. Our model can reproduce this behavior. In Fig. 17b both negative and positive polarizations for dense clusters are enhanced if compared to the sparse case. Interestingly the inversion angle remains the same in all cases. Obviously, light localization is the reason of this enhancement. If a sparse system contains

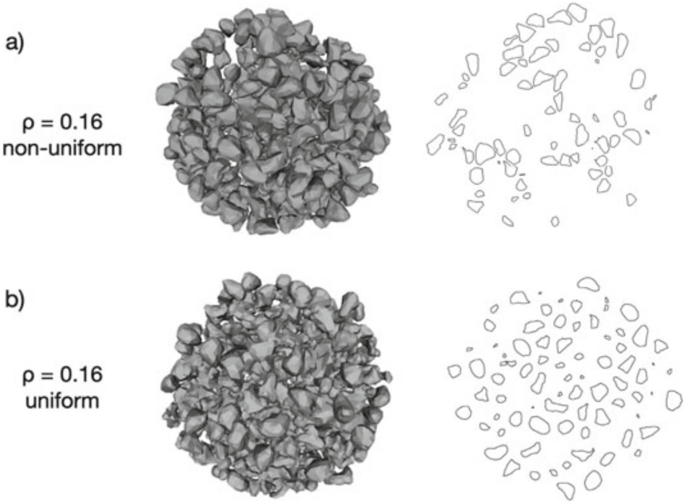

Fig. 16 Samples of clusters of GRF particles with the same packing densities $\rho = 0.16$ but different topologies (Grynko et al. 2020)

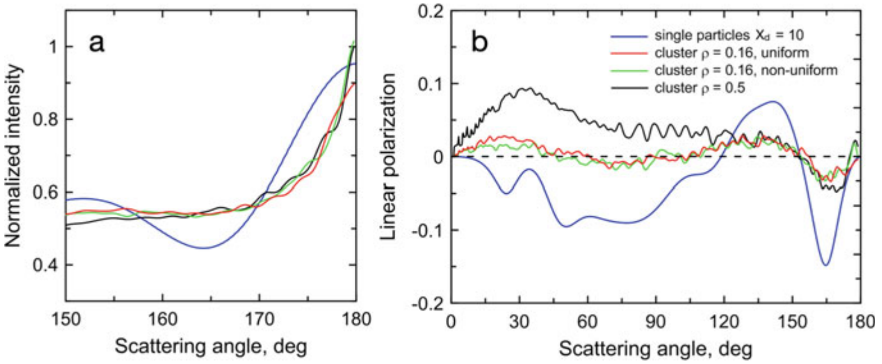

Fig. 17 Scattering angle functions of intensity at backscattering (**a**) and linear polarization (**b**) computed for for single GRF particles with size parameter $X_d = 10$ and clusters of GRF particles with $X_D = 100$: $\rho = 0.16$, uniformly distributed, $\rho = 0.16$, non-uniformly distributed and and $\rho = 0.5$ (Grynko et al. 2020)

large voids or the distances between all the neighbor particles are larger than the wavelength this gives enough space for diffuse multiple scattering. The emergent diffuse scattering background has low degree of polarization. It produces depolarization effect suppressing strong contribution of single particles. At large packing density this possibility disappears and the relative contribution of single scattering increases. At small scattering angles, i.e., at grazing incidence, forward scattering is largely formed by external reflection from the upper-layer particles and, therefore, polarization tends to be positive.

To illustrate this argument, in Fig. 18 we show steady state distributions of the internal fields of clusters probed with a focused beam. The beam is E_x-polarized and the corresponding field component is displayed. For both types of sparse structures at $\rho = 0.16$ the mean free path length is larger than the wavelength. Therefore, light

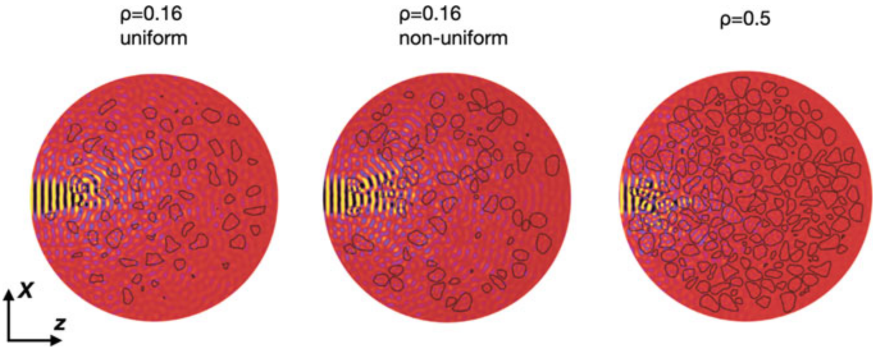

Fig. 18 Distributions of the electric field components E_x at steady state in sparse ($\rho = 0.16$) and dense ($\rho = 0.5$) clusters of GRF particles with diameters $X_D = 100$ illuminated with a focused beam (Grynko et al. 2020)

scattered by the first particles on the way of the incident beam is transported in free space at larger distances. The field becomes distributed in the entire volume of the cluster and many particles participate in multiple scattering although the incident beam has a small cross-section. Light propagation in the dense case is totally different. The incident field is localized in a small region bound to a few particles in the upper layer. It can propagate further only along the paths accidentally created by chains of particles. This behavior also confirms our assumption that the coherent backscattering IS is caused by small agglomerates of particles.

In contrast to the intensity, the polarization curves for uniform and non-unform sparse clusters are very similar. This means that dense agglomerates of this size are able to produce the IS but play small role for the polarization response.

In the end we note that the polarization inversion angle near 150° is the same for all considered sizes and densities of clusters and it is equal to that of isolated particles. This is an indication that single scattering is a source of NP at backscattering from non-absorbing particulate media.

3.2 Absorbing Layers

Another important case is dense particulate media formed by absorbing particles. In this section we consider thick layers and monolayers of highly absorbing GRF particles with sizes much larger than the wavelength (Grynko et al. 2022). The real part of the complex refractive index of the material is Re(m) = 1.5 as in the study of spherical clusters and the imaginary part is Im(m) = 0.3. The size of constituents is $X_d = 30$ which makes them highly absorbing with small single-scattering albedo. The list of target structures includes thick layer samples (Fig. 19) with diameter $X_D = 200$, thickness $X_L = 60$, bulk packing density $\rho = 0.5$ and with the number of constituents $N \approx 150$. The monolayer samples (Fig. 19b) have different diameters from $X_D = 90$ to 250 and numbers of particles from N = 10 to 100.

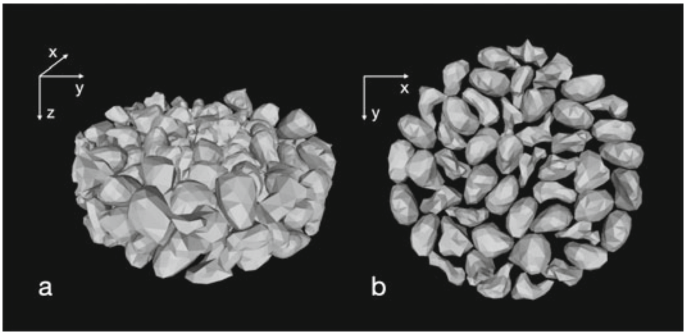

Fig. 19 Samples of a thick layer (**a**) and a monolayer (**b**) of GRF particles with diameters $X_D = 200$ (Grynko et al. 2022)

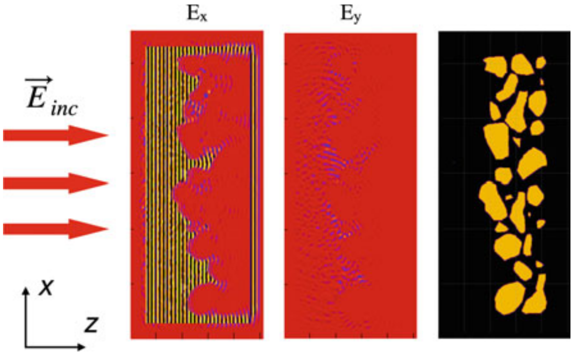

Fig. 20 Distributions of the E$_x$ and E$_y$ electric near field components and a cross-section of a thick layer sample

We simulate normal incidence of a plane wave along Z axis (Fig. 20) and calculate far-field scattering matrix elements as functions of the scattering angle averaged over azimuth. All our results here are averaged over the number of samples from 300 to more than 500.

As in the case of non-absorbing clusters the particles are nearly touching and the minimum distance between them is smaller than the wavelength. At the same time distribution of distances between reflecting surface elements of neighbor particles is broad and can be much larger than the wavelength due to their size. Thus, random variation of heights on the surface of such layers is large enough to avoid specular reflection.

We note that layers with thickness of $X_L = 60$, which corresponds to just 2–3 particles with $X_d = 30$, appear to be optically thick. In Fig. 20 we show a cross-section of such sample and steady-state distributions of the E$_x$ and E$_y$ components of the near-field. Most of the energy is either absorbed or reflected. The incident field does not propagate deeper than one particle size because of the large packing density. Therefore, the backscattering properties of such a structure should be determined by single and the first few orders of multiple scattering in the very upper layer. Generally, this result allows consideration of layers with limited thickness in the numerical modelling, at least for the given size of constituents. This is also a clear reason why an elementary scattering volume cannot be defined here, and the radiative transfer approach cannot be applied to such media.

The results of simulations for thick layers are shown in Fig. 21. One can see the optical thickness effect in the angular dependence of intensity. Reflectance drops quickly from the backscattering direction to 90° due to shadowing. There is a small contribution of single external scattering from the edges at intermediate scattering angles and the forward scattering peak is caused by diffraction from the entire sample. The scattered light has a very high positive polarization near Brewster angle which is a manifestation of Umov's effect. The reason is domination of single scattering in this angular range and little multiple scattering due to low single scattering albedo of particles. However, the situation is different near backscattering. Single scattering here would eventually lead from positive to zero polarization at exact backscattering. Light scattering by large compact particles at high absorption is governed

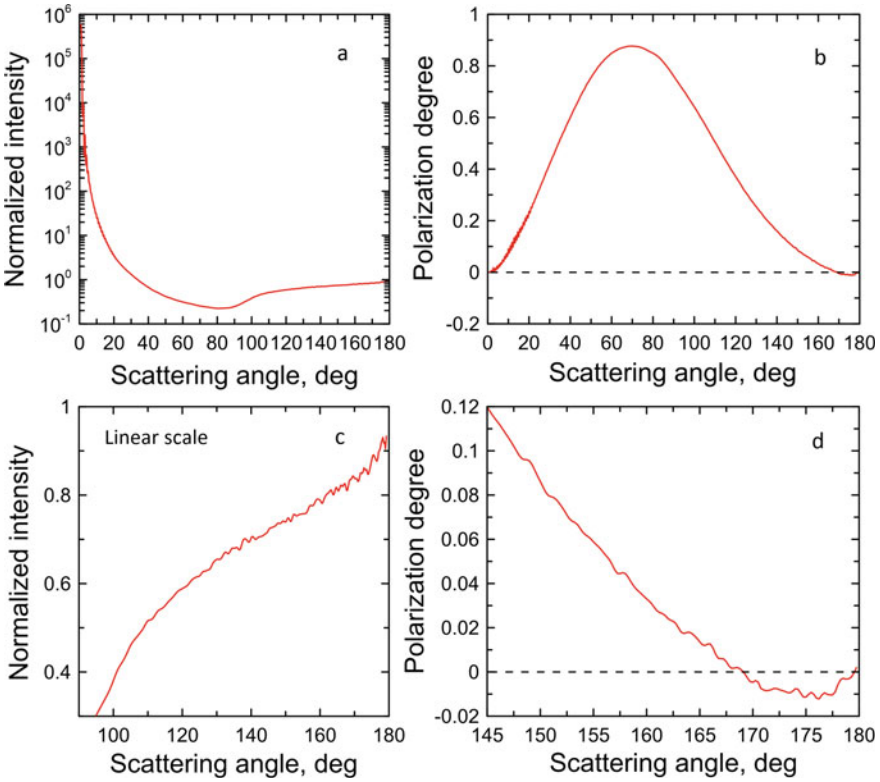

Fig. 21 Scattering angle dependencies of intensity in logarithmic (**a**) and linear (**c**) scales and degree of linear polarization (**b**, **d**) computed for absorbing thick layers. The diameter and the thickness of layers are $X_D = 200$ and $X_L = 60$, respectively. The number of constituents is $N \approx 150$ and the bulk packing density is $\rho = 0.5$ (Grynko et al. 2022)

mostly by the Fresnel reflection which always produces positive polarization. We obtain, however, an NP feature with inversion angle at ≈168°. This result is qualitatively similar to the polarization measurements of dark powder samples with similar particles sizes (e.g., boron carbide). Accounting for small contribution of multiple scattering and its low polarization one can assume that NP is a result of coherent double scattering between close neighbor particles. We note that models of incoherent double and multiple scattering are not able to reproduce NP at backscattering (Shkuratov et al. 1994; Shkuratov and Grynko 2005).

To reduce multiple scattering in the structure one can consider a simplified model of a monolayer of particles with the same size. We did simulations for a set of such samples with a diameter of $X_D = 200$ and a thickness of $X_L = 30$. The number of constituents was $N = 50$ in this case. The results for monolayers and thick layers are compared in Fig. 22. Despite the big difference in intensity the polarization curves are very close to each other for thick layers and monolayers. Monolayers

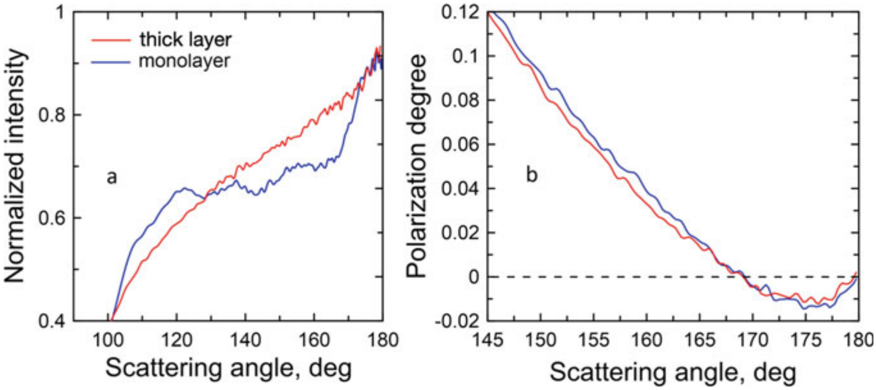

Fig. 22 Comparison of intensity (**a**) and degree of linear polarization (**b**) computed for thick layer and monolayer samples with the same diameters ($X_D = 200$) (Grynko et al. 2022)

show a prominent backscattering peak as a result of coherent enhancement and little dependence at smaller angles, whereas in thick layers the peak is obscured by shadowing that takes effect in the entire angular range. It is, however, not the case for polarization. The result confirms the assumption that NP is caused by double scattering in the very upper layer as higher orders are unlikely to be present in such a structure. This confirms the validity of simple formulas (Shkuratov et al., 1994) for calculating the negative polarization of atmosphere-less celestial bodies and laboratory samples.

With further simplification of the system down to just two particles NP is reduced but does not disappear. In Fig. 23a we decrease the number of constituents in a layer to 10, 4 and 2. Two close irregular particles can produce small but well detected NP feature. This proves the double-scattering coherent mechanism. The effect can be

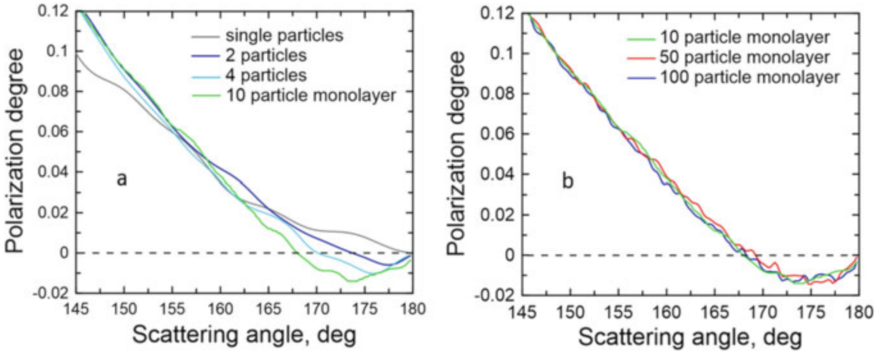

Fig. 23 Comparison of the degree of linear polarization at backscattering computed for single particles, 2-, and 4-particle structures (**a**) and monolayers of 50 ($X_D = 200$) and 100 particles ($X_D = 250$) (**b**) (Grynko et al. 2022)

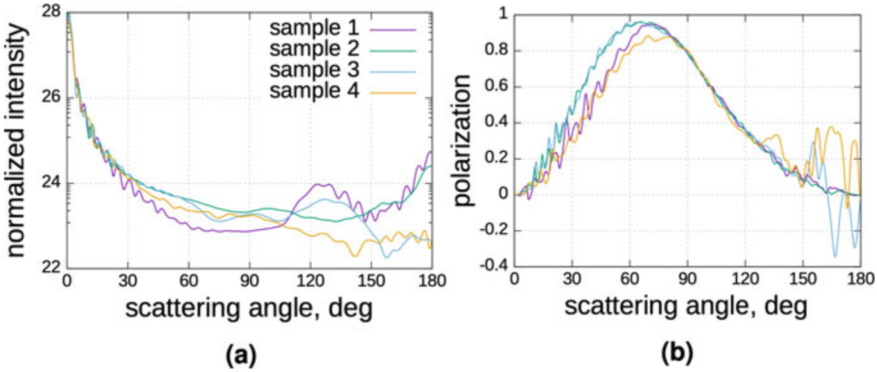

Fig. 24 Scattering angle curves of intensity and linear polarization for single samples of two-particle structures. Each curve corresponds to one simulation (Alhaddad et al. 2022)

quickly enhanced by adding two more particles. This is an effect of relative contributions of single and double scattering and increasing probability for constructive interference at backscattering. In a system of two particles there can be only one path for counterpropagating waves whereas this number is six for a four-particle structure.

We note that double scattering mechanism producing NP requires further detailed study. Our preliminary results for different geometries of pairs of scatterers larger than the wavelength show that this is a non-trivial coherent process. As an example, we show typical intensity and polarization curves computed for single two-particle samples in Fig. 24 (Alhaddad et al. 2022). Depending on the geometry of particles single scattering and Fresnel reflection can dominate at backscattering with low polarization approaching to zero. A corner like geometry is more beneficial for dominating double scattering and interference of two counterpropagating propagating waves reflected from the surfaces of the scatterers. This may lead to both enhanced negative and positive polarization. If the corresponding geometry is characteristic for a large ensemble of random samples NP feature survives after averaging.

The polarization curve should converge at the point where a sample with finite dimensions is large enough and the relative contribution of the edge scattering becomes insignificant. Simulations for monolayers with diameters up to $X_D = 250$ ($N = 100$ particles) (Fig. 23) show that this convergence starts already at the number of $N = 10$ which corresponds to the diameter of $X_D \approx 90$. In the curves corresponding to $X_D = 200$ and $X_D = 250$ the NP feature does not change any more. Thus, for backscattering numerical simulations one should consider monolayers and thick layers with the number of particles on the surface of at least $N = 10$ or a few tens, if their sizes are smaller than $X_d = 30$. Otherwise, the result near backscattering may depend on the size of the sample.

To study the possibilities that our code opens with the available HPC resources we also did test simulation runs for extremely large monolayer samples. In Fig. 25 we compare intensity and polarization curves for the $X_D = 200$ thick layer and monolayer cases and two monolayer samples with $X_D = 300$ and $X_D = 500$ ($N = 400$ particles).

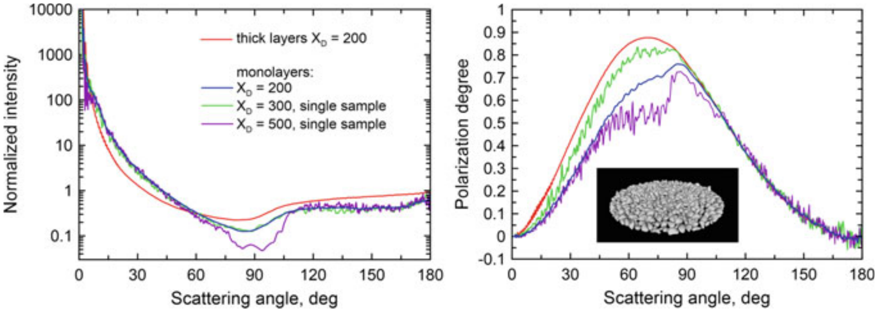

Fig. 25 Comparison of the intensity and linear polarization curves for thick layers and large monolayers of GRF particles with diameters $X_D = 200$ (sample averaged) and single samples with $X_D = 300$ and $X_D = 500$. In the last case the number of constituents is $N = 400$ (see inset). The size of constituents is $X_d = 30$

Surprisingly, monolayers with sizes $X_D = 200 – 500$ show very similar properties in the range of 100 -180°. We note also that at very large sizes single samples provide better statistics per sample and such simulations require smaller number of them for quality averaging. This is an encouraging result showing that numerical simulations for such systems are feasible and can be executed in reasonable time. At this scale it becomes possible to generate multi-particle layers of irregular particles with random topographies, run full wave simulations and compare the results with experimental measurements.

4 Conclusion

We show that the light scattering problem can be solved for large systems of hundreds and thousands of irregular particles avoiding approximations with available HPC resources if an efficient numerical method and a parallel light scattering code are applied. The computed intensity and polarization scattering angle curves start converging at sizes of different model clusters of $X_D = 100 – 200$. Thus, systematic full wave light scattering simulations become feasible for realistic models of particulate media with sizes of samples much larger than the wavelength.

Our results for large clusters of non-absorbing irregular particles clearly demonstrate the crucial role of high packing density for light transport and the backscattering phenomena. In dense particulate media light propagation is highly localized and is similar to a percolation process that is controlled by topology and degree of disorder. The differences in the structure of the considered model clusters are seen in the intensity and polarization scattering angle curves. Comparison of dense and sparse structures with uniform and non-uniform distributions of particles showed that the IS at backscattering is formed by small agglomerates of just a few particles. In polarization, single particles in the very upper layer play a role of sources of NP which is suppressed by the multiple scattering component. If diffuse multiple scattering is reduced at high packing density, the NP feature can be enhanced. This is in agreement with experimental results.

The simulation results for absorbing layers of irregular particles confirm the coherent double scattering mechanism of the origin of NP for low-albedo surfaces. The total optical response is determined in this case by the contributions of single and mostly double scattering in the very upper layer. Due to high bulk packing density the incident light does not penetrate deeper than a few particle sizes if they are larger than the wavelength. This allows considering model layers with limited thickness in the numerical simulations. We can also specify a lower limit for the number of particles in the NP studies which should be larger than ten at $X_d \sim 30$ or a few tens at smaller sizes.

In general, analysis of the distribution of the steady-state near fields shows that in both cases of non-absorbing and absorbing materials and high packing density the radiative transfer approach cannot be applied to the problem of light scattering from powder-like surfaces. The small mean transport length and complex geometry of the propagation pattern make definition of an elementary scattering volume impossible.

Acknowledgements The authors gratefully acknowledge the computing time granted by the Paderborn Center for Parallel Computing (PC^2) and by the John von Neumann Institute for Computing (NIC) on the supercomputer JUWELS at Jülich Supercomputing Centre (JSC).

References

Aegerter CM, Maret G (2009) Coherent backscattering and Anderson localization of light. Prog Opt 52. 1–62. Elsevier

Alhaddad S, Grynko Y, Farheen H, Förstner J (2022) Numerical analysis of the coherent mechanism producing negative polarization at backscattering from systems of absorbing particles. Opt Lett 47:58–61

Angulo LD, Alvarez J, Teixeira FL, Pantoja MF, Garcia SG (2014) J Comput Phys 256:678

Belskaya IN, Shkuratov YuG, Efimov YuS, Shakhovskoy NM, Gil-Hutton R, Cellino A, Zubko ES, Ovcharenko AA, Bondarenko SYu Shevchenko VG, Fornasier D, Barbieri C (2005) The F-type asteroids with small inversion angles of polarization. Icarus 178:213–221

Belskaya I, Cellino A, Levasseur-Regourd A-C, Bagnulo S (2019) Optical Polarimetry of small solar system bodies: from asteroids to debris disks. In: Mignani R, Shearer A, Słowikowska A, Zane S (eds) Astronomical polarisation from the infrared to gamma rays. Astrophysics and Space Science Library, vol 460. Springer Cham, pp 223–246

Bertrand M, Devilez A, Hugonin JP, Lalanne P, Vynck K (2020) Global polarizability matrix method for efficient modeling of light scattering by dense ensembles of non-spherical particles in stratified media. J Opt Soc Am A 37:70–83

Bondarenko S, Ovcharenko A, Shkuratov Y, Videen G, Eversole J, Hart M (2006) Light backscatter by surfaces composed of small spherical particles. Appl Opt 45:3871–3877

Burgess I, Abedzadeh N, Kay T, Shneidman AV, Cranshaw DJ, Lončar M, Aizenberg J (2016) Tuning and freezing disorder in photonic crystals using percolation lithography. Sci Rep 6:19542

Busch K, König M, Niegemann J (2011) Discontinuous Galerkin Methods in Nanophotonics. Laser Phot Rev 5:773–809

Capoglu IR, Taflove A, Backman V (2008) Generation of an incident focused light pulse in FDTD. Opt Express 16:19208–19220

Coumans E, Bai Y (2016–2021) Pybullet, a python module for physics simulation for games, robotics and machine learning. http://pybullet.org

Demirel A, Niegemann J, Busch K, Hochbruck H (2015) J Comput Phys 285:133

Descombes S, Durochat C, Lanteri S, Moya L, Scheid C, Viquerat J (2013) Recent advances on a DGTD method for time-domain electromagnetics. Photonics Nanostruct Fundam Appl 11:291–302

Egel A, Pattelli L, Mazzamuto G, Wiersma DS, Lemmer U (2017) CELES: CUDA-accelerated simulation of electromagnetic scattering by large ensembles of spheres. J Quant Spectrosc Radiat Transf 199:103–110

Fazio B, Irrera A, Pirotta S, D'Andrea C, Del Sorbo S, Faro MJL, Gucciardi PG, Iati MA, Saija R, Patrini M, Musumeci P, Vasi CS, Wiersma DS, Galli M, Priolo F (2017) Coherent backscattering of raman light. Nat Phot 11:170–176

Grynko Y, Förstner J (2017) Simulation of second harmonic generation from photonic nanostructures using the discontinuous Galerkin Time Domain method. In: Agrawal A, Benson T, De La Rue RM, Wurtz GA (eds) Recent trends in computational photonics. Springer, Cham, pp 261–284

Grynko Y, Shkuratov Y (2002) The scattering matrix of transparent particles of random shape in the geometrical optics approximation. Opt Spectrosc 93:885–893

Grynko Y, Shkuratov Y (2003) Scattering matrix calculated in geometric optics approximation for semitransparent particles faceted with various shapes. J Quant Spectrosc Radiat Transf 78:319–340

Grynko Y, Shkuratov Y (2007) Ray tracing simulation of light scattering by spherical clusters consisting of particles with different shapes. J Quant Spectrosc Radiat Transf 106:56–62

Grynko Y, Shkuratov Y (2008) Light scattering from particulate surfaces in geometrical optics approximation. In: Kokhanovsky A (ed) Light scattering reviews, vol III. Springer, Berlin, pp 329–382

Grynko Y, Shkuratov Y, Videen G (2006) Polarization of near-forward-scattered light from particulate substrates illuminated at near-grazing angles. J Quant Spectrosc Radiat Transf 101:522–526

Grynko Y, Zubko E, Foerstner J (2014) Light scattering by random irregular particles of two classes of shape. Opt Lett 39:6723–6726

Grynko Y, Shkuratov Y, Förstner J (2016) Light scattering by irregular particles much larger than the wavelength with wavelength-scale surface roughnes. Opt Lett 14:3491–3493

Grynko Y, Shkuratov Y, Foerstner J (2018) Intensity surge and negative polarization of light from compact irregular particles. Opt Lett 43:3562–3565

Grynko Y, Shkuratov Y, Förstner J (2020) Light backscattering from large clusters of densely packed irregular particles. J Quant Spectrosc Radiat Transf 255:107234

Grynko Y, Shkuratov Y, Alhaddad S, Förstner S (2022) Negative polarization of light at backscattering from a numerical analog of planetary regoliths, Icarus 2022, submitted

Hapke B (1981) Bidirectional reflectance spectroscopy I. Theory. J Geophys Res 86:3039–3054

Hapke B (2012) Theory of reflectance and emittance spectroscopy. Cambridge University Press, Cambridge, p 513

Hesthaven JS, Warburton T (2002) Nodal high-order methods on unstructured grids: I. Time-domain solution of Maxwell's equations. J Comput Phys 181:186–221

Jacques SL (2013) Optical properties of biological tissues: a review. Phys Med Biol 58:R37–R61

Jeong S, Lee Y, Choi W, Kang S, Hong JH, Park J, Lim Y, Park H, Choi W (2018) Focusing of light energy inside a scattering medium by controlling the time-gated multiple light scattering. Nature Phot 12:277–283

Kokhanovsky AA, de Leeuw G, eds (2009) Satellite Aerosol remote sensing over land, Praxis, Chichester, UK, 388 p

Kolokolova L, Ito G, Pitman KM, McMichael K, Reui N (2019) Spectral modeling using radiative transfer theory with packing density correction: demonstration for saturnian icy satellites. Planet Sci J 1:74

Kolokolova L, Hough J, Levasseur-Regourd A-C (eds) (2015) Polarimetry of stars and planetary systems. Cambridge University Press

Levasseur-Regour A-C, Renard J-B, Shkuratov Y, Hadamcik E (2015) Laboratory studies. In: Kolokolova L, Hough J, Levasseur-Regourd A-C (eds) Polarimetry of stars of stars and planetary systems. Cambridge University Press, pp 62–80

Linden S, Niesler FBP, Förstner J, Grynko Y, Meier T, Wegener M (2012) Collective effects in second-harmonic generation from split-ring-resonator arrays. Phys Rev Lett 109:015502

Liu C, Panetta RL, Ping Yang P (2012) Application of the pseudo-spectral time domain method to compute particle single-scattering properties for size parameters up to 200. J Quant Spectrosc Radiat Transf 113:1728–1740

Lyot B (1929) Recherches sur la polarisation de la lumiere des planetes et de quelques substances terrestres. Ann Obs Meudon 8(1):1–161

Markkanen J, Agarwal J, Väisänen PA, Muinonen K (2018) Interpretation of the phase functions measured by the OSIRIS instrument for comet 67P/Churyumov–Gerasimenko. Astrophysl J Lett 868:L16

Mishchenko MI, Dlugach JM, Chowdhary J, Zakharova NT (2015) Polarized bidirectional reflectance of optically thick sparse particulate layers: an efficient numerically exact radiative-transfer solution. J Quant Spectros Radiat Trans 156:97–108

Mishchenko M, Rosenbush V, Kiselev N, Lupishko D, Tishkovets T, Kaydash V, Belskaya I, Efimov Y, N. Shakhovskoy N (2010) Polarimetric remote sensing of Solar System objects**.** Akademperiodyka, Kiev

Muinonen K (1989) Electromagnetic scattering by two interacting dipoles. Proc. URSI Electromagn Theory Symp. Stockholm, Sweden, pp 428–430

Muinonen K, Shkuratov Y, Ovcharenko A, Piironen J, Stankevich D, Miloslavskaya O, Kaasalainen S, Josset J-L (2002) The SMART-1 AMIE experiment: implication to the lunar opposition effect. Planet and Space Sc 5:1339–1344

Muinonen K, Penttilä A, Videen G, (2015a) Multiple scattering of light in particulate planetary media. In: Kolokolova L, Hough J, Levasseur-Regourd A-C (eds) Polarimetry of stars of stars and planetary systems. Cambridge University Press, pp 114–129

Muinonen K, Penttilä A, Videen G (2015b) Multiple scattering of light in particulate planetary media. In: Kolokolova L, Hough J, Levasseur-Regourd A-C (eds) Polarimetry of stars of stars and planetary systems. Cambridge University Press, pp 114–129

Nelson RM, Boryta MD, Hapke BW, Manatt KS, Shkurato Y, Psarev V, Vandervoort V, Kroner D, Nebedum A, Vides CL, Quiñones J (2018) Laboratory simulations of planetary surfaces: understanding regolith physical properties from remote photopolarimetric observations. Icarus 302:483–498

Niegemann J, Koenig M, Stannigel K, Busch K (2009) Higher-order time-domain methods for the analysis of nano-photonic systems. Photonics Nanostruct Fundam Appl 7(1):2

Niegemann J, Diehl R, Busch K (2012) Efficient low-storage Runge-Kutta schemes with optimized stability regions. J Comp Phys 231:364

Ovcharenko AA, Bondarenko SY, Zubko ES, Shkuratov YG, Videen G, Nelson RM, Smythe WD (2006) Particle size effect on the opposition spike and negative polarization. J Quant Spectros Radiat Trans 101:394–403

Pattelli L, Egel A, Lemmer U, Wiersma DS (2018) Role of packing density and spatial correlations in strongly scattering 3D systems. Optica 5:1037–1045

Petrova EV, Tishkovets VP, Nelson RM, Boryta MD (2019) Prospects for estimating the properties of a loose surface from the phase profiles of polarization and intensity of the scattered light. Sol Sys Res 53:172–180

Pitman KM, Kolokolova L, Verbiscer AJ, Mackowski DW, Joseph ECS (2017) Coherent backscattering effect in spectra of icy satellites and its modeling using multi-sphere T-matrix (MSTM) code for layers of particles. Planet Sp Sci 149:23–31

Poch O, Cerubini R, Pommerol A, Jost B, Thomas N (2018) Polarimetry of water ice particles providing insights on grain size and degree of sintering on icy planetary surfaces. J Geophys Res Planets 123:2564–2584

Podowitz DI, Liu C, Yang P, Yurkin MA (2014) Comparison of the pseudo-spectral time domain method and the discrete dipole approximation for light scattering by ice spheres. J Quant Spectrosc Radiat Transf 146:402–409

Schröder SE, Grynko Y, Pommerol A, Keller HU, Thomas N, Roush TL (2014) Laboratory observations and simulations of phase reddening. Icarus 239:201–216

Segev M, Silberberg Y, Christodoulides D (2013) Anderson localization of light. Nature Phot 7:197–204

Shishko V, Konoshonkin A, Kustova N, Timofeev D, Borovoi A (2019) Coherent and incoherent backscattering by a single large particle of irregular shape. Opt Expr 27(23):32984–32993

Shkuratov YG (1985) On the opposition brightness surge and light negative polarization of solid cosmic surfaces. Astron Circ 1400:3–6 (in Russian)

Shkuratov Y (1989) Interference mechanism of opposition spike and negative polarization of atmosphereless planetary bodies. Bull Am Astron Soc 21:989

Shkuratov YG (1991) An interference model of the negative polarization of light scattered by atmosphereless celestial bodies. Sol Syst Res 25:134–142

Shkuratov Y, Grynko Y (2005) Light scattering by media composed of semitransparent particles of different shapes in ray optics approximation: consequences for spectroscopy, photometry, and polarimetry of planetary regoliths. Icarus 173:16–28

Shkuratov Y, Opanasenko N, Kreslavsky M (1992) Polarimetric and photometric properties of the moon: Telescopic observations and laboratory simulations: 1. The negative polarization. Icarus 95:283–299

Shkuratov YG, Muinonen K, Bowell E, Lumme K, Peltoniemi J, Kreslavsky MA, Stankevich DG, Tishkovets VP, Opanasenko NV, Melkumova LY (1994) A critical review of theoretical models for the negative polarization of light scattered by atmosphereless solar system bodies. Earth Moon Planet 65(3):201–246

Shkuratov Y, Ovcharenko A, Zubko E, Miloslavskaya O, Muinonen K, Piironen J, Nelson R, Smythe W, Rosenbush V, Helfenstein P (2002) The opposition effect and negative polarization of structural analogs for planetary regoliths. Icarus 159:396–416

Shkuratov Y, Videen G, Kreslavsky M, Belskaya I, Kaydash VA, Omelchenko V, Opanasenko N, Zubko E (2004) Scattering properties of planetary regoliths near opposition. In: Videen G, Yatskiv Y, Mishchenko M (eds) Photopolarimetry in remote sensing. Springer, Netherlands, pp 191–208

Shkuratov Y, Bondarenko S, Ovcharenko A, Pieters C, Hiroi T, Volten H, Mun˜oz O, Videen G (2006) Comparative studies of the reflectance and degree of linear polarization of particulate surfaces and independently scattering particles. Quant Spectrosc Radiat Transf 100:340–358

Shkuratov Y, Opanasenko N, Zubko E, Grynko Y, Korokhin V, Pieters C (2007a) Multispectral polarimetry as a tool to investigate texture and chemistry of lunar regolith particles. Icarus 187:406–416

Shkuratov Y, Bondarenko S, Kaydash V, Videen G, Muñoz O, Volten (2007b) Photometry and polarimetry of particulate surfaces and aerosol particles over a wide range of phase angles. J Quant Spectrosc Radiat Transf 106:487–508

Shkuratov Y, Kaydash V, Korokhin V, Velikodsky Y, Opanasenko N, Videen G (2011) Optical measurements of the Moon as a tool to study its surface. Planet Space Sci 59:1326–1371

Stankevich D, Shkuratov Y, Grynko Y, Muinonen K (2003) Computer simulations for multiple scattering of light rays in systems of opaque particles. J Quant Spectrosc Radiat Transf 76:1–16

Stannigel K, Konig M, Niegemann J, Busch K (2009) Discontinuous Galerkin time-domain computations of metallic nanostructures. Opt Express 17:14934

Sun W, Nousiainen T, Muinonen K, Fu Q, Loeb NG, Videen G (2003) Light scattering by Gaussian particles: a solution with finite-difference time-domain technique. J Quant Spectrosc Radiat Transf 79–80:1083–1090

Sun W, Videen G, Fu Q, Hu Y (2013) Scattered-field FDTD and PSTD algorithms with CPML absorbing boundary conditions for light scattering by aerosols. J Quant Spectrosc Radiat Transf 131:166–174

Taflove A (1995) Computational electrodynamics:the finite-difference time-domain method. Artech House, Boston

Theobald D, Egel A, Gomard G, Lemmer U (2017) Plane-wave coupling formalism for T-matrix simulations of light scattering by nonspherical particles. Phys Rev A 96:03382

Theobald D, Beutel D, Borgmann L, Mescher H, Gomard G, Rockstuhl C, Lemmer U (2021) Simulation of light scattering in large, disordered nanostructures using a periodic T-matrix method. J Quant Spectrosc Radiat Transf 27:107802

Väisänen T, Markkanen J, Hadamcik E, Renard JB, Lasue J, Levasseur-Regourd A-C, Blum J, Muinonen K (2020) Scattering of light by a large, densely packed agglomerate of small silica spheres. Opt Lett 45:1679–1682

Videen G (2002) Polarization opposition effect and second-order ray tracing. Appl Opt 41:5115–5121

Videen G, Yatskiv Ya, Mishchenko M (eds) (2004) Photopolarimetry in remote sensing. NATO science series. Kluwer Academic Publishers, Netherlands

Warburton T (2008) DGTD codes. http://www.nudg.org

Wiersma DS (2008) The physics and applications of random lasers. Nature Phys 4:359–367

Wiktorowicz SJ, Stam DM (2015) Exoplanets. Polarimetry of stars of stars and planetary systems. Cambridge University Press, pp 439–461

Xu WJ, Liu GY, Yang H (2020) Study on the mechanical behavior of sands using 3D discrete element method with realistic particle models. Acta Geotech 15:2813–2828

Yang P, Feng Q, Hong G, Kattawar GW, Wiscombe WJ, Mishchenko MI, Dubovik O, Laszlo I, Sokolik IN (2007) Modeling of the scattering and radiative properties of nonspherical dust particles. J of Aerosol Sci 38:995–1014

Zhai P-W, Lee Y-K, Kattawar GW, Yang P (2004) Implementing the near to far field transformation in the finite-difference time-domain method. Appl Opt 43:3738–3746

Zubko E, Muinonen K, Muñoz O, Nousiainen T, Shkuratov Y, Sun W (2013) Light scattering by feldspar particles: Comparison of model agglomerate debris particles with laboratory samples. J Quant Spectrosc Radiat Transf 131:175–187

Light Backscattering by Atmospheric Particles: From Laboratory to Field Experiments

A. Miffre

Abstract Atmospheric particles may somewhat counterbalance the global warming effect of the Earth's atmosphere due to greenhouse gases by directly contributing to the Earth's climate through light scattering and absorption processes. According to the IPCC report (IPCC in Climate change 2013: the physical science basis. New York: Cambridge Univ. Press, 2013), the contribution of such particles to the Earth's radiative budget however remains difficult to handle and quantify, mainly due to the complexity of these particles, which present a wide range of sizes, shapes and complex refractive indices. To face such a complexity, a major source of global data on these particles is provided by ground-based and satellite-based lidar remote sensing instruments, which are based on light backscattering and extinction by atmospheric particles. In this context, this book chapter proposes to present some recent advances in the field of light backscattering by complex-shaped atmospheric particles at specific backward scattering angle ($\theta = \pi$) at which lidar instruments operate, for the first time to our knowledge in laboratory where a π-polarimeter has been built and operated for aerosols (Miffre et al. in J Quant Spectrosc Radiat Transf 169:79–90, 2016; Miffre et al. in J Quant Spectrosc Radiat Transf 222–223:45–59, 2019b; Miffre et al. Atmos Meas Tech, 2022). These papers are the results of a team work in which Prof. Rairoux's expertise in lidar remote sensing and laser spectroscopy played a key role. This work also owes much to former PhD students, G. David and D. Cholleton, who also played a key role. Laboratory experiments at near ($\theta < \pi$) backscattering angles are likewise proposed in complement as well as cooperative works with ONERA (Paulien et al. in J Quant Spectrosc Radiat Transf 260, 2021) and chemical colleagues from Lyon University (France) and North Carolina University (USA) (Dubois et al. in Phys Chem Chem Phys 23:5927–5935, 2021) to explore light backscattering by complex-shaped particles. The benefits of this new laboratory approach, in comparison with existing light scattering numerical simulations and lidar field experiments, is discussed. We hope this book chapter will improve

---

A. Miffre (✉)
University of Lyon, Université Claude Bernard Lyon 1, CNRS, Institut Lumière Matière, F-69622, Villeurbanne, France
e-mail: alain.miffre@univ-lyon1.fr

A. Kokhanovsky (ed.), *Springer Series in Light Scattering*, Springer Series in Light Scattering, https://doi.org/10.1007/978-3-031-10298-1_5

our understanding of the complex physical process of light backscattering by atmospheric particles, to in turn improve our understanding of the radiative properties of complex-shaped atmospheric particles, to provide answer to radiative transfer issues.

1 Introduction

1.1 On the Complexity of Atmospheric Particles

The Earth's atmosphere is composed of particles which are extremely complex in size, shape and chemical composition (Mishchenko et al. 2002; Seinfeld and Pandis 2006). While the particles size may vary from a few nanometers (soot monomers) to several micrometers (for pollen), the particles shape is generally highly irregular, sometimes with sharp edges, as for mineral dust. Atmospheric particles are also potentially highly inhomogeneous (Kahnert 2015; Liu et al. 2014; Mishchenko et al. 2013) and may present a rough surface (Kahnert and Rother 2011; Kemppinen et al. 2015; Zubko et al. 2007). Figure 1 highlights the complexity in size and shape of several of such particles, through their laboratory TEM- images.

This situation is obviously much more complex in the atmosphere, where these particles are not isolated but may interact through a complex chemistry (Seinfeld and Pandis 2006) and form particle mixtures (Mishchenko et al. 2004a, b). During advection transport from source regions to remote places where intrusion episodes occur, freshly emitted particles indeed experience chemical reactivity, including potential humidification, possible scavenging, sedimentation processes, water adsorption at the particles surface which may strongly influence their size and their shape. Largest particles, for sizes in the range of ten micrometers, are rapidly removed by gravitational settling. In contrast, finer particles with longer residence times in the Earth's atmosphere, may be transported over large distances and may remain in the troposphere for several weeks (Ovadnevaite et al. 2009) which further reinforce their radiative impact by affecting the Earth's climate at both local, regional and global scales. Hence, after long-range transport, atmospheric particles are highly dispersed and aged, and may present sizes and shapes that can be very different from those observed in the source region. As a result, the vertical layering generally observed at far-range remote sites where intrusion episodes occur is itself complex and has to

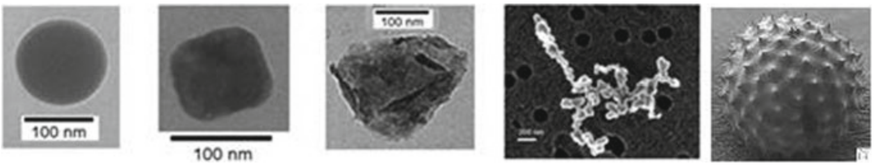

Fig. 1 Atmospheric particles TEM-images (from left to right, taken at iLM): ammonium sulfate, sea-salt below crystallization point, Arizona test dust, soot aggregate, ragweed pollen

be accurately analysed to quantify the Earth's energy balance. For accurate radiative forcing assessments, the particles non-sphericity should be taken into account, by including the particles inhomogeneity. Among the major uncertainties involved in climate change modeling, the lack of knowledge on the atmospheric particles shape is indeed an essential point: non-spherical particles are particularly challenging, because there is no generic, exact light scattering theory for such complex-shaped particles (Kahnert et al. 2014; Mishchenko 2009), except for some specific geometries far away from the observed highly-irregularly shape of atmospheric particles (Mishchenko et al. 2002). Hence, while atmospheric particles contribute to the Earth's radiative budget directly through light scattering and extinction (Mishchenko et al. 2002), applying the century-old Lorenz-Mie theory to such complex-shaped particles may lead to significant errors in aerosol climate forcing and radiance computations, as non-spherical particles scatter light differently from volume or surface-equivalent spheres (Kahnert et al. 2007). In particular, orientation averaging over an ensemble of non-spherical particles does not lead to the same scattering pattern as for spheres (Nousiainen 2009). In conclusion, there is no analytical solution of the Maxwell's equations exists for light-scattering by these particles, which are hard to represent mathematically in climate models. Only recently (Räisänen et al. 2013), climate models started to account for the non-sphericity of atmospheric aerosols by considering spheroids. As a result, light scattering and absorption has to be quantified by taking into account the particles nonsphericity. This is especially true for the specific backward scattering direction, at which most climate satellites operate, including those involving lidar remote sensing instruments such as the CALIPSO mission (Winker et al. 2003).

1.2 On the Importance of Light Backscattering by Atmospheric Particles

To face such a complexity and improve our understanding of the Earth's climate, a powerful methodology is to take benefit from light backscattering by atmospheric particles. Following Mishchenko's text book (Mishchenko et al. 2002), elastic light scattering is the physical process by which particles "*extract some of the incident energy and scatter it in all directions at the frequency of the incident beam, generally giving rise to a polarization state different from that of the incident beam*". In this book chapter, we will focus on elastic light backscattering by atmospheric particles. By light backscattering, we here intend light scattering in the exact (i.e., strict) backward scattering direction of π or 180.0°, hence far from the 90 to 170° scattering angles, sometimes reported in the literature as backward scattering direction. Light scattering may indeed vary when the scattering angle differs from the exact π-backscattering angle. Among all light scattering directions, the backward scattering direction has drawn attention for both practical and fundamental reasons. The motivations for this work, dedicated on light backscattering by atmospheric particles, are hence the following:

- Basically, light backscattering has proven efficiency for providing information on the optical properties of condensed or gaseous matter, with numerous applications in various research fields, such as biomedicine (Vitkin and Studinski 2001; Wang et al. 2012) or fundamental research (Wiersma et al. 1997). This approach should be extended to particles in dilute media such as aerosols. This is especially true for sulfate particles as sulfate particles induce a net cooling of the Earth's atmosphere due to their ability to backscatter light (Dubois et al. 2021). Light backscattering is also important from a more fundamental point of view, as it may lead to the so-called coherent backscattering (Mishchenko et al. 2002). Also, as noted in (Fu et al. 2017), the backward scattering direction has been identified as one of the most sensitive directions to the particles heterogeneities and surface structure, including possible surface roughness. Hence, as discussed in (Kemppinen et al. 2015) through numerical simulations, the most prominent effects of surface roughness are seen close to the exact backscattering direction and the diagonal scattering matrix elements are affected the most in the backscattering direction. We could then investigate the influence of surface roughness on lidar backscattering profiles (Mehri et al. 2018). Also, near the backward scattering direction, light scattering numerical simulations exhibit a narrow double-lobe feature when studying small-scale surface roughness (Kahnert et al. 2012). Finally, for radiative transfer purposes, the scattering phase function needs to be precisely known over the whole scattering angle range, and hence covers the backward scattering direction with precision.
- Practically speaking, light backscattering is involved in ground-based and satellite-based lidar remote sensing instruments which provide a major source of global data on, for instance, mineral dust, which are needed for radiative and climate forcing assessments. Lidar remote sensing provides fast, reliable and unique vertical profiles of particles backscattering, such as mineral dust, under in-situ atmospheric conditions of temperature and humidity. There, the highly irregular shape of mineral dust particles is accounted for by carefully analyzing the polarization state of the electromagnetic radiation, allowing to evaluate the linear depolarization ratio, after robust calibration of the polarization detector (David et al. 2012; Miffre et al. 2019a). Hence, if a sufficiently high sensitivity is achieved on the polarization lidar detector, the complex vertical layering of mineral dust can be revealed in the free troposphere, even when mineral dust are involved in two or three component particle external mixtures, as we published (David et al. 2013; Mehri et al. 2018). However, the downside of such field measurements is that mineral dust particles cannot be identified with a sole polarization lidar backscattering experiment, as the measured depolarization is not mineral dust particles specific but dedicated to particles mixtures. In this context, controlled laboratory measurements are interesting as they allow studying the backscattering property of a determined ensemble of mineral dust particles, which may provide accurate inputs to better constrain lidar inversions.

1.3 Theoretical Considerations

We here consider elastic light backscattering at wavelength λ by an ensemble of particles with complex refractive index *m*, which are not static but move in an unbounded host medium such as ambient air. To describe the interaction of light with such a particles ensemble, the traditional approach is to approximate the particles ensemble as a macroscopic body on which the Maxwell's equations can be solved, hence ignoring the discreteness of matter, which avoids studying underlying quantum effects (Mishchenko et al. 2002). Under these assumptions, the backscattered electromagnetic field is a function of the free space dyadic Green function and the scatterer is perceived as a unique object with a spatial distribution of its complex refractive index *m*. In the far-field approximation, the simpler expression of the Green function leads to a simplified expression of the scattered electric field, then linked to the incident electric field through the amplitude scattering matrix (Mishchenko 2009).

(a) Scattering matrix at near and exact backscattering angles

To describe light backscattering by atmospheric non-spherical particles in laboratory, numerically or in field, the framework is hence that of the scattering matrix $[\boldsymbol{F}_\lambda]$, relating the incident and backscattered Stokes vectors $(St) = [I, Q, U, V]^{\mathrm{T}}$ which describe the polarization state of the incident and scattered light (Bohren and Huffman 1983):

$$\begin{pmatrix} I \\ Q \\ U \\ V \end{pmatrix} = \frac{1}{k^2 d^2}[F_\lambda(\theta)] \begin{pmatrix} I_i \\ Q_i \\ U_i \\ V_i \end{pmatrix} \tag{1}$$

where d is the distance from the particles ensemble to the detector and the i-subscript refers to the incident electromagnetic radiation. The first Stokes component I corresponds to the light intensity, Q and U describe linear polarization, while V accounts for circular polarization. The geometry is fixed by the scattering angle $\theta = (\boldsymbol{k}_0, \boldsymbol{k})$ where $k_0 = k = 2\pi/\lambda$ is the wave vector of the radiation. These wave-vectors define the scattering plane, used as a reference plane for defining the Stokes vectors of both incident and backscattered waves. In what follows, the scattering angle is equal to the lidar π –backscattering angle ($\theta = \pi$, i.e. exact backscattering angle). Near backscattering angles (i.e. $\theta < \pi$) are also considered in complement for the discussion. Under the far-field single scattering approximation (Mishchenko 2009), assuming particles in randomly-oriented, when particles present a plane of symmetry and / or when particles and their mirror particles are present in equal number, the scattering matrix $[\boldsymbol{F}_\lambda(\theta)]$ simplifies to a block-diagonal matrix:

$$[F_\lambda(\theta)] = \begin{bmatrix} F_{11}^\lambda(\theta) & F_{12}^\lambda(\theta) & 0 & 0 \\ F_{12}^\lambda(\theta) & F_{22}^\lambda(\theta) & 0 & 0 \\ 0 & 0 & F_{33}^\lambda(\theta) & F_{34}^\lambda(\theta) \\ 0 & 0 & -F_{34}^\lambda(\theta) & F_{44}^\lambda(\theta) \end{bmatrix} \tag{2}$$

The dimensionless scattering matrix elements $F_{ij}^\lambda(\theta)$ depend on θ and λ (noted as a superscript) but also on the particles size, shape and chemical composition, through their complex refractive index. At specific lidar exact π –backscattering angle ($\theta = \pi$), and as detailed by (van de Hulst 1957), $F_{33,d}^\lambda(\pi) = -F_{22,d}^\lambda(\pi)$ and $F_{12,d}^\lambda(\pi) = F_{34,d}^\lambda(\pi) = 0$ while application of the backscattering theorem leads to $F_{44}(\pi) = F_{11}(\pi) - 2F_{22}(\pi)$. Hence, the scattering matrix $[\boldsymbol{F}_\lambda(\pi)]$ reduces to only two non-vanishing elements $F_{11,d}^\lambda(\pi)$ and $F_{22,d}^\lambda(\pi)$:

$$[F_\lambda(\pi)] = \begin{bmatrix} F_{11}^\lambda(\pi) & 0 & 0 & 0 \\ 0 & F_{22}^\lambda(\pi) & 0 & 0 \\ 0 & 0 & -F_{22}^\lambda(\pi) & 0 \\ 0 & 0 & 0 & F_{11}^\lambda(\pi) - 2F_{22}^\lambda(\pi) \end{bmatrix} \tag{3}$$

Moreover, for spheres, $F_{22}(\theta) = F_{11}(\theta)$ and $F_{33}(\theta) = F_{44}(\theta)$ whatever the scattering angle [39] so that $F_{22}(\theta) = F_{11}(\theta)$ and $F_{33}(\theta) = F_{44}(\theta)$. Hence, for spheres at backscattering angle, $F_{22}(\pi) = -F_{33}(\pi) = -F_{44}(\pi) = F_{11}(\pi)$.

(b) Particles depolarization ratio at near and exact backscattering angles

At scattering angle θ and wavelength λ, the expression of the so-called particles depolarization ratio, hereafter briefly noted *PDR*, can be found in light scattering textbooks (Bohren and Huffman 1983; Mishchenko et al. 2002):

$$PDR(\lambda, \theta) = \frac{I - Q}{I + Q} = \frac{1 - F_{22}^\lambda(\theta)/F_{11}^\lambda(\theta)}{1 \pm 2F_{12}^\lambda(\theta)/F_{11}^\lambda(\theta) + F_{22}^\lambda(\theta)/F_{11}^\lambda(\theta)} \tag{4}$$

where the positive (resp. negative) sign corresponds to p-polarized (resp. s-polarized) incident electromagnetic radiation. As for the $F_{22}^\lambda(\pi)/F_{11}^\lambda(\pi)$-ratio, the particles depolarization *PDR* is an intrinsic property of the ensemble of non-spherical particles, which is mainly governed by the particles shape (Mishchenko et al. 2002). However, many other subtle effects such as particles inhomogeneity (Kahnert 2015; Liu et al. 2014) or surface roughness (Kemppinen et al. 2015) may play a role. For F_{11}^λ, F_{12}^λ and F_{22}^λ vary with the scattering angle θ depending on the size, the shape and the complex refractive index of the considered particles, so does the corresponding*PDR*. Therefore, the *PDR* at near backscattering angles ($\theta < \pi$) differs from that obtained at specific exact backscattering angle ($\theta = \pi$) at which lidar instruments operate as F_{11}^λ, F_{12}^λ and F_{22}^λ at near backscattering angles ($\theta < \pi$) may differ from their value at exact backscattering angle ($\theta = \pi$). The deviation of F_{11}^λ, F_{12}^λ and F_{22}^λ from their value at exact backscattering angle cannot be quantified because there is no analytical theory for light scattering by complex-shaped non-spherical particles such as mineral dust. Even if other existing light scattering laboratory experiments are approaching the specific π-angle very closely, close to the exact backward scattering direction, optical properties (and hence F_{11}^{λ}, F_{12}^{λ} and F_{22}^{λ}) may strongly vary as underscored in Mishchenko et al. (2002), so that accurate determinations of the particles depolarization, which are suitable for inverting remote sensing data and improving our fundamental knowledge of the backscattering process, can only be addressed at the specific π-angle. In this context, accurate laboratory evaluations of the dust lidar *PDR* are coveted and can only arise om laboratory experiments at lidar exact backscattering angle ($\theta = \pi$), for which Eq. (4) becomes:

$$PDR(\lambda, \pi) = \frac{I - Q}{I + Q} = \frac{1 - F_{22}^{\lambda}(\pi)/F_{11}^{\lambda}(\pi)}{1 + F_{22}^{\lambda}(\pi)/F_{11}^{\lambda}(\pi)} \tag{5}$$

Where the dependence of the dust lidar *PDR* with the π–backscattering angle has been omitted to ease the reading. In the lidar literature, the *PDR* is often also noted δ. Here, we will keep the *PDR* abbreviation for clarity. Following Eq. (5), to carry out accurate evaluations of the lidar *PDR*, the ratio $F_{22}^{\lambda}(\pi)/F_{11}^{\lambda}(\pi)$ must be precisely determined and $PDR(\lambda, \pi)$ should be clearly distinguished from its value at near backscattering $PDR(\lambda, \theta)$. In the literature, numerical extrapolations up to the π–backscattering angle exist (Gómez Martín et al. 2021; Liu et al. 2003) but we should wary of such extrapolations which are based on simplifying assumptions, which should be carefully checked. For that, laboratory experiments at exact backscattering angle are coveted.

1.4 State of the Art on LightBackscattering

The literature on light backscattering by atmospheric particles is abundant with field and laboratory experiments, completed with numerical simulations. To our knowledge, there is however a dearth of laboratory experiments to which this book chapter contributes to fill. We here recall the main contributions at near and exact backscattering angles.

(a) **Light backscattering numerical simulations**

To face such a complexity in size and shape, light-scattering numerical models have been developed which are becoming more and more realistic, with improved accuracies allowing an evaluation of the influence of the particles inhomogeneity (Kahnert 2015; Liu et al. 2014) and surface roughness (Kemppinen et al. 2015) on the scattering matrix elements. Such numerical simulations are now currently performed over the whole scattering angle range, hence including the exact backward scattering direction $\theta = \pi$. The literature on light backscattering numerical simulations is abundant (see http://www.scattport.org). Hence, the goal of this small paragraph is not to give an extensive overview of this important research field. To quote only a few reference examples on the case study of mineral dust, (Dubovik et al. 2006a) revealed the importance of the mathematical spheroidal model for accurate modelling of light scattering properties of complex-shaped particles such as mineral dust. The spheroidal model was tested by Müller et al. (2013) during the SAMUM field campaign. Using the spheroidal shape model for mineral dust during the SAMUM field campaign, (Müller et al. 2013) retrieved vertical profiles of microphysical properties by combining mineral dust polarization lidar with sun photometer measurements, and compared their results to airborne in situ observations. However, as underlined by Veselovskii et al. (2016), "*we should keep in mind that the spheroidal model was not specifically designed for lidar applications where scattering in the backward direction was considered*". Indeed, (Zubko et al. 2013) found that spheroids appeared to be inadequate for describing the dust particles' spectral dependence of linear polarization, while (Kemppinen et al. 2015) reported on difficulties in using ellipsoids to correctly retrieve dust particle properties from scattering data. The discrete-dipole approximation (DDA) numerical code was applied by Gasteiger et al. (2011) as another approach to compute light-scattering properties of mineral dust, though computationally demanding. In complement, (Kahnert et al. 2020) recently reviewed the size-dependence of the dust lidar *PDR* with a homogeneous spheroidal model, and also studied the dependence of the dust lidar *PDR* with the hematite volume fraction (Kahnert 2015). Recently, (Huang et al. 2020) revealed the importance of the dust complex refractive index for the development of a model of dust optical properties. Also, (Saito et al. 2021) developed a database of the optical properties of irregular aerosol particles for applications to radiative transfer simulations involving aerosols, particularly dust and volcanic ash particles. However, as underscored in (Haarig et al. 2022), complex particle shape models (Gasteiger et al. 2011; Mehri et al. 2018; Saito et al. 2021) are computationally expensive. The field of coherent backscattering was likewise studied by Videen and Muinonen (2015) who examined the evolution of light-scattering properties as a volume of particles increases from wavelength-sized to several hundreds of wavelengths, using the radiative-transfer coherent backscattering (RT–CB) model. Care should however be taken as no analytical solution to the Maxwell's equations exists for complex-shaped mineral dust so that these light scattering numerical simulations rely on simplifying assumptions that should be carefully checked. Hence, for these clear major advances to be fully beneficial, the underlying assumptions inherent to these numerical simulations should be carefully validated and for that controlled laboratory experiments are coveted, to in turn help developing even more accurate light-scattering models.

(b) Light backscattering in field: lidar remote sensing experiments

The lidar*PDR*, as retrieved from lidar remote sensing instruments, is commonly used to discriminate between low (rather spherical aerosol) and highly depolarizing particles (as mineral dust, (David 2013; David et al. 2013). The lidar *PDR* is also a crucial input for the CALIOP VFM production and categorization of aerosol subtype. As for above numerical simulations, the literature on lidar field measurements is really abundant and we here limit to some specific case studies, to which our group contributes (David et al. 2013; Mehri 2018; Miffre et al. 2012, 2019a, 2020). Moreover, in complex particle mixtures, the spectral behavior of the *PDR* can provide additional information on the plume composition (Haarig et al. 2018) and help to better constrain lidar inversions. As a result, for accurate assessments of aerosol microphysical properties, the accuracy on the retrieved lidar *PDR* is critical. Future lidar missions with UV (EarthCare) or spectral (AOS) depolarization capabilities will enhance our understanding of such mixing and its impact on climate and air quality, in areas where scarce ground-based observations are often available. However, to successfully retrieve the microphysical properties of for instance, mineral dust particles from such polarization lidar measurements, a robust inversion algorithm is required and for this, accurate input parameters are needed, at least to avoid confusions between mineral dust, sea-salt particles and other non-spherical particles. Hence, a precise knowledge of the mineral dust particles depolarization or dust *PDR* is required.

Several lidar field campaigns have hence been performed on mineral dust (Ansmann et al. 2011), studying the spectral dependence of *PDR* for dust as underscored by Burton et al. (2016) or Haarig et al. (2018). Recently, (Hofer et al. 2020) studied the optical properties of Central Asian aerosol for space borne lidar applications and aerosol typing at 355 and 532 nm. Likewise, (Haarig et al. 2022) provided the first triple triple-wavelength lidar observations of depolarization and extinction-to-backscatter ratios of Saharan dust. There, these authors finally underscored that "*it would be helpful—and a good addition to field observations – if laboratory measurements of the depolarization (…) in the 180_ backscatter direction could be realized for well-defined size fractions of real dust particles.*" A remaining issue is then to study the variation of the lidar *PDR* as a function of the particles size (close to the source, after long-range transport) and as a function of the particles origin or mineralogyx.

(iii) Light backscattering in laboratory

Starting from pioneering work by Hunt (1973), Liou and Lahore (1974) and Perry et al. (1978), light scattering by particles embedded in laboratory ambient air has been largely studied in laboratory with increased accuracies and accessible scattering angle ranges, as gathered in Table 1 at near ($\theta < \pi$) and exact backscattering angles ($\theta = \pi$). Apart from the accessible scattering angle range, the existing laboratory experimental set-ups differ from one another from the wavelength of the radiation, the studied samples and the nature of the laser source (CW, pulsed). Also, from a detailed reading of the corresponding papers, it seems difficult to know if the far-field single scattering conditions are fulfilled.

Light backscattering has been observed and applied however only on dense media such as solid GaAs crystals (Wiersma et al. 1997), biological tissues (Vitkin and Studinski 2001), or PSL spheres in liquid water (Kuga and Ishimaru 1984), or liquid animal blood (Wang et al. 2012). However, up to now to our knowledge, no laboratory experiment exists that covers the exact backward scattering direction for particles embedded in an unbounded host medium such as ambient air. As underscored by Huang et al. (2015), "*the phase matrix can be obtained only at specific wavelengths and in limited angular scattering regions, for example, from 3° to 177°*". Hence, the

Table 1 Existing laboratory light scattering experimental set-up for particles in air at near ($\theta < \pi$) and exact backscattering angles ($\theta = \pi$). To our knowledge, no laboratory experimental set-up exists addressing light scattering by aerosols at the specific lidar exact π–backscattering angle ($\theta = \pi$)

Sample	θ (°)	λ (nm)	Reference
Single dust particle	168.0–176.0	680	(Glen and Brooks 2013)
Ash, dust, water, NaCl	3–177	488, 520, 647	(Muñoz and Hovenier 2011)
Ice crystals Mineral dust	178.2	488	(Järvinen et al. 2016; Schnaiter et al. 2012)
Aerosol	0.3–177.6	532	(Gautam et al. 2020)
NaCl, water	179.2	532	(Sakai et al. 2010)
Mineral dust, water, pollen	176.0–180.0, 178	355 532	(Miffre et al. 2016, 2019b, 2022), Cholleton et al. (2020, 2022)

lack of experimental data in the backward direction limits the direct applicability of the measured scattering matrix elements for radiative transfer calculations. In particular, the absolute dependence on the F_{11}-element and hence the scattering phase function, remains unknown. The measured phase function is then normalized to unity at a particular scattering angle, chosen equal to 30° (Dabrowska et al. 2013; Liu et al. 2003; Volten et al. 2001).

In the absence of laboratory backscattering measurements, extrapolations have been performed to obtain data over the entire scattering angle range from 0° to 180°, as required for accurate radiative transfer calculations. To cover the exact backward scattering direction, polynomial extrapolations have then been proposed (Laan et al. 2009; Muñoz and Hovenier 2011; Volten et al. 2001). Videen et al. (2018) discussed on the interpolation of light scattering responses from irregularly-shaped particles and noted that the greatest discrepancy between the experiment and the modelled data occurs in the backscatter region. Though a synthetic scattering matrix has built (Laan et al. 2009), the added data points are somewhat artificial and the assumptions inherent to these extrapolations should be carefully checked, as analyzed by Liu et al. (2003) and more recently by (Huang et al. 2015). This requires to increase the accessible range of laboratory light scattering experiments to cover the gap from 177° up the π-backscattering angle with a high angular resolution (better than 1°). Hence, measurements of the scattering matrix at very large scattering angles are coveted.

Ideally, such a laboratory backscattering experiment should be conducted at several wavelengths, under the far-field single scattering approximation (Michael I Mishchenko et al. 2004a, b), to ease the comparison with numerical models (Dubovik et al. 2006a; Zubko et al. 2013). The Fig. 1 from Tesche et al. (2019) summarizes the state-of-the knowledge on the evaluation of the lidar *PDR* at backscattering angle as retrieved from field measurements, numerical simulations and laboratory experiments: while field measurements and numerical simulations are numerous, the dearth of laboratory *PDR* measurements at exact lidar backscattering angle ($\theta = \pi$)

is clearly underscored. Likewise, a laboratory approach is necessary to circumvent particles backscattering to a specific aerosol type instead of considering that of particle mixtures, which a priori differs (Miffre et al. 2011).

1.5 Outline of this Book Chapter

The goal of this book chapter is to present the current state-of-the-art on light backscattering by atmospheric particles. On account of the above considerations and to face the need for controlled laboratory experiments at exact backscattering angle, this book chapter mainly focuses on controlled laboratory experiments at near ($\theta < \pi$) and exact ($\theta = \pi$) backscattering angles for particles embedded in ambient air. These laboratory measurements of lidar *PDR* can help to better constrain future lidar inversions, but for that fundamental laboratory intensive work is required to address the dependence of the lidar *PDR* with size and mineralogy at lidar observation wavelengths (mostly 355 and 532 nm). Section 2 is then dedicated to a controlled-laboratory experiment at near backscattering angles (Miffre et al. 2019b). There, to complement existing laboratory light scattering experimental set-ups, the scattering matrix elements $F_{ij}^{\lambda}/F_{11}^{\lambda}(\theta)$ from 176.0° to backscattering angle with a 0.4° angular step for mineral dust. The ability of the mathematical spheroidal model to mimic light scattering by mineral dust at near backscattering angles is then verified. Section 3 is then specifically dedicated to the cutting-edge laboratory π-polarimeter at exact backscattering angle or lidar angle ($\theta = \pi$), with emphasis on its ability to accurately measure the backscattered light intensity and the corresponding lidar*PDR*. This laboratory π-polarimeter is important to interpret lidar observations, which operate at strict backscattering angle $\theta = \pi$. Several case studies are then presented on laboratory light backscattering by:

- *Spherical inorganic sulfates,* for sulfates are responsible for a net cooling of the Earth's atmosphere due to their ability to backscatter light, and also as a way to validate the laboratory π-polarimeter as light backscattering by spherical sulfates follow the Lorenz-Mie theory.
- *Core–shell organic sulfates,* for the sulfate aerosol may give rise to core–shell structures in the presence of organic compounds in the atmosphere. The question is there to quantify the modification of the sulfates ability to backscatter light (Dubois et al. 2021).
- *Freshly-emitted soot,* as black carbon is the second contributor to global warming after CO_2 and a major absorber of solar radiation (Stier et al. 2007). Additionally, the carbon aerosol has a strong impact on human health, especially in urban polluted areas, as being carcinogenic. Moreover, understanding light backscattering by soot particles is essential for radiative transfer, as well as to develop carbon reduction emission strategies. In the literature, the soot lidar *PDR* has

been the subject of several publications, from light scattering numerical simulations at backscattering, but also from lidar field experiments in plumes. The proposed controlled-laboratory experiment complements these publications.

- *Mineral dust,* for it is one of the major contributors to the Earth's global aerosol load, with emission rates as large as 1000 to 3000 $\mathrm{Tg.yr}^{-1}$ from the Earth's surface (Monge et al. 2012). This abundant aerosol is uplifted into the atmosphere through favorable winds and can be transported by advection over several thousands of kilometers, hence affecting the Earth's climate at both local, regional and global scales. The radiative properties of mineral dust are however difficult to handle mainly due to the complexity in shape of these particles, which are highly irregularly-shaped, with sharp edges and sometimes even surface roughness. Hence, the dust particles non-sphericity is still a major issue for accurate radiative forcing assessments (Mehri et al. 2018). The intrinsic lidar *PDR* of mineral dust is analyzed for several dust samples differing in sizes and mineralogy by taking benefit from the laboratory π-polarimeter at exact backscattering angle (Miffre et al. 2016, 2019b, 2022).

Implications of this laboratory work on aerosols light backscattering in lidar remote sensing experiments are proposed and discussed in Sect. 4. The chapter ends with a conclusion and proposes outlooks.

2 Light Scattering at Near Backscattering Angles ($\theta < \pi$)

2.1 The Laboratory π+ε Polarimeter

The laboratory π+ε-polarimeter is schemed in Fig. 1 from Miffre et al. (2019b). To evaluate the ratios $F_{ij}^{\lambda}/F_{11}^{\lambda}(\theta)$ of the scattering matrix elements at near backscattering angles ($\theta < \pi$) and wavelength λ for particles in ambient air, light scattering measurements are carried out for a set of incident polarization states, namely $(p, 45+, RC)$, as explained below. The scattering angle is varied from 176.0° up to 180.0° with 0.4° angular resolution by modifying the wave-vector $\boldsymbol{k_i}$ of the incident radiation by 0.2° steps, which in turn varies the scattering angle $\theta = (\boldsymbol{k_i}, \boldsymbol{k_s})$, while $\boldsymbol{k_s}$ is the wave-vector of the backscattered radiation. The light detector is identical to that used in the exact backward scattering experimental set-up to be described in the paragraph below. In this way, the same light detector is used for evaluating the scattering matrix ratios $F_{ij}/F_{11}(\theta)$ at both near ($\theta < \pi$) and exact ($\theta = \pi$) backscattering angles, which minimizes biases in the $F_{ij}/F_{11}(\theta)$-evaluation.

2.2 Scattering Matrix Elements Retrieval at Near Backscattering ($\theta < \pi$)

Basically, the Stokes vectors (St_i) and (St) of the incident and backscattered radiations relate with the Mueller matrix $\left[\boldsymbol{M}_{\boldsymbol{\theta}}^{\boldsymbol{\lambda}}\right]$ of the π(+ε)-polarimeter at scattering angle θ and wavelength λ as follows $(St) = \left[\boldsymbol{M}_{\boldsymbol{\theta}}^{\boldsymbol{\lambda}}\right](St_i)$. $\left[\boldsymbol{M}_{\boldsymbol{\theta}}^{\boldsymbol{\lambda}}\right]$ can be obtained by taking into account the successive Mueller matrices encountered by the laser pulse from the laser source to the particles then back to the light detector. Following Fig. 3, the Mueller matrix of the set-up is equal to $[\mathbf{PBC}][\mathbf{QWP}][\boldsymbol{F}_{\boldsymbol{\lambda}}(\theta)]$ where $[\boldsymbol{F}_{\boldsymbol{\lambda}}(\theta)]$ is the scattering matrix at scattering angle θ and wavelength λ as given in Eq. (2) for $\theta < \pi$ and in Eq. (3) for $\theta = \pi$. At scattering angle θ and wavelength λ, the detected scattered intensity is then given by the first component of (St):

$$I_\theta^\lambda = \frac{\eta_\lambda P_{0,\lambda}}{d^2}(P_j)[\mathbf{PBC}][\mathbf{QWP}][\boldsymbol{F}_{\boldsymbol{\lambda}}(\theta)](St_i) \tag{6}$$

where η_λ is the electro-optics efficiency of the detector at wavelength λ, $P_{0,\lambda}$ is the incident laser power and $(P_j) = [1, 0, 0, 0]$ is a projection unitary raw vector. In this book chapter, we will mainly focus on exact backscattering ($\theta = \pi$) of light by particles in line of the motivations presented in Sect. 1.4 for studying exact light backscattering and noticeably for lidar purposes. Readers interested by retrieving the scattering matrix elements $F_{ij}^\lambda/F_{11}^\lambda(\theta)$ at near backscattering angles ($\theta < \pi$) by using the laboratory π+ε-polarimeter can refer to Miffre et al. (2019b) where the methodology is extensively described and where the calculus are detailed. We here only briefly present the outputs of these calculations for completeness. Following (Miffre et al. 2019b), the detected scattered intensity can then be written as follows:

$$I_\theta^\lambda(\psi) = I_{11}^\lambda(\theta) \times \left[a_\theta^\lambda - b_\theta^\lambda \sin(2\psi) - c_\theta^\lambda \cos(4\psi) - d_\theta^\lambda \sin(4\psi)\right] \quad \text{for } \theta < \pi \tag{7}$$

where the superscript refers to the wavelength of the radiation while the coefficients a_θ^λ to d_θ^λ are given in Table 2 for incident polarization states (p, 45+, RC). $I_{11}^\lambda = \eta_\lambda P_{0,\lambda} F_{11}^\lambda/(4d^2)$ is the detected scattered phase function, as being proportional to

Table 2 Expression of the coefficients the a_θ to d_θ appearing in the expression of the scattered light intensity in Eq. (11) as a function of the scattering matrix elements $f_{ij}^\lambda(\theta) = F_{ij}^\lambda/F_{11}^\lambda(\theta)$ for incident polarization states (p, 45+, RC). The dependence of f_{ij} with scattering angle θ has been omitted to ease the reading

State	(St_i)	a_θ^λ	b_θ^λ	c_θ^λ	d_θ^λ
p	$[1, 1, 0, 0]^T$	$2 - f_{22} + f_{12}^\lambda$	0	$f_{12}^\lambda + f_{22}$	0
45+	$[1, 0, 1, 0]^T$	$2 - f_{12}^\lambda$	$2f_{34}^\lambda$	f_{12}^λ	f_{33}^λ
RC	$[1, 0, 0, 1]^T$	$2 - f_{12}^\lambda$	$-2f_{44}^\lambda$	f_{12}^λ	f_{34}^λ

F_{11}^{λ}. To ease the reading, we will use the following reduced notation $f_{ij}^{\lambda} = F_{ij}^{\lambda}/F_{11}^{\lambda}$. From Table 2, it is clear that the scattering matrix elements at $\theta < \pi$ can then be retrieved as follows:

$$f_{33}^{\lambda}(\theta) = 2d_{\theta,45+}^{\lambda}/(a_{\theta,45+}^{\lambda} + c_{\theta,45+}^{\lambda}) \tag{8a}$$

$$f_{44}^{\lambda}(\theta) = -b_{\theta,RC}^{\lambda}/(a_{\theta,45+}^{\lambda} + c_{\theta,45+}^{\lambda}) \tag{8b}$$

$$f_{12}^{\lambda}(\theta) = 2c_{\theta,RC}^{\lambda}/(a_{\theta,45+}^{\lambda} + c_{\theta,45+}^{\lambda}) \tag{8c}$$

$$f_{34}^{\lambda}(\theta) = 2d_{\theta,RC}^{\lambda}/(a_{\theta,45+}^{\lambda} + c_{\theta,45+}^{\lambda}) \tag{8d}$$

$$f_{22}^{\lambda} = [f_{12}^{\lambda}(\theta) \cdot \left(c_{\theta,p}^{\lambda} - a_{\theta,p}^{\lambda}\right) + 2c_{\theta,p}^{\lambda}]/\left(a_{\theta,p}^{\lambda} + c_{\theta,p}^{\lambda}\right) \tag{8e}$$

where subscripts $(p, 45+, RC)$ respectively refer to considered $(p, 45+, RC)$ incident polarization states. From a practical point of view, the coefficients a_{θ}^{λ} to d_{θ}^{λ} are retrieved by adjusting the $I_{\theta}^{\lambda}(\psi)$-variations with Eq. (7). To gain in accuracy in the $f_{ij}^{\lambda}(\theta)$-evaluation, the backscattered light intensity is measured for different positions of the QWP, over a complete rotation of QWP (ψ-modulation angle).

The scattered intensity $I_{\theta}(\psi)$ for incident polarization (p) exhibits several minima equal to $1 - f_{22}^{\lambda}$, to be related to particles deviation from isotropy or linear depolarization. The sensitivity of $I_{\theta}(\psi)$ to a modification in f_{33}^{λ} and f_{34}^{λ} is seen with incident polarization(45+), which exhibit different secondary maxima and minima. The sensitivity of $I_{\theta}(\psi)$ to f_{44}^{λ} is seen with incident polarization(RC), where the minima are equal to $1 + f_{44}^{\lambda}$ and related to circular depolarization. These latter minima are not null, even for spherical particles, since f_{44}^{λ} only equals unity at exact backscattering angle, as explained in Sect. 1.3.

2.3 Light Scattering by Mineral Dust at Near Backscattering Angles ($\theta < \pi$)

In Fig. 6 from Miffre et al. (2019b) are plotted the variations of the light intensity $I_{\theta}^{\lambda}(\psi)$ scattered by the generated ATD-particles at scattering angles $\theta = 176.0°$ and $\theta = 178.0°$ for incident polarization states $(p, 45+, RC)$ at 532 nm wavelength. The observed variations of $I_{\theta}^{\lambda}(\psi)$ are representative of a determined size and shape distribution of the generated mineral dust particles: if the size of the dust sample was varying, the variations of $I_{\theta}^{\lambda}(\psi)$ would not exhibit constant maxima while rotating the QWP. Likewise, the shape distribution of the dust particles did not vary during the acquisitions, otherwise, $I_{\theta}^{\lambda}(\psi)$ would exhibit varying minima (recall: these minima are related to particles non-sphericity, as being equal to $1 - f_{22}^{\lambda}$). It is hence clear that mineral dust are non-spherical particles since the minima of $I_{\theta}(\psi)$ are not null, at both scattering angles. As a result, $f_{22}^{\lambda}(\theta)$ differs from unity. Also, the minima, equal to $1 + f_{44}^{\lambda}$, are far from zero, as a clear signature of circular depolarization of the generated mineral dust particles. By adjusting these experimental data points with Eq. (11), the coefficients a_{θ}^{λ} to d_{θ}^{λ} can be retrieved for each scattering angle to precisely evaluate the ratios $f_{ij}^{\lambda}(\theta)$ of scattering matrix elements by applying Eq. (7), as given in Fig. 7 from Miffre et al. (2019b). Within our experimental error bars, we conclude that $f_{22}^{\lambda}(\theta) < 1$ and $f_{33}^{\lambda}(\theta)$ differs from $f_{44}^{\lambda}(\theta)$ at all scattering angles as optical signatures of linear and circular depolarization from mineral dust. At exact backscattering angle, we evaluate $f_{22}^{\lambda}(\pi) = 0.57 \pm 0.02$ shows that $f_{44}^{\lambda}(\theta)$ tends towards $1 - 2f_{22}^{\lambda}(\pi) = -0.14$, as expected when approaching the exact backward scattering angle. Likewise, $f_{33}^{\lambda}(\theta)$ tends towards $-f_{22}^{\lambda}(\pi) = -0.57$, as expected. With the generated size distribution of mineral dust to be seen in Fig. 6(f), the scattering matrix elements slightly vary in the scattering angle range between 176.0° and 180.0°, but this should not be considered as a general establish fact for mineral dust may present different size, shape distributions and mineralogy leading to other light scattering properties. This is especially true close to the backscattering angle where optical properties may strongly vary. Hence, to draw such a conclusion, complementary studies should be carried out. Section 3.6 starts tackling this important issue.

2.4 Comparison with T-matrix Numerical Simulations

As the laboratory π+ε-polarimeter operates in the far-field single scattering approximation, the ability of the mathematical spheroidal model to mimic light backscattering can be discussed by comparison with our laboratory findings. This work hence extends the conclusions by Dubovik et al. (2006b) up to the backward scattering direction. Though the highly irregular shape of mineral dust is difficult to account for in mathematical models, we tested the applicability of the widely used spheroidal model, for the first time to our knowledge in the scattering angle range between 176.0° and 180.0°. For our laboratory π-polarimeter fulfills the far-field single-scattering approximation, the measured depolarization can be compared with the results from numerical simulations. In this section, we discuss the applicability of a spheroidal model for numerically simulating the dust particles scattering at near and exact backscattering angles. The T-matrix method (Mishchenko and Travis 1998), based on the spheroidal model, is an exact analytical solution of the Maxwell equations, allowing averaging over particle orientations. The T-matrix method is extensively described in the literature. In a few words, in the T-matrix method, the size-shape distribution of randomly-oriented mineral dust particles can be mimicked with size-shape distributions of spheroids, the simplest shape for non-spherical particles, with axial symmetry and a geometry described by the aspect ratio $\varepsilon = b/a$, where a and b are the major (minor) and minor (major) axis lengths for oblate (prolate) spheroids respectively. The aspect ratios were then distributed either as equiprobable ($f(\epsilon) = \varepsilon^n$ with $n = 0$) or with a $n = 3$ power-law shape distribution, in an attempt to better account for polarization effects (Merikallio et al. 2011). Using $m = 1.555 + 0.005i$ for the refractive index of ATD at $\lambda = 532$ nm [34], we then applied Mishchenko's T-matrix numerical code (Mishchenko and Travis 1998) to retrieve the ratios of scattering matrix elements after size-integration using Fig. 5(f). To derive the size distribution for non-spherical ATD-particles, we took benefit from recent publication by Chien et al. (2016), allowing to correlate optical diameters to aerodynamic diameters. More precisely, Eqs. (5) and (9) from Chien et al. (2016) were applied, using 1.5 for the shape factor for non-spherical ATD-particles, to convert the mobility diameters (from our SMPS) and the optical diameter (from our particle counter) to volume equivalent diameters, as plotted in Fig. 6(f). Our numerical results are presented in Fig. 6(a) to (e) in dashed lines for the $n = 3$ shape distribution and in dotted lines for the $n = 0$ shape distribution. Interestingly, within our experimental error bars, the output of T-matrix numerical simulation agrees with our laboratory findings for $f_{44}^{\lambda}(\theta), f_{12}^{\lambda}(\theta)$ and also for a majority of points for $f_{34}^{\lambda}(\theta)$ and $f_{22}^{\lambda}(\theta)$. The agreement is better when using the $n = 3$ shape distribution rather than the equiprobable shape distribution of spheroids, in agreement with [34], where we observed a similar behaviour at specific backscattering angle. This conclusion cannot however be supported by electron microscopic images, since as underscored by Kahnert et al. (2014): ""*single spheroids do not share the single-scattering properties of non-spheroidal particles with the same aspect ratios, so one should not think that when using spheroids to mimic scattering by more complex particles, best results would be achieved using aspect ratios of the target particles for the spheroids*." A slight discrepancy of 0.06 is however observed for $f_{33}^{\lambda}(\theta)$ even with the $n = 3$ shape distribution.

We should however keep in mind that the uncertainty on the scattering angle is $\pm 0.2°$ and that the size distribution displayed in Fig. 7(f) from Miffre et al. (2019b) is not error-free. Also, the refractive index of ATD is itself not error-free: its calculation in Miffre et al. (2016) is based on the Aspens formula which requires prior knowledge of the refractive indices of each oxide present in ATD as well as their volume fractions. Interestingly, our laboratory evaluation of the scattering matrix elements agrees with that computed in the well-known paper by Dubovik et al. (2006b): at near and exact backscattering, his computed phase matrix elements were indeed equal to: $P_{12}/P_{11} \simeq 0$, $P_{22}/P_{11} \simeq 0.55$, $P_{33}/P_{11} \simeq -0.55$, $P_{34}/P_{11} \simeq 0$ and $P_{44}/P_{11} \simeq -0.15$. Care should however be taken since scattering matrix elements depend on the particles size distribution and refractive index.

3 Light Backscattering at Exact Backscattering Angle ($\theta = \pi$)

Addressing light backscattering by particles embedded in ambient air in laboratory is challenging as two main difficulties then arise:

- The first intricacy is relative to the finite size of the detector, which may block the incident radiation. The insertion of a beam splitter, as often performed for condensed matter phases usually limits the accuracy on the backscattering measurement as its specifications are imperfectly known and represent an important artifact, source of systematic error (Wiersma et al. 1997). Inserting a beam splitter plate also creates stray light affecting the particles backscattering signal, as for solid biological tissues (Studinski and Vitkin 2000).
- The second intricacy is relative to the intensity of the backscattered radiation itself, which might be weak for particles in air, especially for non-spherical particles for which backscattering is weaker (Kahnert et al. 2014). Hence, any stray light may overcome the particles backscattered radiation. For condensed matter phases, lock-in detection has been applied on continuous incident radiation (Studinski and Vitkin 2000; Vitkin and Studinski 2001), but for particles in ambient air, the particles backscattering signal is so weak that even this technique has not been successfully applied.

Hence, observing exact light backscattering ($\theta = \pi$) by atmospheric particles in laboratory requires a high angular resolution (to avoid blocking the incident light with the detector) and a high dynamical range (to discriminate the weak backscattered radiation from background stray light). In (Miffre et al. 2016, 2019b, 2022), for the first time to our knowledge, we overcame these two intricacies as detailed below in the so-called laboratory π-polarimeter. This π-polarimeter allows accurate retrievals of $F_{22}^{\lambda}/F_{11}^{\lambda}(\pi)$ and hence of the lidar *PDR*, without any extrapolation based on numerical simulations, which are actually performed in the literature (Gómez Martín et al. 2021; Liu et al. 2003).

3.1 The Laboratory π-polarimeter ($\theta = \pi$)

The laboratory π-polarimeter is a cutting-edge experiment, schemed in Fig. 1 from Miffre et al. (2016). It is actually composed two π-polarimeters, one per wavelength (see Fig. 3 from Miffre et al. (2016)), to allow addressing the spectral dependence of the lidar *PDR* at 355 and 532 nm wavelengths simultaneously, as often performed in lidar applications (Haarig et al. 2018, 2022). The exact backscattering geometry ($\theta = \pi$) is achieved by precisely aligning (1 mm out of 10 m) a retro-reflecting polarizing beam splitter cube (PBC) along the z-optical axis from a laser source to the particles scattering volume, to cover the lidar exact backscattering direction with accuracy: θ = (180.0±0.2)°. In the exact backward scattering direction, stray scattered light from optical components can be significant and to overcome this difficulty, the particles backscattering radiation is discriminated from background stray light by achieving time-resolved measurements synchronized with the laser pulse, to address the time-of-flight $2d/c$ taken by the laser pulse to reach the detector after the scattering event. Particles light backscattering can then be distinguished from that due to laboratory ambient air, by first recording the backscattered light intensity in the presence of the particles, then in their absence, to retrieve the particles backscattered light intensity I_π^λ by subtracting these latter two (David 2013). The experiment is carried out in laboratory ambient air: chamber walls and windows, with inherent AR-coatings, may indeed provoke a strong backscattering signal or/and modify the polarization of the backscattered radiation which has to be accurately analyzed. The particles are not static but move in a few millimeters wide beam, whose section is defined by the 2.5 mm diameter injection nozzle, chosen to fill the 8 cm^3 detected backscattering volume. Moreover, to ease the comparison with numerical simulations and field experiments, the laboratory π-polarimeter operates in the far-field single scattering approximation and efficiently collects the backscattered radiation, while minimizing any stray light, within a very small (3 mrad) field of view, as in lidar applications, to cover the exact backscattering direction with accuracy $\theta = (180.0 \pm 0.2)°$. The lidar *PDR* can then be evaluated from the ratio $F_{22}^\lambda / F_{11}^\lambda$ following the methodology described below (Miffre et al. 2016).

3.2 Scattering Matrix Elements and Lidar PDR Retrieval at Backscattering ($\theta = \pi$)

At exact backscattering angle ($\theta = \pi$), following Fig. 7, due to the co-axial geometry, the incident Stokes vector is determined by the combination of the PBC and the QWP and expresses as $(St_i) = \left[QWP\right][PBC][1, 1, 0, 0]^T = [1, \cos(2\psi) - \sin(4\psi)/2, -\sin(2\psi)]^T$. As detailed in Appendix A of (Miffre et al. 2019b), we hence get for the detected backscattered intensity:

$$I_\pi^\lambda(\psi) = I_{11}^\lambda(\pi) \times \left[a_\pi^\lambda - c_\pi^\lambda \cos(4\psi)\right] \tag{9}$$

where the coefficients a_π^λ and c_π^λ depend on the backscattering matrix elements at wavelength λ as follows: $2a_\pi^\lambda = 1 + F_{22}^\lambda / F_{11}^\lambda$ and $2c_\pi^\lambda = 3F_{22}^\lambda / F_{11}^\lambda - 1$. Hence, following Eq. (9), the $c_\pi^\lambda / a_\pi^\lambda$-ratio can be determined from the $I_\pi^\lambda(\psi)$-variations independently on $I_{11}^\lambda(\pi)$. As a result, $F_{22}^\lambda / F_{11}^\lambda(\pi)$ can be precisely evaluated from the c_π / a_π-ratio [34]:

$$F_{22}^\lambda / F_{11}^\lambda(\pi) = (1 + c_\pi^\lambda / a_\pi^\lambda)/(3 - c_\pi^\lambda / a_\pi^\lambda) \tag{10}$$

As a result, accurate evaluations of the aerosol lidar *PDR* can then be retrieved as:

$$PDR_{\pi}^{\lambda} = \left(1 - c_{\pi}^{\lambda}/a_{\pi}^{\lambda}\right)/2 \tag{11}$$

independently of $I_{11}^{\lambda}(\pi)$. Accordingly, the applied voltage to the UV and VIS-photodetectors will be adjusted to each particles sample to gain in accuracy in the retrieved lidar *PDR*. From a practical point of view, the coefficients a_{π}^{λ} and c_{π}^{λ} are retrieved by adjusting the $I_{\pi}^{\lambda}(\psi)$-variations with Eq. (11) to get accurate determinations of $I_{11}^{\lambda}(\pi) \times a_{\pi}$ and $I_{11}^{\lambda}(\pi) \times c_{\pi}$, then $c_{\pi}^{\lambda}/a_{\pi}^{\lambda}$ and the *PDR* from Eq. (11). To fix ideas, as long as the lidar *PDR* increases, the backscattered light intensity becomes weaker, in agreement with the literature (Kahnert et al. 2014). All curves exhibit non-vanishing minima as the observed minima are equal to$a_{\pi}^{\lambda} - c_{\pi}^{\lambda} = 1 - F_{22}^{\lambda}/F_{11}^{\lambda}$, which never cancels for nonspherical particles such as soot or mineral dust. These minima can be used as an indicator for particles' deviation from isotropy. The lidar *PDR* is however also determined by the curve maxima equal to $a_{\pi}^{\lambda} + c_{\pi}^{\lambda} = 2F_{22}^{\lambda}/F_{11}^{\lambda}$. Indeed, if $I_{\pi,m}^{\lambda}$ and $I_{\pi,M}^{\lambda}$ refer to the curve minimum and maximum, following Eq. (12), the lidar *PDR* can be retrieved from $I_{\pi,m}^{\lambda}/(I_{\pi,m}^{\lambda} + I_{\pi,M}^{\lambda})$, independently of I_{11}^{λ}.

Special care has been taken to precisely evaluate the uncertainties on the retrieved *PDR*. The systematic errors in the backscattering π-polarimeter are that encountered in 2λ-polarization lidar experiments (Freudenthaler et al. 2009; Haarig et al. 2022), which we extensively studied in a dedicated paper (David et al. 2012). In a few words, systematic errors then arise from:

- *Imperfect definition of the polarization state of the incident radiation.* In the $\pi-$polarimeter, the polarization state of the electromagnetic radiation emerging from the laser is precisely set to $[1, 1, 0, 0]^T$ (i.e. with no remaining ellipticity) by using two successive *PBC*.
- *Polarization cross-talks between the emitter and the detector polarization axes.* Likewise, on the detector side, to account for the imperfections of the retro-reflecting *PBC* ($R_s > 99.5\%, T_p > 90\%$), a secondary *PBC* is inserted between the retro-reflecting *PBC* and the light detector to ensure polarization cross-talk or undesired fraction R_pT_s originating from the *p*-component of the backscattered radiation to be fully negligible. Hence, the π–polarimeter is sensitive to the *s*-component of the backscattered radiation only. Also, the emitting *PBC* being used as retro-reflecting PBC, any possible mismatch between the *s*-polarization axis of the emitted and detected backscattered radiations cannot occur. Introducing controlled amounts of polarization cross-talks is however interesting to calibrate polarization lidars as explained in Sect. 4 and in Miffre et al. (2019a).
- *Wavelength cross-talks between the UV and the VIS-backscattered radiations.* Likewise, wavelength cross-talks are minimized by using selective interference filters exhibiting an optical density higher than 5 at 355 nm wavelength in the VIS π–polarimeter and at 532 nm wavelength in the UV π–polarimeter.
- *Multiple scattering may eventually occur and cause further light depolarization.* However, the single-scattering approximation (*SSA*) is rather safe in our laboratory backscattering experiment (Mishchenko et al. 2007) where the particles are moving in a thin (2.5 mm) wide beam so that the volume element is optically thin in contrary to atmospheric chambers.

3.3 Light Backscattering by Spherical Sulfates in Laboratory

Light backscattering by sulfate particles is extremely important as sulfates are responsible for a net cooling of the Earth's atmosphere due to their ability to backscatter light. Figure 4 from Miffre et al. (2016) displays the measured variations of $I_\pi^\lambda = f(\psi)$ at both UV and VIS wavelengths. Both curves exhibit zero minima, showing the zero-depolarization of spherical sulfate particles, in agreement with Lorenz-Mie theory. To be quantitative, we adjusted the UV and VIS curves and their respective successive minima and maxima by using Eqs. (3–5) to retrieve the F_{22}/F_{11} ratio:

$$\begin{aligned} F_{22}^\lambda/F_{11}^\lambda(sulfates, \lambda = 355\,nm) &= 0.9945 \pm 0.0065 \\ F_{22}^\lambda/F_{11}^\lambda(sulfates, \lambda = 532\,nm) &= 1.0037 \pm 0.0049 \end{aligned} \tag{12}$$

The precision on the F_{22}/F_{11} ratio is remarkable and results from the precision achieved in the laboratory π-polarimeter and on the stability of the particles generator. The corresponding *PDR* is then obtained by applying Eqs. (3–6):

$$\begin{aligned} PDR_\pi^\lambda(sulfates, \lambda = 355\,nm) &= (0.28 \pm 0.33)\% \\ PDR_\pi^\lambda(sulfates, \lambda = 532\,nm) &= (0.19 \pm 0.24)\% \end{aligned} \tag{13}$$

The observed zero depolarization is compatible with Lorenz-Mie theory, which in turn validates the ability of the laboratory π-polarimeter to accurately measure the lidar *PDR* of sulfates at both wavelengths. Although more than a century has now elapsed since G. Mie presented his theory (Mie 1908), even though measurements of water clouds do not contradict the Mie theory, it is surprising that its experimental proof had never been achieved in laboratory in the exact backscattering direction for aerosols, such as spherical water droplets or sulfate particles, while, in the literature, a considerable number of papers apply the Lorenz-Mie theory, as for environmental purposes, such as in remote sensing and radiative transfer applications.

3.4 Light Backscattering by Core–Shell Organic Sulfates in Laboratory

Conversely, the impact of organic aerosol on the Earth's radiative balance remains elusive as it is associated with large uncertainties. While it was assumed that sulfur is primarily present in its inorganic forms (e.g., SO_4^{2-}, HSO_4^-, HSO_3^-), field and laboratory studies (Riva et al. 2019; Shakya and Peltier 2013, 2015; Surratt et al. 2008; Tolocka and Turpin 2012) recently showed that organosulfur compounds, including organosulfates, are important contributors to the total sulfate aerosol mass. This paragraph summarizes the outputs of a cooperative work between our group and chemical colleagues (Dubois et al. 2021). There, we revealed an unexpected trend with a net decrease in light backscattering by the sulfate aerosol in the presence of organic compounds, giving rise to core–shell structures. These complex organic compounds (isoprene epoxydiols, IEPOX) or organosulfates are the most important secondary organic aerosol precursors in the atmosphere. This finding suggests that, when organic compounds, including organosulfates are present, the ability of inorganic sulfate particles to backscatter light is greatly decreased. Hence, our laboratory findings are key for quantifying the direct radiative forcing of sulfates in the presence of organic compounds, thus more clearly resolving the impact of such aerosol particles on the Earth's climate.

In more details, measuring the light backscattered by organic sulfates represented a real experimental challenge due to the very low backscattering cross-section of such particles presenting sizes in the hundreds of nanometers range only. However, the sensitivity achieved in the laboratory backscattering polarimeter was sufficiently high: using the laboratory π-polarimeter, controlled-laboratory experiments were performed to compare the backscattered light intensity by organic / inorganic sulfates. Figure 3 from Dubois et al. (2021) displays the corresponding backscattered light intensity $I_{\pi}^{\lambda} = f(\psi)$ at both UV and VIS-wavelengths. The curve minima being null, organic and inorganic sulfates remained spherical during the acquisition. The curve maxima $I_{\pi,M}^{\lambda}$ of $I_{\pi}^{\lambda} = f(\psi)$, which correspond to an incident s-polarized radiation, could then be used as a metrics of the backscattered light intensity (the π-polarimeter measures the s-polarization component of the backscattered radiation, which is preserved during the backscattering process for spherical particles). A precise evaluation of these maxima was then performed by adjusting our experimental data points with a $\cos(4\psi)$ curve.

The key point is that the $I_{\pi,M}^{\lambda}$ maxima were representative of a determined particles number density, size distribution and refractive index. Indeed, if the particles number density or size distribution had varied during the backscattering experiments, the maxima $I_{p,M}$ would not have remained constant when varying the wave-plates orientation. Likewise, potential variations in particle number concentrations when considering the conversion from inorganic to organic sulfates were accounted for by considering $I_{\pi,M}^{\lambda}/N_{tot}$ where N_{tot} is the integral of the particle number density over the particles size distribution (Dubois et al. 2021). Hence, the observed decrease can only be due to variations in the complex refractive index from inorganic to organic sulfates. To be quantitative, the experiment was then repeated for increased organic (IEPOX) gas phase concentrations to reveal a net decrease in the normalized backscattered light intensity $I_{\pi,M}^{\lambda}/N_{tot}$ of 16% at 532 nm wavelength and 12% at 355 nm wavelength from inorganic to organic sulfates.

We then compare our laboratory findings with the outputs given by Lorenz-Mie light scattering numerical simulations to compute the backscattering cross-section C_{back} (resp. $C_{back,0}$) of organic (resp. inorganic) particles using the particles size distributions measured for the sulfate and organics mixture. As a first step, C_{back} was computed for the refractive index of ammonium sulfate ($m = 1.445$) (Cotterell et al. 2017) and organics (IEPOX-derived secondary organics aerosols, $m = 1.43 + 0.002j$) (Nakayama et al. 2018). The observed decrease in C_{back} could not be reproduced by size effects only and was therefore related to variations in the complex refractive index. To account for the presence of both AAS and IEPOX-derived SOA compounds, we then applied effective medium theories, by applying the Aspens formula, providing the effective particles complex refractive index of a backscattering medium containing a mixture of AAS and IEPOX-derived SOA products. As displayed in Fig. 5 from Dubois et al. (2021) however, the variations of $C_{back}/C_{back,0}$ did not more faithfully reproduce our laboratory observations when considering AAS volume fractions in the AAS and IEPOX-derived SOA particle mixtures ranging from 0.96 to 1.00, with 0.02 step, consistent with performed chemical analyses. As a result, the effect on C_{back} of a possible change in the internal structure of the particles was investigated. Indeed, the reactive uptake of IEPOX is known to produce core–shell structures.(Olson et al. 2019; Riva et al. 2019; Zhang et al. 2018) To investigate the case of a stratified dielectric sphere (i.e., a spherical inorganic core coated by a spherical organic shell), we applied the numerical code from (Ackerman and Toon 1981) an extension of the Lorenz-Mie theory, suitable for thin film absorbent particles as was expected in our experiments. When adjusting the core/shell radius to consider the above volume fractions, we reproduced a part of the observed decrease inC_{back}. Considering an IEPOX refractive index of $1.43 + 0.5j$ led to a decrease in the backscattering cross-section$C_{back}/C_{back,0}$ by about 18% at 532 nm wavelength (see Fig. 5 from (Dubois et al. 2021)), in the same range as that observed in laboratory. Hence, the formation of an inorganic core organic shell structure can be key for explaining the reported decrease, though effective medium theories may also be key.

3.5 Light Backscattering by Soot Particles in Laboratory

Likewise, the laboratory π-polarimeter has been used to quantify the lidar *PDR* of freshly emitted soot particles from a pool jet fire, in cooperation with ONERA. This paragraph summarizes the outputs of this cooperative work (Paulien et al. 2021). In a few words, Table 3 gathers the main laboratory findings, with a lidar *PDR* in the range of 10%. The soot morphology and non-sphericity is clearly seen in Fig. 3 from Paulien et al. (2021) where the minima, which are related to $1-F_{22}^{\lambda}/F_{11}^{\lambda}$, are not null. The retrieved value of the lidar *PDR* interestingly compare with lidar field measurements of the lidar *PDR* by Burton et al. (2016) who retrieved a value of the lidar *PDR* 9.3%

Table 3 First laboratory measurement of the ratio $F_{22}^{\lambda}/F_{11}^{\lambda}$ of scattering matrix elements and corresponding lidar *PDR* of freshly-emitted soots (JET A1 pool fire) at exact backscattering angle ($\theta = \pi$)

Wavelength (nm)	$F_{22}^{\lambda}/F_{11}^{\lambda}$	*PDR*
355	0.79 ± 0.03	11.7 ± 2.3
532	0.84 ± 0.03	8.7 ± 2.1

lidar at 532 nm compatible with our laboratory findings, despite aged smoke was there considered. T-matrix numerical simulations of these aged soot by Mishchenko et al. (2018) also well compare at least at 532 nm. To address the lidar *PDR* of freshly emitted soot, Paulien et al. (2021) applied the superposition T-Matrix (STM) method to numerically simulate the soot aggregates backscattering properties for different soot particles refractive indices, monomer radii and monomer numbers. The range of these parameters which ensures the lowest discrepancy between the laboratory-measured soot lidar *PDR* and the STM-computations was discussed within experimental and numerical error bars. The polydisperse monomers model was found to give an overall better evaluation of the ratio$F_{22}^{\lambda}/F_{11}^{\lambda}$. In the polydisperse case, our numerical and laboratory experimental findings agree at both wavelengths for a refractive index m = 2.65 + i1.32 and monomer number >40 at a mean monomer radius of 30 nm.

3.6 Light Backscattering by Mineral Dust in Laboratory

We here present laboratory experiments on mineral dust at exact backscattering lidar angle using the π-laboratory polarimeter. The motivations of this work are numerous. First of all, revealing the intrinsic lidar *PDR* of mineral dust is necessary for accurate interpretation of lidar returns and for that focusing on the exact lidar backscattering angle in laboratory is essential, as explained in the previous sections. Secondly, for aerosol identification purposes, the dependence of the dust lidar *PDR* has to be analyzed for different dust samples, deferring in sizes and complex refractive index, and for that laboratory intensive work is required (Miffre et al. 2022). Ideally, this laboratory study must be carried out at several lidar wavelengths (355, 532 nm) to better constrain future lidar inversions (Burton et al. 2016). In turn, the ability of the mathematical spheroidal model to reproduce mineral dust particles backscattering at several wavelengths in the exact backward scattering direction may then be discussed. We start from this numerical approach (Miffre et al. 2016).

(a) Ability of the spheroidal model to reproduce the spectral dependence of the dust lidar PDR

In Miffre et al. (2016), using the laboratory π-polarimeter, the lidar *PDR* of two determined particle size distributions of Arizona Test Dust (ATD) were evaluated in laboratory at 355 and 532 nm wavelength simultaneously. Interestingly, these laboratory findings agree with T-matrix numerical simulations, at least for a determined particle size distribution and at a determined wavelength, showing the ability of the spheroidal model to reproduce mineral dust particles in the exact backward scattering direction. However, the spectral dependence of the laboratory-measured *PDR* could not be reproduced with the spheroidal model, even for not evenly distributed aspect ratios.

In more details, we considered a power-law shape distribution of spheroids, i.e.$f(\varepsilon) = \varepsilon^n$, where n is an integer and studied three successive cases: $n = 0$

(equiprobable shape distribution), $n = 3$ then $n = 10$, the latter favoring extreme aspect ratios at the expense of nearly spherical spheroids. After size integration over the particles size distribution (*SD*), the spheroidal model was found capable of reproducing our laboratory experimental results in the exact backscattering direction whatever the radiation wavelength (i.e. either 355 or 532 nm wavelength). The assumption of spheroids evenly distributed over aspect ratio (equiprobable shape distribution) seemed however to decrease the ability of the spheroidal model to account for the particles depolarization. Nevertheless, even by taking into account the spectral dependence of the complex refractive index, the spectral dependence of the dust lidar *PDR* could not be reproduced at both UV and VIS-wavelengths simultaneously. This finding agrees with (Dubovik et al. 2006b), who noted that "the measured spectral dependence (could) only be reproduced by spheroids only if we assume differences for the size distributions for each of the two wavelengths", and was also pointed out in Zubko et al. (2013). Our contribution shows that this statement also applies in the exact backward direction, at least for the particles size distribution considered in this study. As a conclusion, in the exact backward scattering direction, the spheroidal model is well-adapted for reproducing the dust lidar*PDR*, but only at one determined wavelength, either 355 or 532 nm. Readers interested by this specific question can refer to Miffre et al. (2016) for detailed information. We here focus on the dependence of the lidar *PDR* with size and complex refractive index, as presented at the ELS Conference 2021 and in Miffre et al. (2022).

(b) Mineral dust laboratory samples differing in size and mineralogy

To study the dependence of the dust lidar *PDR* with size and mineralogy, we here consider the following mineral dust samples:

- Silica, or silicon oxide (SiO_2), as it is the main pure chemical component present in mineral dust.
- Iron oxide, or hematite (Fe_2O_3), as a secondary pure chemical component present in mineral dust, also selected as a light absorbent in the shortwave spectral region (Zong et al. 2021), which recently gained in interest with papers specifically dedicated to this constituent (Gautam et al. 2020; Go et al. 2022).
- Arizona dust, as it is an important case study of natural mineral dust sample involving a mixture of the above two oxides. Arizona dust is composed of silica (68–76%), while hematite is only weakly present in Arizona dust (2–5%). In short, Arizona dust is hence rather silica-rich.
- Asian dust, as an important case study of natural mineral dust sample, presenting however a lower proportion of silica (34–40%) and a higher proportion of hematite (17–23%). Hence, compared with Arizona dust, Asian dust is more hematite-rich.

To address the dependence of the dust lidar *PDR* with the dust particles size distribution (*SD*), the light backscattered by each above dust sample was measured with the laboratory π-polarimeter in the presence, then in the absence of a cyclone. The retrieved particles *SD* are displayed in Miffre et al. (2022) and are in agreement with the specifications provided by the manufacturers. In the presence of the cyclone, the *SD* is more representative of mineral dust samples after long-range transport, i.e.

Table 4 Laboratory measurement of the ratio $F_{22}^{\lambda}/F_{11}^{\lambda}$ of scattering matrix elements and corresponding lidar PDR(see Eq. 5) for Arizona and Asian dust at exact backscattering angle ($\theta = \pi$), evaluated from the laboratory π-polarimeter (Miffre et al. 2016, 2022)

Mineralogy	λ(nm)	Finer *SD*		Coarser *SD*	
		$F_{22}^{\lambda}/F_{11}^{\lambda}$	*PDR*(%)	$F_{22}^{\lambda}/F_{11}^{\lambda}$	*PDR*(%)
Arizona dust	355	0.514 ± 0.007	32.1 ± 0.6	0.489 ± 0.012	34.3 ± 1.0
	532	0.512 ± 0.012	32.3 ± 1.0	0.464 ± 0.012	36.6 ± 1.1
Asian dust	355	0.603 ± 0.009	24.7 ± 0.6	0.603 ± 0.011	24.8 ± 0.8
	532	0.622 ± 0.009	23.3 ± 0.7	0.558 ± 0.011	28.4 ± 0.8

farther from the dust source regions and will be hereafter referred to as the finer *SD*. Likewise, in the absence of the cyclone, the *SD* corresponds to dust particles closer to dust source regions, will be referred to as the coarser *SD*. The backscattered light intensity was then measured for each dust sample (silica, hematite, Arizona dust, Asian dust) at 355 and 532 nm wavelength for both the finer and the coarser *SD* and the corresponding dust lidar *PDR* was accurately evaluated.

(iii) Laboratory measurement of the lidar PDR of dust particles mixtures at lidar exact backscattering angle

Let us first argue on the retrieved dust lidar *PDR* for Arizona and Asian dust with the coarser *SD*. The variations of the normalized backscattered light intensity by Arizona dust, then Asian dust for the *FinerSD* (left panels) and the *CoarserSD* (right panels) are displayed in Miffre et al. (2022). As above explained, for each light backscattering curve exhibits constant extrema, in each panel, the size and the shape of the dust sample did not vary during the acquisition. As a result, the observed variations relate to the spectral and polarimetric light backscattering characteristics of the considered dust sample and the corresponding experimental data points can be adjusted with Eq. (9) to evaluate $F_{22,d}^{\lambda}/F_{11,d}^{\lambda}$ then the dust lidar *PDR b*y applying Eq. (11). Table 4 gathers the retrieved dust lidar *PDR* for Arizona and Asian dust, for the finer and the coarser *SD* at 355 and 532 nm wavelength. The precision on the $F_{22,d}^{\lambda}/F_{11,d}^{\lambda}$ evaluation is remarkable and results from the accuracy of the laboratory π-polarimeter. Care should be taken when comparing the light backscattering curves from Arizona and Asian dust for the applied voltage to the UV and VIS-photodetectors were adjusted to increase the signal-to-noise ratio, as explained in Sect. 3.2. Hence, for the coarser*SD*, the dust lidar *PDR* is higher for Arizona dust. Within experimental error bars, the Arizona and Asian dust lidar *PDR* clearly differ, whatever the chosen wavelength. The generally admitted value of around 33% for the dust lidar *PDR* (Tesche et al. 2009) is indeed observed but for Arizona dust only: Asian dust exhibits a lower depolarization ratio in the range from 24 to 28% depending on the considered *SD* and wavelength. This suggests that the dust lidar *PDR* is primarily governed by the dust particles refractive index. The sensitivity of the dust lidar *PDR* with the considered *SD* is indeed less pronounced: from the coarser to the finer *SD*, a reduction in the dust lidar *PDR* of at most 5% is observed at 532 nm wavelength. At 355 nm wavelength however, the Arizona and Asian dust lidar *PDR* seems practically insensitive to variations in the considered *SD*.

(iv) Laboratory measurement of the lidar PDR of silica and hematite (pure components) at backscattering angle

By applying the same methodology, we retrieved the silica and hematite lidar *PDR* gathered in Table 5 which is the analogue of Table 4 for silica and hematite dust samples. As for Arizona and Asian dust samples, the dust lidar *PDR* for silica and hematite primarily depends on the particles mineralogy and complex refractive index at least at 355 nm wavelength where the silica lidar *PDR* ranges from 23 to 33% depending on the considered *SD* while the hematite lidar *PDR* reaches 10% only. The silica and hematite lidar *PDR* hence strongly depend on the chosen lidar wavelength, with higher depolarization at 355 nm for silica (at 532 nm for hematite). The silica lidar *PDR* strongly depends on the *SD* from the coarser to the finer SD, the reduction in the silica dust lidar PDR reaches 10% at both wavelengths. The dependence of the hematite dust lidar *PDR* with the *SD* is less pronounced, especially at 355 nm wavelength.

(e) Dependence of the dust lidar PDR with size and complex refractive index at exact backscattering angle

The laboratory π-polarimeter however allows discussing on the dependence of the dust lidar *PDR* with the *SD* and complex refractive index (Miffre et al. 2022). Comparing our laboratory findings with other laboratory experiments is not feasible at present to our knowledge, for none of these set-ups operates at lidar exact backscattering angle for aerosols, while the dust lidar *PDR* can be very different at near and exact backscattering angles, as explained in Sect. 1.3. In the literature dedicated to lidar field experiments (Tesche et al. 2009), a dust lidar *PDR* of 33% is often considered in lidar retrievals. This value is indeed measured with our laboratory π-polarimeter for silica oxide, which is the main oxide present in mineral dust, and also for Arizona dust, which is rather silica-rich. Comparison of our laboratory findings with this literature however remains difficult because in lidar field experiments, the measured depolarization is nevertheless that of particle mixtures. Our laboratory findings can however be compared with light scattering numerical simulations,

Table 5 Laboratory measurement of the ratio $F_{22}^{\lambda}/F_{11}^{\lambda}$ of scattering matrix elements and corresponding lidar PDR (see Eq. 5) of silica and hematite at exact backscattering angle ($\theta = \pi$), evaluated from the laboratory π-polarimeter (Miffre et al. 2016, 2022)

Mineralogy	λ (nm)	Finer *SD*		Coarser *SD*	
		$F_{22}^{\lambda}/F_{11}^{\lambda}$	*PDR*(%)	$F_{22}^{\lambda}/F_{11}^{\lambda}$	*PDR*(%)
Silica	355	0.622 ± 0.014	23.3 ± 0.9	0.506 ± 0.011	32.8 ± 1.0
	532	0.751 ± 0.016	14.2 ± 0.9	0.618 ± 0.016	23.6 ± 1.1
Hematite	355	0.805 ± 0.050	10.8 ± 2.5	0.823 ± 0.015	9.7 ± 0.7
	532	0.652 ± 0.055	21.1 ± 3.5	0.715 ± 0.019	16.6 ± 1.1

which are becoming more and more accurate. Light scattering numerical simulations (Kahnert 2015) show that the dust lidar *PDR* is strongly modulated by the particles inhomogeneity, especially in the presence of hematite. In Kahnert (2015), it was stressed that this feature was particularly pronounced in the lidar backward scattering direction and our laboratory findings show that the dust lidar *PDR* is indeed strongly modulated by the particles inhomogeneity. In the most general case, the dust lidar *PDR* appears as a complex function of the particles mineralogy, size distribution and wavelength Though this triple dependence is difficult to disentangle, based on our laboratory findings, we see that the mineralogy primarily affects the dust lidar, at least when hematite is involved. Indeed, hematite is a light absorbent and the presence of an imaginary part for the complex refractive index of hematite modifies the backscattering matrix elements, so does the corresponding dust lidar*PDR*. In turn, Asian dust, which is more hematite rich than Arizona dust, exhibits a lower depolarization ratio. The impact of hematite on dust absorption wavelengths ranging from 0.2 to 1.0 μm was indeed recently evaluated in the literature using the T-matrix spheroidal model by Zong et al. (2021). Hence and as a result, when hematite, which is a light absorbent, is present, it mainly governs the depolarization ratio, though size and wavelength effects also clearly play a role.

4 Light Backscattering in the Atmosphere: Lidar Field Experiments

4.1 Atmospheric Lidar Implications

(a) Circular versus linear depolarization ratio

The above laboratory measurements at near ($\theta < \pi$) and exact backscattering ($\theta = \pi$) allow retrieved the linear and circular particles depolarization ratios which are used in lidar applications. Following Mishchenko and Hovenier [36], the linear *PDR*(here noted $\delta_L(\pi)$ for lidar purposes) and circular $\delta_C(\pi)$ ddepolarization ratios relate to the laboratory measurements at scattering angle θ as follows:

$$\begin{aligned}\delta_L(\theta) &= (1 - f_{22}^{\lambda}(\theta) / \big(1 \pm 2 f_{12}^{\lambda}(\theta) + f_{22}^{\lambda}(\theta)\big) \\ \delta_C(\theta) &= \big(1 \pm f_{44}^{\lambda}(\theta)\big) / \big(1 \mp f_{44}^{\lambda}(\theta)\big)\end{aligned} \tag{14}$$

where reduced notations have been used ($f_{ij}^{\lambda} = F_{ij}^{\lambda}/F_{11}^{\lambda}$) and the positive (negative) sign corresponds to incident p (s) polarization state for *PDR* and to incident RC (LC) polarization state for PDR_C. From Fig. 7 from Miffre et al. (2019b), at exact backscattering ($\theta = \pi$),$\delta_L(\pi) = (27.3 \pm 1.6)\%$ while $\delta_C(\pi) = (75.4 \pm 6.1)\%$. The circular depolarization ratio δ_c exhibits pronounced variations, due to variations in $f_{44}(\theta)$, increasing from 62.6% at 176.0° scattering angle up to 75.4% at 180.0°. For the first time to our knowledge, within our experimental error bars, we may conclude that the relationship $\delta_C(\pi) = 2\delta_L(\pi)/(1 - \delta_L(\pi))$ only applies at exact backscattering angle, as theoretically set by Mishchenko and Hovenier (1995). In what follows, the lidar linear *PDR* will be noted δ for $\delta_L(\pi)$.

(b) Lidar partitioning algorithms

The downside of such field lidar depolarization measurements is that the measured depolarization ratio is nevertheless that of a mixture. Hence, care should be taken when comparing the lidar-measured depolarization ratio with our laboratory findings, which reveal the intrinsic depolarization ratio of a determined size and shape distribution of a given aerosol, as we demonstrated (Mehri et al. 2018; Miffre et al. 2011). The intrinsic depolarization ratio remains key for precise retrievals of vertical profiles of atmospheric particles backscattering dedicated to a given aerosol, for instance mineral dust (David et al. 2013; Mehri et al. 2018; Miffre et al. 2011).

Hence, lidar partitioning algorithms have been developed to disentangle particle mixtures. Our group contributed to that research field in line of (Tesche et al. 2009) ‘s contribution by developing the $1\beta + 1\delta$ partitioning algorithm. Moreover, we extended this approach to three-component particle external mixtures by developing the $2\ \beta + 2\delta$ partitioning algorithm (David et al. 2013). We here briefly present the $1\ \beta + 1\delta$ partitioning algorithm. Interested readers can find more details in the corresponding publications (Mehri et al. 2018; Miffre et al. 2011).

Let us consider a two-component particle external mixture$(p) = \{s, ns\}$, composed of both spherical (s) and nonspherical (ns)-particles of different origin. After long-range transport, an example such a mixture is given by the external mixing of mineral dust (d) particles with spherical (s) particles, most likely hydrated sulfates. To quantify the contribution of mineral dust particles in the two-component particle external mixture$(p) = \{s, ns\}$, a careful analysis of the polarization of the backscattered radiation must be performed. The starting point is the lidar observable, the lidar particles backscattering coefficient:

$$\beta_p = \int_{SD} \mathrm{C}_{back,p} n_p(r)dr \cdot = \int_{SD} \mathrm{C}_{sca,p} \frac{F_{11,p}}{4\pi} n_p(r)dr \tag{15}$$

where $C_{back,p}$ is the particle backscattering cross-section and the dependence with wavelength λ has been omitted to ease the reading. A polarization lidar experiment at wavelength λ provides accurate vertical profiles of polarization-resolved particles backscattering $\beta_{p,//}$ and $\beta_{p,\perp}$, on each $\pi = (//, \perp)$ polarization channel, defined with respect to the laser linear polarization. Noting that β_p is additive and that $\delta_{ns} = \beta_{ns,\perp}/\beta_{ns,//}$, we get (David et al. 2013; Miffre et al. 2011):

$$\beta_{ns} = \beta_{p,\perp}(1 + 1/\delta_{ns}) \tag{16}$$

As a result, vertical profiles of particles backscattering specific to non-spherical mineral dust can be retrieved by coupling polarization-resolved particles backscattering $\beta_{p,\perp}$ with accurate laboratory measurements of the intrinsic dust lidar *PDR*, as presented in Sect. 3. Examples of applications of this approach are here detailed, using the Lyon (France) lidar station, the only to our knowledge whose polarization lidar detector is based on the laboratory π-polarimeter.

4.2 Field Version of the Laboratory π-polarimeter

As show in David et al. (2012; Miffre et al. 2019a), a field version of the laboratory π-polarimeter presented in Sect. 3 has been implemented as lidar detector, to avoid any possible bias when exploiting the synergy between laboratory and field experiments. This approach allowed to specify the polarization and wavelengths cross-talks of our lidar detector in laboratory, in the form of a detector transfer matrix, relating the entrance I_π^λ and output $\left(I_\pi^\lambda\right)^*$ intensity of the π-polarimeter (David et al. 2012):

$$\begin{bmatrix} \left(I_p^{355nm}\right)^* \\ \left(I_s^{355nm}\right)^* \\ \left(I_p^{532nm}\right)^* \\ \left(I_s^{532nm}\right)^* \end{bmatrix} = \begin{bmatrix} \eta_p(355nm) & 0 & 0 & 0 \\ 4\times10^{-8} & \eta_s(355nm) & 0 & 0 \\ 0 & 0 & \eta_p(532nm) & 0 \\ 0 & 0 & 0 & \eta_s(532nm) \end{bmatrix} \begin{bmatrix} I_p^{355nm} \\ I_s^{355nm} \\ I_p^{532nm} \\ I_s^{532nm} \end{bmatrix} \tag{17}$$

The detector transfer matrix being diagonal (with 4×10^{-8} accuracy), wavelength and polarization cross-talks are negligible, which allows a robust calibration of the lidar *PDR* to be achieved, as published in (Miffre et al. 2019a). This calibration consists in evaluating the electro-optics gain calibration constant G of the lidar detector at wavelength λ to retrieve the intrinsic lidar *PDR* from the measured lidar δ^*. In the literature, existing calibration methods rely on a molecular atmosphere (Behrendt and Nakamura 2002), which however does not rigorously exist, or on the ±45° methodology (Freudenthaler et al. 2009), which may saturate the photodetector. Rather, we proposed and successfully applied the methodology illustrated in Fig. 1 in Miffre et al. (2019a). At wavelength λ, a precise evaluation of G is achieved by introducing controlled amounts of polarization cross-talks, using a half-wavelength plate (HWP), inserted on the optical pathway from the laser to the atmosphere. The variations of the measured atmospheric depolarization δ^* with the modulation angle φ of the HWP can then be adjusted in the framework of the scattering matrix formalism to get precise value of G. Indeed, the lidar intensity detected at wavelength λ on each $\pi = (p, s)$polarization channel is given by:

$$I_\pi = \frac{\eta_\pi P_{0,\lambda}}{z}\left(P_j\right)[PBC][F_\lambda(\theta = \pi)][HWP][St_i] \tag{18}$$

where, as in Sects. 2 and 3, $[\boldsymbol{PBC}]$ and $[\boldsymbol{HWP}]$ are the Mueller matrices of the polarizing beam-splitter cube (PBC) and the HWP respectively while $(St_i) = [1, 1, 0, 0]^T$.

In Eq. (19), η_π is the optoelectronics constant of the π-polarization channel (defined with respect to the incident laser polarization) and the gain-optics calibration constant G relates to this quantity as $\mathrm{G} = \eta_s/\eta_p$. The measured depolarization is then $\delta^* = I_s/I_p$ is then retrieved by using Eq. (5) to replace $F_{22}^{\lambda}/F_{11}^{\lambda}$ as a function of the lidar *PDR*. Hence, at wavelength λ, the measured atmospheric depolarization δ^* relates to the intrinsic particles depolarization δ as follows:

$$\delta^* = G\frac{1 + \delta - (1 - \delta)\cos(4\varphi)}{1 + \delta + (1 - \delta)\cos(4\varphi)} \tag{19}$$

As a result, the calibration constant G can be evaluated at wavelength λ with 2% accuracy by adjusting the φ-variations of the measured δ^* with Eq. (20), as illustrated in Fig. 1 from Miffre et al. (2019a) at 355 and 532 nm wavelength. The sensitivity of our laboratory π-polarimeter, when combined with this accurate calibration, allowed to reveal accurate vertical profiles of particles depolarization ratios directly in the atmosphere from volcanic ashes released from the Icelandic volcano (Miffre et al. 2012), mineral dust particles brought to France from Saharan dust outbreaks (David et al. 2013; Mehri et al. 2018), or even the subsequent growth following new particle formation events promoted by mineral dust (Miffre et al. 2019a).

4.3 Application Case Study: Time-Altitude Maps of Dust Particles Backscattering Revealing the Underlying Complex Physical-Chemistry

We here evaluate the dust particles backscattering coefficient corresponding to a Saharan dust outbreak that occurred at Lyon in July 2010. During this event, non-spherical particles were identified as desert dust particles, as confirmed by air mass back-trajectories as published in Dupart et al. (2012) as a supplementary material. Figure 4 from David et al. (2014) presents the corresponding time-altitude maps of the lidar-retrieved backscattering coefficients, measured at Lyon at λ = 355 nm in July 2010 during a Saharan dust outbreak by taking benefit from the laboratory π-polarimeter. Mineral dust particles, for which $\beta_{p,.}$ is not null, are mainly located above 3 km altitude while a $\beta_{p,//}$-enhancement is observable in the free troposphere between 2 and 3 km altitude, which is not observed on the $\beta_{p,\perp}$-map. Interestingly, an enhancement is to be seen in the time-altitude map corresponding to non-dust particles, which are spherical. We could relate this behavior to the subsequent growth following a new particle formation event promoted by mineral dust through a photo-catalytic process (Dupart et al. 2012). Interested readers can find more information in the corresponding publications (David et al. 2014; Miffre et al. 2019a, 2020). As a conclusion, the laboratory approach we followed with the laboratory π-polarimeter enables to reveal the underlying physico-chemical processes involved in the atmosphere, which in turn reinforces our understanding of light backscattering by such complex-shaped particles.

5 Conclusion and Outlooks

This book chapter is dedicated to light backscattering by atmospheric particles. This research topic is extremely important for both fundamental and applicative purposes:

- From a fundamental point of view, light backscattering has proven efficiency for providing information on the optical properties of condensed or gaseous matter (Vitkin and Studinski 2001; Wang et al. 2012) and also as involved in the so-called coherent backscattering effect [8], which is still to be understood. Also, near and exact backscattering are interesting to study as light scattering numerical simulations exhibit a narrow double-lobe feature when studying small-scale surface roughness [16]. Finally, for radiative transfer purposes, the scattering phase function needs to be precisely known over the whole scattering angle range, and hence covers the backward scattering direction with precision.
- From an applicative point of view, light backscattering is the key physical process involved in ground-based and satellite-based lidar remote sensing instruments which provide a major source of global data on mineral dust, which are needed for radiative and climate forcing assessments.

While a large number of references exist in the literature on light scattering numerical simulations and on lidar remote sensing data at backscattering angle, there is a dearth of laboratory experiments providing the so-called lidar *PDR* at exact lidar backscattering angle ($\theta = \pi$). On account of the above considerations, after reviewing the corresponding literature, this book chapter mainly focuses on controlled laboratory experiments at near ($\theta < \pi$) and exact ($\theta = \pi$) backscattering angles for particles embedded in ambient air.

- In Sect. 2, to complement existing laboratory light scattering experimental set-ups, we then proposed a new laboratory experiment, the π+ε-laboratory polarimeter (Miffre et al. 2019a, b), to retrieve the scattering matrix elements $F_{ij}^{\lambda}/F_{11}^{\lambda}(\theta)$ from 176.0° to backscattering angle with a 0.4° angular step for mineral dust. The ability of the mathematical spheroidal model to mimic light scattering by mineral dust at near backscattering angles is then verified.
- In Sect. 3, we specifically focused on the cutting-edge laboratory π-polarimeter at exact backscattering angle or lidar angle ($\theta = \pi$), (Miffre et al. 2016), with emphasis on its ability to accurately measure the backscattered light intensity and the corresponding lidar *PDR* of aerosols. Case studies on spherical inorganic sulfates, core–shell organic sulfates (Dubois et al. 2021), freshly-emitted soot (Paulien et al. 2021) and mineral dust (Miffre et al. 2022) were studied. In the latter study, the dependence of the lidar PDR with size and complex refractive index was

studied in laboratory for the first time to our knowledge at exact backscattering lidar angle ($\theta = \pi$).
- In Sect. 4, implications of this laboratory work on aerosols light backscattering in lidar remote sensing experiments were proposed and discussed. There, the sensitivity and accuracy achieved on the laboratory π-polarimeter at exact backscattering angle allowed providing calibrated polarization lidar measurements, which in turn have the ability to reveal the underlying complex vertical layering of the atmosphere (David et al. 2014; Miffre et al. 2019a, 2020). In particular, while the vertical layering of the atmosphere is extremely complex, vertical profiles specific to non-spherical particles backscattering could be accurately retrieved by taking benefit from the laboratory π-polarimeter.

We hope that this work will contribute to provide a better understanding of the physical process of light backscattering and may provide accurate inputs to better constrain lidar inversions. Still, lots of work need to be done in laboratory to better understand the dependence of the lidar *PDR* with the particles size and complex refractive index at specific backscattering angle, a direction particularly sensitive to particles inhomogeneity. In this context, a first interesting complementary step would be to extend the applicability of the laboratory π-polarimeter to the 1064 nm wavelength, to better constraint both light scattering numerical simulations and lidar inversions.

References

Ackerman TP, Toon OB (1981) Absorption of visible radiation in atmosphere containing mixtures of absorbing and nonabsorbing particles. Appl Opt 20:3661. https://doi.org/10.1364/AO.20.003661

Ansmann A, Petzold A, Kandler K, Tegen I, Wendisch M, Müller D, Weinzierl B, Müller T, Heintzenberg J (2011) Saharan Mineral Dust Experiments SAMUM–1 and SAMUM–2: what have we learned? Tellus B Chem. Phys Meteorol 63:403–429. https://doi.org/10.1111/j.1600-0889.2011.00555.x

Behrendt A, Nakamura T (2002) Calculation of the calibration constant of polarization lidar and its dependency on atmospheric temperature. Opt Express 10:805–817. https://doi.org/10.1364/OE.10.000805

Bohren CF, Huffman DR (1983) Absorption and scattering of light by small particles. Wiley-VCH, Weinheim

Burton SP, Chemyakin E, Liu X, Knobelspiesse K, Stamnes S, Sawamura P, Moore RH, Hostetler CA, Ferrare RA (2016) Information content and sensitivity of the 3 $\beta + 2\ \alpha$ lidar measurement system for aerosol microphysical retrievals. Atmos Meas Tech 9:5555–5574. https://doi.org/10.5194/amt-9-5555-2016

Chien C-H, Theodore A, Wu C-Y, Hsu Y-M, Birky B (2016) Upon correlating diameters measured by optical particle counters and aerodynamic particle sizers. J Aerosol Sci 101:77–85. https://doi.org/10.1016/j.jaerosci.2016.05.011

Cholleton D, Bialic E, Dumas A, Kaluzny P, Rairoux P, Miffre A (2020) Laboratory evaluation of the (VIS, IR) scattering matrix of complex-shaped ragweed pollen particles. J Quant Spectrosc Radiat Transf 254:107223. https://doi.org/10.1016/j.jqsrt.2020.107223

Cholleton D, Bialic É, Dumas A, Kaluzny P, Rairoux P, Miffre A (2022) Laboratory evaluation of the scattering matrix of ragweed, ash, birch and pine pollen towards pollen classification. Atmos Meas Tech 15:1021–1032. https://doi.org/10.5194/amt-15-1021-2022

Cotterell MI, Willoughby RE, Bzdek BR, Orr-Ewing AJ, Reid JP (2017) A complete parameterisation of the relative humidity and wavelength dependence of the refractive index of hygroscopic inorganic aerosol particles. Atmos Chem Phys 17:9837–9851. https://doi.org/10.5194/acp-17-9837-2017

Dabrowska DD, Muñoz O, Moreno F, Nousiainen T, Zubko E, Marra AC (2013) Experimental and simulated scattering matrices of small calcite particles at 647nm. J Quant Spectrosc Radiat Transf 124:62–78. https://doi.org/10.1016/j.jqsrt.2013.02.010

David G (2013) Polarization-resolved backscattering from nanoparticles in the atmosphere: field and laboratory experiments

David G, Miffre A, Thomas B, Rairoux P (2012) Sensitive and accurate dual-wavelength UV-VIS polarization detector for optical remote sensing of tropospheric aerosols. Appl Phys B 108:197–216. https://doi.org/10.1007/s00340-012-5066-x

David G, Thomas B, Dupart Y, D'Anna B, George C, Miffre A, Rairoux P (2014) UV polarization lidar for remote sensing new particles formation in the atmosphere. Opt Express 22:A1009. https://doi.org/10.1364/OE.22.0A1009

David G, Thomas B, Nousiainen T, Miffre A, Rairoux P (2013) Retrieving simulated volcanic, desert dust and sea-salt particle properties from two/three-component particle mixtures using UV-VIS polarization lidar and T matrix. Atmos Chem Phys 13:6757–6776. https://doi.org/10.5194/acp-13-6757-2013

Dubois C, Cholleton D, Gemayel R, Chen Y, Surratt JD, George C, Rairoux P, Miffre A, Riva M (2021) Decrease in sulfate aerosol light backscattering by reactive uptake of isoprene epoxydiols. Phys Chem Chem Phys 23:5927–5935. https://doi.org/10.1039/D0CP05468B

Dubovik O, Sinyuk A, Lapyonok T, Holben BN, Mishchenko M, Yang P, Eck TF, Volten H, Muñoz O, Veihelmann B, van der Zande WJ, Leon J-F, Sorokin M, Slutsker I (2006a) Application of spheroid models to account for aerosol particle nonsphericity in remote sensing of desert dust. J Geophys Res 111:D11208. https://doi.org/10.1029/2005JD006619

Dubovik O, Sinyuk A, Lapyonok T, Holben BN, Mishchenko M, Yang P, Eck TF, Volten H, Muñoz O, Veihelmann B, van der Zande WJ, Leon J-F, Sorokin M, Slutsker I (2006b) Application of spheroid models to account for aerosol particle nonsphericity in remote sensing of desert dust. J Geophys Res Atmos 111. https://doi.org/10.1029/2005JD006619

Dupart Y, King SM, Nekat B, Nowak A, Wiedensohler A, Herrmann H, David G, Thomas B, Miffre A, Rairoux P, D'Anna B, George C (2012) Mineral dust photochemistry induces nucleation events in the presence of SO2. Proc Natl Acad Sci U S A 109:20842–20847. https://doi.org/10.1073/pnas.1212297109

Freudenthaler V, Esselborn M, Wiegner M, Heese B, Tesche M, Ansmann A, MüLLER D, Althausen D, Wirth M, Fix A, Ehret G, Knippertz P, Toledano C, Gasteiger J, Garhammer M, Seefeldner M (2009) Depolarization ratio profiling at several wavelengths in pure Saharan dust during SAMUM 2006. Tellus B Chem Phys Meteorol 61:165–179. https://doi.org/10.1111/j.1600-0889.2008.00396.x

Fu R, Wang C, Muñoz O, Videen G, Santarpia JL, Pan YL (2017) Elastic back-scatteringpatterns via particle surface roughness and orientation from single trapped airborne aerosol particles. J Quant Spectro Radiat Transfer 187:224–231

Gasteiger J, Wiegner M, GROß S, Freudenthaler V, Toledano C, Tesche M, Kandler K (2011) Modelling lidar-relevant optical properties of complex mineral dust aerosols. Tellus Ser B Chem Phys Meteorol 63:725–741. https://doi.org/10.1111/j.1600-0889.2011.00559.x

Gautam P, Maughan JB, Ilavsky J, Sorensen CM (2020) Light scattering study of highly absorptive, non-fractal, hematite aggregates. J Quant Spectrosc Radiat Transf 246:106919. https://doi.org/10.1016/j.jqsrt.2020.106919

Glen A, Brooks SD (2013) A new method for measuring optical scattering properties of atmospherically relevant dusts using the Cloud and Aerosol Spectrometer with Polarization (CASPOL). Atmos Chem Phys 13:1345–1356. https://doi.org/10.5194/acp-13-1345-2013

Go S, Lyapustin A, Schuster GL, Choi M, Ginoux P, Chin M, Kalashnikova O, Dubovik O, Kim J, da Silva A, Holben B, Reid JS (2022) Inferring iron-oxide species content in atmospheric mineral dust from DSCOVR EPIC observations. Atmos Chem Phys 22:1395–1423. https://doi.org/10.5194/acp-22-1395-2022

Gómez Martín JC, Guirado D, Frattin E, Bermudez-Edo M, Cariñanos Gonzalez P, Olmo Reyes FJ, Nousiainen T, Gutiérrez PJ, Moreno F, Muñoz O (2021) On the application of scattering matrix measurements to detection and identification of major types of airborne aerosol particles: Volcanic ash, desert dust and pollen. J Quant Spectrosc Radiat Transf 271:107761. https://doi.org/10.1016/j.jqsrt.2021.107761

Haarig M, Ansmann A, Baars H, Jimenez C, Veselovskii I, Engelmann R, Althausen D (2018) Depolarization and lidar ratios at 355, 532, and 1064 nm and microphysical properties of aged tropospheric and stratospheric Canadian wildfire smoke. Atmos Chem Phys 18:11847–11861. https://doi.org/10.5194/acp-18-11847-2018

Haarig M, Ansmann A, Engelmann R, Baars H, Toledano C, Torres B, Althausen D, Radenz M, Wandinger U (2022) First triple-wavelength lidar observations of depolarization and extinction-to-backscatter ratios of Saharan dust. Atmos Chem Phys 22:355–369. https://doi.org/10.5194/acp-22-355-2022

Hofer J, Ansmann A, Althausen D, Engelmann R, Baars H, Fomba, KW, Wandinger U, Abdullaev SF, Makhmudov AN (2020) Optical properties of Central Asian aerosol relevant for spaceborne lidar applications and aerosol typing at 355 and 532 nm. Atmos Chem Phys 20:9265–9280. https://doi.org/10.5194/acp-20-9265-2020

Huang X, Yang P, Kattawar G, Liou K-N (2015) Effect of mineral dust aerosol aspect ratio on polarized reflectance. J Quant Spectrosc Radiat Transf 151:97–109. https://doi.org/10.1016/j.jqsrt.2014.09.014

Huang Y, Liu C, Yao B, Yin Y, Bi L (2020) Scattering matrices of mineral dust aerosols: a refinement of the refractive index impact. Atmos Chem Phys 20:2865–2876. https://doi.org/10.5194/acp-20-2865-2020

Hunt AJ (1973) A new polarization-modulated light scattering instrument. Rev Sci Instrum 44:1753. https://doi.org/10.1063/1.1686049

IPCC (2013) Climate change 2013: the physical science basis: Working Group I contribution to the Fifth Assessment Report of the Intergovernmental Panel on Climate Change. Cambridge Univ. Press, New York, NY.

Järvinen E, Kemppinen O, Nousiainen T, Kociok T, Möhler O, Leisner T, Schnaiter M (2016) Laboratory investigations of mineral dust near-backscattering depolarization ratios. J Quant Spectrosc Radiat Transf Electromagnetic Light Scattering Nonspherical Particles XV: Celebrating 150 years of Maxwell's electromagnetics 178:192–208. https://doi.org/10.1016/j.jqsrt.2016.02.003

Kahnert M (2015) Modelling radiometric properties of inhomogeneous mineral dust particles: Applicability and limitations of effective medium theories. J Quant Spectrosc Radiat Transf 152:16–27. https://doi.org/10.1016/j.jqsrt.2014.10.025

Kahnert M, Kanngießer F, Järvinen E, Schnaiter M (2020) Aerosol-optics model for the backscatter depolarisation ratio of mineral dust particles. J Quant Spectrosc Radiat Transf 254:107177. https://doi.org/10.1016/j.jqsrt.2020.107177

Kahnert M, Nousiainen T, Lindqvist H (2014) Review: Model particles in atmospheric optics. J Quant Spectrosc Radiat Transf 146:41–58. https://doi.org/10.1016/j.jqsrt.2014.02.014

Kahnert M, Nousiainen T, Räisainen P (2007) Mie simulations as an error source in mineral aerosol radiative forcing calculations. QJR 133:299–307. https://doi.org/10.1002/qj.40

Kahnert M, Nousiainen T, Thomas MA, Tyynelä J (2012) Light scattering by particles with small-scale surface roughness: comparison of four classes of model geometries. J Quant Spectrosc Radiat Transf Electromagnetic Light Scatter Non-Spherical Particles XIII 113:2356–2367. https://doi.org/10.1016/j.jqsrt.2012.03.017

Kahnert M, Rother T (2011) Modeling optical properties of particles with small-scale surface roughness: combination of group theory with a perturbation approach. Opt Express 19:11138–11151. https://doi.org/10.1364/OE.19.011138

Kemppinen O, Nousiainen T, Lindqvist H (2015) The impact of surface roughness on scattering by realistically shaped wavelength-scale dust particles. J Quant Spectrosc Radiat Transf 150:55–67. https://doi.org/10.1016/j.jqsrt.2014.05.024

Kuga Y, Ishimaru A (1984) Retroreflectance from a dense distribution of spherical particles. J Opt Soc Am A 1:831–835

Laan EC, Volten H, Stam DM, Muñoz O, Hovenier JW, Roush TL (2009) Scattering matrices and expansion coefficients of martian analogue palagonite particles. Icarus 199:219–230. https://doi.org/10.1016/j.icarus.2008.08.011

Liou K, Lahore H (1974) Laser sensing of cloud composition: a backscattered depolarization technique. J Appl Meteorol

Liu C, Lee Panetta R, Yang P (2014) Inhomogeneity structure and the applicability of effective medium approximations in calculating light scattering by inhomogeneous particles. J Quant Spectrosc Radiat Transf 146:331–348. https://doi.org/10.1016/j.jqsrt.2014.03.018

Liu L, Mishchenko MI, Hovenier JW, Volten H, Muñoz O (2003) Scattering matrix of quartz aerosols: comparison and synthesis of laboratory and Lorenz-Mie results. J Quant Spectrosc Radiat Transf 79–80:911–920. https://doi.org/10.1016/S0022-4073(02)00328-X

Liu L, Mishchenko MI (2018) Scattering and radiative properties of morphologically complex carbonaceous aerosols: a systematic modeling study. Remote Sens 10(10). https://doi.org/10.3390/rs10101634

Mehri T (2018) Rétrodiffusion (UV, VIS) résolue en polarisation de particules d'origine désertique: expériences de laboratoire et en atmosphère réelle par lidar

Mehri T, Kemppinen O, David G, Lindqvist H, Tyynelä J, Nousiainen T, Rairoux P, Miffre A (2018) Investigating the size, shape and surface roughness dependence of polarization lidars with light-scattering computations on real mineral dust particles: Application to dust particles' external mixtures and dust mass concentration retrievals. Atmospheric Res 203:44–61. https://doi.org/10.1016/j.atmosres.2017.11.027

Merikallio S, Lindqvist H, Nousiainen T, Kahnert M (2011) Modelling light scattering by mineral dust using spheroids: assessment of applicability. Atmospheric Chem. Phys. 11:5347–5363. https://doi.org/10.5194/acp-11-5347-2011

Mie G (1908) Beiträge zur Optik trüber Medien, speziell kolloidaler Metallösungen. Ann Phys 330:377–445. https://doi.org/10.1002/andp.19083300302

Miffre A, Cholleton D, Mehri T, Rairoux P (2019a) Remote Sensing Observation of New Particle Formation Events with a (UV, VIS) Polarization Lidar. Remote Sens 11:1761. https://doi.org/10.3390/rs11151761

Miffre A, Cholleton D, Noel, C. and Rairoux P (2022) Investigating the dependence of mineral dust depolarization on complex refractive index and size with a laboratory polarimeter at 180.0° lidar backscattering angle, submitted to Atmos Meas Tech

Miffre A, Cholleton D, Rairoux P (2020) On the use of light polarization to investigate the size, shape, and refractive index dependence of backscattering Ångström exponents. Opt Lett 45:1084. https://doi.org/10.1364/OL.385107

Miffre A, Cholleton D, Rairoux P (2019b) Laboratory evaluation of the scattering matrix elements of mineral dust particles from 176.0° up to 180.0°-exact backscattering angle. J Quant Spectrosc Radiat Transf 222–223:45–59. https://doi.org/10.1016/j.jqsrt.2018.10.019

Miffre A, David G, Thomas B, Rairoux P (2011) Atmospheric non-spherical particles optical properties from UV-polarization lidar and scattering matrix. Geophys Res Lett 38:L16804. https://doi.org/10.1029/2011GL048310

Miffre A, David G, Thomas B, Rairoux P, Fjaeraa AM, Kristiansen NI, Stohl A (2012) Volcanic aerosol optical properties and phase partitioning behavior after long-range advection characterized by UV-Lidar measurements. Atmos Environ 48:76–84. https://doi.org/10.1016/j.atmosenv.2011.03.057

Miffre A, Mehri T, Francis M, Rairoux P (2016) UV–VIS depolarization from Arizona Test Dust particles at exact backscattering angle. J Quant Spectrosc Radiat Transf 169:79–90. https://doi.org/10.1016/j.jqsrt.2015.09.016

Mishchenko MI (2009) Electromagnetic scattering by nonspherical particles: a tutorial review. J Quant Spectrosc Radiat Transf 110:808–832. https://doi.org/10.1016/j.jqsrt.2008.12.005

Mishchenko MI, Hovenier JW (1995) Depolarization of light backscattered by randomly oriented nonspherical particles. Opt Lett 20:1356. https://doi.org/10.1364/OL.20.001356

Mishchenko MI, Hovenier JW, Mackowski DW (2004a) Single scattering by a small volume element. J Opt Soc Am A Opt Image Sci Vis 21:71–87. https://doi.org/10.1364/JOSAA.21.000071

Mishchenko MI, Liu L, Travis LD, Lacis AA (2004b) Scattering and radiative properties of semi-external versus external mixtures of different aerosol types. J Quant Spectrosc Radiat Transf 88:139–147. https://doi.org/10.1016/j.jqsrt.2003.12.032

Mishchenko MI, Liu L, Videen G (2007) Conditions of applicability of the single-scattering approximation. Opt Express 15:7522. https://doi.org/10.1364/OE.15.007522

Mishchenko MI, Travis L, Lacis A (2002) Scattering, absorption, and emission of light by small particles. Cambridge

Mishchenko MI, Travis LD (1998) Capabilities and limitations of a current FORTRAN implementation of the T-matrix method for randomly oriented, rotationally symmetric scatterers. J Quant Spectrosc Radiat Transf 60:309–324. https://doi.org/10.1016/S0022-4073(98)00008-9

Mishchenko MI, Dlugach ZM, Zakharova NT (2013) Direct demonstration of the concept of unrestricted effective-medium approximations. Opt Lett 39:3935–3938

Monge M, Rosenorn T, Favez O, Müller M, Adler G, Abo Riziq A, Rudich Y, Hermann H, George C, D'Anna B (2012) Alternative pathway for atmospheric particles growth. Proc 109, 6840–4. https://doi.org/10.1073/pnas.1120593109

Müller D, Veselovskii I, Kolgotin A, Tesche M, Ansmann A, Dubovik O (2013) Vertical profiles of pure dust and mixed smoke–dust plumes inferred from inversion of multiwavelength Raman/polarization lidar data and comparison to AERONET retrievals and in situ observations. Appl Opt 52:3178. https://doi.org/10.1364/AO.52.003178

Muñoz O, Hovenier JW (2011) Laboratory measurements of single light scattering by ensembles of randomly oriented small irregular particles in air: a review. J Quant Spectrosc Radiat Transf 112:1646–1657. https://doi.org/10.1016/j.jqsrt.2011.02.005

Nakayama T, Sato K, Imamura T, Matsumi Y (2018) Effect of oxidation process on complex refractive index of secondary organic aerosol generated from isoprene. Environ Sci Technol 52:2566–2574. https://doi.org/10.1021/acs.est.7b05852

Nousiainen T (2009) Optical modeling of mineral dust particles: a review. J Quant Spectrosc Radiat Transf 110:1261–1279. https://doi.org/10.1016/j.jqsrt.2009.03.002

Olson N, Lei Z, Craig RL, Zhang Y, Chen Y, Lambe AT, Zhang Z, Gold A, Surratt JD, Ault AP (2019) Reactive uptake of isoprene epoxydiols increases the viscosity of the core of phase-separated aerosol particles. ACS Earth Space Chem. acsearthspacechem.9b00138. https://doi.org/10.1021/acsearthspacechem.9b00138

Ovadnevaite J, Ceburnis D, Plauskaite-Sukiene K, Modini R, Dupuy R, Rimselyte I, Ramonet M, Kvietkus K, Ristovski Z, Berresheim H, O'Dowd CD (2009) Volcanic sulphate and arctic dust plumes over the North Atlantic Ocean. Atmos Environ 43:4968–4974. https://doi.org/10.1016/j.atmosenv.2009.07.007

Paulien L, Ceolato R, Fossard F, Rairoux P, Miffre A (2021) (UV, VIS) Laboratory evaluation of the lidar depolarization ratio of freshly emitted soot aggregates from pool fire in ambient air at exact backscattering angle. J Quant Spectrosc Radiat Transf 260:107451. https://doi.org/10.1016/j.jqsrt.2020.107451

Perry R, Hunt A, Huffman D (1978) Experimental determinations of Mueller scattering matrices for nonspherical particles. Appl Opt 17:2700–2710. https://doi.org/10.1364/AO.17.002700

Räisänen P, Haapanala P, Chung CE, Kahnert M, Makkonen R, Tonttila J, Nousiainen T (2013) Impact of dust particle non-sphericity on climate simulations. QJR Meteorol Soc 139:2222–2232. https://doi.org/10.1002/qj.2084

Riva M, Chen Y, Zhang Y, Lei Z, Olson N, Boyer HC, Narayan S, Yee LD, Green H, Cui T, Zhang Z, Baumann KD, Fort M, Edgerton ES, Budisulistiorini S, Rose CA, Ribeiro I, de Oliveira RL, Santos E, Szopa S, Machado C, Zhao Y, Alves E, de Sa S, Hu W, Knipping E, Shaw S, Duvoisin Junior S, Souza RAF. de Palm BB, Jimenez JL, Glasius M, Goldstein AH, Pye HOT, Gold A, Turpin BJ, Vizuete W, Martin ST, Thornton J, Dutcher CS, Ault AP, Surratt JD (2019) Increasing Isoprene Epoxydiol-to-Inorganic Sulfate Aerosol (IEPOX:Sulf $_{\text{inorg}}$) ratio results in extensive conversion of inorganic sulfate to organosulfur forms: implications for aerosol physicochemical properties. Environ Sci Technol acs.est.9b01019. https://doi.org/10.1021/acs.est.9b01019

Saito M, Yang P, Ding J, Liu X (2021) A comprehensive database of the optical properties of irregular aerosol particles for radiative transfer simulations. J Atmos Sci 78:2089–2111. https://doi.org/10.1175/JAS-D-20-0338.1

Sakai T, Nagai T, Zaizen Y, Mano Y (2010) Backscattering linear depolarization ratio measurements of mineral, sea-salt, and ammonium sulfate particles simulated in a laboratory chamber. Appl Opt 49:4441. https://doi.org/10.1364/AO.49.004441

Schnaiter M, Büttner S, Möhler O, Skrotzki J, Vragel M, Wagner R (2012) Influence of particle size and shape on the backscattering linear depolarisation ratio of small ice crystals-cloud chamber measurements in the context of contrail and cirrus microphysics. Atmos Chem Phys 12:10465–10484. https://doi.org/10.5194/acp-12-10465-2012

Seinfeld JH, Pandis SN (2006) Atmospheric chemistry and physics: from air pollution to climate change, 2nd edn. J. Wiley, Hoboken, N.J

Shakya KM, Peltier RE (2015) Non-sulfate sulfur in fine aerosols across the United States: insight for organosulfate prevalence. Atmos Environ 100:159–166. https://doi.org/10.1016/j.atmosenv.2014.10.058

Shakya KM, Peltier RE (2013) Investigating missing sources of sulfur at fairbanks. Alaska Environ Sci Technol 47:9332–9338. https://doi.org/10.1021/es402020b

Stier P, Seinfeld JH, Kinne S, Boucher O (2007) Aerosol absorption and radiative forcing. Atmos Chem Phys 25

Studinski RC, Vitkin IA (2000) Methodology for examining polarized light interactions with tissues and tissuelike media in the exact backscattering direction. J Biomed Opt 5:330–337. https://doi.org/10.1117/1.430004

Surratt JD, Gómez-González Y, Chan AWH, Vermeylen R, Shahgholi M, Kleindienst TE, Edney EO, Offenberg JH, Lewandowski M, Jaoui M, Maenhaut W, Claeys M, Flagan RC, Seinfeld JH (2008) Organosulfate formation in biogenic secondary organic aerosol. J Phys Chem A 112:8345–8378. https://doi.org/10.1021/jp802310p

Tesche M, Ansmann A, Müller D, Althausen D, Engelmann R, Freudenthaler V, Groß S (2009) Vertically resolved separation of dust and smoke over Cape Verde using multiwavelength Raman and polarization lidars during Saharan Mineral Dust Experiment 2008. J Geophys Res 114. https://doi.org/10.1029/2009JD011862

Tesche M, Kolgotin A, Haarig M, Burton SP, Ferrare RA, Hostetler CA, Mueller D (2019) 3+2 + X: what is the most useful depolarization input for retrieving microphysical properties of non-spherical particles from lidar measurements using the spheroid model of Dubovik et al. (2006)

Tolocka MP, Turpin B (2012) Contribution of organosulfur compounds to organic aerosol mass. Environ Sci Technol 46:7978–7983. https://doi.org/10.1021/es300651v

van de Hulst HC (1957) Light scattering by small particles. Courier Corporation

Veselovskii I, Goloub P, Podvin T, Bovchaliuk V, Derimian Y, Augustin P, Fourmentin M, Tanre D, Korenskiy M, Whiteman DN, Diallo A, Ndiaye T, Kolgotin A, Dubovik O (2016) Retrieval of optical and physical properties of African dust from multiwavelength Raman lidar measurements during the SHADOW campaign in Senegal. Atmos Chem Phys 16:7013–7028. https://doi.org/10.5194/acp-16-7013-2016

Videen G, Muinonen K (2015) Light-scattering evolution from particles to regolith. J Quant Spectrosc Radiat Transf 150:87–94. https://doi.org/10.1016/j.jqsrt.2014.05.019

Videen G, Zubko E, Arnold JA, MacCall B, Weinberger AJ, Shkuratov Y, Muñoz O (2018) On the interpolation of light-scattering responses from irregularly shaped particles. J Quant Spectrosc Radiat Transf 211:123–128. https://doi.org/10.1016/j.jqsrt.2018.03.009

Vitkin IA, Studinski RCN (2001) Polarization preservation in diffusive scattering from in vivo turbid biological media: effects of tissue optical absorption in the exact backscattering direction. Opt Commun 190:37–43

Volten H, Muñoz O, Rol E, de Haan JF, Vassen W, Hovenier JW, Muinonen K, Nousiainen T (2001) Scattering matrices of mineral aerosol particles at 441.6 nm and 632.8 nm. J Geophys Res 106:17375. https://doi.org/10.1029/2001JD900068

Wang X, Lai J, Li Z (2012) Polarization studies for backscattering of RBC suspensions based on Mueller matrix decomposition. Opt Express 20:20771

Wiersma DS, Bartolini P, Lagendijk A, Righini R (1997) Localization of light in a disordered medium. Nature 390:671–673. https://doi.org/10.1038/37757

Winker DM, Pelon JR, McCormick MP (2003) The CALIPSO mission: spaceborne lidar for observation of aerosols and clouds. In: Singh UN, Itabe T, Liu Z (eds) Presented at the Third international asia-pacific environmental remote sensing remote sensing of the atmosphere, ocean, environment, and space, Hangzhou, China, p. 1. https://doi.org/10.1117/12.466539

Zhang Y, Chen Y, Lambe AT, Olson NE, Lei Z, Craig RL, Zhang Z, Gold A, Onasch TB, Jayne JT, Worsnop DR, Gaston CJ, Thornton JA, Vizuete W, Ault AP, Surratt JD (2018) Effect of the Aerosol-Phase State on secondary organic aerosol formation from the reactive uptake of isoprene-derived epoxydiols (IEPOX). Environ Sci Technol Lett 5:167–174. https://doi.org/10.1021/acs.estlett.8b00044

Zong R, Weng F, Bi L, Lin X, Rao C, Li W (2021) Impact of hematite on dust absorption at wavelengths ranging from 0.2 to 1.0 μm: an evaluation of literature data using the T-matrix method. Opt Express 29:17405–17427. https://doi.org/10.1364/OE.427611

Zubko E, Muinonen K, Muñoz O, Nousiainen T, Shkuratov Y, Sun W, Videen G (2013) Light scattering by feldspar particles: comparison of model agglomerate debris particles with laboratory samples. J Quant Spectrosc Radiat Transf 131:175–187. https://doi.org/10.1016/j.jqsrt.2013.01.017

Zubko E, Muinonen K, Shkuratov Y, Videen G, Nousiainen T (2007) Scattering of light by roughened Gaussian random particles. J Quant Spectrosc Radiat Transf 106:604–615. https://doi.org/10.1016/j.jqsrt.2007.01.050

Index

A. Kokhanovsky (ed.), *Springer Series in Light Scattering*, Springer Series in Light Scattering, https://doi.org/10.1007/978-3-031-10298-1